Universidade do Minho
Escola de Engenharia

Ali Dalalbashi Esfahani

Multi-scale investigation of the durability performance of TRM-strengthened masonry

May 2022

Multi-scale investigation of the durability performance of TRM-strengthened masonry
Ali Dalalbashi
UMinho | 2022

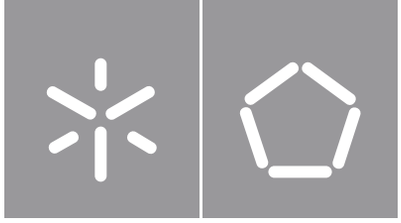

Universidade do Minho
Escola de Engenharia

Ali Dalalbashi Esfahani

Multi-scale investigation of the durability performance of TRM-strengthened masonry

Dotoral thesis
Civil engineering

Work performed under the supervision of
Professor Doctor Daniel V.Oliveira
Professor Doctor Bahman Ghiassi

May 2022

Acknowledgments

This thesis has been carried out at the Civil Engineering Department of the University of Minho, Portugal, under the supervision of Associate Professor Dr. Daniel V. Oliveira from the University of Minho and Associate Professor Dr. Bahman Ghiassi from the University of Birmingham. This work was partly financed by FEDER funds through the Competitively Factors Operational Program (COMPETE), by national funds through the Foundation for Science and Technology (FCT) within the scope of the project POCI-01-0145-FEDER-007633, and grant SFRH/BD/131282/2017, all grateful acknowledgments.

It is my honor to express my gratitude and appreciation to my study leaders, Dr. Ghiassi and Dr. Oliveira, whose continuous support, encouragement, technical discussions, and guidance made this voyage possible and a worthwhile experience. Their continued support allowed me to follow my ideas and develop the outlined work. They have encouraged my research and allowed me to grow as a researcher. It has been a pleasure to work with them.

Without the enthusiastic dedication of the laboratory technicians, the experiment would not have been completed so efficiently. Especial thanks to laboratory technicians, Mr. Antonio Matos, Marco Jorge, Carlos Jesus, and José Gonçalves, for their support and assistance throughout my experimental work.

I should also appreciate Dr. Stefano De Santis from Roma Tre University, Italy, for his collaboration in scientific discussions of cyclic tests. I would like to express my gratitude to all the master students who helped me during my research: Ana Freitas from the University of Minho, Gianluca Cocco from Università di Bologna, and Andrea Della Torre from Roma Tre University. Additionally, it is my pleasure to thank my colleagues and friends for their constant support, pep talks, and technical discussions (You are all wonderful!).

This thesis is dedicated to my family, who deserve acknowledgment. I am deeply grateful to my parents and sister for their emotional and moral support. I am grateful to my wife for all her care, support, understanding, and love, without which I would never have made it through.

Statement of integrity

I hereby declare having conducted this academic work with integrity. I confirm that I have not used plagiarism or any form of undue use of information or falsification of results along the process leading to its elaboration.

I further declare that I have fully acknowledged the Code of Ethical Conduct of the University of Minho.

University of Minho, May 2022

Full name: Ali Dalalbashi Esfahani

Signature: _____

Resumo

As argamassas reforçadas com têxteis (TRM) receberam recentemente uma importância significativa como reforço exterior (EBR) de alvenaria e estruturas de betão armado. São constituídas por uma malha de alta resistência embebida numa matriz inorgânica. As malhas são compostas por fios bidireccionais contendo basalto, carbono, vidro resistente aos álcalis, aramida, ou fios de PBO, ou malhas unidireccionais contendo cordões de aço de alta resistência. Os têxteis são aplicados utilizando matrizes tais como argamassas de cimento, cal, ou geopolímero. Na literatura científica e técnica, há também a utilização de outros nomes e acrónimos, tais como matriz cimentícia reforçada com fibras (FRCM) e calda reforçada com aço (SRG) quando são utilizadas malhas de aço.

Devido à novidade desta solução, questões como a durabilidade e o desempenho a longo prazo são desconhecidas em grande escala e não existem ainda normas de ensaio e métodos de dimensionamento relevantes. Para colmatar esta lacuna, este estudo apresenta uma investigação experimental e analítica abrangente a vários níveis sobre o desempenho mecânico dos compósitos TRM utilizados para o reforço de estruturas de alvenaria existentes. O objectivo é fornecer novos conhecimentos sobre o efeito das condições ambientais críticas sobre o TRM-alvenaria em diferentes escalas e correlacionar a degradação do material com o desempenho estrutural global através da realização de testes de envelhecimento acelerado em sistemas TRM-alvenaria. Assim, a resposta micro (ligação malha-argamassa), meso (ligação TRM-substrato), e macro (resposta do TRM em tração e resposta no plano e para fora do plano da alvenaria reforçada) dos TRM são combinadas e investigadas em profundidade sob condições ambientais naturais e de gelo-degelo (FT). Compostos TRM à base de fibras de aço e vidro feitos com argamassa hidráulica à base de cal são utilizados para reforçar painéis de alvenaria de tijolo cerâmico sólido.

Os resultados mostram que o comportamento a longo prazo dos compósitos TRM para diferentes idades é significativamente dependente da combinação de argamassa e fibras e, portanto, pode mudar notavelmente entre diferentes soluções TRM. Também se observa que os TRM à base de cal não podem atingir as suas propriedades mecânicas totais em condições interiores, mesmo após 3 anos. As condições exteriores levam a uma melhor cura das amostras e à obtenção de propriedades mecânicas significativamente mais elevadas nestes compósitos. No entanto, também pode levar a uma deterioração significativa em idades posteriores. Os resultados indicam também que as condições de exposição ao gelo-degelo consideradas neste estudo não têm efeitos prejudiciais sobre a resistência da argamassa. Contudo, o comportamento de ligação fibra-argamassa pode deteriorar-se, sendo o nível de deterioração dependente do tipo de fibra, do comprimento embebido e da configuração da fibra.

Palavas-chave:

TRM composto; Aderência fibra/matriz; gelo-degelo; comportamento a longo prazo; modelação analítica.

Abstract

Textile-reinforced mortars (TRM) have recently received significant attention for the externally bonded reinforcement (EBR) of masonry and reinforced concrete structures. They are comprised of a high-strength mesh bonded with an inorganic matrix. The meshes are composed of bidirectional yarns containing basalt, carbon, alkali-resistant glass, aramid or PBO yarns, or unidirectional textiles containing ultra-high tensile strength steel cords. Textiles are bonded using matrices such as cement, lime, or geopolymer mortars. In scientific and technical literature, there is also a use of other names and acronyms: fabric-reinforced cementitious matrix (FRCM) and steel-reinforced grout (SRG) when using steel fabrics.

Due to the novelty of this solution, several issues such as durability and long-term performance are unknown to a large extend, and relevant test standards and design methods do not exist yet. To address this gap, this study presents a multi-level comprehensive experimental and analytical investigation on the mechanical performance of TRM composites to strengthen existing masonry structures. The purpose is to provide new insights into the effect of critical environmental conditions on TRM-masonry at different scales and correlate material degradation to the global structural performance by performing accelerated aging tests on TRM-masonry systems. Hence, micro (fabric-to-mortar bond), meso (TRM-to-substrate bond), and macro (TRM tensile response and in-plane and the out-of-plane response of TRM-strengthened masonry) response of TRMs are combined and investigated in-depth under natural environmental and freeze-thaw (FT) conditions. Steel and AR-glass-based TRM composites made with hydraulic lime-based mortar are used for strengthening clay brick-based masonry panels.

The results show that the long-term behavior of TRM composites for different ages is significantly dependent on the mortar and fiber combination and, therefore, can change notably between different TRM solutions. It is also observed that lime-based TRMs cannot reach their total mechanical properties under indoor conditions even after three years. Outdoor conditions lead to better curing of the samples and achieving significantly higher mechanical properties in these composites. However, it can also lead to a significant deterioration at later ages. The results also indicate that the freezing-thawing exposure conditions considered in this study do not have detrimental effects on the mortar strength. However, the fiber-to-mortar bond behavior can deteriorate, because the level of deterioration depends on the fiber type, embedded length, and fiber configuration.

Keywords:

TRM composite; Fiber/matrix bond; Freeze-Thaw; Long-term behavior; Analytical modeling.

Contents

List of Figures

List of Tables

List of symbols

A	area of specimen in water absorption due to capillary action test
A_f	the cross-sectional area of fiber
A_m	the cross-sectional area of mortar
A_n	net area of the in-plane wallet specimen
b_m	width of masonry panel under flexural test
C	water absorption coefficient due to capillary action
c	depth of the effective compressive block
d_f	fiber diameter
$E_{1,2,3}$	Elastic modulus corresponding to three different tensile responses of TRM composites
E_f	fiber elastic modulus
E_m	mortar elastic modulus
E	the toughness or absorbed energy
E_{deb}	debonding energy
E_{po}	pull-out energy
E_{max}	the area under the load-displacement curve of masonry panel under flexural test until the maximum load
E_{cr}	the area under the load-displacement curve of masonry panel under flexural test until the cracking load
ε_f	the local strain in the fiber
ε_m	the local strain in the mortar
F	the local force in the fiber
f'_m	compressive strength of masonry
f'_t	tensile strength of masonry
f_{fe}	the effective tensile stress level in the TRM composite
f_{fv}	tensile strength of the TRM reinforcement
f_{xk}	flexural strength of masonry
G	shear modulus of masonry panel
G_d	chemical bond energy
H_w	height of the masonry panel
K	Initial stiffness
L′	length of the masonry panel
L	the embedded length of fiber in a mortar
L_b	bond length

L_g	the axial gauge length of masonry panel under diagonal compressive load
L_s	outer span length of masonry panel under flexural test
M	the local force in the mortar
M_n	nominal flexural strength of TRM strengthened-masonry panel
M_{Rd}	nominal flexural strength of unreinforced masonry panel
OSR	orthogonal strength ratio of masonry panel (anisotropy degree of masonry)
P	the total force bearing by mortar and fiber
P/S	the slope of the initial portion of the experimental pull-out curve
p_0	open porosity
P_b	bonded force
P_{cr}	cracking load of masonry panel
P_{crit}	critical pull-out load
P_d	debonding force
P_f	frictional load
P_P	peak load
$P_{P'}$	second peak load corresponding to slip hardening
Q	$1/A_fE_f + 1/A_mE_m$
R	modulus of rupture of masonry panel under flexural test
r_f	fiber radius
R_N	modulus of rupture of masonry panel under flexural test failure normal to bed joint
R_P	modulus of rupture of masonry panel under flexural test failure parallel to bed joint
S	the local slip between fiber and mortar
S_0	relative slip of the fiber at full debonding
S_{dyn}	relative slip of the fiber at the dynamic stage
$S_{modulus}$	section modulus of un-crack masonry wallet
s_P	slip corresponding to peak load
$s_{P'}$	slip corresponding to the second peak load
t	the thickness of the masonry panel
t_c	TRM composite thickness
t_f	interfacial frictional shear flow
t_{max}	maximum allowable interfacial shear flow
u	debonding length
v	rigid-body displacement of the yarn
V_f	shear strength provided by TRM composites
V_m	shear strength provided by the masonry
V_n	nominal shear capacity of TRM strengthened-masonry panel
V_{ss}	shear strength of masonry panel
$W_{24hr.}$	specimen mass after 24 hours

$W_{absorption}$	moisture uptake content at time t
W_d	the dry weight of the specimen
W_i	the apparent mass of saturated specimen immersed in water
$W_{sat.}$	mass of saturated mortar or brick
W_t	weight of specimen at time t
X	saturation crack spacing of TRM composite under tensile load
α	A_m/A_f
β	slip hardening
β	strain-hardening coefficients
γ	masonry shear strain
δ	the coefficient of fiber-matrix misfit
Δ_{cr}	corresponding deflection of the cracking load of masonry panel
δ_f	the elongation of the fiber
Δ_h	transversal extension of masonry panel under diagonal compressive load
δ_m	the elongation of the mortar
Δ_v	axial shortening of masonry panel under diagonal compressive load
$\varepsilon_{1, 2, 3}$	strain stress corresponding to three different tensile responses of TRM composites
η'	reflecting the slope of the pull-out curve
κ	the bond modulus
λ	$(\kappa\psi Q)^{1/2}$
μ	friction coefficient assumed 0.2
μ_0	coefficient of internal shear friction in mortar joint
$\mu_{bending}$	ductility parameter of masonry panel under flexural test
$\mu_{diagonal}$	the pseudo-ductility ratio of masonry panel under diagonal compressive load
ν_f	poisson ratio of fiber
ν_m	poisson ratio of mortar
ρ_w	density of water
$\sigma_{1, 2, 3}$	tensile stress corresponding to three different tensile responses of TRM composites
σ_{mu}	the direct tensile strength of the mortar
τ	the local shear at the fiber-matrix interface
τ'	masonry shear stress
τ_0	the shear bond strength between mortar and brick
τ_{dyn}	The dynamic shear strength
τ_f	maximum frictional bond shear stress
τ_{max}	the maximum shear strength
υ_f	volumetric fractions of the yarns
υ_m	volumetric fractions of the mortar
ψ	the perimeter of the fiber

List of Acronyms

AR-glass fabric	alkaline resistance glass fabric
CTE	coefficient of thermal expansion
DTA	differential thermal analyses
EBR	externally bonded reinforcement
FRCM	fiber reinforced cementitious materials
FRP	fiber-reinforced polymer
FT conditions	freeze-thaw conditions
IRA	initial rate absorption
LVDT	linear variable differential transformer
PBO fabric	polybenzoxazole fabric
SRG	steel-reinforced grout
TRM	textile-reinforced mortar
URM	unreinforced masonry
XRD	X-ray diffraction

Chapter 1: Introduction

Cultural heritage buildings and other iconic masonry structures, as the main elements of built heritage, should be preserved in order to maintain their cultural and socioeconomic values for future generations. Built heritage is exposed to continuous natural (environmental conditions and earthquakes) and man-made hazards, threatening their performance. Over the last few decades, there have been several devastating earthquakes worldwide, resulting in large amounts of cultural heritage structures being damaged or even destroyed. Furthermore, natural aging has affected the mechanical performance of masonry constructions over the years, for which proper conservation approaches should be looked for and applied [1].

Many unreinforced masonry (URM) structures are prone to failure during earthquakes due to their weakness against in-plane and out-of-plane seismic loads [2]. The development of strategies for repairing and strengthening structures made of these materials has been the object of many studies during the last decades. Among these, externally bonded reinforcement (EBR) is one of the most common strengthening methodologies in which composite material is attached to the external surface of weak structural components. Traditionally, fiber-reinforced polymers (FRPs) were mainly used as the strengthening material in this system. However, the issues related to sustainability, durability, poor performance at high temperatures, and compatibility of these composites with masonry substrate indicated the need to use and develop novel and more compatible repair materials. In an attempt to alleviate the drawbacks that arise from the use of FRPs [3,4], textile-reinforced mortar (TRM) composites have been proposed in the last years [5,6].

TRMs (also known as FRCMs: fiber-reinforced cementitious materials) are composed of continuous yarns/fibers embedded in an inorganic matrix and present several advantages: they have a good thermal capacity, are applicable to wet surfaces, are removable, and can be compatible with masonry and concrete surfaces [3,7]. The large variety of available fabric types and mortars allows TRM composites to develop with an extensive range of mechanical properties [8,9]. When properly designed, TRMs show a pseudo-ductile response with distributed cracking, making them interesting for seismic strengthening applications [10,11].

Despite the recent attention these composites have found as a suitable strengthening material, many issues regarding their mechanical response and durability are still unknown. Recent studies have mainly focused on the tensile response of TRMs, the bond of TRM-to-masonry, and the bond of fiber-to-mortar [12–19]. Structural scale tests (diagonal compression and out-of-plane tests on TRM-strengthened masonry) are still few and mainly focused on the effect of textile and substrate types [20,21], the number of textile layers [22], and symmetrical or asymmetrical application of the repair [23–25].

This document aims to investigate TRM performance before and after degradation to determine the short and long-term performance of strengthening masonry structures. For this purpose, material characterizations of glass and steel textiles, lime-based mortar, and brick as a substrate will be explored. Then, the bond durability of fiber-to-mortar and TRM-to-substrate and tensile behavior will be examined under pull-out, single-lap shear, and tensile tests. After that, the long-term performance of masonry strengthened by TRM systems will be investigated. Moreover, the analytical analysis will be performed for both verifying results.

1.1. Motivation and objectives

Composite-based strengthening systems in cultural heritage buildings are quite spread nowadays. A critical aspect is the long-term behavior of these systems. Important recent work has been developed on the durability of FRP strengthening systems [26–29], but almost nothing is known about the performance of TRM-based strengthening systems applied to masonry substrates due to the novelty of the method. Durability aspects are of significant importance as TRM is increasingly seen as the best substitute of FRP for masonry due to its much better compatibility with the substrate [30].

The main purpose of this study is the multi-scale characterization of the durability performance of TRM-strengthened masonry systems through extensive experimental and analytical activities. The materials will be brick masonry as the substrate, lime-based mortar as the matrix of the reinforcing system, and glass and steel fibers as the reinforcing materials.

The focus will be on understanding the mechanics and degradation mechanisms at the material level (brick, mortar, fiber), at the bond level (fiber-to-mortar bond and TRM-to-masonry bond), the composite level (TRM composites), and the structural level (TRM-strengthened masonry components). A comprehensive series of relevant tests and simulation methods will be used/developed for achieving the ambitious objectives established in the research plan. As several issues related to TRM-strengthened masonry are still open and test methods and standards are not available yet, a critical investigation on the suitability of different test setups and test methods will also be performed.

The durability performance will be investigated by performing accelerated aging tests under critical environmental conditions (freeze-thaw and natural environmental conditions). The tests will be designed to develop a clear understanding of the active degradation mechanisms and establish correlations between the observed mechanisms at different performance levels. The experimental data will develop suitable time-dependent constitutive laws for analytical simulations. According to the gathered data, a

refined predictive analytical model will be developed for simulating the long-term performance of TRM-strengthened masonry under different exposure conditions.

Hence, the following Research Questions (RQ) are formulated. The RQs are designed in a way to follow a natural path to consider all aspects related to the long-term performance assessment of TRM-strengthened masonry systems.

- Which are the critical parameters controlling the effectiveness of a TRM strengthening system?
- How is the short-term and long-term performance of TRMs?
- How is the durability of TRM systems, and what are the corresponding degradation mechanisms?

1.2. Outline and methodology of the thesis

Using a quantitative methodology, the thesis describes the development and analysis of a combined experimental and analytical campaign. It consists of eight chapters that reflect the tasks. In each chapter, there are highlights (except in Chapter 1 and Chapter 8), the main text, and the conclusions. The chapters are as follows:

- **Chapter 1- Introduction:** presents the motivation for conducting the research, the objectives of the research, its scope, and a summary of the thesis.
- **Chapter 2- Overview on TRM composites:** expands the background and research focus presented in the previous chapter, discussing the necessary techniques to accomplish the objectives and highlighting current research gaps. Moreover, it identifies the critical gaps in the test methods and durability behavior of TRM-masonry composites.
- **Chapter 3- Experimental plans and test methods:** describes the detailed procedures for preparing the specimens and performing the tests. A description of the materials and methods of material characterization is provided. In addition, the test methods conducted for investigating the TRM behavior from the micro to the structural level are described.
- **Chapter 4- Material results:** presents and discusses experimental results of physical and mechanical properties of materials under different environmental conditions.
- **Chapter 5- Mechanical performance of TRM composites:** investigates the effective parameters deeply on the fiber-to-mortar bond behavior such as test setup, bond length, fiber configurations, slip rate, and cyclic loading. Further, the effect of different curing conditions on the fiber-to-mortar and TRM-to-substrate bond behavior and the durability performance of TRM composites under freeze-thaw and natural environmental conditions are examined and discussed.

- **Chapter 6- Mechanical performance of TRM-strengthened masonry panels:** describes the effect of surface treatment on the structural behavior of TRM-strengthened masonry. Additionally, the short and long-term behavior of TRM-strengthened masonry panels is investigated by performing diagonal compression and out-of-plane tests.
- **Chapter 7- Analytical modeling:** proposes a new bond-slip law and analytical model, which predicts the bond behavior of lime and cement-based TRM composites considering the slip hardening and softening effects observed in experimental tests. In addition, the shear and flexural strength of the masonry panels were computed and compared with the experimental results.
- **Chapter 8- Conclusion:** summarizes the main points gleaned from the research described in the previous chapter and suggests areas that should be investigated further.

Chapter 2: Overview on TRM composites

This chapter provides an overview of current research findings on the TRM composites' behavior and points out current research gaps. There are several highlights in this chapter:

- The main techniques for characterizing TRM systems are pull-out, single-lap shear, tensile, and flexure tests. Additionally, diagonal compression and out-of-plane tests are conducted to investigate the structural behavior of TRM-strengthened masonry walls.
- Lime mortars are suitable for strengthening historical and masonry structures because of their compatibility, sustainability, breathability, and ability to accommodate structural movements. In general, cementitious matrices are used to strengthen structures stronger than traditional masonry constructions.
- TRM composites show a pseudo-ductile response and multiple cracking by reaching their bond strength, making them suitable for seismic strengthening applications.
- Several parameters have been analyzed on TRM behavior from a macro level (e.g., tensile, flexural, and TRM-to-substrate tests) to structural level, including fiber types, coating, layout, ratios, overlap, as well as mortar strength, and symmetrical or asymmetrical configurations.
- TRM mechanics and durability continue to be poorly understood, which is one of the impediments to their widespread use.

2.1. Introduction

Textile-reinforced mortar (TRM) composites, as an externally bonded reinforcement technique, have received extensive attention as a sustainable solution for seismic strengthening of masonry and historical monuments. Besides TRM, other names and acronyms are used in scientific and technical documents such as fabric reinforced cementitious matrix (FRCM), inorganic matrix-based composites, and (when comprising steel textiles) steel-reinforced grout (SRG). TRMs, an attractive alternative to the Fiber Reinforced Polymer (FRP) systems, are composed of continuous fabrics embedded in an inorganic matrix [31]. Compared to FRPs, TRMs have some advantages, physical, chemical, and mechanical compatibility, fire resistance, installation time and cost, and removability, since they are manufactured from inorganic matrices rather than resins [3,7,32]. The textile is usually made of glass, steel, basalt, carbon, or even natural fibers (e.g., hemp, flax), and matrices are either cementitious or lime-based. Lime mortars are suitable for strengthening masonry and historical constructions because of compatibility aspects, sustainability issues, breathability, and the capability of accommodating structural movements [33–38]. Cementitious matrices are usually used to strengthen structures stronger than traditional masonry constructions [39–42].

Although the mechanical behavior of lime-based TRMs has been the subject of many recent studies [8,13,14,32,43–45], very little is known about these systems' long-term behavior and durability or the effects of local material degradation on the global behavior of the structure. However, the durability performance of TRM composites has recently received attention from a few studies, in which the effect of freeze-thaw cycles, water attack, alkaline environment, and salt crystallization on the mechanical performance of TRM composites have been examined [46–51].

2.2. Fiber-to-mortar bond behavior

The fiber-to-mortar bond behavior has only received limited attention, especially in the case of lime-based TRMs [31,52]. A fundamental understanding of this mechanism and the parameters affecting that, currently missing, is critical for developing TRM composites with enhanced mechanical properties and for the fit-for-purpose design of TRMs for strengthening applications. The effectiveness of the TRM strengthening technique is strongly dependent on the nonlinear properties of the TRM composite and the TRM-to-substrate bond properties. At the same time, the nonlinear properties of TRMs are dependent on the fiber and mortar properties as well as fiber-to-mortar bond behavior [53–55]. The layout of the textile and the roughness of its surface influence the mechanical interlocking with the mortar. The presence of

coating or impregnating resins affects the chemical bond with the mortar [15,56]. The strength of the mortar and its curing duration [17] and conditions [57] affect the load transfer mechanism with the textile. Finally, the filaments bond in a yarn plays an important role; it is improved by the deep penetration of resin or mortar in the cross-section of the yarn, whereas when the bond between the outer filaments and the mortar is stronger than that between the outer and the inner filaments telescopic failure may occur [58]. Load-slip curves generally exhibit a first stage, during which the load transfer relies on chemical bond and interlocking, followed by a second stage associated with the onset of relative slippage and the combined contribution of adhesion and friction, and by a final stage, in which the load transfer relies on friction only [16].

2.2.1. Pull-out test setup

Although there is a gap in the literature on fiber-to-mortar bond response in TRM composites (made of lime-based mortars), much information can be found regarding this mechanism in textile reinforced concrete (TRC), where cementitious mortars and short fibers are utilized [59]. Various pull-out test setups have been used in literature to characterize the fiber-to-mortar (or concrete) bond behavior. These can generally be categorized into pull-push (or single-sided) [60–62] and pull-pull (or double-sided) [63,64] tests. However, the differences between the experimental results obtained from different test setups are poorly addressed. In the pull-push tests (Fig. 2-1a), the mortar is fixed from the top, and the fiber is pulled out from the same direction. Therefore, compressive stresses are generated in the mortar near the loaded end in this test configuration. In the pull-pull tests (Fig. 2-1b), on the other hand, the mortar is fixed from the bottom, and the fiber is pulled out from the top (or vice versa), simulating direct tensile tests. Tensile stresses are therefore developed in the mortar in this test setup. Therefore, due to the different stress conditions imposed on the specimens in these test configurations, different pull-out responses are expected.

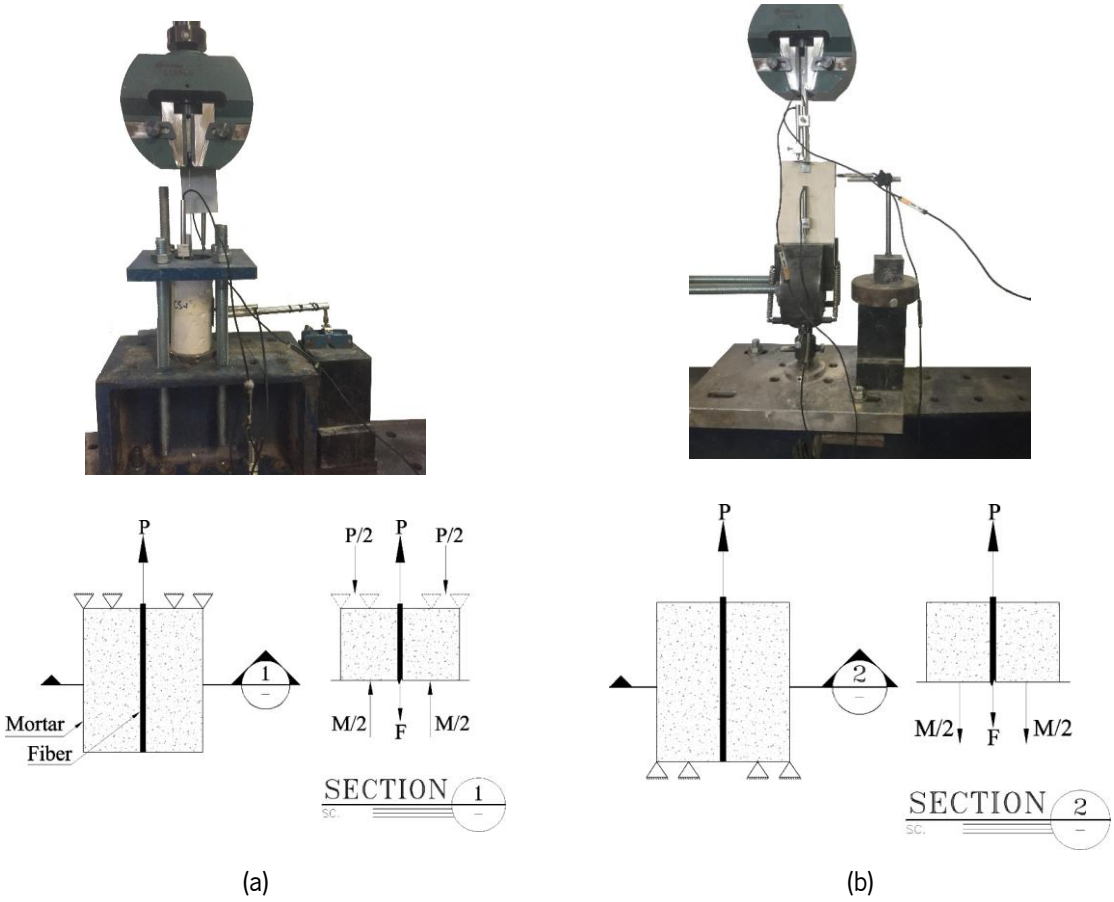

Fig. 2-1. Common layout of pull-out tests: (a) pull-push; (b) pull-pull.

Among the few available studies on the characterization of fiber-to-mortar bond behavior of TRM-strengthened masonry, Ghiassi et al. [31] used a single-sided pull-out test configuration on fibers embedded in cylindrical specimens (Fig. 2-2). They, however, reported difficulties in the preparation of the specimens (vertical alignment of the fibers) and the measurement of the slip during the tests due to the flexibility of the fibers. Hence, a pre-load was applied to specimens to ensure a straight alignment of the fiber at the loaded end and to facilitate the installation of the LVDT before the initiation of the tests. Additionally, due to the geometrical limitations of the test setup, the LVDTs used for slip measurements were attached at a certain distance from the mortar edge. Therefore, the elastic deformation of the fibers had to be reduced from the recorded values with the LVDTs that could lead to additional uncertainty in the slip measurements.

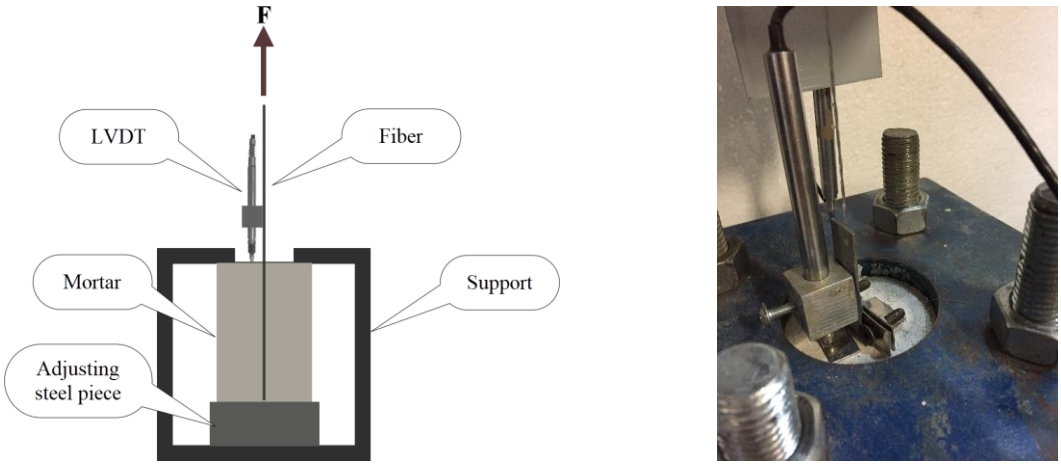

(a) (b)

Fig. 2-2. Pull-out test conducted by Ghiassi et al. [31]: (a) test setup; (b) details of LVDT position.

2.2.2. Pull-out mechanism

Two typical loads versus slip response curves of a monotonic pull-out test are shown in Fig. 2-3. As shown in Fig. 2-3, the pull-out curve typically consists of three stages: elastic, nonlinear, and dynamic stages [31,61,62,65,66]. In the elastic stage (section OA), a perfect bond exists between the fiber and the mortar, and the adhesive bond is active. In the nonlinear stage (section AB), debonding initiates, and the response becomes nonlinear due to the progressive destruction of the adhesive bond. By reaching the peak load (P_P), the dynamic stage initiates. The transition from the progressive debonding stage to the dynamic stage can either be a sudden drop in the pull-out load (Fig. 2-3a) if the frictional bond is smaller than the adhesive bond or smooth and upward (Fig. 2-3b) [67–70]. The pull-out load corresponding to point C (in this case, P_f) represents the total frictional load resisted by the system [69,71].

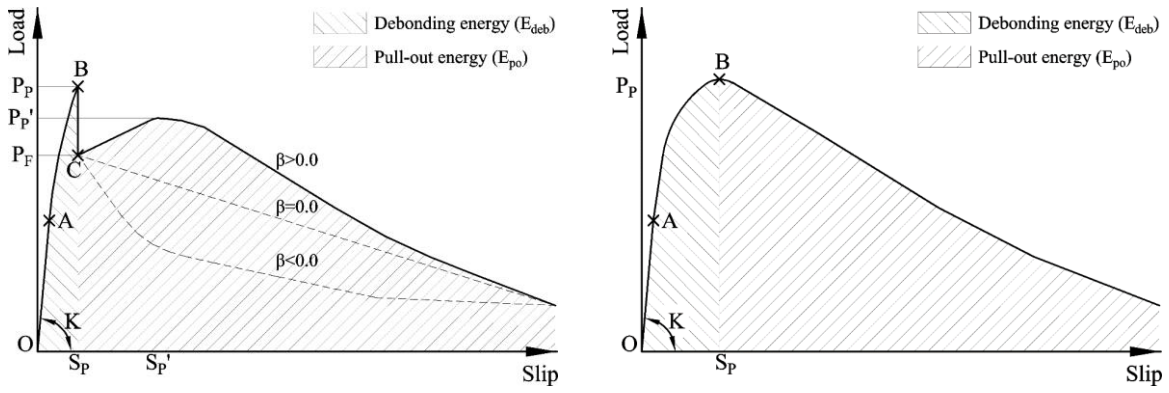

(a) (b)

Fig. 2-3. Typical pull-out curves with the different transitions from nonlinear stage to dynamic stage: (a) load drop; (b) smooth.

At the dynamic stage, the only resisting mechanism is friction between the textile and the matrix [68,69,72,73]. In the dynamic stage, a constant (β= 0.0), a slip hardening (β> 0.0), or a slip softening (β< 0.0) can be observed [67,70,72,74–76]. When a slip hardening is observed in the dynamic stage, the load increases with a lower slope than that of the static one. Slip hardening occurs when the frictional stress between the fiber and the mortar increases due to the shape of fibers, embedded length, and the abrasion effect [69,72,73,76–78]. As the test progresses, the portion of the textile-to-mortar interface where friction holds progressively becomes smaller as the debonding length becomes larger. A second load peak (P_P') is attained (at a slip of s_P') when the interaction of the damaged yarn surface is diminished, and friction becomes the sole resistance mechanism. With the increment of the debonded length, the load resistance of the system reduces until the end of the tests.

The peak load (P_P) and its corresponding slip (s_P), initial stiffness (K), toughness or absorbed energy (E), and chemical bond energy (G_d) are the main outcomes of the pull-out tests [62,66,69], as shown in Fig. 2-3. These parameters are used for investigation of the bond behavior and can significantly affect the experimental interpretations or the extracted bond-slip laws. The initial stiffness is obtained as the slope of the linear portion of the load-slip curve and corresponds to the initial stage of the stress transfer before the occurrence of any interfacial cracking [31,62,66]. The toughness or absorbed energy is defined as the area under the load-slip curve [62,66,79–81] and includes debonding energy (E_{deb}) and pull-out energy (E_{po}). Debonding energy expresses the energy dissipated during the complete fiber debonding and is measured as the area under the load-slip curve until the peak load [69,82]. Material deformation and new surfaces by cracking characterize the debonding energy [80]. The pull-out energy is the energy dissipated by the fiber-to-mortar frictional interface during the dynamic stage. It is measured as the area under the load-slip curve from the peak load until the end [69,80]. Additionally, the pull-out energy attributes the post-peak behavior of the fiber-to-mortar bond, which is significant in the pseud-ductility behavior of TRM composites. Meanwhile, the chemical bond energy (G_d) is expressed as follows [68,73,83]:

$$G_d = \frac{2(P_P - P_F)^2}{\pi^2 E_f d_f^3}, \; N/mm \qquad \text{Eq. 2-1}$$

E_f is the fiber elastic modulus, and d_f is the fiber diameter. The chemical bond energy will be zero if the frictional bond is equal to the adhesive bond. It occurs in the load-slip curves with a smooth and upward trend at the transition from the nonlinear stage to the dynamic stage.

2.2.3. Analytical modeling

A fiber-to-mortar bond can be analyzed with the assumption of a perfect or non-perfect bond to determine cohesive interface models [84]. The perfect bond models do not consider any slip between the reinforcing element and the matrix and are usually used in composites in which the deformability of the matrix is larger or similar to that of the fiber, such as in fiber-reinforced polymers. Conversely, the cohesive interface models allow for a slippage between the fiber and the surrounding matrix. They are typically used to analyze the bond behavior in composite materials where the matrix has much less deformability than the fiber, like fiber-reinforced mortars.

A wide range of analytical and numerical models have been proposed and used in the literature to simulate the pull-out response or extract bond-slip laws from experimental pull-out curves. The shear lag models, such as the one proposed by Naaman et al. [65,85], Mobasher [66], and Banholzer et al. [84,86], are among the most commonly used techniques as they provide a realistic explanation of the debonding phenomenon by considering both adhesive and friction bond effects [87,88]. Using these models, bond-slip laws can be derived indirectly from pull-out tests [89,90]. Various multi-linear or nonlinear [65,66,85] and N-piecewise [84,86] bond-slip laws have been proposed in the literature, as shown in Fig. 2-4. The fiber pull-out problem usually comprises a reinforcing element, a matrix, and the interfacial region. Depending on the stress level and distribution, this interfacial region can involve the bonded, the debonded, and the sliding zones. These zones occur during the pull-out test consecutively or simultaneously throughout the embedded length of the fiber.

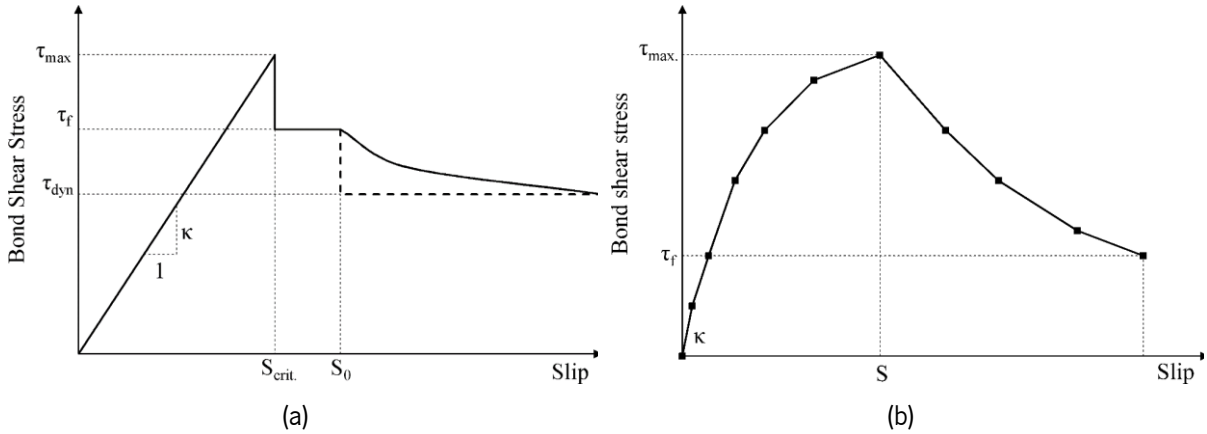

Fig. 2-4. Typical bond-slip law: (a) multi linear; (b) N-piecewise.

2.3. TRM tensile behavior

2.3.1. Tensile test

In spite of the fact that the tensile behavior of TRM composites cannot yet be fully exploited, direct tensile tests are required for the mechanical characterization of textile-reinforced matrix systems and should become a fundamental component of product qualification. In addition to providing the ultimate stress, tensile tests also provide Young's modulus of composite, which is an essential property to factor into reinforcement designs. Additionally, tensile tests provide information about fiber-to-matrix bond properties, which is crucial for cracking [30]. Specimen production, dimensions, and shape, as well as load application and test setup, affect the tensile behavior of TRM composite response [91]. Hence, the following are the tensile mechanism of TRM composites and some issues concerning their tensile behavior based on literature reports.

2.3.2. Tensile mechanism

Fig. 2-5 shows the schematic tensile behavior of TRM composites [8,14,31,43,92–94]. Three stages are usually identified in the tensile response: a linear stage which presents the behavior of uncracked composite material [92–94] (stage I); a crack development stage, in which multiple cracks are formed in the specimen (stage II). The distance, the width, and the number of cracks strictly depend on the fiber-to-mortar bond behavior in this stage [92–94]. Finally, no further cracking occurs in the last stage, and the load is only resisted by the bundles/yarns (stage III). The peak tensile stress (σ), the strain corresponding to the peak stress (ε), and tensile modulus (E) in each stage and the saturated crack spacing are the critical characteristics of the tensile response of TRM composites.

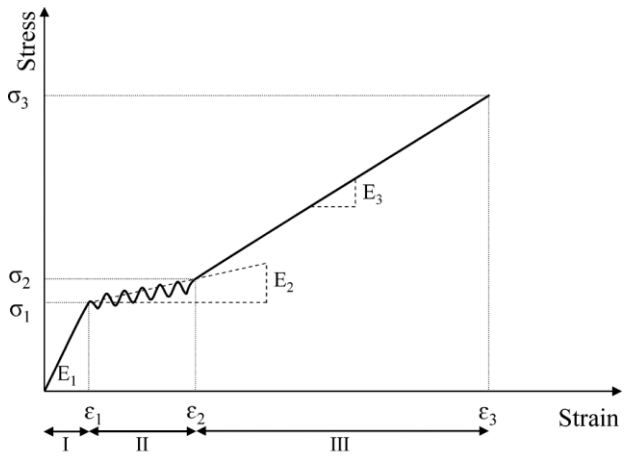

Fig. 2-5. Typical tensile stress-strain behavior of TRMs.

2.3.3. Influence parameters on TRM tensile behavior

Tensile tests on TRM systems have been carried out with two different test setups, the rigid load application (clevis-grip) method recommended by ACI-549.4R [95] and AC434 [96] and the soft clamping-grip method suggested by RILEM TC 232-TDT [97] (Fig. 2-6). However, some recommendations and studies have already been made regarding the test setup [32,43,98,99]. In the clevis-grip method, the main transfer mechanism is an adhesive in tension and shear. In addition, to avoid potential adverse effects from possible eccentricity and misalignment, one of the grips shall allow rotation in two parallel planes [100]. In the clamping-grip method, friction load transfer causes the applied load to increase gradually. In this case, the clamps can produce high compressive stresses at the end of the specimens [32]. Different boundary conditions between these two tests can lead to significantly different results [99,101].

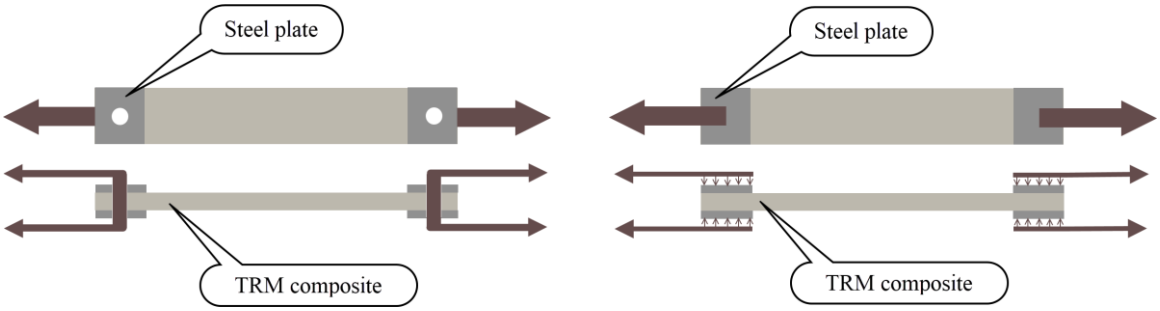

Fig. 2-6. Typical tensile test methods: (a) rigid load; (b) soft clamping-grip.

Several studies have focused on the tensile behavior of TRM composites by considering the effect of different material properties. The fiber type (e.g., carbon, AR-glass, basalt, PBO, and natural fibers) [8,32,102] and different coating treatments [103,104] had a significant effect on the tensile response of TRM composites. According to the results, fiber layout, such as mesh size [32], the ratio [43,105], layer number [106,107], and overlap [108], affect the tensile mechanism. Besides, some research studies have revealed that the development of the tensile properties of TRM composites is critically influenced by the mortar properties [105] and additive [109]. All these variables were investigated under monotonic loading, while in some studies [110–112], the effect of fatigue loading and fiber pre-stress on the tensile performance of TRM composites were examined.

2.4. TRM-to-substrate bond behavior

In the perspective of using TRM composites as a strengthening system, bond behavior between the mortar and the substrate should be carefully characterized. The bond behavior of TRM systems to substrates is studied using two approaches: single-lap and double-lap shear tests (see Fig. 2-7). The composite is applied to one side of the substrate during the single-lap shear test; however, in the second layout, the composite is placed on both sides of the substrate and tested simultaneously. The following paragraphs present the findings from the stress-transfer study at the TRM-to-substrate interface.

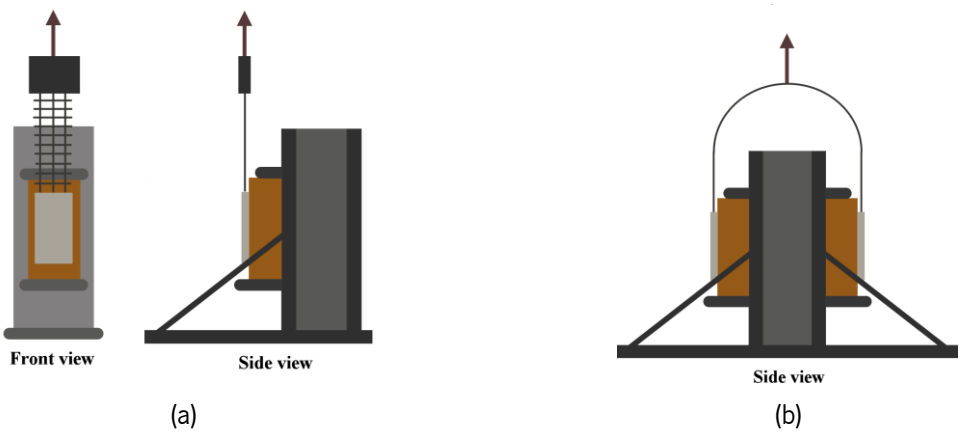

Fig. 2-7. The schematics of shear bond test: (a) single-lap shear test; (b) double-lap shear test.

Studies on advanced TRM-to-masonry systems have highlighted the complexity of their bond behavior [113]. It is generally accepted that shear stress transfer mechanisms govern overall performance and that the tensile capacity of textile reinforcement is not always optimally used. Several factors can influence the bonding between TRM and substrate, including fiber and mortar properties [13], surface preparation [114], load rating [115], and fatigue behavior [116]. In the literature, there have been tests of several types of fibers: carbon [117,118], steel [118,119], PBO [41,116], basalt [45,118], glass [13,118], and natural fiber [113] and their single-lap shear response were experimentally examined. Besides, the effect of the number of fiber layer and mortar layer on the TRM-to-substrate bond behavior was investigated [44,120]. The outcomes displayed that bond strength increases about twofold for two layers, but it increases nonlinearly for more layers, which indicates that the fibers are exploited less effectively [44]. Additionally, the anchorage length of the jacket must be sufficient to safely transfer tensile loads from the masonry substrate to the TRM without premature debonding occurring [121]. The fiber embedded length in mortar also impacts both the failure load and the failure mechanism [32,122]. Consequently, the

mechanical properties of mortar and fiber, textile layout, bond length, and the substrate surface improved bond performance [30,123].

It is of vital importance for the efficiency of the strengthening system that the mortar, reinforcement, and substrate are all closely bonded since debonding can lead to premature failure and low fiber activation. Accordingly, the desirable failure mode of masonry elements reinforced with TRM will either involve masonry failure in compression or textile failure in tension [121]. Failure modes of masonry substrate strengthened by TRM depend on the substrate properties, the mortarshear strength, the fiber tensile strength, and the fiber-to-mortar and TRM-to-substrate bond [118]. Fig. 2-8 shows the typical failure modes of the TRM-to-masonry: (a) debonding at the interface between TRM and substrate (Fig. 2-8a, b), (b) slipping between fiber and mortar (Fig. 2-8c-e), and (c) fiber rupture (Fig. 2-8f). Depending on the failure mode, the obtained load-slip curves might include only an elastic part or an elastic stage followed by a nonlinear stage [119].

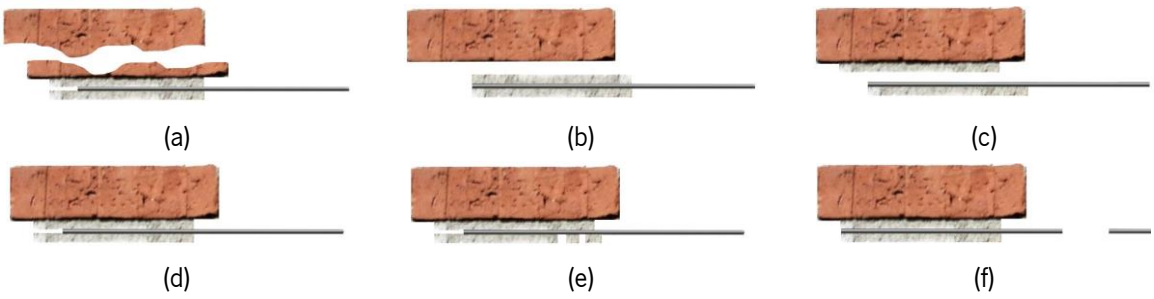

Fig. 2-8. Typical failure modes observed for TRM-to-masonry joints: (a) debonding with cohesive failure of the substrate; (b) debonding at the mortar-to-substrate interface; (c) debonding at the textile-to-mortar interface; (d) textile slippage within the mortar; (e) textile slippage within the mortar with cracking of the outer layer of mortar; (f) tensile rupture of the textile [31].

2.5. TRM-strengthened masonry panels

Many unreinforced masonry (URM) structures are prone to catastrophic failure during earthquakes [124,125] due to their weakness against in-plane and out-of-plane seismic loads [2]. The development of strategies for repairing and strengthening structures made of these materials has been the object of many studies during the last decades. Among these, externally bonded reinforcement is one of the most common strengthening methodologies, in which composite material is attached to the external surface of weak structural components. Traditionally, FRPs were mainly used as the strengthening material in this system [126,127]. However, the sustainability, durability, poor performance at high temperatures and

compatibility of these composites with masonry indicated the need to use and develop novel repair materials. In an attempt to alleviate the drawbacks that arise from the use of FRPs [128–130], TRM composites have been proposed in the last years [10,131,132].

Many studies have been published to evaluate the performance of TRM-strengthened masonry, but these studies are at the structural scale [23,133–135]. The performance of these systems from the material to the structural level, which is the main goal of this study, is still lacking [136,137]. Many studies have examined the in-plane and out-of-plane performance of TRM-strengthened masonry with particular attention to the effect of textile and substrate types [20,21], the number of textile layers [22,25], and symmetrical or asymmetrical configurations [23,24]. The results show that TRM composites increase the load-bearing capacity of masonry elements and improve their structural behavior by reducing brittle failure modes [138,139]. In addition, the TRMs provide pseudo-ductility and improve the strength and stiffness of masonry panels under diagonal compression and out-of-plane loads [134,139,140].

An in-plane lateral load can cause masonry walls to crack at diagonals, slide at shear joints, and even crush at the toe. These failure modes vary with the masonry's physical and mechanical characteristics and its compression state and aspect ratio [141]. The tendency for diagonal tensile cracks to develop through masonry units can be observed in the formation of a single crack. There is the possibility of shear sliding along a single mortar bed joint or multi-bed joints in a step format. The compressed corners may cause toe-crushing failure [141]. By contrast, masonry walls strengthened by TRM cracks at diagonals under an in-plane load, showing improvement in the in-plane performance of masonry walls [10].

Most existing exterior masonry walls, particularly URM, are not strong enough to withstand out-of-plane loads. Due to earthquakes or high wind pressure, their failure is sudden and brittle [142]. The out-of-plane behavior of masonry panels has been investigated in two directions: failure parallel and perpendicular (normal) to the bed joints [143]. The experimental results indicate that a single crack formed across the URM panel and along the bed joint in failure parallel to the bed joint. However, in failure normal to the bed joint, the cracks started in the head joint and progressed around the units in alternate courses [143,144]. The experimental results showed that the TRM composites did not affect the failure of panels parallel to bed joints so that after cracking the TRM composites, the strengthened panel failed at the masonry bed joints [144]. In contrast, under failure normal to bed joint, TRM-strengthened panels failed through the masonry units [144].

2.6. Durability aspects

The mechanical behavior of TRM composites has been the subject of an increasing number of experimental and analytical studies; however, their durability and long-term performance have received less attention. Therefore, it is difficult to characterize the main mechanisms contributing to the degradation of TRM composite and ascertain their short-term and long-term performance [47]. It is clear that the effectiveness of using externally bonded reinforcement (EBR) systems like TRM composites depends on the long-term bond behavior of the fibers to the bricks and the TRM to the concrete. Following are sections where the degradation mechanism and available studies about the durability characteristics of TRM composites will be discussed.

2.6.1. Degradation mechanism

The performance of structural components over time is determined by the durability of their materials and components against the degradation agents existing in service. According to the literature, the durability of structural components and materials is defined as their ability to resist cracking, chemical degradation, and delamination under specified load and environmental conditions [145]. As for durability tests, several environmental conditions have been already highlighted in the experimental reports, such as chemical attack (acid, saline, and alkaline solutions), freeze-thaw conditions, fire, hot water, creep, and fatigue [46,146]. Aging or Degradation is the process of changing a material's physical or mechanical properties, classified into three chemical, physical, and mechanical mechanisms [147]. Depending on the material characteristics and the environment, these mechanisms may interact in an additive or subtractive manner. Physical degradation is characterized by reversible changes to the material properties, whereas irreversible changes define chemical degradation. Finally, the degradation of materials under mechanical stress is known as mechanical degradation. As a result, degradation profoundly impacts the durability and serviceability of materials, and understanding its mechanisms is essential to assessing long-term performance [147].

2.6.2. Durability tests

As Table 2-1 displays, most literature discusses the effect of acid, saline, and alkaline solutions on the mechanical performance of TRM composites [39,50,51,148–154]. A variety of methods has been utilized to evaluate the effect of chemical attacks on the performance of TRM composites since there are no well-established standard procedures. The methods include immersing samples in a solution or performing

wet-dry cycles for various times or temperatures, summarized in Table 2-1. Most studies have considered alkaline environments, with very few considering acidic or saline environments. Researchers tended to focus on tensile behavior of TRM composites under chemical attack [148,149,152–154], while flexural [39], fiber-to-matrix [39], and TRM-to-substrate (pull-off [148,151] and single-lap shear [50,51]) tests received much less attention. Among the fabrics studied, glass and carbon are the most common, while steel, basalt, PBO, and natural fibers, which are most relevant in strengthening applications, receive less attention.

There have been contradictory results observed in experiments. Some studies report improved mechanical performance (tensile strength) following exposure to alkaline or saline conditions [155]. In contrast, others reported deterioration of mechanical response when cement or lime-based TRMs were used [149,156]. In acidic solutions, the results are also contradictory, so that some studies show sufficient resistance while others reveal a great deal of vulnerability [149]. It is also essential to consider the type of mechanical tests and test setups used after the aging of materials. In some cases, the chemical attack did not deteriorate tensile strength, while it did deteriorate flexural strength due to the role of boundary conditions on the durability test results [157]. A similar observation has also been reported for bond strength and failure mode in saline and alkaline environments, where test setup (pull-off [155,158] or single-lap shear tests [159]) had a significant impact on results.

Observations on the effect of freeze-thaw (FT) environmental conditions on the mechanical performance of TRMs indicate that the deterioration level strongly depends on the mortar strength, the fiber-to-mortar, and the TRM-to-substrate bond. Besides, the exposure conditions such as the temperature level, the number of cycles, and the degree of mortar saturation influence the durability performance of TRM composites [39,48,148,149,151,153,160–162]. Table 2-2 reports the existing studies on the effect of FT conditions on the TRM composite's performance. Due to the lack of well-established standards for evaluating the freeze-thaw resistance of TRC composites, various researchers used different protocols and some cycles, which makes performing critical comparisons between different experimental databases difficult. In addition, a limited number of studies have been conducted in this field that only focuses on mechanical properties (tensile and flexural) of TRM composites. A few studies have examined the changes in bond strength between TRM and substrate with pull-off test [151] and fiber and matrix with pull-out test [39]. Under FT conditions, the results present dual behavior of TRM composites, so that in some of them, mechanical degradation has been observed [48,154,160,161], and in others, mechanical behavior has improved [148,149,153].

Table 2-1. Literature review on the durability of TRM composites under chemical attacks.

Ref.	Fiber	Matrix	Standard	Methodology	Solution	Duration	post-exposed tests
[39]	hybrid fabric	concrete	GB/T 50082-2009	wet-dry	saline [5% NaCl]	90, 120, and 150 cycles (each cycle includes 12 hrs. wet & 12 hrs. dry)	pull-out & flexural
[50]	AR-glass	lime	ASTM D7705	immersion	saline [3.5% NaCl]	1000 hrs. at 60°C	single-lap
				wet-dry		10 cycles (each cycle includes 2 days wet & 2 days dry at 60°C)	
[51]	steel	lime and cement	-	wet-dry	saline [2% NaCl+ 8% $Na_2SO_4.10H_2O$]	6 cycles (each cycle includes 2 days wet by capillary & 3 days dry at 60°C)	single-lap
[148]	carbon & PBO	cement	AC434	immersion	saline [ocean]	1000 & 3000 hrs. at 22°C	tensile & pull-off
					alkaline [$Ca(OH)_2$+ NaOH+ KOH, pH> 12.5]		
[149]	glass	HPC cement	JSCE-E 549-2000	immersion	alkaline [10% NaOH, pH= 13]	1440 hrs.	tensile
					acidic [10% H_2SO_4, pH= 0.2 to 3.4]		
[150]	E-glass, AR-glass, carbon, basalt, PBO, steel	-	ASTM E2098 ETAG 029	immersion	alkaline [16% $Ca(OH)_2$, pH= 12.6] [16%$Ca(OH)_2$+1%NaOH+1.4%KOH, pH= 13] [0.2% KOH, pH= 12.5] [5% $Ca(OH)_2$, pH= 14]	168, 720, 1440, 2160, 4320 hrs. at 20 and 45°C	tensile
[151]	carbon	cement, lime	RILEM MS A.1, 1998	wet-dry	saline [10% Na_2SO_4]	11 cycles	pull-off
[152]	AR-glass	hydrated and air lime	-	immersion	saline [3.5% NaCl]	1000 hrs. at 23°C	tensile
					alkaline [$NaHCO_3$, pH= 10]		
[153]	carbon	pozzolan	-	immersion	saline [3.5% NaCl]	1000 hrs.	tensile
					alkaline [$NaHCO_3$, pH= 10]		
					acidic [HCl, pH= 2.5]		
[154]	AR-glass	cement	ASTM D1141-98	immersion	saline [2.45% NaCl+ 0.41% Na_2SO_4]	1000 hrs. at 40°C	tensile
					alkaline [4% NaOH, pH= 13]		

Table 2-2. Literature review on the durability of TRM composites under freeze-thaw conditions.

Ref.	Fiber	Matrix	Standard	Conditions	Duration	post-exposed tests
[39]	hybrid fabric (carbon and E-glass)	concrete	GB/T 50082-2009	-18°C ↔ 5°C immersing in saline	50, 70, 90 cycles (3 hrs. freezing and thawing)	pull-out & flexural
[48]	AR-glass	cement	ASTM C666	-18°C ↔ 4°C (100% RH)	25, 50, 100, 150, 500 cycles (30 min freezing and 30 min thawing)	tensile
[148]	carbon & PBO	cement	AC434	-18°C ↔ 37.7°C (100% RH)	20 cycles (4 hrs. freezing and 12 hrs. thawing)	tensile
[153]	carbon	lime	AC434	-18°C ↔ 37.7°C (100% RH)	20 cycles (4 hrs. freezing and 12 hrs. thawing)	tensile
[160]	glass	lime	-	-20°C ↔ 25°C (100% RH)	14 cycles (6 hrs. freezing and 2 hrs. thawing)	tensile & flexural
[161]	AR-glass	cement	NBN EN 12467	-20°C ↔ 20°C (100% RH)	50 cycles (2 hrs. freezing and 2 hrs. thawing)	tensile
[149]	glass	concrete	CSN 731322	-18°C ↔ 20°C (immersing in water)	50, 100, 150 cycles (4 hrs. freezing and 2 hrs. thawing)	tensile
[151]	carbon	cement, lime	-	-10°C ↔ 70°C (60% RH)	40 cycles (3 hrs. freezing and 3 hrs. thawing)	pull-off

2.7. Main conclusions

This chapter aimed to provide information about the current knowledge regarding the necessary techniques for accomplishing the objectives and highlighted the current research gaps. The following is a list of knowledge gaps regarding TRM composites:

- While several studies can be found in the literature devoted to the characterization of mechanical properties of TRMs, or the characterization of TRM-to-masonry bond behavior, the fiber-to-mortar bond response in these systems has only received limited attention.
- Various pull-out test setups have been used in literature to characterize the fiber-to-mortar (or concrete) bond behavior. These can generally be categorized into pull-push (or single-sided) and pull-pull (or double-sided) tests. However, the differences between the experimental results obtained from different test setups are poorly addressed.
- A fundamental understanding of the fiber-to-mortar bond mechanism and the parameters affecting that is currently missing. These parameters are the fiber-embedded length and different fiber configurations (number of fibers and presence of transverse fibers).
- The bond behavior of short fibers and cement-based matrices has been studied extensively in the literature; however, several issues remain regarding the characterization and modeling of the fiber-to-mortar bond mechanism in the lime- and cement-based TRM composites. Therefore, it is necessary to develop a comprehensive bond-slip law model.
- Among the issues that still deserve further investigation, the effects of slip rate and the response under cyclic loading are significant to develop analytical and numerical predictive models, improve test methods, and orient design criteria.

- There is a lack of understanding of the parameters controlling the response at the structural scale. This understanding can be developed through a comprehensive experimental and analytical study from materials to structural scale.
- The mechanical behavior of lime-based TRMs has been the subject of many recent studies. The role of curing conditions before performing mechanical tests is a critical factor yet to be discussed or explored. The majority of published experimental results do not contain this information, which makes comparing and analyzing the data of different laboratories a challenge.
- However, the durability performance of TRM composites has recently received attention from a few studies; there is a paucity of data on the durability of TRM composites. The long-term performance of TRM composites remains unaddressed and not understood. In previous studies, chemical attacks have primarily been studied at different TRM composite scales (micro-scale: pull-out tests, and macro scales: tensile and flexural tests), while their freeze-thaw behavior has been explored by a few at macro scales. Further, parameters controlling the durability performance of TRM composites are not known in multi-level (micro, macro, and structural levels). Hence, an in-depth investigation must be conducted from material to structural scale.

Chapter 3: Experimental plans and test methods

The experimental campaign consisted of the characterization of micro, meso, and macro responses of TRM composites. The detailed procedure followed for preparing the specimens and performing the tests is given in this section. The main highlights from this chapter can be listed as follows:

- Material characterization tests include mechanical tests and physical tests.
- The pull-out test is used to investigate textile-to-mortar bond behavior.
- The single-lap shear test is utilized to determine TRM-to-substrate bond behavior.
- The direct tensile test is conducted to evaluate the tensile behavior of TRM composites.
- Diagonal compression tests and flexural tests are used to characterize the in-plane and out-of-plane behavior of masonry panels.
- The effects of different environmental conditions (mortar curing, brick moisture condition, mortar age, natural environmental condition, and freeze-thaw conditions) on the TRM composites' behavior are examined.

3.1. Materials

Two commercially available hydraulic lime-based mortars were used as TRM matrix, as shown in Fig. 3-1a, b. These mortars are referred to as M1 and M2 throughout this study. Mortar M1 is a high-ductility hydraulic lime mortar (Planitop HDM Restauro) composed of hydraulic lime (NHL), Eco-Pozzolan, natural sand, special additives, synthetic polymers in water dispersion, and short fibers. This mortar is prepared by mixing the powder with the liquid provided by the manufacturer (5:1 powder to liquid ratio according to the technical datasheets) in a low-speed mechanical mixer for four minutes to form a homogenous paste. Mortar M2 is a pure natural hydraulic lime (NHL 3.5) and mineral geo-binder base (Kerakoll GeoCalce Fino) prepared by mixing 1 kg powder with 0.212 kg water for seven minutes. Besides, for building the masonry wallets, a commercial mortar is utilized based on lime and ecopozzolan (Mape-Antique MC), named mortar M3 (Fig. 3-1c). This mortar is prepared by mixing 1 kg powder with 0.14 kg water for four minutes. Moreover, solid clay bricks (200×100×50 mm^3) are used to build the masonry wallets and the single-lap shear specimens (Fig. 3-1d). Appendix 1 presents the technical data sheets provided by the manufacturers.

The reinforcing materials are glass and steel fibers, as shown in Fig. 3-1e, f. The glass fabric is a woven biaxial fabric mesh made of alkali-resistance fiberglass (Mapegrid G220), in which weft yarns passed through the warp yarns and were welded with each other. Its mesh size and area per unit length are equal to 25×25 mm^2 and 35.27 mm^2/m, respectively. The steel fiber is a unidirectional ultra-high tensile steel sheet (GeoSteel G600), with a density of 670 g/m^2 and an effective area of one cord (five wires) equaled to 0.538 mm^2. Each steel fiber is made by twisting five individual wires together, three straight filaments wrapped by two filaments at a high twist angle, forming a uniform cord. Appendix 1 presents the technical data sheets provided by the manufacturers.

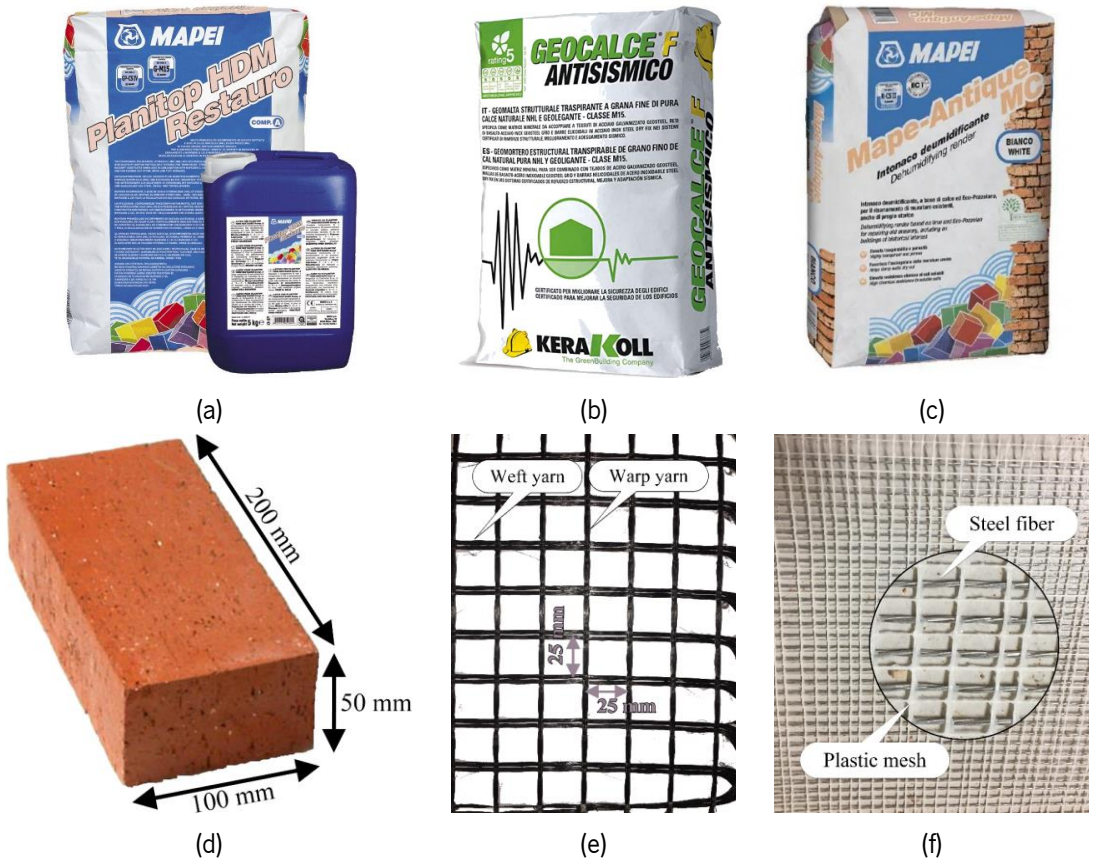

Fig. 3-1. Materials used: (a) mortar M1; (b) mortar M2; (c) mortar M3; (d) clay brick; (e) glass fabric; (f) steel fiber.

3.2. Microstructural analysis

3.2.1. X-ray diffraction test

X-ray diffraction (XRD) test was performed to quantify the crystalline phases of mortar. Bruker D8 Discover was used with Cu Kα radiation (λ= 1.54060A) at 40 kV and 40 mA. The sample was scanned from 5° to 90° 2θ at the speed of 0.02°s^{-1}.

3.2.2. Differential thermal analyses

Differential thermal analyses (DTA) were conducted with a Q600 TA Instrument apparatus to quantify and identify chemical composition by observing the thermal behavior of samples during mortar age. To prepare DTA samples, 5 g of mortar was ground and crushed (Fig. 3-2a). As reported in [163–165], isopropanol, ethanol, methanol, acetone, and diethylene ether are the most popular solvents for preventing mortar hydration stoppage. In this study, the crushed mortar was immersed in isopropanol

(50 mL) for 15 minutes to stop the hydration process [166], as shown in Fig. 3-2b. Afterward, the solid part was separated with a paper filter (Fig. 3-2c), and diethylene ether (10 mL) was used to remove isopropanol from the solid part [166]. Finally, the sample was dried in an oven (40°C for 10 minutes) or a vacuum desiccator for a short period. 25 mg of sample was used for the DTA test, as shown in Fig. 3-2d. For performing the test, an aluminum pan was utilized (Fig. 3-2e). The samples were heated from 50°C to 1000°C at a 10°C/min rate and 100 ml/min of N_2 flow. The tests were performed on all three mortars (M1, M2, and M3).

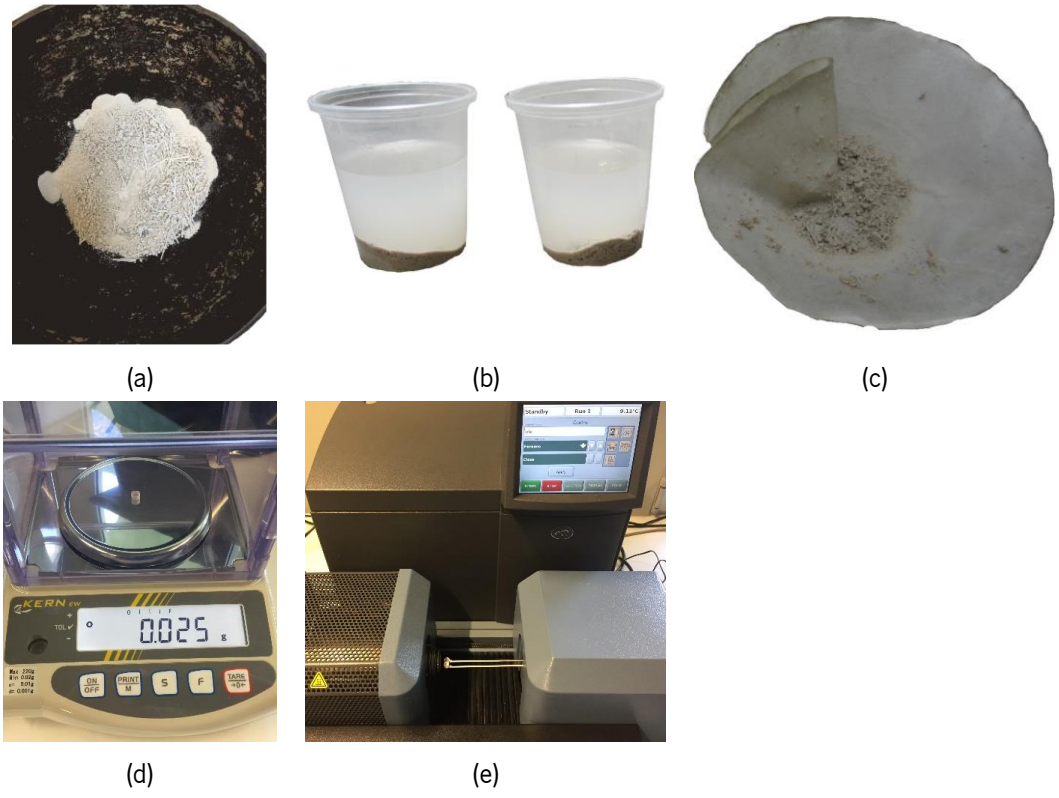

(a) (b) (c)

(d) (e)

Fig. 3-2. Preparation of DTA samples: (a) crushing mortar; (b) solving in isopropanol; (c) separating the solid part; (d) removing isopropanol; (d) weighting sample; (e) performing DTA test.

3.3. Material characterization

3.3.1. Mortar and brick

Table 3-1 and Table 3-2 present an overview of the conducted material characterization tests on the mortars and the brick, respectively.

Table 3-1. Conducted material characterization tests on the mortars.

Test	mortar M1	mortar M2	mortar M3	Code
Compressive strength	✓	✓	✓	ASTM C109
Flexural strength	✓	✓	✓	BS EN 1015-11
Splitting tensile strength	✓	✓	✓	BS EN 12390-13
Elastic modulus	✓	✓	✓	ASTM C496
Thermal conductivity	✓	-	-	ISO 8301
Thermal expansion	✓	-	-	-
Shrinkage strain	✓	✓	-	EN 12617-04
Water absorption- capillary	✓	✓	✓	BS EN 1015-18
Water absorption- immersion	✓	✓	✓	-
Dry bulk density	✓	✓	✓	BS EN 1015-10
Water desorption	-	✓	-	-
Open porosity	✓	-	-	BS EN 1936

Table 3-2. Conducted material characterization tests on the brick.

Tests	Brick moisture content			Brick surface		
	Dry	Semi-saturated	saturated	flatwise	lengthwise	widthwise
Compressive strength [a]	✓	✓	✓	✓	✓	✓
Flexural strength [b]	✓	✓	✓	✓	✓	-
Elastic modulus [c]	✓	✓	✓	-	-	✓
Water absorption- capillary	✓	-	-	✓	✓	✓
Open porosity	✓	-	-	-	-	-
Dry bulk density	✓	-	-	-	-	-
Initial rate absorption (IRA)	✓	-	-	✓	✓	✓
Water absorption- immersion	✓	-	-	-	-	-
Water desorption	-	-	✓	✓	✓	✓

(a): Compressive strength was measured in the flatwise direction of the dry, semi-saturated, and saturated bricks. For lengthwise and widthwise, only semi-saturated brick was used.
(b): Flexural strength was measured in the flatwise direction of the dry, semi-saturated, and saturated bricks. For lengthwise only semi-saturated brick was used.
(c): Elastic modulus was measured in the widthwise direction of the dry, semi-saturated, and saturated bricks.

The mortars and the brick were subjected to several mechanical and physical tests. According to ASTM C109 [167] and BS EN 1015-11 [168], the compressive and flexural strength of the mortars and the brick were experimentally obtained. Compressive specimens were cubes (50×50×50 mm^3 for mortars and 40×40×40 mm^3 for brick), and the flexural specimens had a prismatic shape (40×40×160 mm^3), as shown in Fig. 3-3a-d. The compressive strength of the brick was characterized perpendicular to all three directions, and the flexural strength was characterized perpendicular to the lengthwise and flatwise of the brick surface. In addition, the splitting strength of the mortars characterized based on ASTM C496 [169] had a cylinder shape with 70 mm diameter and 150 mm in length (Fig. 3-3e). The elastic modulus of the mortars and the brick was determined, according to BS EN 12390-13 [170]. The mortar specimens were cylinders with 70 mm diameter and 150 mm in length, while the brick specimens had a prismatic shape

(40×40×160 mm^3), as shown in Fig. 3-3f and Fig. 3-3g. It should be mentioned that the elastic modulus of the brick was measured perpendicular to its widthwise surface.

A Lloyd testing machine applied the compressive and the flexural tests under force-controlled conditions at a rate of 150 N/s and 10 N/s, respectively. In the compressive tests, for reducing the friction at the specimens' boundaries and ensuring a uniform distribution of stresses at the center of the specimens, a pair of friction-reducing Teflon sheets with a layer of oil in between is placed between the specimens and the compression plates (Fig. 3-3a and Fig. 3-3b). The flexural tests are performed according to the three-point bending test scheme with a 100 mm distance between the supports (Fig. 3-3c and Fig. 3-3d). The universal testing machine also was used to perform the tensile splitting strength of mortars under displacement-controlled conditions (0.12 mm/min), Fig. 3-3e. The elastic modulus was characterized by a universal testing machine (load capacity of 100 kN) and LVDTs (3 for cylinder and 4 for prismatic specimens) with a 5 mm range and 1-μm sensitivity, as shown in Fig. 3-3f and Fig. 3-3g.

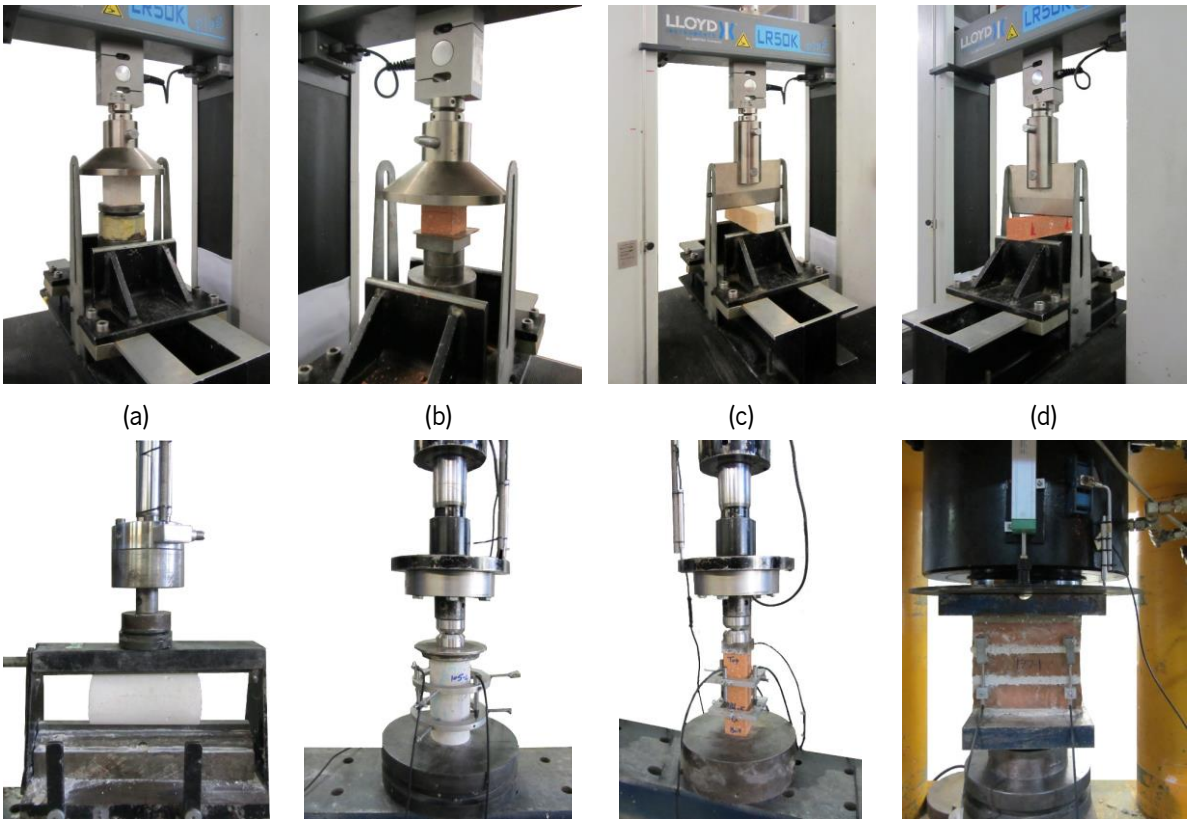

Fig. 3-3. Mechanical characterization test setups: (a) mortar compressive; (b) brick compressive; (c) mortar flexural; (d) brick flexural; (e) mortar splitting; (f) mortar elastic modulus; (g) brick elastic modulus; and (h) masonry prism compressive tests.

The compressive strength of masonry prisms was characterized according to ASTM C1414 [171]. The prisms were constructed by three bricks and 20 mm bed joint mortar (M3), as shown in Fig. 3-3h. Compressive tests were also performed using the universal testing machine (load capacity of 1000 kN) and introducing monotonic displacements at a 0.3 mm/min rate.

Water absorption coefficient due to capillary action was measured on cube specimens (50×50×50 mm^3 for mortars and 40×40×40 mm^3 for brick) according to BS EN 1015-18 [172]. For this purpose, four faces of the specimens were sealed with a Silirub to measure the water absorption in one direction. Then, the specimens were dried in a ventilated oven at a temperature of 90°C until reaching a constant mass. Finally, the specimens were immersed in water until a depth of 10 mm, and the mass changes of the samples in time were measured periodically, as shown in Fig. 3-4a. The process was repeated until the change in the sample mass was less than 0.2% of the previously determined value. The water absorption coefficient due to capillary action was computed from the straight-line slope between 10 and 90 minutes. Furthermore, the initial rate absorption (IRA) of the brick also was measured, according to BS EN 772-11 [173]. It should be mentioned that the water absorption coefficient due to capillary and IRA rate of the brick was measured for all surfaces.

(a) (b) (c)

(d) (e) (f)

Fig. 3-4. Mortar physical tests: (a) water absorption- capillary; (b) water absorption- immersion; (c) open porosity; (d) shrinkage tests; (e)thermal conductivity; (f) thermal expansion.

Water absorption immersion tests were also conducted on the unsealed mortars (M1, M2, and M3) and brick specimens according to ASTM C67 [174]. Firstly, cube specimens were dried in a ventilated oven at a temperature of 90°C until reaching a constant mass. Then, specimens were immersed fully in water (see Fig. 3-4b), and their weight was measured periodically. This was also repeated until the change in the samples mass was less than 0.2% of the previously determined mass.

In addition, water desorption of mortar and brick was measured. When the specimens used for the water absorption capillary tests were saturated, one free side of the specimens was sealed. Then the saturated specimens were stored in the chamber room at 20°C, and 60% RH and their weights were measured periodically. It should be mentioned that the water desorption of the brick was measured for all surfaces.

The dry bulk density of the mortars (M1, M2, and M3) and the brick was determined according to BS EN 1015-10 [175]. Additionally, according to BS EN 1936 [176], the mortar M1 and the brick's open porosity was measured experimentally on cube specimens, as shown in Fig. 3-4c. First, specimens were dried until they reached a constant mass. After measuring the weight of the specimens, they were placed inside the vacuum, and the test was run.

The mortar shrinkage strain was also measured based on EN 12617-04 [177] by using prismatic shape specimens (40×40×160 mm^3), as presented in Fig. 3-4d. The shrinkage strain was computed after demolding the specimens at two-day ages. During these tests, specimens were stored in a climatic chamber room at 20°C and 60% RH.

According to ISO 8301 [178], the thermal conductivity of mortar M1 was measured experimentally. Thermal conductivity was determined using the Alambeta instrument and disk-shaped specimens (100 mm diameter and 5 mm thickness) (Fig. 3-4e). Moreover, the coefficient of thermal expansion (CTE) of the mortar M1 and the brick was investigated using a strain gauge. Mortar specimens with prismatic shape (150×70×10 mm^3) were tested after 90 days. Strain gauges were installed on the surface of both the mortar and the brick in two perpendicular directions, as shown in Fig. 3-4f. Then, the specimens were stored in a climatic chamber room and exposed to different temperatures. CTE is computed from the measured thermal strains (ε) with the temperature change (ΔT= +30 to -10°C).

3.3.2. Fiber

The steel and glass fibers' tensile strength, strain, and elastic modulus were measured through direct tensile tests (Fig. 3-5). For this purpose, two steel plates (75×50×3 mm^3) were attached to the end of the fibers 48 hours before the test day to facilitate gripping during the tests. The tests were performed on single cords/yarns with a free length of 300 mm. For this purpose, a universal testing machine (load

capacity of 10 kN) was used under displacement-controlled conditions (0.3 mm/min), a 100 mm clip gauge located at the center of the specimen, and the internal LVDT of the machine measured the yarn deformation.

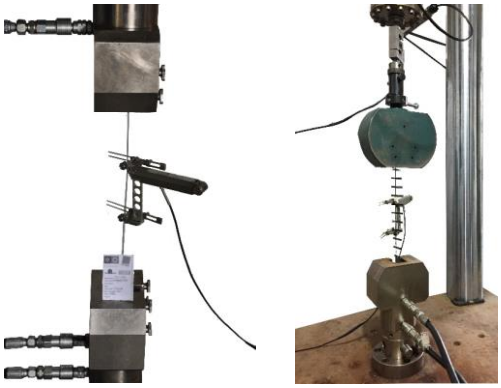

(a) (b)

Fig. 3-5. Yarn/cord direct tensile test: (a) steel cord; (b) glass yarn.

3.4. Fiber-to-mortar bond characterization

3.4.1. Effect of the test setup

A comprehensive investigation was initially performed to identify the most reliable pull-out test setup to characterize the textile-to-mortar bond behavior. Two pull-push and one pull-pull test setups were developed for this purpose, as shown in Fig. 3-6. In the pull-push tests (Fig. 3-6a, b), the mortar was fixed from the top, and the fiber was pulled out from the same direction. Therefore, compressive stress was generated in the mortar near the loaded end in this test configuration. In the pull-pull tests (Fig. 3-6c), on the other hand, the mortar was fixed from the bottom, and the fiber was pulled out from the top (or vice versa), simulating direct tensile tests. Tensile stress was therefore developed in the mortar in this test setup. Due to the different stress conditions imposed on the specimens in these test configurations, different pull-out responses were expected. Single steel fibers were embedded into mortar M2 and provided 150 mm of bond length for the TRM composite. Table 3-3 reports the overview of the experimental tests.

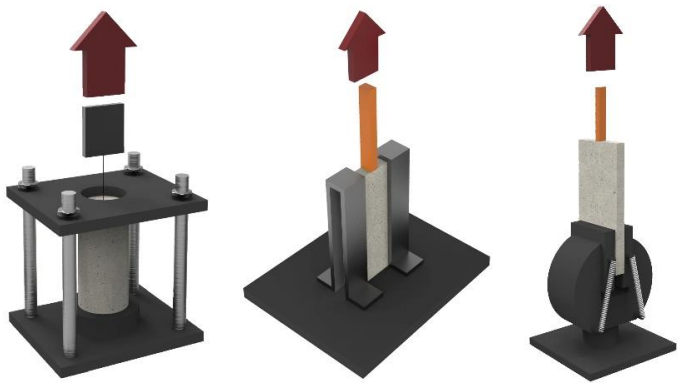

(a) (b) (c)

Fig. 3-6. Different pull-out test setups: (a) pull-push I; (b) pull-push II; (c) pull-pull.

Table 3-3. Overview of the test setup effect experiment.

Test	Objective	Mortar	Fiber	Bond length [mm]
Pull-push I	Test setup effect on the pull-out response	M2	Single steel cord	150
Pull-push II				
Pull-pull				

3.4.1.1. Setup 1: pull-push I

The first pull-push test setup (pull-push I) was the one used by Ghiassi et al. [31]. The specimens were made of fibers embedded in mortar cylinders with a 150 mm free length for gripping in these tests. The preparation of the specimens was performed following the procedure detailed in Ghiassi et al. [31]: (1) cleaning the fibers; (2) adjusting the PVC mold on the base; (3) placing the cleaned fibers in the center of the mold; (4) applying the first layer of mortar until half of the mold height; (5) tamping the mortar; and (6) pouring the second layer of mortar. The diameter and height of specimens were 75 mm and 150 mm, respectively. Two steel plates were attached to the end of the fibers 48 hours before the test day to facilitate gripping during the tests. Fig. 3-7a presents the geometry of the pull-push I specimens. For performing the tests, a supporting frame was placed on top of the mortar cylinders and was fixed from the bottom to a rigid steel frame to avoid specimens movements during the tests, as shown in Fig. 3-7b. An LVDT was attached to the fiber at a 6.3 mm distance from the mortar edge to measure the fiber slip. It was, therefore, necessary to reduce the elastic deformation of the fiber along this 6.3 mm from the measured experimental values to obtain the fiber slip.

(a) (b)

Fig. 3-7. Pull-push I tests: (a) specimens configurations; (b) test setups.

3.4.1.2. Setup 2: pull-push II

The second pull-push test setup (pull-push II) was designed to mitigate the problems related to slip measurements in the pull-push I test setup. Therefore, the sample geometry, the supporting system, and the gripping methods were changed accordingly. In this test setup, shown in Fig. 3-8a, the mortar was prepared in a disk shape with the dimensions of 150×125×16 mm^3 to facilitate the preparation of the specimens and alignment of the fiber inside the mortar. The free length of the fiber was also embedded in an epoxy resin block over a length of 200 mm and with a rectangular cross-sectional area of 10×16 mm^2. This block offered protection against early and uncontrolled failure caused by clamping and, at the same time, facilitated slip measurements during the tests. This technique was first proposed by Banholzer [179]. The preparation of the specimens was as follows: (1) embedment of the fiber-free length in epoxy resin and curing for 48 hours (Fig. 3-9a); (2) preparation and cleaning of the mold and the fiber; (2) applying the first layer of mortar with a thickness of 8 mm inside the molds (Fig. 3-9b); (3) placing the fiber on top of the first mortar layer; (4) applying a second layer of mortar with a thickness of 8 mm (Fig. 3-9c). The specimens were tested in a similar test configuration as the pull-push I test setup. However, a U-shape steel support was used here for supporting the specimens, as shown in Fig. 3-8b. A mechanical clamp was used to grip the epoxy resin (and thus the fiber) from the top and perform the tests. Two LVDTs with a 20 mm range and 2-µm sensitivity were located at both sides of the epoxy block to record the slip. The average of these LVDTs measurements was presented as the slip in the experimental results.

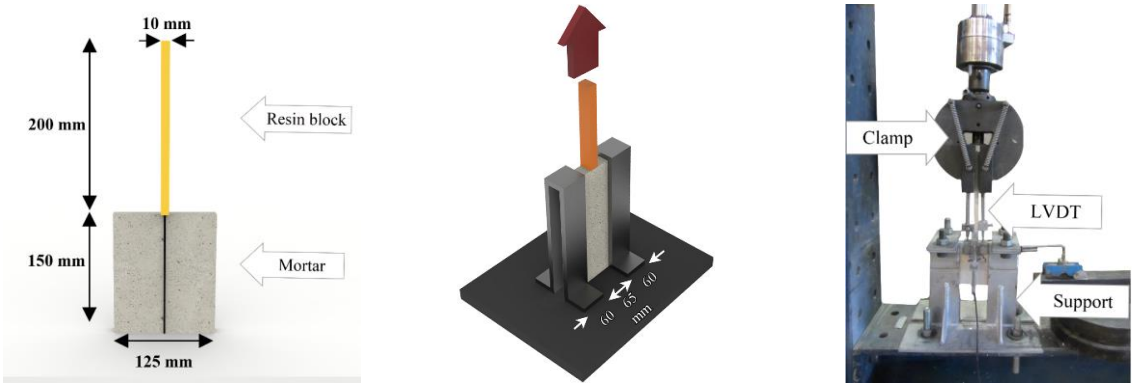

(a) (b)

Fig. 3-8. Pull-push II tests: (a) specimens configurations; (b) test setups.

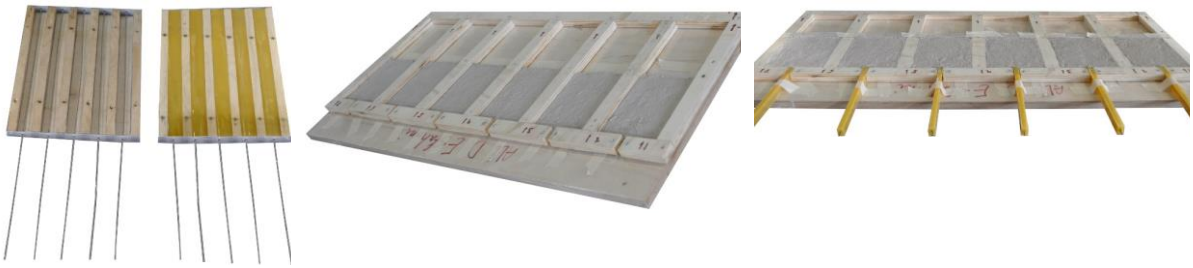

(a) (b) (c)

Fig. 3-9. The stages of preparation of the pull-push II specimens: (a) embedment of the fibers in resin; (b) applying the first layer of the mortar; (c) adjusting fiber and pouring the second layer of the mortar.

3.4.1.3. Setup 3: pull-pull

In the third test setup type (pull-pull), specimens had a similar geometry to the pull-push II test setup, but the supporting system was different. As shown in Fig. 3-10, the specimens were gripped from the bottom in this test setup, thus simulating tensile tests. The specimens were prepared following the same procedure as pull-push II tests. The specimens were slightly longer in this case. The mortar disks were with dimensions of 250×125×16 mm^3 to provide additional space for gripping from the bottom. To prevent crushing of the mortar in the gripping area during the tests, the lower part of the specimens was reinforced by placing additional steel fibers as shown in Fig. 3-10a. A mechanical clamp was used to grip the epoxy resin (and thus the fiber) from the top and another to grip the mortar from the bottom (Fig. 3-10b). The LVDTs were placed at similar locations as in the pull-push II tests, and the average of these LVDTs measurements was presented as the slip in the experimental results.

(a) (b)

Fig. 3-10. Pull-pull tests: (a) specimens configurations; (b) test setups.

All specimens were demolded after 24 hours of preparation and were placed in a damp environment for seven days. After that, specimens were stored in the lab environmental conditions (20°C, 60% RH) until the test day (for 60 days of mortar curing). Five pull-out specimens were tested for each test setup. All the tests were carried out using a servo-hydraulic system with a maximum capacity of 25 kN at a displacement rate of 1.0 mm/min.

3.4.2. Effect of bond length

The effect of bond length on the pull-out response of TRM composites was examined by using single glass yarns extracted from the textile mesh in the longitudinal (warp) direction or steel cords as presented in Table 3-4. The glass yarns were used together with the mortar M1 and the steel fibers with the mortar M2. The specimens were made with embedded lengths of 50, 100, 150, and 200 mm for steel fibers and 50, 75, and 100 mm for glass fibers. These values were selected based on the experimental results reported by Ghiassi et al. [31] and observations during the tests.

Specimens were demolded after 24 hours of preparation and placed in a damp environment for seven days. Then, the specimens were stored in the lab environmental conditions (20°C, 60% RH) until the testing day (at 60 days of age). Five specimens were prepared and tested for each material and bond length, resulting in 20 specimens made for steel-based TRM and 15 specimens for glass-based TRM. Since the pull-push II test setup was used in this section, the reader is referred to section 3.4.1 for more information on the preparation and test setup of the pull-push II specimens.

Table 3-4. Summary of the bond length effect tests.

Test	Objective	Mortar	Fiber	Fiber configuration	Bond length [mm]
Embedded bond length	Effective bond length	M1	Glass	Single yarn	50
					75
					100
		M2	Steel	Single cord	50
					100
					150
					200

3.4.3. Effect of fiber configuration

Aiming to understand better the fiber-to-mortar response in TRM composites made of unidirectional and bidirectional fibers, the effect of fiber configuration (the effect of the number of fibers and the presence of transverse fibers) on the bond response of these composites was investigated (see Table 3-5).

Table 3-5. Summary of the fiber configuration tests.

Test	Objective	Mortar	Fiber	Fiber configuration	Bond length [mm]
Fiber configuration	Effect of fiber configuration on the bond behavior	M1	Glass	Single yarn	50
				Single yarn + transverse	
				Group (2 yarns)	
		M2	Steel	Single cord	150
				Group (2 cords)	
				Group (4 cords)	

Three cases were considered for each material type, as shown in Fig. 3-11. For the glass-based TRMs, these cases included embedment of “single yarn,” “single yarn + transverse elements,” and “group of yarns” with a 50 mm bond length embedded in mortar M1. For “single yarn” specimens, the transverse fibers (weft yarns) were cut before embedment in the mortar (Fig. 3-11a). In the case of “single yarn + transverse elements,” one yarn (warp yarn) with two transverse elements (weft yarns) was embedded in the mortar, as shown in Fig. 3-11a. The transverse elements had a total length of 25 mm (12.5 mm from each yarn side equal to half of the mesh size). In the case of “group of yarns,” two yarns (warp yarns) with two transverse elements (weft yarns) in between were embedded in the mortar (the distance between longitudinal fibers was 25 mm), see Fig. 3-11a. For the steel-based TRMs, since a unidirectional steel

fiber mesh was used in this study, the specimens were prepared with the embedment of “single cord,” “two cords,” and “four cords” in the mortar M2 with a 150 mm embedment length (see Fig. 3-11b).

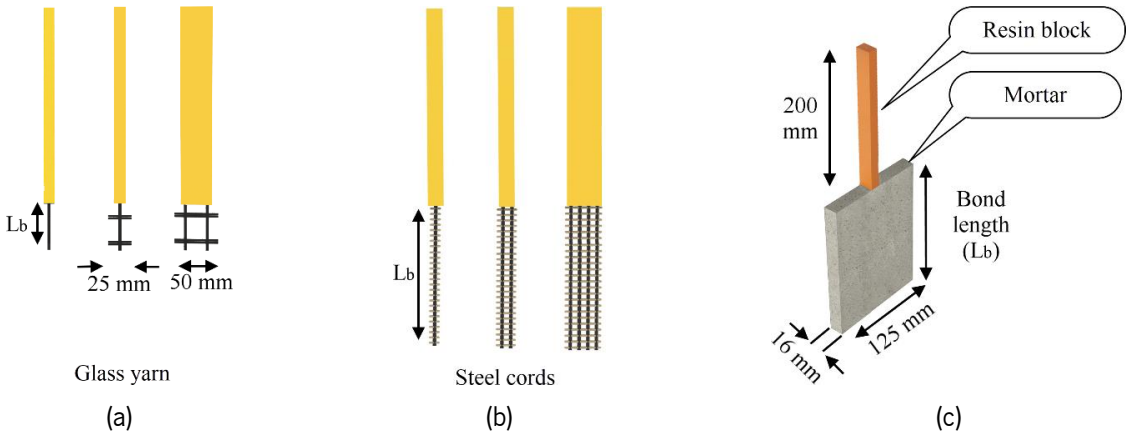

Fig. 3-11. Considered fiber configurations: (a) glass yarns; (b) steel cords; (c) 3D view of pull-out specimens.

After 24 hours of preparation, the specimens were demolded and placed in damp conditions for seven days. The specimens were then stored in the lab environment (20°C, 60% RH) until the test day (for 60 days). The single-sided pull-out test setup (pull-push II) was performed in these tests (more information related to the specimens preparation and test setups are provided in section 3.4.1).

3.4.4. Effect of slip rate

The slip rate effect on the bond behavior of fiber-to-mortar was also examined using the pull-push II test setup (see further information on the test setup in section 3.4.1). The specimens comprised single glass yarns extracted from the textile mesh in the longitudinal (warp) direction or single steel cords embedded in mortar M1. The bond lengths were 50 mm for the glass yarns and 150 mm for the steel cords, equal to the effective bond lengths. Five different slip rates were considered, namely 0.2, 1.0, 5.0, 10.0, and 20.0 mm/min. Five specimens were prepared and tested for each slip rate, resulting in 25 specimens for the glass TRM and 25 for the steel TRM (Table 3-6).

The specimens were demolded after three days of casting, were cured in a damp environment for seven days, and then stored in laboratory environmental conditions (20°C, 60% RH) for 50 days. The testing age of the specimens was 60 days.

Table 3-6. Summary of the slip rate effect tests.

Test	Objective	Mortar	Fiber	Fiber configuration	Bond length [mm]	Slip rate [mm/min]
Monotonic tests	Effect of slip rate on the textile-to-mortar bond behavior	M1	Glass	Single yarn	50	0.2
						1.0
						5.0
						10.0
						20.0
		M1	Steel	Single cord	150	0.2
						1.0
						5.0
						10.0
						20.0

3.4.5. Effect of cyclic loading

Cyclic pull-out tests were performed on glass yarns and steel cords embedded in mortars M1 and M2, respectively. Loading-unloading cycles were performed with progressively increasing maximum (target) slip, from 0.3 mm to 20 mm, whereas the minimum slip was corresponding to a load of 50 N in the unloading phase to avoid yarn/cord instability ensure that its position was kept. Two cycles for each target slip were carried out, with a slip rate of 1.0 mm/min (up to a target slip of 9 mm) and of 3.0 mm/min (increased for a timesaving reason) until the end of the tests (Fig. 3-12).

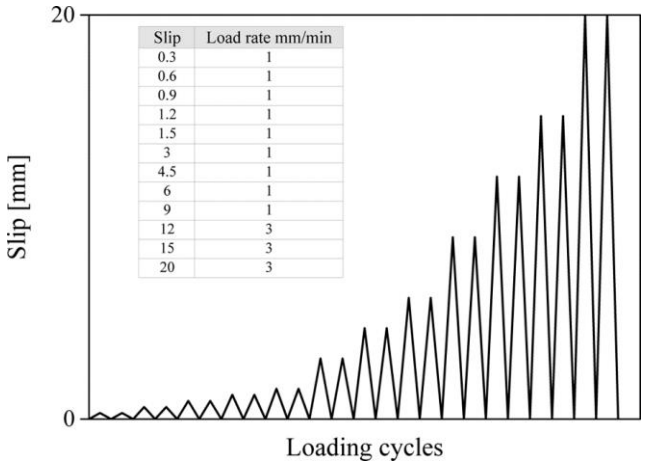

Fig. 3-12. Cyclic pull-out loading procedure.

Various configurations of specimens were used in these tests. Glass-based TRMs included embedding "single yarns" with 50 mm and 75 mm bond lengths and "single yarn + transverse elements" with 50 mm bond lengths. The transverse elements had a total length of 25 mm, 12.5 mm at each side, equal to half of the mesh size. Moreover, "group of yarns" specimens (consisted of two yarns and two transverse

elements) were used with 50 mm and 75 mm bond lengths. All specimens of glass-based TRM were manufactured with mortar M1.

With regard to steel-based TRM, the parameters investigated were mortar type (mortars M1 and M2), bond length (50 mm and 150 mm), and the number of steel cords (single, two, and four). The steel mesh was unidirectional, and there were no weft elements. The overview of the experimental plan is presented in Table 3-7.

Table 3-7. Summary of the cyclic pullout tests.

Test	Objective	Mortar	Fiber	Fiber configuration	Bond length [mm]	Slip rate [mm/min]
Cyclic tests	Effect of cyclic loading on the textile-to-mortar bond behavior	M1	Glass	Single yarn	50	1.0 mm/min until 9 mm slip and 3.0 mm/min from 9 mm to the end of the test
				Single yarn + transverse		
				Group (2 yarns)		
				Single yarn	75	
				Group (2 yarns)		
		M1	Steel	Single cord	50	
					150	
				Group (2 cords)	150	
				Group (4 cords)		
		M2		Single cord	50	
					150	
				Group (2 cords)	150	

The specimens were demolded after three days of casting, were cured in a damp environment for seven days, and then stored in laboratory environmental conditions (20°C, 60% RH) for 50 days. The final age of the specimens at testing was 60 days. Pull-push II test setup and configuration were performed on the cyclic specimen (more information is presented in section 3.4.1).

3.5. TRM tensile behavior

Direct tensile tests were conducted on prismatic specimens with a length, width, and thickness of 550 mm, 60 or 70 mm, and 10 mm, respectively, as shown in Fig. 3-13a. The samples consisted of a 100 mm free fiber length at each side and a 350 mm central region where the fabrics were embedded in the mortar (Fig. 3-13a). The tensile specimens were prepared as follows: applying the first layer of mortar inside the wood molds (5 mm thickness), placing the fabric mesh, and finally applying the second layer of mortar with 5 mm thickness. The number of fibers (parallel to tensile load) in each TRM system was eight and three (with the area ratio of 0.0072 and 0.0044), respectively, for the steel and the glass-

based TRM specimens (that was due to specific geometrical properties of each mesh). Glass fabric was used with mortar M1, whereas steel fibers were used with mortar M2. The information related to curing conditions and ages of tensile specimens is presented in section 3.8 and section 3.9.1.

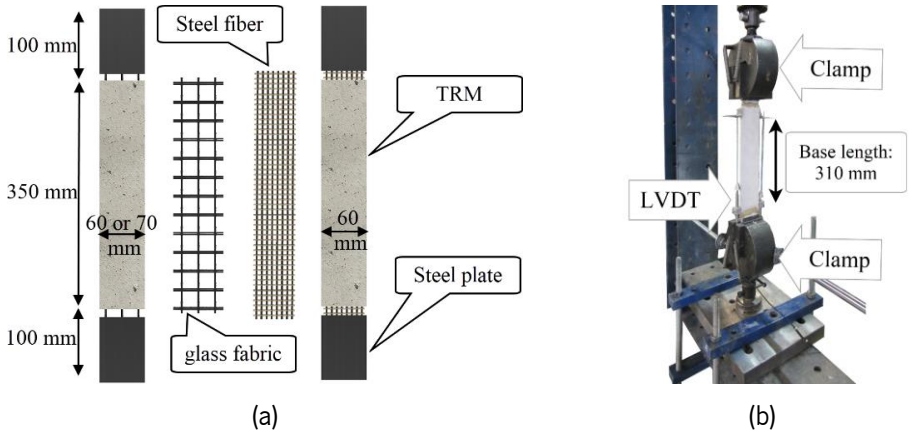

Fig. 3-13. Tensile specimens: (a) configurations; (b) test setups.

One week before the test date, the free part of fibers was embedded in resin to avoid rupture of the fabric in the clamping area. In addition, two steel plates (100×75×10 mm^3) were glued to the free part of fibers to apply a uniform load to the fiber mesh. A mechanical clamp was used to grip the samples for performing the tests, see Fig. 3-13b. Two LVDTs with a 20 mm range and 2-µm sensitivity were placed at both sides of the tensile specimen and recorded the displacement. A servo-hydraulic jack with a maximum capacity of 25 kN applied the direct tensile load to the specimens under a displacement control rate of 0.3 mm/min. The introduced stress was calculated by dividing the load by the cross-section area of the dry textile (steel and glass mesh areas were equal to 4.3 mm^2 and 2.65 mm^2, respectively). The strain was measured by dividing the mean value of the displacements recorded from the two LVDTs by their base length (310 mm). In particular, the RILEM TC-250 recommendations were followed whenever possible.

3.6. TRM-to-substrate bond

Single-lap tests were performed to investigate the TRM-to-masonry bond behavior. For the preparation of the specimens, the bricks surfaces were initially sandblasted to increase the surface roughness, as suggested in [119]. Then, bricks (with dimensions of 200×100×50 mm^3) were cleaned with an air compressor to remove the dust. After that, the bricks were immersed in water for one hour to ensure a semi-saturated condition. After removing the bricks from the water and wiping the excess superficial water,

the mortar was applied in two layers of 5 mm thickness each. The bond area between the mortar and the substrate was 150 mm× 70 mm for the steel-based TRM and 100 mm× 70 m for the glass-based TRM (see Fig. 3-14a). After applying the first layer of the mortar, fiber mesh (including eight longitudinal cords for steel and three warp yarns for glass fibers) was placed on the mortar, followed by application of the second mortar layer. The embedded lengths of steel and glass-based TRM were 150 mm and 100 mm, while the free length of both fiber meshes was 250 mm (Fig. 3-14a). Two aluminum plates were attached to the extremity of the fibers 48 hours before testing to facilitate the gripping of the specimens during the tests and to ensure a uniform load transfer. The information related to curing conditions and the age of single-lap shear specimens is presented in sections 3.8 and 3.9.

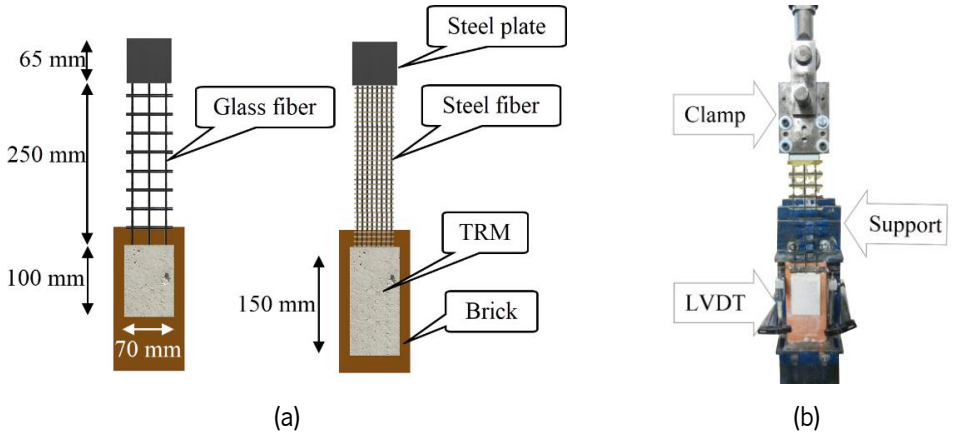

Fig. 3-14. Single-lap shear test specimens: (a) specimen's configurations; (b) test setup.

A closed-loop servo-controlled testing machine with the maximum load capacity of 50 kN at a displacement rate of 0.3 mm/min was used for performing the single-lap shear tests. It is noteworthy that the velocities for each test were selected based on the literature and were in the quasi-static range [180–183]. A stiff supporting frame and two clamps were used to support the specimens, as shown in Fig. 3-14b. Attention was given to dry fiber and TRM composite alignment with the applied force. The slip of the fiber-to-mortar was measured by means of two LVDTs with a 20 mm range and 2-μm sensitivity placed at the loaded end (Fig. 3-14b). A preload equal to 200 N was applied to specimens before testing to facilitate attachment of the LVDTs [31].

3.7. Masonry panels

Solid clay brick and mortar M3 were used to build the masonry wallets. Similar to single-lap shear specimens, bricks were immersed in water for one hour before being used. Thirty days after constructing

and curing wallets in lab environmental conditions (20°C, 67% RH), a layer of glass-based TRM composite was applied (with 10 mm thickness mortar M1), and wallets were stored in the lab for 90 days. Hence, wallets were tested after 120 days. During the first week, the wallets strengthened with TRM composites were cured under wet clothes and plastic. The information related to curing conditions and ages of specimens is presented in section 3.9.2.

3.7.1. In-plane behavior

According to ASTM E519 [184], diagonal compression tests were performed on masonry wallets with dimensions of 540×540×100 mm^3, as shown in Fig. 3-15a. A servo-hydraulic system with a maximum capacity of 300 kN was used for performing these tests at a displacement rate of 0.3 mm/min. The load was applied through steel shoes (115×115×15 mm^3) placed at diagonally opposing bottom and top corners of the wallets [134]. As shown in Fig. 3-15b, two LVDTs with 20 mm range and 2-μm sensitivity measure the vertical and horizontal deformation of the wallets during the tests.

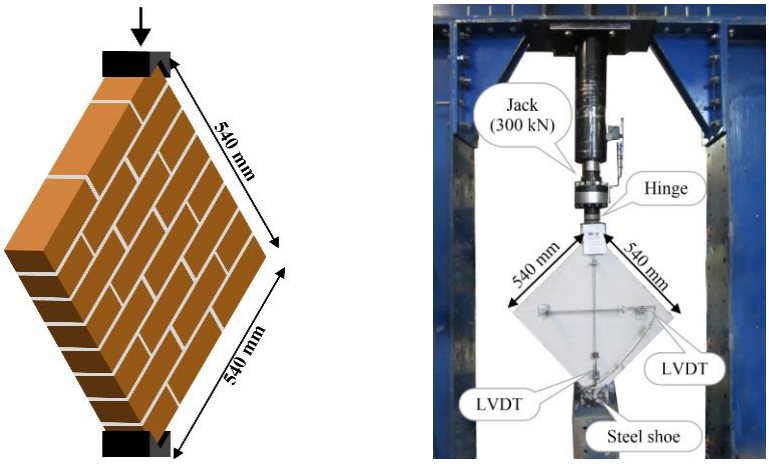

(a) (b)

Fig. 3-15. Diagonal compression tests: (a) geometric details; (b) test setups.

3.7.2. Out-of-plane behavior

Flexural tests were performed promoting preferential damage and failure either parallel or normal (perpendicular) to bed joints and according to EN 1052-2 [185]. Dimensions of the out-of-plane wallets failure parallel and normal to bed joint were 540×420×100 mm^3 and 520×330×100 mm^3, respectively, as shown in Fig. 3-16a and Fig. 3-16b. The fabric mesh was placed so that the warp yarns were parallel

to the longitudinal axis of specimens. In total, there were 17 and 12 warp yarns in the out-of-plane wallets parallel and normal, respectively. Meanwhile, 21 weft yarns were in both types of flexural wallets.

Specimens were tested in a vertical configuration (to omit the effect of self-weight on the results) under four-point bending so that the strengthened face was subjected to tension. The distance between the outer and inner bearings was 420 mm and 170 mm, respectively. Four LVDTs were used with a 20 mm range and 2-μm sensitivity to measure the sample deformation at the middle and the location of inner bearings, as shown in Fig. 3-16a and Fig. 3-16b. The tests were performed at a displacement rate of 0.3 mm/min and with a servo-hydraulic jack with a maximum load capacity of 50 kN.

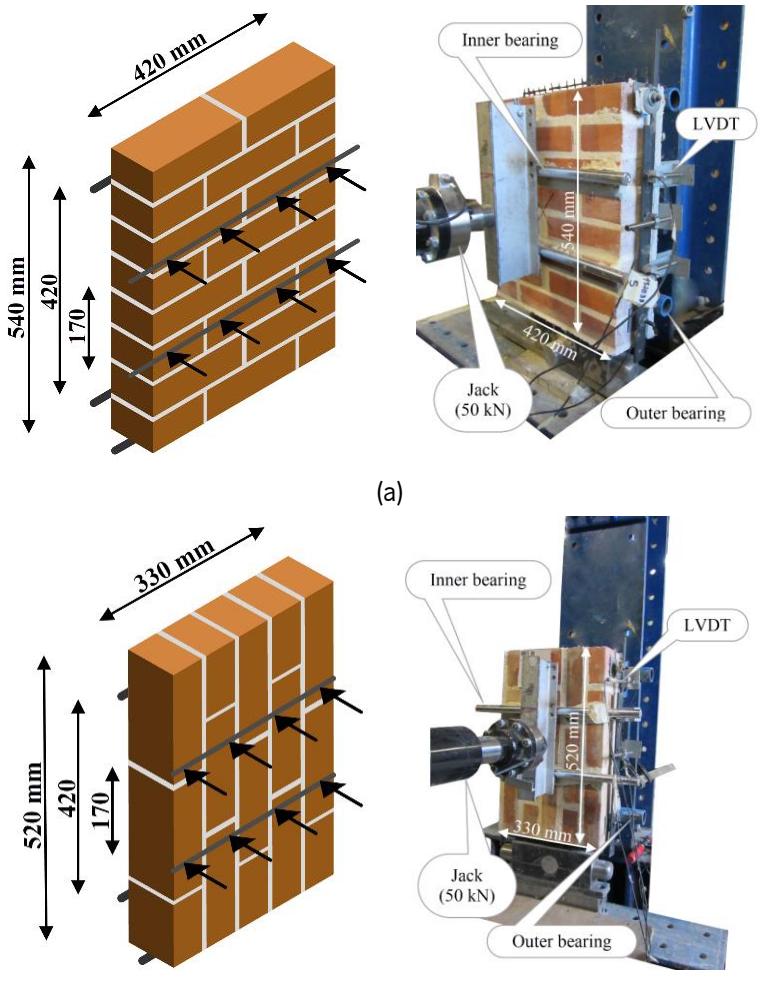

Fig. 3-16. Geometric details and test setups used for out-of-plane tests: (a) bending tests parallel to bed joint; (b) bending tests, normal to bed joints.

3.7.3. The role of surface preparation

The brick surface preparation effect on the structural performance of TRM-strengthened masonry was investigated. For this reason, two groups of samples were prepared: in one group, original bricks were used, while in the second group, sandblasted bricks were used (lengthwise direction) to build the wallets. For this purpose, six wallets were constructed and strengthened with a layer of glass-based TRM composites (with mortar M1) at both sides to examine their compressive diagonal behavior. Three out of the six strengthened panels were made with the original bricks, and the other three with the sandblasted bricks.

Out-of-plane tests were performed to promote damage and failure parallel to the bed joints or normal (perpendicular) to the bed joints. Six specimens were prepared for each direction and strengthened with a layer of glass-based TRM composites at one side of the wallets (opposite side of the loading). Three wallets were constructed with the original bricks and three wallets with the sandblasted bricks.

3.8. Curing conditions

The experimental campaign involved the martial characterization tests, pull-out tests, and single-lap shear tests by performing the steel- and glass-based TRM composite and the mortars M1 and M2. Three different curing conditions were considered for the mortars: (1) curing of specimens in the laboratory (20°C, 60% RH) under a plastic sheet for a day (named as PL-1); (2) curing of the specimens in the laboratory (20°C, 60% RH) covered with damp cloths and stored under a plastic sheet for seven days (PL-7); (3) curing of the specimens inside a chamber room (20°C, 90% RH) for seven days (RH-7). After that, all the specimens were stored in the laboratory until the testing day. For the preparation of the single-lap shear specimens, the bricks were conditioned to three different initial moisture contents (named as D, SS, and SA, respectively) before application of the TRM system: (1) dried (in the oven for two days at the temperature of 90°C); (b) semi-saturated (60% moisture content); (c) saturated (immersed in water for two days). Combined with the curing methods, these conditions lead to nine different conditions for the single-lap shear specimens. Fig. 3-17 and Table 3-8 present the general overview of the curing condition effect tests.

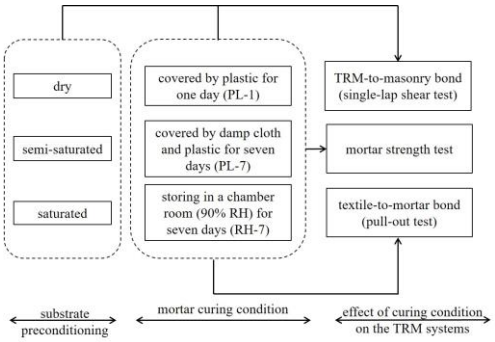

Fig. 3-17. General overview of the curing condition effect tests.

Table 3-8. Overview of the curing condition tests.

Test type		Objective	Mortar curing condition	Brick moisture condition	Age [day]
Mortar (M1 and M2)	Compressive	Effect of different curing conditions on the mortar strength	PL-1, PL-7, RH-7	-	60
	Flexural				
	Elastic modulus				
	Splitting				
	DTA	Effect of different curing conditions on the mortar physical and chemical properties			1,7, 60
	Shrinkage strain				3 to 250
	Capillary coefficient				60
	Desorption				
Brick	Compressive	Effect of different brick moisture contents on the brick strength	-	D, SS, SA	-
	Flexural				
	Elastic modulus				
	Capillary coefficient	Effect brick surface on its physical properties test	-	-	
	Desorption test				
Fiber-to-mortar bond	Pull-out	Effect of different curing conditions of the mortar on the fiber-to-mortar bond	PL-1	-	60
			PL-7		
			RH-7		
TRM-to-substrate bond	Single-lap shear	Effect of different curing conditions of the mortar and the brick on the TRM-to-masonry bond	PL-1	D	60
			PL-7		
			RH-7		
			PL-1	SS	
			PL-7		
			RH-7		
			PL-1	SA	
			PL-7		
			RH-7		

PL-1: curing of specimens in the laboratory (20°C, 60% RH) under a plastic sheet for a day; PL-7: curing of the specimens in the laboratory (20°C, 60% RH) covered with damp cloths and stored under a plastic sheet for seven days; RH-7: curing of the specimens inside a chamber room (20°C, 90% RH) for seven days; D: dry brick; SS: semi-saturated brick; SA: saturated brick.

3.8.1. Material characterization

The mechanical properties (compressive, flexural, splitting strength, and elastic modulus) of the mortars M1 and M2 were determined under different curing conditions, as described in section 3.8 (PL-1, PL-7, and RH-7). All the specimens were tested at the age of 60 days, so five specimens were tested for each curing condition and each type of test. Water absorption and desorption of mortars M1 and M2 were also determined. The water absorption and desorption of mortars were characterized only in one direction (perpendicular to the surface into which the mortar was poured), and three specimens were used for each curing condition, as isotropic behavior is expected. The effect of curing conditions on the shrinkage strain of mortars M1 and M2 also was determined. Three specimen types were considered for shrinkage measurements. Type I and II specimens were cured under PL-1 (one day under a plastic sheet) and PL-7 (seven days covered by damp cloths and under a plastic sheet) conditions. Meanwhile, either type III specimens were prepared with a layer of AR-glass fabric (with mortar M1) or steel mesh (with mortar M2) placed in the middle and cured under the PL-7 conditions to understand the role of reinforcement on the shrinkage results. The specimens were demolded after two days when the measurement of the shrinkage strains was initiated.

The mechanical properties (compressive, flexural strengths, and elastic modulus) of the bricks were measured under different moisture content of the brick, as mentioned in section 3.8 (dry, semi-saturated, and saturated). The compressive and flexural strengths were characterized perpendicular to the flatwise direction of the brick, and the elastic modulus was measured only along the lengthwise direction. Five specimens were used for each brick moisture condition and type of test. Also, the water absorption due to capillary, water desorption, and initial rate absorption (IRA) of the brick were characterized in all three directions (flatwise, lengthwise, and widthwise) by using three specimens for each direction. Simultaneously with the water absorption capillary test, the moisture content of the brick was also determined.

3.8.2. Fiber-to-mortar bond

The single-sided pull-out test (pull-push II type) was used to investigate the effect of different mortar curing conditions on the fiber-to-mortar bond behavior. Pull-out tests were carried out on single cords/yarns embedded in mortar. The single steel cord and glass yarns were embedded in the mortars M2 and M1, respectively, with 150 mm and 50 mm bond lengths. Five specimens were prepared and tested for each curing condition. The specimens were demolded after 24 hours of preparation and then were cured in

three different conditions as described at the beginning of this section. The tests were performed at the age of 60 days. For details on the pull-out test procedure, see section 3.4.1.

3.8.3. TRM-to-substrate bond

Single-lap shear tests were performed on the steel-based TRM composite and substrate to investigate the TRM-to-masonry bond behavior. The embedded and free length of the fiber mesh was 150 mm and 250 mm, respectively (see Fig. 3-14). The specimens were cured as described at the beginning of this section. More details related to the single-lap shear test procedure are provided in section 3.6.

3.9. Environmental aging

3.9.1. Natural aging

Table 3-9 presents an overview of the experimental tests under natural aging. The experimental campaign investigated the changes in materials properties (compressive and flexural strength), textile-to-mortar bond behavior, and the tensile response of TRM composites with time under indoor and outdoor environmental conditions. To address this aim, a set of samples were placed in laboratory conditions (20°C, 60% relative humidity) for 920 days to replicate indoor conditions. A second set was placed outside under direct exposure to rain and sunlight at the University premises to simulate outdoor conditions. The outdoor specimens were initially cured inside the laboratory for 90 days, then placed outside in January 2017 and for 830 days. Fig. 3-18 shows the changes in mean air temperature and relative humidity in the location of samples during outdoor exposure.

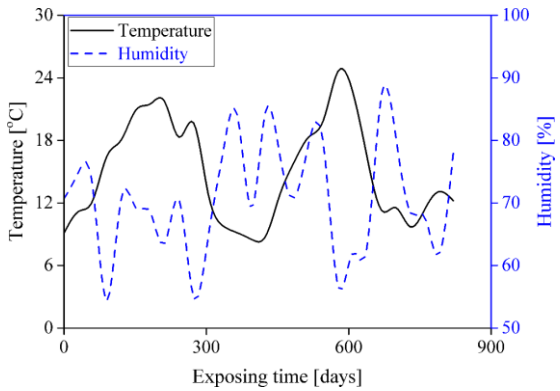

Fig. 3-18. Temperature and air humidity variation outside the University premises during outdoor exposure.

Table 3-9. Overview of the experimental tests under natural aging.

Test type	Objective	Mortar	Fiber	Bond length [mm]	Age [days]
Mortar strength	Effect of the mortar age on its strength	M1-M2	-	-	15
					30
					60
					90
					180
					920
	Effect of the real environmental condition on the mortar strength	M1-M2	-	-	180
					920
Pull-out	Effect of the mortar age on the textile-to-mortar bond	M1- M2	Glass-Steel	50- 150	15
					30
					90
					180
					270
					920
	Effect of the real environmental condition on the textile-to-mortar bond	M1- M2	Glass-Steel	50- 150	180
					270
					920
	Effect of mortar type	M1- M2	Steel	150	90
					920
Tensile	Effect of the mortar age on the tensile behavior of TRM composites	M1- M2	Glass-Steel	350	90
					180
					270
					920
	Effect of the real environmental condition on the tensile behavior of TRM composites	M1- M2	Glass-Steel	350	180
					270
					920

3.9.1.1. Material characterization tests

The compressive and flexural strength of the mortars M1 and M2 was experimentally obtained at different ages (3, 7, 14, 30, 60, 90, 180, and 920 days). Five cubes (for the compressive test) and five prismatic (for flexural test) specimens were prepared for each test at each age. Also, fifteen specimens were prepared to study the effect of real environmental exposure on the mechanical properties of the mortars. These specimens were cured in the lab environment for 90 days, then stored outside, and tested at the ages of 180 and 920 days (hence exposed to the real environmental conditions for 90 and 830 days, respectively). After 24 hours of preparation, the specimens were demolded and placed in the lab environment (20°C, 60% RH) until testing or exposure to the real environment.

3.9.1.2. Pull-out test

This experimental campaign used TRM composites reinforced with either steel cord or glass yarn (warp direction). The steel fiber was embedded in the mortar M2 with a bond length of 150 mm, while the glass

yarn was embedded in the mortar M1 with a bond length of 50 mm. Specimens were demolded 24 hours after preparation and placed in a lab environment (20°C, 60% RH) until testing or exposure to the real environment. For details on the pull-out test procedure (pull-push II type), see section 3.4.1.

Pull-out tests were performed at 15, 30, 90, 180, 270, and 920 days of mortar age to study its effect on the fiber-to-mortar bond behavior. Four specimens were prepared and tested for each testing age, resulting in 24 specimens for each steel-based and glass-based TRMs. Further, the effect of mortar type on the long-term bond behavior of textile-to-mortar was also examined by comparing the pull-out response of the steel fibers embedded in mortars M1 and M2 at 90 and 920 days of aging.

Twelve samples from each TRM type were also prepared and placed outside the laboratory at the age of 90 days to be exposed to natural environmental conditions. These specimens were tested at 180, 270, and 920 days. Therefore, specimens were exposed to natural environmental conditions for 90, 180, and 830 days.

3.9.1.3. Tensile test

Direct tensile tests were conducted on prismatic specimens with length, width, and thickness of 550 mm, 60 mm, and 10 mm, respectively. Tensile specimens were made using either steel fiber mesh and mortar M2 or glass fabric mesh and mortar M1. After preparing tensile specimens, samples were covered with plastic for one day, then demolded and cured in the laboratory conditions (20°C, 60% RH) until the test days. Detailed information about specimen preparation and performing tensile tests is provided in section 3.5.

The tensile tests were performed at the mortar ages of 90, 180, 270, and 920 days. Five specimens were tested at each age resulting in 20 specimens for each steel and glass-based TRM type. In addition, 15 specimens from each TRM type were stored in natural environmental conditions and tested at the age of 180, 270, and 920 days (corresponding to outside storage days of 90, 180, and 830, respectively).

3.9.2. Freeze-Thaw exposure

The Freeze-Thaw experimental campaign examined changes in materials properties, the tensile response, fiber-to-mortar bond behavior, TRM-to-mortar bond behavior, and masonry structural behavior (with and without TRM strengthening system). For this purpose, glass fabric with the mortar M1 was used as the TRM composite for preparing specimens. In addition, the masonry wallets were built with clay brick and the mortar M3. Once the TRM composite was cured for 90 days and the panels with a cure time of 120 days, a part of them was exposed to FT cycles on an automated basis.

A Fitoclima 6400 EC25 climatic chamber was used to expose the samples to freeze-thaw (FT) conditions. The FT cycles consisted of thawing the samples at 30°C and 90% RH for two hours; then, the temperature decreased at a rate of 0.111°C/min till reaching -10°C. After this point, samples were frozen for two hours, followed by a temperature increase at a rate of 0.111°C/min till reaching the 30°C. Fig. 3-19a shows the imposed FT cycles under the planned and the real conditions. This cycle of sixteen hours was repeated 360 times.

The selected FT environmental condition aims to create an environment in the laboratory to represent real environmental conditions but in an accelerated way. A similar FT condition was also performed in another study [28] to investigate the performance of FRP strengthening systems. A number of controlled samples were also prepared and placed in the laboratory in parallel to the FT tests. The environmental condition of the storage laboratory during this period is presented in Fig. 3-19b (average temperature and humidity was 18°C and 75% RH).

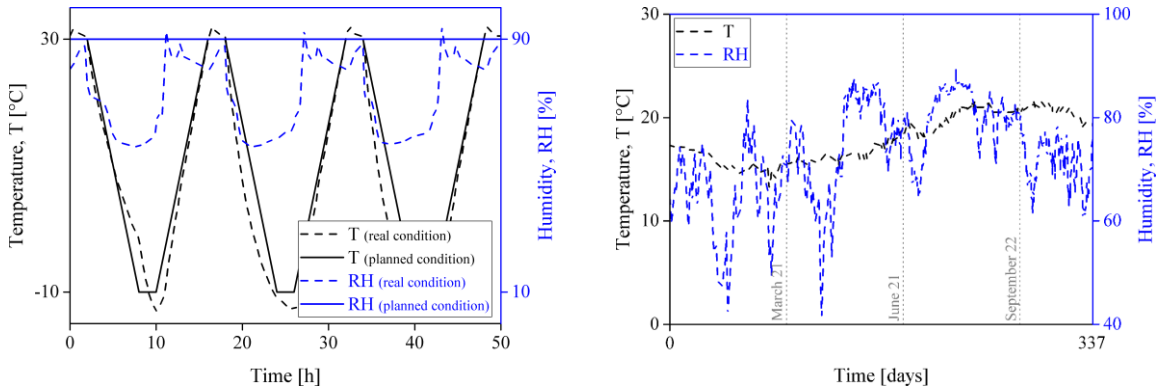

Fig. 3-19. (a) Freeze-thaw exposure condition; (b) environmental lab condition.

As shown in Fig. 3-20, at every 60 cycles (equal to 40 days) and when the inside temperature of the chamber was 20°C, five specimens were taken from the chamber and stored seven days in the lab to conduct post-exposure tests. It should be noticed that four specimens of masonry panels were taken from the chamber after 360 cycles. Table 3-10 shows the experimental program details such as conducted post-exposure tests, number of FT cycles, and the total number of samples (included control and exposure specimens). The detailed information regarding specimens preparation and conducting the post-exposure tests are provided in section 3.2 to section 3.7.

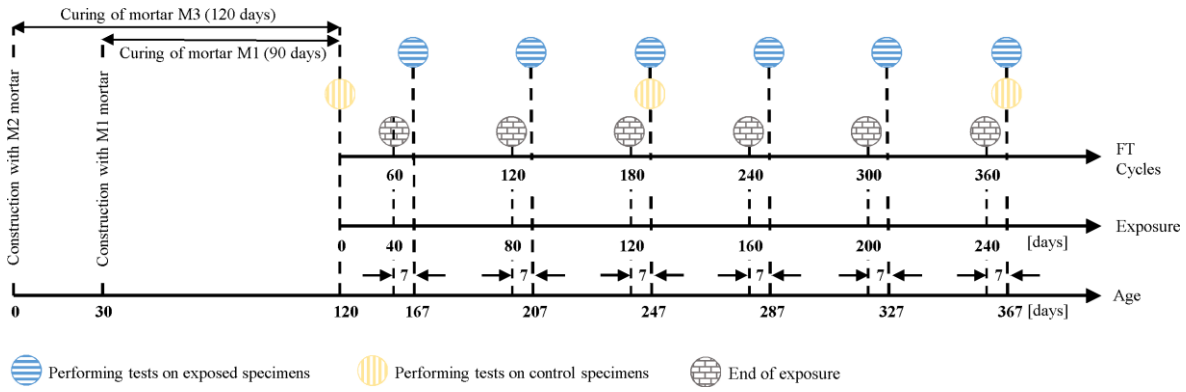

Fig. 3-20. Schematic representation of the test program under the freeze-thaw condition.

Table 3-10. Experimental program under Freeze-Thaw condition.

Test	Material	Freeze-Thaw (FT) cycles							Total number of specimens
		0	60	120	180	240	300	360	
Compressive	M1	●	●	●	●●	●	●	●●	45
	M3	●	-	-	●●	-	-	●●	25
	Brick	●	-	-	-	-	-	●●	15
	Masonry prism	●	-	-	-	-	-	●●	15
Flexural	M1	●	-	-	●●	-	-	●●	25
	M3	●	-	-	-	-	-	●●	15
	Brick	●	-	-	-	-	-	●●	15
Elastic modulus	M1	●	-	-	●●	-	-	●●	25
	M3	●	-	-	-	-	-	●●	15
	Brick	●	-	-	-	-	-	●●	15
Splitting	M1	●	-	-	●●	-	-	●●	25
	M3	●	-	-	-	-	-	●●	15
Tensile	Glass fiber	●	-	-	-	-	-	●●	15
	TRM composite	●	●	●	●●	●	●	●●	45
Pull-out	Textile-to-mortar bond	●	●	●	●●	●	●	●●	45
Single-lap shear	TRM-to-substrate	●	●	●	●●	●	●	●●	45
Diagonal compressive	URM panel	●	-	-	-	-	-	●●	12
	Strengthened panel	●	-	-	-	-	-	●●	12
Bending test (failure parallel to bed joint)	URM panel	●	-	-	-	-	-	●●	12
	Strengthened panel	●	-	-	-	-	-	●●	12
Bending test (failure normal to bed joint)	URM panel	●	-	-	-	-	-	●●	12
	Strengthened panel	●	-	-	-	-	-	●●	12

●Test exposed specimens; ●●Tested both control and exposed specimens.

In addition to the experiments listed above, the effect of FT conditions on the fiber-to-mortar bond behavior was investigated. To address this aim, a set of pull-out specimens (with different bond length and fiber

configurations) were prepared and, after 90 days of curing in the laboratory, the specimens were exposed to 360 FT cycles or stored in the environmental lab condition as the control specimens. After that, a series of pull-out tests on the steel- and glass-based TRM composites (made with mortar M1) were conducted as the post-exposure tests (see Table 3-11 for detailed experimental plan).

Table 3-11. Pull-out experimental program under Freeze-Thaw condition.

Test	Mortar	Fiber	Fiber configuration	Bond length [mm]	Freeze-thaw cycles					Total number of specimens
					0	60	180	300	360	
Pull-out (embedded length)	M1	Glass	Single yarn	50	●	●	●	●	●●	30
				75	●	●	●	●	●●	30
				100	●	●	●	●	●●	30
		Steel	Single cord	50	●	●	●	●	●●	30
				150	●	●	●	●	●●	30
				200	●	●	●	●	●●	30
				250	●	●	●	●	●●	30
Pull-out (fiber configuration)		Glass	Single yarn + transverse	50	●	●	●	●	●●	30
			Group (2 yarns)		●	●	●	●	●●	30
		Steel	Group (2 cords)	150	●	●	●	●	●●	30
			Group (4 cords)		●	●	●	●	●●	30

●Test exposed specimens; ●●Tested both control and exposed specimens.

Chapter 4: Material results

This chapter presents and discusses experimental results of physical and mechanical properties of the lime-based mortar, brick, and fibers used in this Thesis. For this purpose, several micro and meso-scale tests were performed, as described in chapter 3. The main highlights from this chapter can be listed as follows:

- The effect of different curing conditions on mortar's physical and mechanical properties is investigated.
- The effect of brick moisture content on the mechanical properties of the brick is examined.
- Lime-based mortars are characterized under natural environmental conditions and aging.
- Brick, fibers, and lime-based mortars are exposed to freeze-thaw conditions to investigate their possible deterioration.

4.1. Microstructural analysis

4.1.1. X-ray diffraction result

The X-ray diffraction (XRD) analysis was carried out using a Bruker D8 Discover diffractometer. The XRD pattern of the mortar M1 is presented in Fig. 4-1. The samples were extracted at the fiber-to-mortar interface (pull-out specimens prepared for freeze-thaw tests) at 90 days of age to avoid differences in the carbonation depth. The crystalline phase includes SiO_2 (33.5%), $MgCaCO_3$ (26.1%), $MgSiO_3$ (17.1%), $Al_3Si_2O_7(OH)_3$ (11.7%), and $CaCO_3$ (11.5%). Hence calcite ($CaCO_3$) and silicon dioxide (SiO_2) are the main components of the mortar, causing the mortar strength to improve.

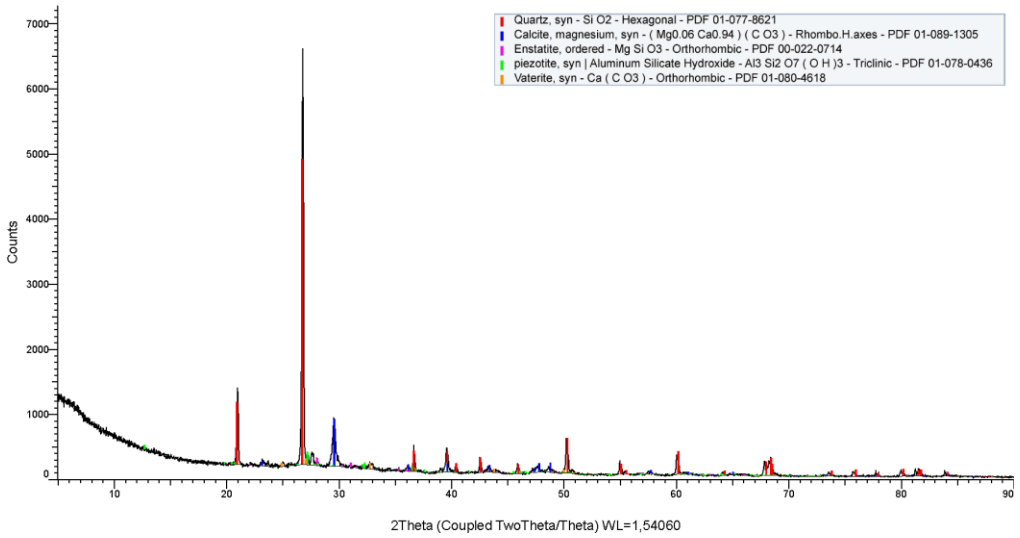

Fig. 4-1. XRD profiles of mortar M1.

4.2. Physical properties of materials

4.2.1. Thermal expansion result

The coefficient of thermal expansion (CTE) of brick and mortar was evaluated based on [27]. The CTE of the mortar M1 and the brick are 20.2×10-6/°C (Coefficient of Variation: CoV= 13%) and 16.5×10-6/°C (CoV= 11%), respectively. Both the brick and the mortar M1 have almost the same CTE. This result shows that the two materials are compatible, and the mortar-to-brick interface has a very low probability of cracking due to temperature changes.

4.2.2. Thermal conductivity

Since only mortar M1 was used as the matrix of TRM composites in the freeze-thaw conditions test, the thermal conductivity of this material only was determined, according to ISO 8301 [178]. The average thermal conductivity of mortar M1 is 0.154 W/mK (coefficient of variation, CoV= 6%), which is in the low-medium thermal conductivity range, according to [186].

4.2.3. Water absorption capillary

Testing mortars and bricks for water absorption due to capillary action was performed according to BS EN 1015-18 [172]. The water absorption is calculated as follows:

$$C = \frac{\left(W_t - W_d\right)}{A} \qquad \text{Eq. 4-1}$$

Where W_t is the weight of the specimen at time t, W_d is the dry weight of the specimen, and A is the are of the specimen. Fig. 4-2 presents the average curves of the mortars and brick water absorption capillary obtained from five specimens for each test. Mortars M1 and M2 show higher water absorption rates in contrast to mortar M3. In addition, brick surfaces show different water capillary behavior due to the nonhomogeneous of this material. Table 4-1 presents the water absorption rate due to capillary actions for all mortars and brick. This coefficient was computed by the slope of the straight line between 10 and 90 minutes, based on [172]. The capillary coefficient of the mortar M1 mortar decreases as the mortar age increases. This observation can be due to the carbonation process occurring over time and/or delayed hydration of C_2S as the leading hydraulic phase of hydraulic lime-based mortar [187]. Hence, by closing the pores, water absorption is reduced. On the other hand, the capillary coefficient of the mortar M2 at all ages is almost the same. The capillary coefficient of the brick at all three surfaces is different due to the anisotropic properties of this material.

4.2.1. Water absorption- immersion

Testing mortars and bricks for water absorption was performed according to the ASTM C67 [174] (gravimetric sorption test method). For each test, five specimens were used. The difference between initial and post-immersion weight represents the amount of moisture absorbed (see Eq. 4-2).

$$W_{absorption} = \frac{\left(W_t - W_d\right)}{W_d} \times 100 \qquad \text{Eq. 4-2}$$

Where $W_{absorption}$ is the moisture uptake content at time t. The average moisture uptake of mortars and brick is presented in Table 4-2 and Fig. 4-3. Mortar M1 absolves more water than the other mortars.

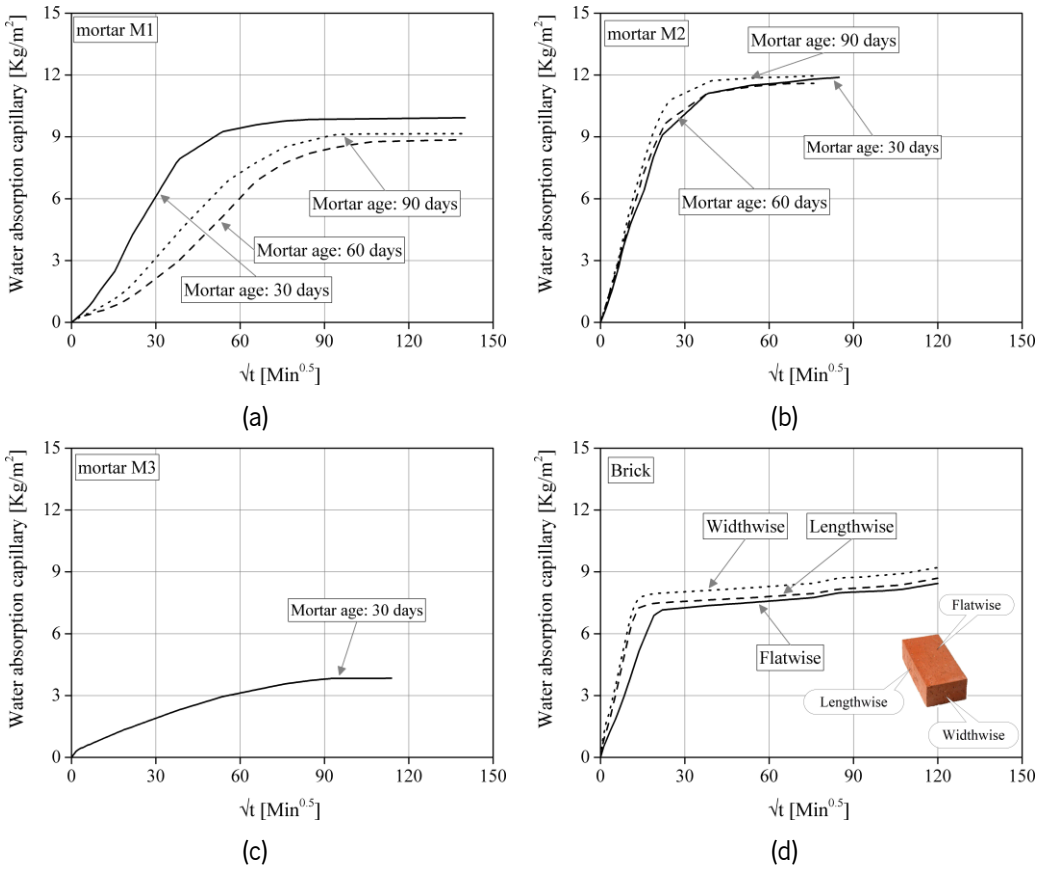

Fig. 4-2. Water absorption due to capillary action: (a) mortar M1; (b) mortar M2; (c) mortar M3; (d) brick.

Table 4-1. Water absorption capillary rate (kg/ ($m^2min^{0.5}$)) of materials.

Material	30 days	60 days	90 days	flatwise	lengthwise	widthwise
Mortar M1	0.153	0.040	0.056	-	-	-
Mortar M2	0.504	0.490	0.554	-	-	-
Mortar M3	0.057	-	-	-	-	-
Brick	-	-	-	0.32	0.59	0.61

Table 4-2. Moisture uptake content of the materials.

-	Mortar M1		Mortar M2			Mortar M3	Brick
	30 days	90 days	30 days	60 days	90 days	30 days	-
$W_{absorption}$ [%]	17.6	17.9	15.5	15.5	16.1	9.2	11.3

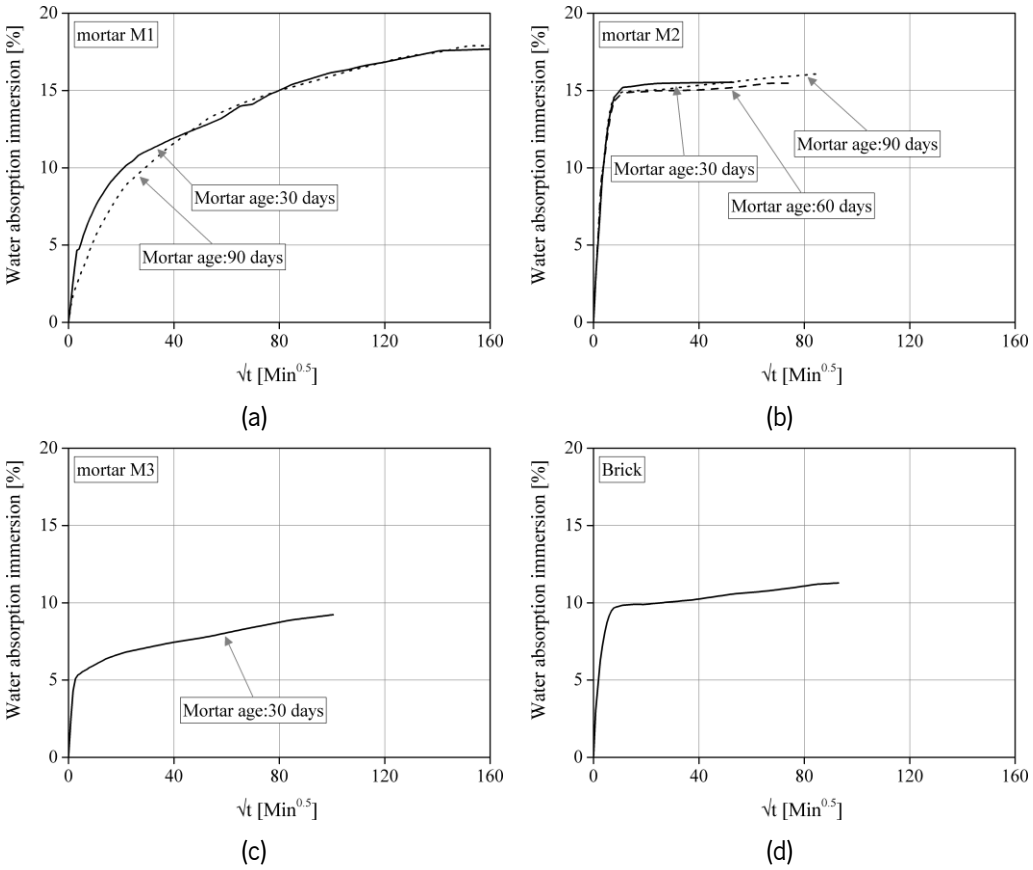

Fig. 4-3. Water absorption due to immersion: (a) mortar M1; (b) mortar M2; (c) mortar M3; (d) brick.

4.2.2. Dry bulk density

The dry bulk density of the mortars and the brick was determined according to BS EN 1015-10 [175]. For this purpose, dry bulk density is calculated by the ratio of dried mortar weight (W_d) to the volume of the specimen (V_s), which is defined in Eq. 4-3:

$$V_s = \frac{W_{sat.} - W_i}{\rho_w} \qquad \text{Eq. 4-3}$$

Where $W_{sat.}$ is the mass of saturated mortar or brick, W_i is the apparent mass of saturated specimen immersed in water, and ρ_w is the density of water. Table 4-3 lists the dry bulk density of the mortars and the brick.

Table 4-3. Dry bulk density of materials.

Material	Mortar M1	Mortar M2	Mortar M3	Brick
Bulk density [kg/m³]	1489	1587	1867	1984

4.2.3. Open porosity

Open porosity only was measured for the mortar M1 and the brick. According to BS EN 1936 [176], the open porosity (p_o) of a specimen is determined by the ratio (in percentage terms) of the volume of open pores to the apparent specimen volume, expressed by Eq. 4-4:

$$p_o = \frac{\left(W_{sat.} - W_d\right)}{\left(W_{sat.} - W_i\right)} \times 100 \qquad \text{Eq. 4-4}$$

The open porosity of the mortar M1 and the brick is equal to 40% and 26%, respectively. These results are in line with the dry bulk density observations.

4.3. Effect of curing conditions

4.3.1. Mortar

The aim is to investigate the effect of different curing conditions on the mortar strength. Therefore, three different curing conditions were considered for the mortars M1 and M2 named PL-1, PL-7, and RH-7 (see section 3.8 provides more details).

Fig. 4-4 shows DTA results of the mortar M2 at 1, 7, and 60 days. The curves present three different peak points: water evaporation (at 50~100°C), dehydroxylation (losing chemically bound water of $Ca(OH)_2$ at 360~440°C), and decarboxylation (losing chemically bound CO_2 of $CaCO_3$ at 600~850°C) [188,189]. The DTA results illustrate that the specimens cured under PL-7 condition show the highest water evaporation at 1 and 7 days. This indicates that the internal moisture of the samples is maintained under the PL-7 conditions. Specimens cured under PL-7 and RH-7 conditions show a higher dehydroxylation level at seven days than those cured under PL-1 conditions. During the first seven days, more moisture was available in PL-7 and RH-7 conditions, leading to the advancement of the hydration reactions and forming more $Ca(OH)_2$ in those samples [190]. The level of dihydroxylation, however, becomes similar in all curing conditions at 60 days, indicating the hydration reactions have ceased. Decarboxylation level is higher in the specimens cured under PL-7 and RH-7 conditions than those cured under PL-1 conditions at all tested ages. This shows the presence of a higher $CaCO_3$ and carbonation degree in those samples. The increase of the decarboxylation peak (and so $CaCO_3$) at 60 days (Fig. 4-4c) is consistent with the reduction of the dehydroxylation peak and $Ca(OH)_2$ showing achievement of a higher level of carbonation in those samples.

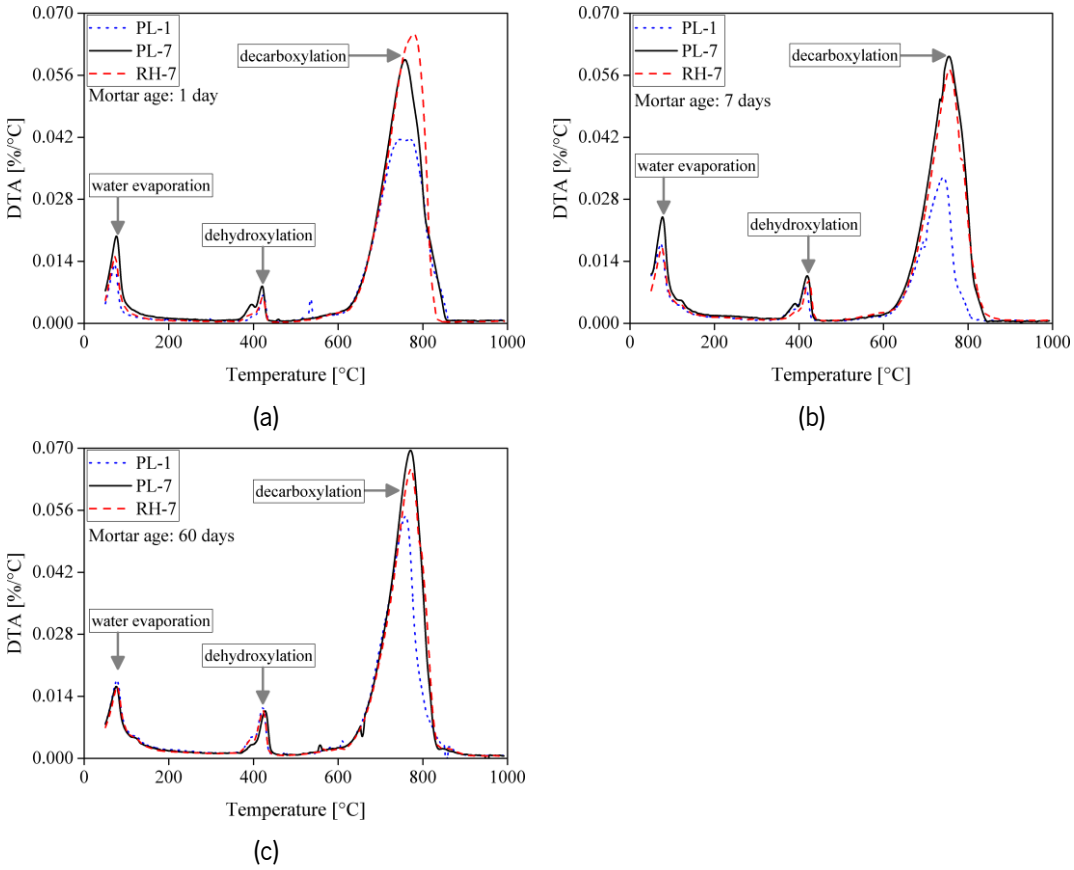

Fig. 4-4. Differential thermal analysis (DTA) results of mortar M2 at: (a) 1 day; (b) 7 days; (c) 60 days.

The mean strength (compressive, flexural, and splitting) of the mortars M1 and M2 at different curing conditions are presented in Table 4-4. The results indicate that the higher the humidity, the higher the mortar strength, which can be the result of higher hydration and carbonation after 60 days. This observation shows the importance of moisture conservation in the early curing ages. The positive impact of moisture on mortars, however, has been different, as mortar M1 is more affected by humidity (PL-7 and RH-7 conditions) than mortar M2. As an example, the compressive strength of mortar M1 has been increased by 31% and 47% under PL-7 and RH-7 conditions, respectively, compared to PL-1 conditions. However, these values for mortar M2 are only 8% and 9%, respectively. Similar results are also found for other mechanical strengths. It may be because the mortar M1 contains pozzolan. High humidity causes the pozzolan to react with moisture and the hydration process to increase [34], resulting in a higher strength for mortar M1.

The effect of preservation of humidity for seven days (in PL-7 and RH-7 conditions) on the pore structure (porosity, connectivity, and tortuosity) can be indirectly seen in the water absorption results (Table 4-4). The capillary coefficient of the mortar M2 stored under PL-1 conditions is higher than that of the specimens stored under higher humidity conditions (PL-7 and RH-7), showing that the microstructure of

these mortars has a more porous and connected microstructure [187]. At the same time, the average weight of specimens cured under PL-1, PL-7, and RH-7 conditions was 208 g (CoV=0.5 %), 202 g (CoV=0.7 %), and 220 g (CoV=1.4 %). Nevertheless, the coefficient of desorption does not change.

Table 4-4. Mortar mechanical properties under three different curing conditions (at 60 days)*.

Test	Mortar	Curing conditions		
		PL-1	PL-7	RH-7
Compressive strength [MPa]	M1	6.70 (14)	8.79 (12)	9.82 (2)
	M2	6.89 (6)	7.47 (5)	7.51 (14)
Flexural strength [MPa]	M1	4.07 (5)	5.20 (12)	5.22 (5)
	M2	1.68 (6)	1.78 (10)	2.08 (5)
Elastic modulus [MPa]	M1	6265 (11)	7177 (9)	8038 (5)
	M2	8759 (8)	9216 (6)	9748 (6)
Splitting tensile strength [MPa]	M1	0.93 (9)	1.16 (8)	1.33 (7)
	M2	0.39 (18)	0.71 (23)	1.12 (9)
Shrinkage strain	M1	0.14 (15)	0.28 (7)	-
	M2	0.13 (3)	0.19 (4)	-
Capillary coefficient [kg/(m^2×min$^{0.5}$)]	M2	0.45 (10)	0.37 (11)	0.38 (8)
Desorption [%]	M2	-10.6 (1)	-11.0 (2)	-9.5 (2)

*CoV of the results is given in percentage inside parentheses. PL-1: curing under plastic for one day; PL-7: curing under plastic and covered with damp cloths for seven days; RH-7: curing inside a chamber room with 90% RH.

Fig. 4-5 and Table 4-4 show the average shrinkage strain changes based on the mortar M1 and M2 age. As expected, shrinkage strain changes of mortar M1 are stopped in all types when the weight reduction process stops (10 and 40 days for the specimens cured under PL-1 and PL-7 conditions, respectively), as shown in Fig. 4-5a. Shrinkage strain changes of mortar M2 are stopped after 10 and 20 days for PL-1 and PL-7 curing conditions (Fig. 4-5b). The effect of curing conditions on the shrinkage strain of mortars is significant. The mortar M1 cured under PL-7 conditions shrinks twice as much as the specimens cured under PL-1 conditions. This value for mortar M2 is 38%. A higher humidity at an early age may explain this difference between the results of PL-7 and PL-1 conditions. An explanation could be due to chemical reactions (e.g., hydration and carbonation of lime) [191,192]. Furthermore, since the mortar M1 consists of pozzolan, higher humidity causes the pozzolanic reactions to accelerate and consume more moisture within the mortar, resulting in higher shrinkage [193]. Further investigation is necessary to determine how hydration, carbonation, and pozzolanic reactions contribute to shrinkage.

The effect of fabric on the mortar shrinkage strain is notable. The mortar M1 specimens reinforced with the glass fabric (PL-7_reinforced) show 12% less shrinkage compared to the unreinforced specimens cured under similar conditions (PL-7). This value for the mortar M2 and steel fiber is 38%. These observations are in line with [194].

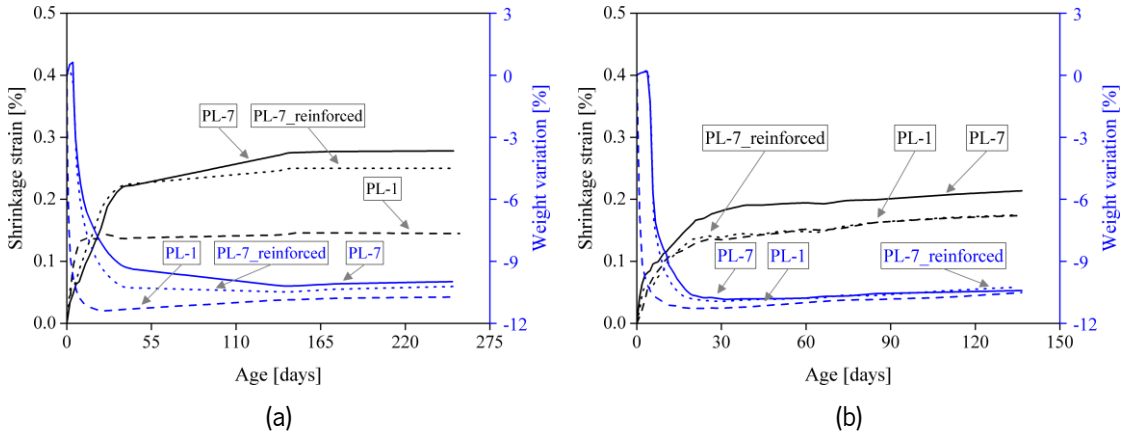

Fig. 4-5. Shrinkage strain and weight changes vs. mortar age: (a) mortar M1; (b) Mortar M2.

4.3.2. Bricks

Mechanical and physical properties of the brick were investigated in three different moisture content: dry, semi-saturated, and saturated bricks. Table 4-5 shows the average of the mechanical properties of the clay brick obtained from five specimens. The compressive and flexural strength were characterized perpendicular to the flatwise surface of the brick, and the elastic modulus was measured only along the lengthwise direction. The effect of moisture content on the mechanical properties of the brick is significant- the more water content, the lower the brick strength. For instance, the compressive strength of the semi-saturated and saturated brick decreases by 7% and 27%, respectively, in contrast to the dry brick. This reduction rate for the flexural strength is equal to 7% and 11%, respectively, and for the elastic modulus is 3%. Table 4-5 lists the average of the mechanical properties of the clay brick for flatwise, lengthwise, and widthwise surfaces. The brick compressive strength is different in each direction owing to its anisotropic properties. Meanwhile, the flexural strength of the clay brick is almost equal in flatwise and lengthwise directions.

Table 4-5 also reports the average of the physical properties of the brick at each surface. The IRA of the brick is 0.47, 0.79, and 1.03 Kg/ (m^2×min) for flatwise, lengthwise, and widthwise directions, respectively. This value is in line with the range previously reported for clay bricks [195,196]. Moreover, the capillary coefficient of the brick at each direction is different, as reported in Table 4-5; however, the moisture desorption is approximately equal in all directions.

The moisture content ratio to the water absorption of the brick at all surfaces and at 24 hours is calculated as follows:

$$\text{Moisture content} = \frac{\left(W_t - W_d\right)}{\left(W_{24hr.} - W_d\right)} \times 100 \qquad \text{Eq. 4-5}$$

Table 4-5. Brick mechanical properties under three different moisture conditions*.

Effect of moisture content	Brick conditions		
	Dry	Semi saturated	Saturated
Compressive strength [MPa]	25.2 (2)	23.5 (5)	18.4 (6)
Flexural strength [MPa]	5.5 (1)	5.1 (9)	4.9 (13)
Elastic modulus [MPa]	10660 (5)	10363 (4)	10328 (2)
Effect of direction	Brick surface		
	flatwise	lengthwise	widthwise
Compressive strength [MPa]	23.5 (5)	22.3 (10)	18.6 (10)
Flexural strength [MPa]	4.5 (14)	4.4 (4)	-
IRA [kg/(m²×min)]	0.47 (9)	0.79 (2)	1.03 (5)
Capillary coefficient [kg/(m²×min$^{0.5}$)]	0.32 (1)	0.59 (2)	0.61 (8)
Desorption [%]	-10.2 (1)	-10.0 (1)	-10.3 (1)

*CoV of the results is given in percentage inside parentheses.

where $W_{24hr.}$ is the specimen mass after 24 hours. The moisture content ratio to the water absorption reaches 33.7%, 54.8%, and 57.2% after 60 minutes for the flatwise, lengthwise, and widthwise surfaces, respectively, see Fig. 4-6. The optimum range of moisture content for achieving the highest flexural bond strength between the clay bricks and lime mortars was reported in [195,196] between 40% and 80%. Accordingly, the bricks of the single-lap shear specimens (section 5.7.2) with the semi-saturated condition are immersed in water at the flatwise surface and for 165 min, which results in moisture content of nearly 60 % of saturation (Fig. 4-6).

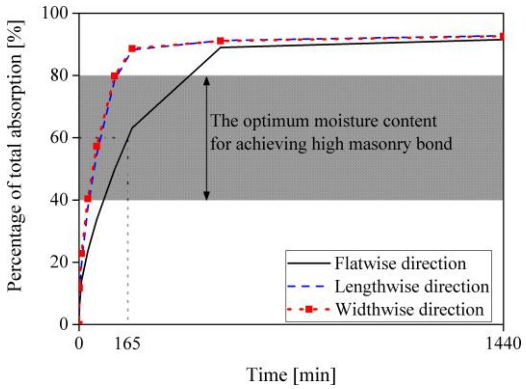

Fig. 4-6. The moisture content of the brick to the total absorption as a function of time in the capillary test.

4.4. Effect of aging of lime-based mortar

In this section, the effect of mortar age on the mechanical properties of mortars M1 and M2 is investigated. As mentioned in section 3.9.1, the specimens were stored in the environmental lab (named indoor specimens) or outside at real environmental conditions for 920 days (named outdoor specimens). The following paragraphs present the obtained results.

Table 4-6 and Table 4-7 summarize the variation of compressive and flexural strength of both mortar M1 and mortar M2 types aged under indoor and outdoor conditions. Although the peak compressive strength of both mortars is similar, this value is reached at different ages showing governance of different hydration rates in these two mortars. In addition, it can be observed that the peak strength (the maximum compressive and flexural stress) is not reached at a specific age in these lime-based mortars, as opposed to typical cementitious mortars. The peak compressive strength of mortar M1 under indoor conditions occurs at 60 days (8.3 MPa), while its peak flexural strength is only reached at 180 days (6.0 MPa). Interestingly, a slightly higher compressive strength but lower flexural strength is obtained under outdoor conditions. In contrast, the peak compressive strength in mortar M2 (stored indoor) is observed at 30 days (9.5 MPa), and the peak flexural strength is reached at 920 days (3.1 MPa). Both flexural and compressive strengths of this mortar are slightly lower under outdoor conditions (except for compressive strength at 180 days). Overall, mortar M1 has a flexural strength higher than mortar M2 despite having a lower compressive strength, which indicates a less fragile response of the mortar M1 due to the existence of short fibers in the mortar mix.

Table 4-6. Mechanical properties of mortars aged under indoor conditions*.

Mortar	Test	3 days	7 days	14 days	30 days	60 days	90 days	180 days	920 days
M1	Compressive strength (f_c) [MPa]	0.9 (4)	3.8 (5)	5.9 (8)	7.1 (9)	8.3 (11)	7.8 (4)	7.5 (10)	5.7 (12)
	f_c / $f_{c\text{-}30\ days}$ [%]	0.13	0.53	0.84	1.00	1.17	1.11	1.06	0.81
	Flexural strength (f_{fl}) [MPa]	-	2.5 (7)	4.0 (3)	4.7 (7)	5.1 (3)	5.6 (10)	6.0 (10)	5.2 (11)
	f_{fl} / $f_{fl\text{-}30\ days}$ [%]	-	0.53	0.86	1.00	1.08	1.09	1.18	1.02
M2	Compressive strength (f_c) [MPa]	3.9 (7)	6.5 (7)	8.8 (7)	9.5 (10)	8.8 (12)	8.9 (5)	7.5 (9)	7.9 (5)
	f_c / $f_{c\text{-}30\ days}$ [%]	0.41	0.68	0.92	1.00	0.92	0.93	0.79	0.83
	Flexural strength (f_{fl}) [MPa]	1.4 (3)	1.5 (3)	1.8 (12)	2.5 (9)	2.1 (7)	2.3 (9)	2.6 (13)	3.1 (12)
	f_{fl} / $f_{fl\text{-}30\ days}$ [%]	0.55	0.60	0.71	1.00	0.82	0.92	1.03	1.23

*CoV of the results is given in percentage inside parentheses.

It can be indicated that outdoor conditions cause both mortars M1 and M2 to reach higher compressive strength when compared to the indoor aged specimens. This observation can be due to the presence of more moisture and more hydration of mortars. In contrast, indoor aged specimens dry faster, and the hydration processes stop.

Table 4-7. Mechanical properties of mortars aged under outdoor conditions*.

Mortar	Test	90 days	180 days	920 days
M1	Compressive strength (f_c) [MPa]	7.8 (4)	9.7 (16)	6.6 (8)
	Flexural strength (f_{fl}) [MPa]	5.6 (10)	5.3 (7)	4.1 (11)
M2	Compressive strength (f_c) [MPa]	8.9 (5)	10.9 (12)	6.3 (5)
	Flexural strength (f_{fl}) [MPa]	2.3 (9)	2.3 (12)	2.3 (3)

*CoV of the results is given in percentage inside parentheses.

4.5. Effect of freeze-thaw conditions

In this part, the effect of freeze-thaw (FT) conditions on the material properties are discussed experimentally. The mortars M1 and M3, brick, steel cords, and glass yarns were exposed to 360 FT cycles (after a lab curing duration of 90 days at 18°C and 75% RH condition, see section 3.9.2), and their strength variations were compared to the control specimens stored under environmental lab conditions.

4.5.1. Mortar

Fig. 4-7 shows the DTA analysis of the mortars M1 and M3 (based on lime and ecopozzolan, respectively), which were obtained for different FT cycles, as mentioned in Fig. 4-7. DTA analysis graph the mortar M1 shows three peaks (Fig. 4-7a) attributed to water evaporation (50-100°C), dehydroxylation (losing bound water at 380-400°C), and decarboxylation (releasing CO_2 at 680-780°C) [38,190,197,198]. However, the DTA result of the mortar M3 only shows one peak point at 800°C due to decarboxylation. DTA results show that decarboxylation increases with time under both the control and the FT conditions due to the large amount of $CaCO_3$ when it is compared to the control specimens at 90 days of age (C0). The dehydroxylation and decarboxylation changes obtained from the DTA test show that the used lime-based mortar is still hardening at older ages under both the control and the FT conditions. Generally, hydraulic

lime-based mortar hardens with a combination of hydration and carbonation, according to [187]. Therefore, from these outputs and previous results [199,200], it can be concluded that using a hydraulic lime-based mortar at an early age for durability tests can lead to erroneous results.

Table 4-8 summarizes the varying strength of the mortar M1 and M3 under both the control and the FT conditions. After exposing 360 FT cycles, the compressive, flexural, and splitting strength, as well as elastic modulus of the mortar M1, increased by 12%, 11%, 57%, and 11%, respectively, compared to 0-cycle (C0) specimens. Under the control conditions, the compressive and flexural strength of C360 specimens do not change compared to C0 specimens, but the splitting strength and the elastic modulus increase by 50% and 21%, respectively. These observations show that the considered FT conditions do not have a detrimental effect on the mortar strength but lead to a slight enhancement of properties, possibly by promoting mortar hydration under high humidity conditions [201]. This conclusion is supported by differences in the DTA for the mortar M1 under the FT condition. The changes of mortar M3 strength differ from those of mortar M1. Under both the control and the FT conditions, the mechanical properties of this mortar do not change. However, its elastic modulus under the control conditions shows a decreasing trend.

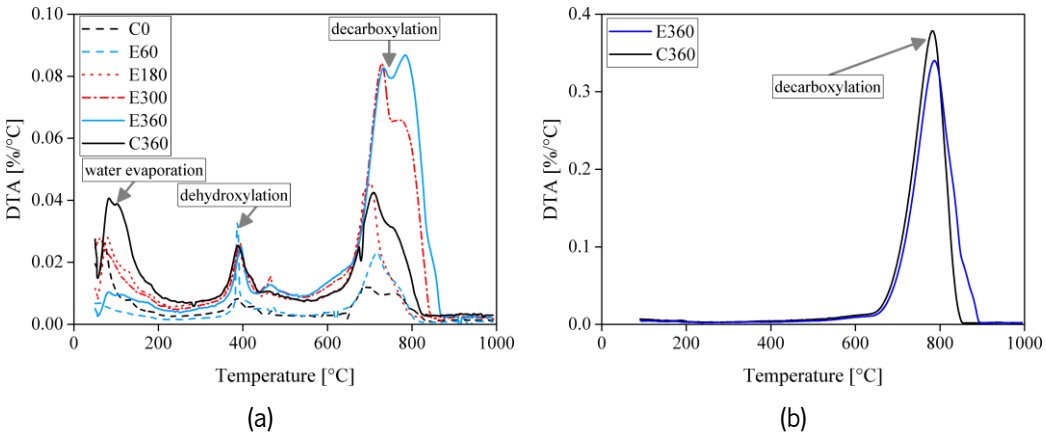

Fig. 4-7. Differential thermal analyses (DTA) result: (a) mortar M1; (b) mortar M3.

Table 4-8. Mechanical properties of the mortar M1 and mortar M3 under freeze-thaw conditions*.

Strength	Material	Control specimens [cycles]			Exposed specimens [cycles]					
		C0	C180	C360	E60	E120	E180	E240	E300	E360
Compressive strength [MPa]	M1	16.8 (11)	20 (12)	17.3 (10)	17.0 (10)	19.0 (22)	19.5 (5)	17.5 (4)	17.3 (2)	18.8 (3)
	M3	8.7 (6)	6.0 (9)	7.8 (4)	-	-	8.3 (6)	-	-	9.8 (5)
Flexural strength [MPa]	M1	4.5 (2)	4.5 (12)	4.7 (5)	-	-	5.8 (5)	-	-	5.0 (5)
	M3	8.7 (6)	6.0 (9)	7.8 (4)	-	-	8.3 (6)	-	-	9.8 (5)
Elastic modulus [MPa]	M1	6713 (6)	8280 (11)	8095 (10)	-	-	7593 (1)	-	-	7462 (12)
	M3	5236 (10)	-	3301 (8)	-	-	-	-	-	4875 (13)
Splitting strength [MPa]	M1	1.4 (8)	2.0 (14)	2.1 (8)			2.2 (3)			2.2 (9)
	M3	0.5 (7)	-	0.6 (15)	-	-	-	-	-	0.6 (17)

*CoV of the results is given in percentage inside parentheses.

4.5.2. Brick

The compressive and the flexural strengths of the brick were determined perpendicular to the flatwise surface of the brick, while the elastic modulus was characterized perpendicular to the widthwise surface. Table 4-9 presents the brick strength changes under the FT conditions. In general, the brick strength does not change significantly, which is in accordance with the results reported in [28]. In addition, the compressive strength of the masonry prism does not degrade under both conditions, which is in line with the mortar M3 and brick behavior.

Table 4-9. Mechanical properties of the brick under freeze-thaw conditions*.

Strength	Material	Control specimens [cycles]		Exposed specimens [cycles]
		0	360	360
Compressive strength [MPa]	Brick	23.5 (5)	-	22.5 (7)
	Masonry prism	11.1 (8)	10.1 (17)	9.7 (13)
Flexural strength [MPa]	Brick	4.5 (14)	-	4.5 (6)
Elastic modulus [MPa]	Brick	9650 (2)	-	9476 (2)

*CoV of the results is given in percentage inside parentheses.

4.5.3. Fibers

The tensile strength of the steel cords and glass yarns was also determined under freeze-thaw conditions. Since the glass fabric is bi-directional (see Fig. 3-1e), its tensile behavior at both warp and weft directions was measured; however, the steel cord is a unidirectional mesh, and its strength was only measured in one direction. Table 4-10 reports the tensile stress, Young's modulus, and rupture strain of the steel and the glass fibers before and after freezing-thawing exposure. The glass fibers do not show any deterioration, but the tensile strength and elastic modulus of steel cords under the FT conditions declined slightly by 5% and 9%, respectively.

Table 4-10. Mechanical properties of the steel and glass fibers under freeze-thaw conditions*.

Tensile parameter	Material	Control specimens	Exposed specimens to 360 FT cycles
Tensile strength [MPa]	Steel cord	2972 (8)	2819 (1)
	Glass fiber (warp)	875 (13)	899 (5)
	Glass fiber (weft)	685 (9)	676 (12)
Young's modulus [MPa]	Steel cord	189340 (8)	173000 (2)
	Glass yarn (warp)	65940 (5)	70720 (3)
	Glass yarn (weft)	69870 (4)	72910 (3)
Rupture strain [%]	Steel cord	1.88 (9)	2.07 (5)
	Glass yarn (warp)	1.77 (10)	1.86 (8)
	Glass yarn (weft)	1.45 (11)	1.29 (15)

*CoV of the results is given in percentage inside parentheses.

4.6. Main conclusions

This chapter discusses a comprehensive experiment designed to characterize the material properties under different conditions (mortar curing conditions, brick moisture conditions, indoor and outdoor exposure, and freeze-thaw conditions). Accordingly, the following main conclusions can be reached:

- The mortar strength increased under high humidity conditions due to improved hydration and carbonation, as expected. Additionally, brick strength is affected by moisture content, so that dry brick demonstrated the best strength.
- Results indicate that particular attention needs to be paid to the hydration degree of lime mortar in lime-based TRM composites and its effects on both short-term and long-term properties. The 30-day curing testing age, which is normally used for cementitious matrices, appears to be less appropriate when referring to hydraulic lime-based TRMs.

- Under the considered FT conditions, the mortar mechanical properties slightly improved. Control specimens showed similar behavior as well. Based on the findings, it is concluded that the hardening process for the mortar continued after 360 cycles (337 days).
- Freeze-thaw conditions did not affect the mechanical properties of glass fibers, while the tensile strength of the steel fibers decreased slightly.

Chapter 5: Mechanical performance of TRM composites

This chapter presents and discusses experimental results of the mechanical behavior of TRM composites tested under varied parameters and conditions. For this purpose, pull-out tests, tensile tests, and single-lap shear tests were performed as described in chapter 3. The main highlights from this chapter are as follows:

- An optimized test setup for performing the pull-out tests is developed.
- The effect of different variables (e.g., bond length, fiber configuration, slip rate, and cyclic loading) on the textile-to-mortar bond behavior are investigated.
- The effects of mortar curing and brick moisture conditions on the TRM composite performance are explored.
- Pull-out response and tensile behavior of TRM composites under indoor and outdoor conditions are evaluated for 920 days.
- The durability performance of TRM composites under freeze-thaw conditions is investigated.

5.1. Effect of the pull-out test setup

Three different pull-out test setups were used in this section: pull-push I, pull-push II, and pull-pull, as described in section 3.4.1. The envelope and average of the load-slip curves obtained from each test setup are illustrated in Fig. 5-1. The failure mode obtained for all three types of test setups was pull-out of the fiber from the mortar, which causes the load-slip curves from different test setups to be similar. Nevertheless, there are some differences in the peak load (P_F), the initial stiffness (K), and consequently the toughness or energy absorption (E) due to the effect of the test setup. These parameters are the main outcomes of the pull-out tests that are used for investigating the bond behavior [62,66] and can significantly affect the experimental interpretations or the extracted bond-slip laws.

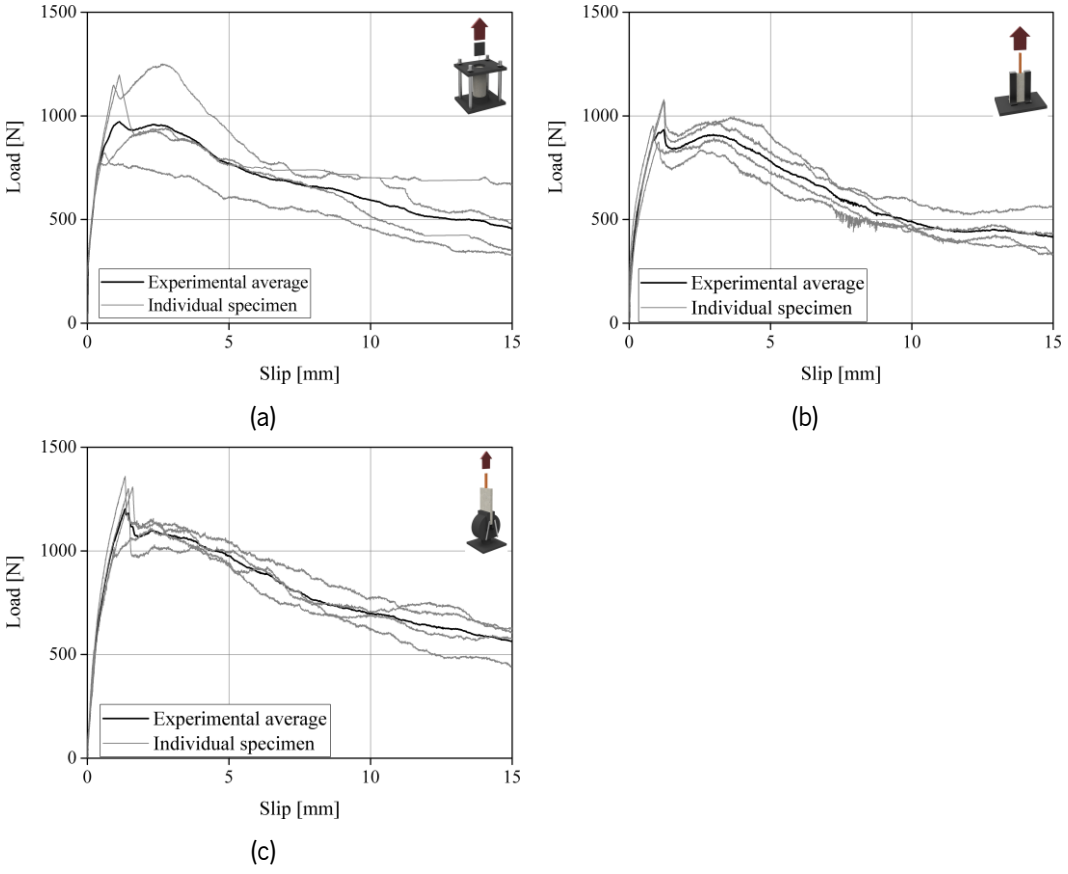

Fig. 5-1. Envelope load-slip curves for different test setups: (a) pull-push I; (b) pull-push II; (c) pull-pull.

The peak load (P_F) and its corresponding slip (s_F) are directly obtained from the experimental load-slip curves. The initial stiffness (K) is obtained as the slope of the linear portion of the load-slip curve and corresponds to the initial stage of the stress transfer before the occurrence of any interfacial cracking [31,62,66]. The toughness or absorbed energy is defined as the area under the load-slip curve [62,66,79–81]. The bond between the fiber and the mortar has a significant influence on the fiber's ability

to stabilize crack propagation in the mortar and consequently on the total energy consumption. Here, as also suggested in the literature [61,202], the area under the load-slip curve until the peak load is considered as the toughness or debonding energy absorption (E_{deb}). These parameters are obtained from the results of each test configuration, and the values are presented in Table 5-1.

It can be observed that the variation of the results obtained from the pull-push I test setup is higher than the other two setups and is in the same range as reported in Ghiassi et al. [31]. The specimens tested in the pull-pull configuration have a higher pull-out load (average of 1245 N) when compared to pull-push tests (equal to 987 N and 992 N in pull-push I and II tests, respectively). The reason for such an observation can be described by analyzing the global force equilibrium. As shown in Fig. 5-2a, the applied load (P) in the pull-push tests is equal to the tensile force in the fiber (F) that is balanced by a compressive force in the mortar (M), and the reaction forces in the boundaries (on top of the specimen). On the other hand, in pull-pull specimens, tensile forces in the fiber and the mortar balance the applied load (P), as presented in Fig. 5-2b. In other words, in the pull-pull test setup, both the fiber bond and the mortar contribute to the tensile resistance, which leads to a higher peak load in these tests. The gripping conditions in pull-pull configuration (supporting specimens from the bottom side), as well as the contribution of the mortar in resisting tensile stresses, can also lead to mortar cracking at the bottom, as shown in Fig. 5-3.

Table 5-1. Effect of test setup on the pull-out tests results*.

Test setup	Specimen	s_P [mm]	P_P [N]	E_{deb} [N.mm]	K [N/mm]
pull-push I	1	0.44	782	249	1504
	2	0.94	1149	743	1818
	3	1.13	1197	936	1834
	4	0.59	824	358	1893
	average	0.78 (35)	987 (19)	571 (49)	1762 (9)
pull-push II	1	1.03	874	603	3139
	2	1.23	1066	857	2972
	3	0.828	952	566	3662
	4	1.225	1079	895	3206
	average	1.08 (15)	992 (8)	730 (20)	3245 (8)
pull-pull	1	0.95	1016	600	2184
	2	1.34	1360	1188	1863
	3	1.45	1299	1251	2712
	4	1.60	1309	1353	2166
	average	1.33 (18)	1245 (11)	1098 (27)	2231 (14)

*CoV of the results is given in percentage inside parentheses; s_P: slip corresponding to peak load; P_P: peak load; E_{deb}: debonding energy; K: initial stiffness.

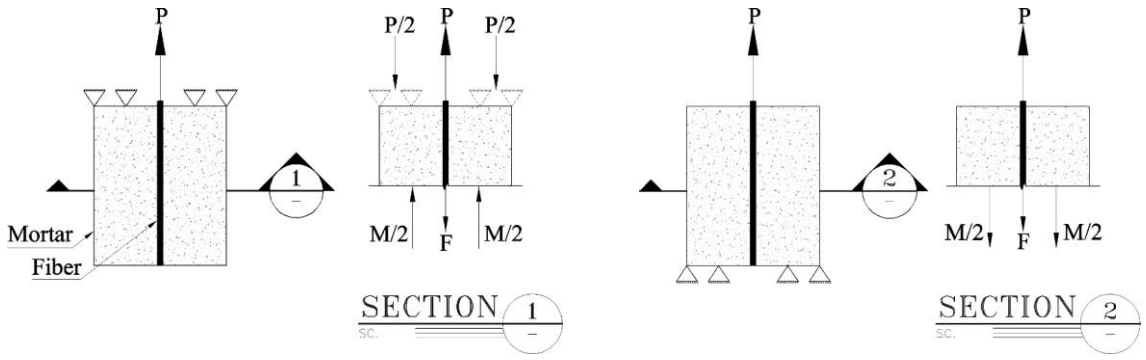

(a) (b)

Fig. 5-2. Global force equilibrium: (a) pull-push test; (b) pull-pull test.

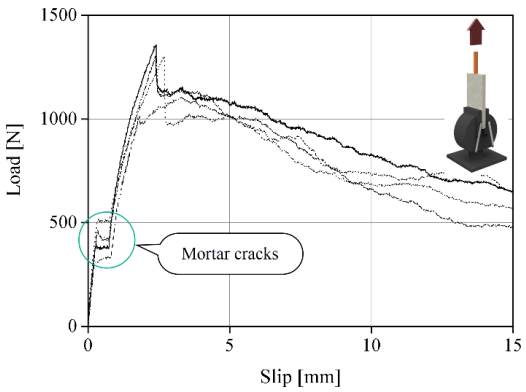

Fig. 5-3. Load-slip curves of pull-pull specimens obtained from the internal LVDT of the machine.

Regarding the initial stiffness (K), the results from the pull-push I shows the lowest value followed by pull-pull and pull-push II test setups, see Table 5-1. In this test setup (pull-push I), as explained before, the flexibility of the fibers increases the complexity of the slip measurements. Moreover, due to the space limitations, the LVDTs are usually attached at a small distance from the loaded end, and the slip values are measured by the reduction of the elastic deformation of the fibers. This adds an additional source of error in the results. Embedment of the fibers in the resin block in pull-push II and pull-pull specimens has, therefore, a significant role in accurate measurement of the fiber slip during the tests. This resin block significantly reduces the elastic deformation of the fiber in the un-bonded length and additionally protects the fibers from premature failure due to handling, clamping, or stress concentrations during the tests. A comparison between the load-slip curves obtained from the internal LVDT of the hydraulic actuator and the LVDT attached to the fibers in pull-push I and pull-push II test setups confirm the significant reduction of the elastic deformation of the fibers during the tests (Fig. 5-4).

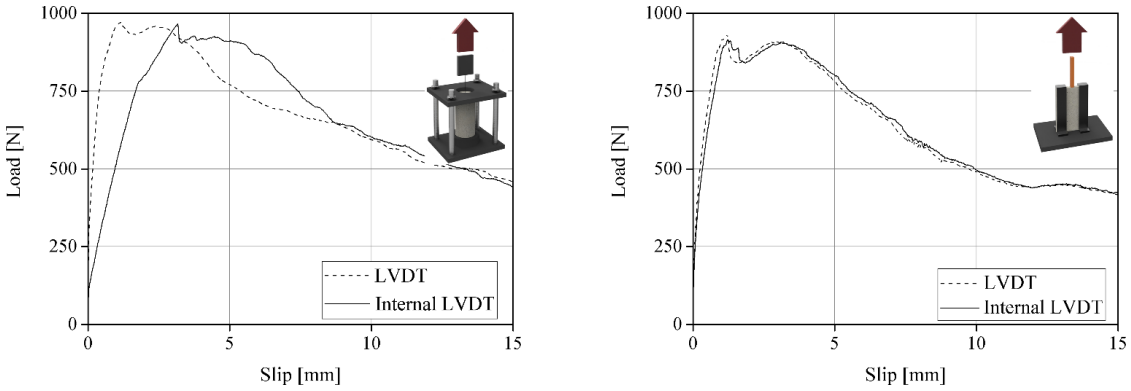

Fig. 5-4. Average load-slip curves obtained from LVDT and internal LVDT of the machine: (a) pull-push I; (b) pull-push II.

The differences in the peak load (P_P) and initial stiffness (K) of the experimental load-slip curves have also led to a significant difference in the toughness (E_{deb}) of the specimens. It can be observed in Table 5-1 that the highest debonding energy is obtained for the pull-pull tests followed by the pull-push II and pull-push I, as expected.

In addition to the variation of the obtained results, the complexities related to the construction and testing, as well as the effectiveness of the test setups, are critical. As explained before, preparation of the cylindrical specimens in pull-push I test setup is a difficult task. During the installation of the fibers inside the molds, complete alignment of the fibers is extremely challenging and difficult to control [31]. Additionally, a pre-load shall be applied to specimens in pull-push I test specimens to ensure a straight alignment of the fiber at the loaded end and to facilitate installation of the LVDT before initiation of the tests. These problems have been resolved in the pull-push II and pull-pull specimens by preparing disk-shaped molds for the mortar and embedment of the free-length fiber in a block of epoxy resin. Gripping of the pull-pull specimens from the bottom, however, remain tricky as it can lead to crushing/cracking of the mortar before starting the tests.

5.2. Effect of bond length

To investigate the bond length effect in TRM composites, single glass yarns were embedded into the mortar M1 mortar, and single steel cords were embedded into the mortar M2. For steel fibers, embedded lengths of 50, 100, 150, and 200 mm were considered, and for glass fibers, embedded lengths of 50, 75, and 100 mm were considered, based on previous studies [15,31]. A more detailed description of the tests is provided in section 3.4.2.

5.2.1. Steel-reinforced mortar

The load-slip curves obtained from single fiber steel-based TRMs with different embedded lengths are shown in Fig. 5-5. As illustrated, the maximum pull-out load is lower than the tensile strength of the steel fibers in all cases. The pull-out response consists of the typical elastic, nonlinear, and dynamic stages in all embedded lengths [31,61,62,65,66], with the failure mode being slippage of the fiber from the mortar in all specimens, except for three specimens, in which vertical cracks occurred in the mortar (Fig. 5-6). The effect of mortar cracking is clearly observable on the pull-out response of the specimens, see Fig. 5-5a, b.

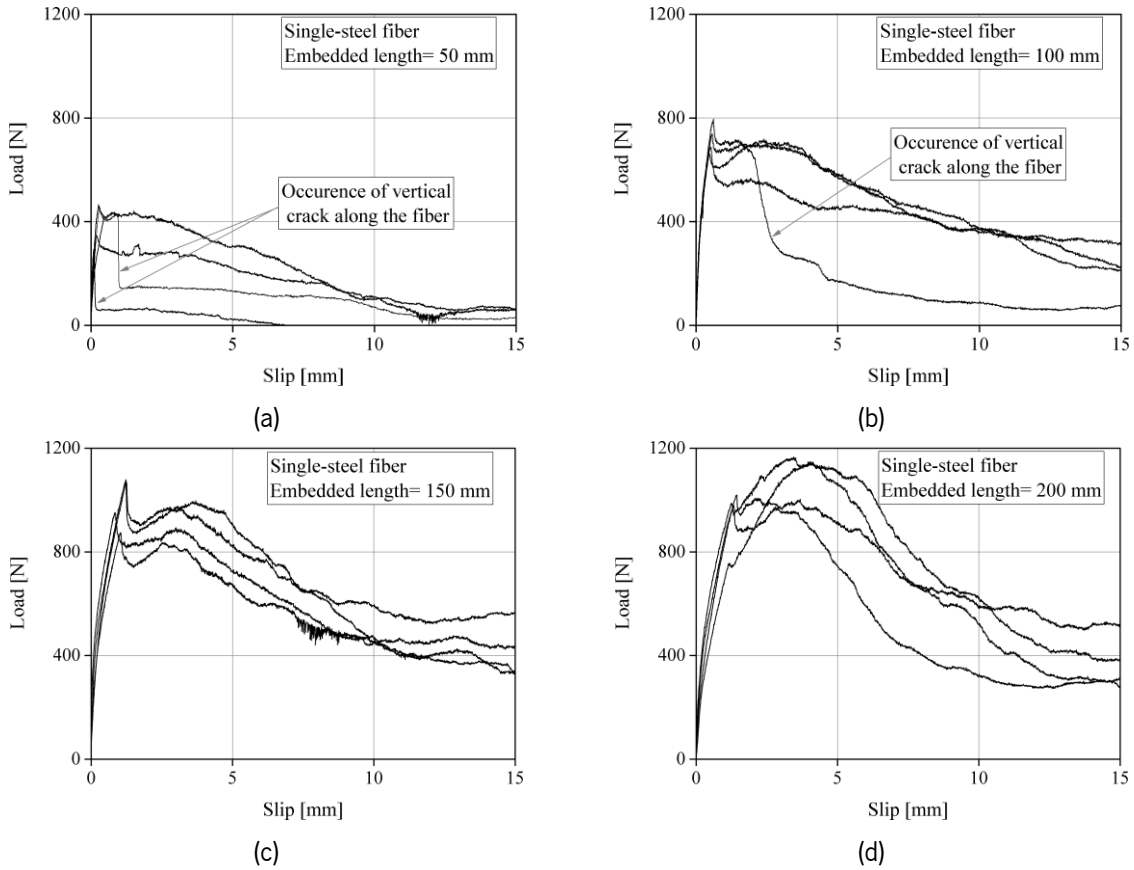

Fig. 5-5. Load-slip response of single steel fibers with different embedded lengths: (a) 50 mm; (b) 100 mm; (c) 150 mm; (d) 200 mm.

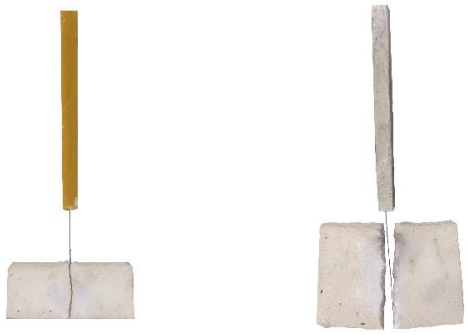

(a) (b)

Fig. 5-6. The cracking failure mode of steel-based TRM obtained for: (a) two specimens of 50 mm bond length; (b) a specimen of 100 mm bond length.

The pull-out curves show that after the peak load is reached, a sudden drop occurs in the force, followed by a slip hardening behavior [53,203]. It can be observed that the slope of the slip hardening increases with the increment of the embedded length. It is clear that the pull-out response after the peak load is mainly dependent on the frictional stresses between the fiber and the matrix. High frictional stress leads to a slip hardening response, while a slip softening is observed when low frictional stress exists [77,204]. By increasing the embedded length, the total frictional force and consequently the slope of the slip hardening region increase (as shown in Fig. 5-5). When the applied load or induced transverse stresses reach the matrix tensile strength, mortar cracking or splitting occurs, which can lead to a sudden drop in the load.

The average peak load (P_P), the slip corresponding to the peak load (s_P), the toughness or debonding energy (E_{deb}), and the initial stiffness (K) for each embedded length are presented in Fig. 5-7. In addition, Table 5-2 presents pull-out parameters for the individual specimens. It can be observed that the peak load and its corresponding slip as well as the toughness increase until 150 mm embedded length and do not change significantly thereafter. These are indications of reaching the effective bond length in the range of 150- 200 mm (see Fig. 5-7a-c). This range is also in agreement with the findings of previous experimental studies on similar steel-based TRMs [31,119]. At the same time, a reverse trend is observed for the initial stiffness with an increment of embedded length (Fig. 5-7d). This phenomenon has also been observed in the experimental results reported in [53,79,205–208].

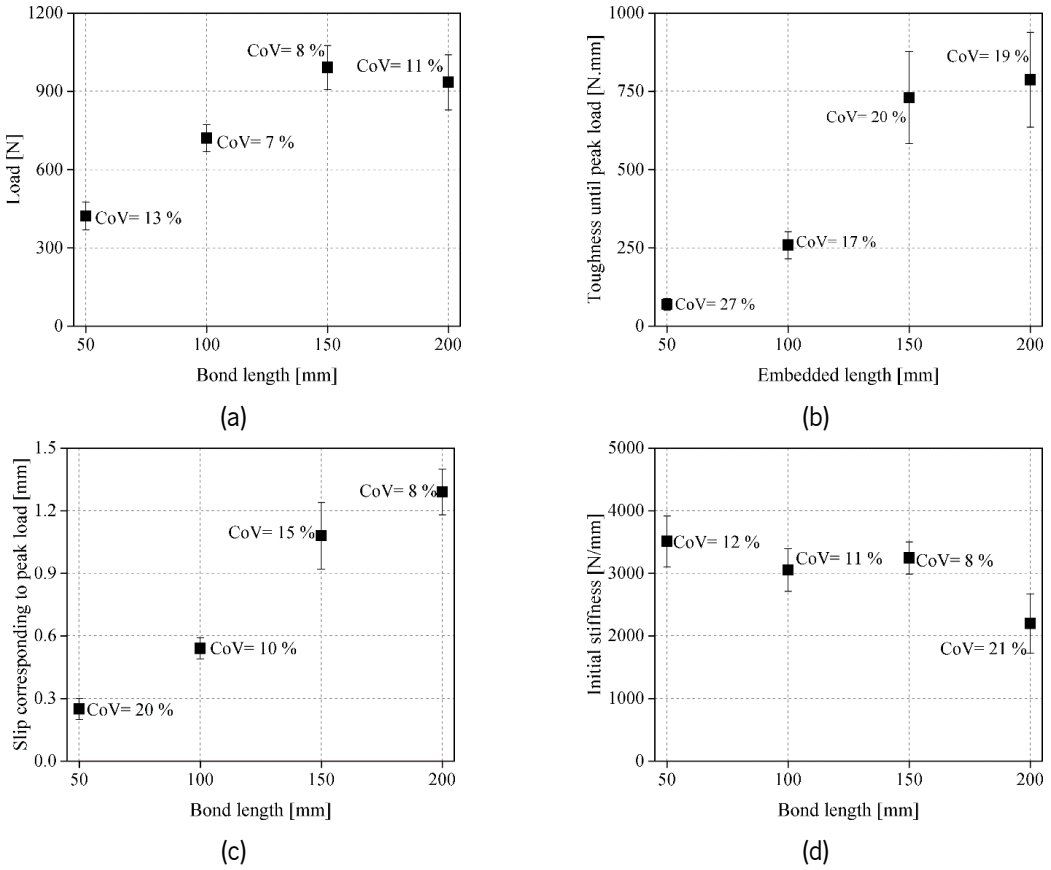

Fig. 5-7. Bond properties changes of single steel fiber based on different embedded lengths: (a) peak load; (b) toughness until peak load; (c) slip corresponding to peak load; (d) initial stiffness.

Table 5-2. Bond properties changes of single steel fiber based on different embedded lengths*.

Bond length [mm]	Specimen	s_P [mm]	P_P [N]	E_{deb} [N.mm]	K [N/mm]
50	1	0.19	347	43	3981
	2	0.31	453	87	2995
	3	0.26	466	77	3558
	average	0.25 (20)	422 (13)	69 (27)	3511 (12)
100	1	0.52	687	239	3395
	2	0.61	797	324	3393
	3	0.47	662	207	2713
	4	0.56	739	266	2714
	average	0.54 (10)	721 (7)	259 (17)	3054 (11)
150	1	1.03	874	603	3139
	2	1.23	1066	857	2972
	3	0.828	952	566	3662
	4	1.225	1079	895	3206
	average	1.08 (15)	992 (8)	730 (20)	3245 (8)
200	1	1.33	979	858	2208
	2	1.25	989	839	2847
	3	1.44	1019	924	2219
	4	1.15	755	531	1518
	average	1.29 (8)	936 (11)	788 (19)	2198 (21)

*CoV of the results is given in percentage inside parentheses; s_P: slip corresponding to peak load; P_P: peak load; E_{deb}: debonding energy; K: initial stiffness.

5.2.2. Glass-reinforced mortar

The experimental load-slip curves of the glass-based TRM specimens (single yarn) with different embedded lengths are shown in Fig. 5-8. Again, the test results indicate the significant effect of the embedded length on the bond behavior. The failure mode of the specimens changed from yarn slippage to yarn tensile rupture with increasing embedded length. In the specimens with 50 mm embedded length yarn, pull-out (slippage) occurs, and the load-slip curves consist of all the three conventional stages of the bond response (Fig. 5-8a). In the specimens with 75 mm embedded length, tensile rupture of the yarns occurs after a certain slip, and the load-slip curves only consist of the linear and the nonlinear stages, Fig. 5-8b. Finally, in the specimens with 100 mm embedded length, tensile rupture of the yarns occurs with a smaller slip value, and therefore the load-slip curves consist of an elastic stage followed by a short nonlinear stage (Fig. 5-8c).

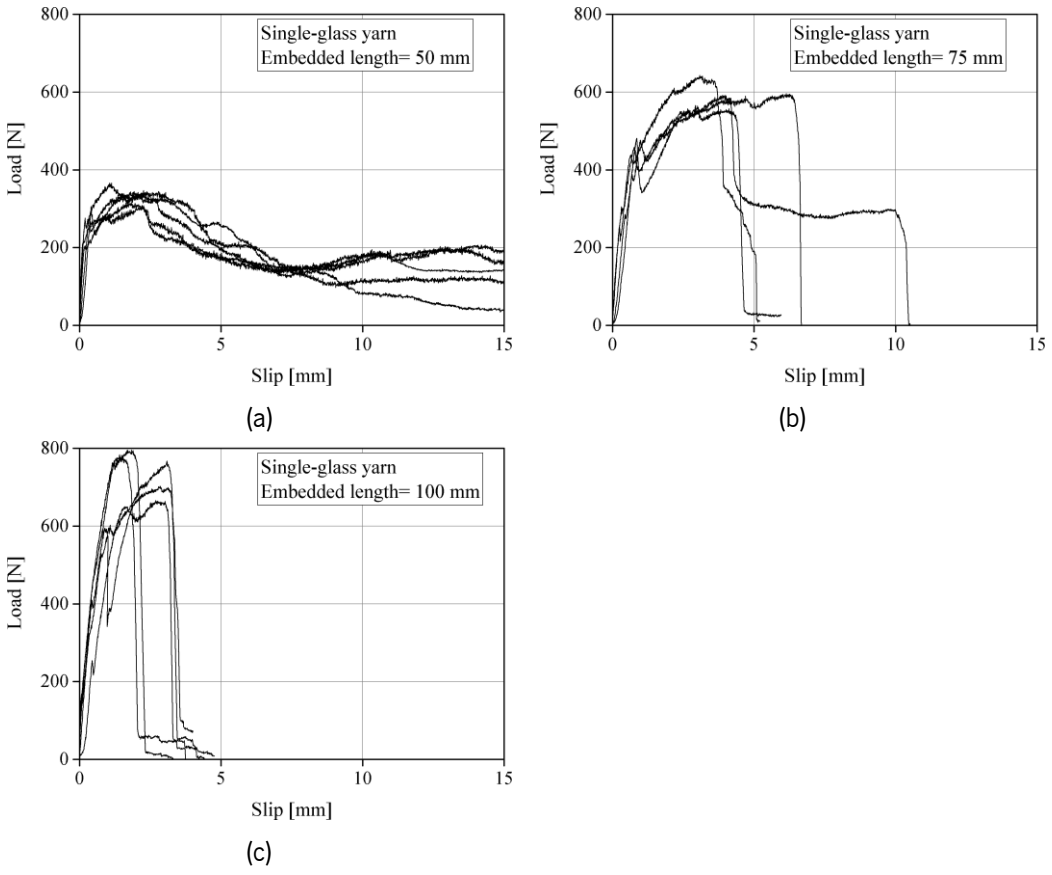

Fig. 5-8. Load-slip response of single glass fiber with different embedded lengths: (a) 50 mm; (b) 75 mm; (c) 100 mm.

The changes of the main parameters of the load-slip curves with embedded length are presented in Fig. 5-9 and Table 5-3. It can be observed that by increasing the embedded length, the peak load (P_P) increases

until yarn rupture occurs (Fig. 5-9a). The peak load at 100 mm embedded length is very near the yarn tensile strength obtained from direct tensile tests. The debonding energy absorption (E_{deb}) increases from 50 mm to 75 mm embedded length and then decreases at 100 mm (Fig. 5-9b). This is expected, as the yarn slipping (that governs the specimens with 50 and 75 mm bond length) dissipates more energy than the yarn tensile failure. The changes of the slip corresponding to the peak load (S_P) with embedded length are also affected by the failure mode in the specimens (Fig. 5-9c). At the same time, the initial stiffness (K) decreases with the increment of the embedded length that is a similar observation to steel-based TRMs, as shown in Fig. 5-9d.

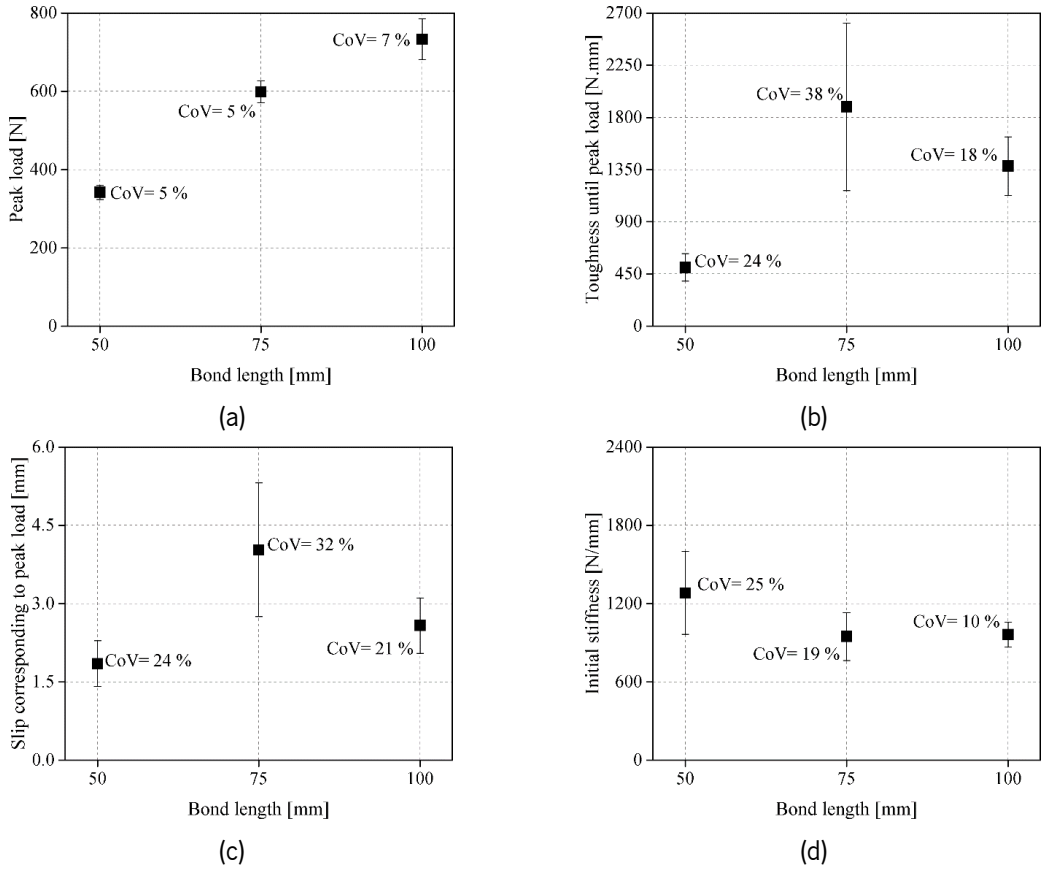

Fig. 5-9. Bond properties changes of single glass yarn based on different embedded lengths: (a) peak load; (b) toughness until peak load; (c) slip corresponding to peak load; (d) initial stiffness.

Table 5-3. Bond properties changes of single glass yarn based on different embedded lengths*.

Bond length [mm]	Specimen	s_P [mm]	P_P [N]	E_{deb} [N.mm]	K [N/mm]
50	1	2.26	347	641	945
	2	1.13	366	331	1706
	3	1.83	317	467	1469
	4	2.17	337	584	1009
	average	1.85 (24)	342 (5)	506 (24)	1282 (25)
75	1	3.08	643	1512	1089
	2	6.13	597	3097	1170
	3	2.93	566	1202	785
	4	3.96	592	1754	748
	average	4.03 (32)	599 (5)	1891 (38)	948 (19)
100	1	2.69	666	1454	809
	2	2.85	703	1479	1049
	3	3.09	768	1633	950
	4	1.68	796	960	1039
	average	2.58 (21)	733 (7)	1381 (18)	962 (10)

*CoV of the results is given in percentage inside parentheses; s_P: slip corresponding to peak load; P_P: peak load; E_{deb}: debonding energy; K: initial stiffness.

5.3. Effect of fiber configuration

The effect of fiber configuration on the fiber-to-mortar bond behavior is investigated. The steel-based TRM composite included single, two, and four cords embedded in the mortar M2 with a 150 mm embedment length. The glass-based TRM composites were single yarn, single yarn, and transverse elements, and a group of yarns reinforcing the mortar M1 with 50 mm bond length. In chapter 3, the tests are described in more detail.

5.3.1. Steel-reinforced mortar

The average and envelope of the load-slip curves obtained from steel-based TRMs with different configurations are shown in Fig. 5-10. The results are presented in terms of the applied load per fiber (load divided by the number of fibers) versus slip to facilitate comparison between different configurations. It can be observed that although the steel fibers are unidirectional, the pull-out response of single cords is different from that of the multiple cords. The failure mode of the specimens also changes from fiber slippage in single cord specimens to mortar cracking and splitting in multiple cords specimens, as shown in Fig. 5-11. The pull-out curve of the single cord specimens (Fig. 5-10a) shows a second peak load followed by a load reduction after complete debonding. This second peak load is not observed in the multiple cords specimens (Fig. 5-10b, c), which can be due to the occurrence of mortar cracking and splitting after the peak load. From the presented curves, it can be observed that in contrast to the single

cord specimens (Fig. 5-10a), the slip measurements are different from that of internal LVDT measurements in the multiple cords specimens. Although this difference does not affect the obtained results, it shows that by increasing the number of cords, the deformation of the resin block used for gripping the specimens becomes significant, leading to a large difference between these two measurements.

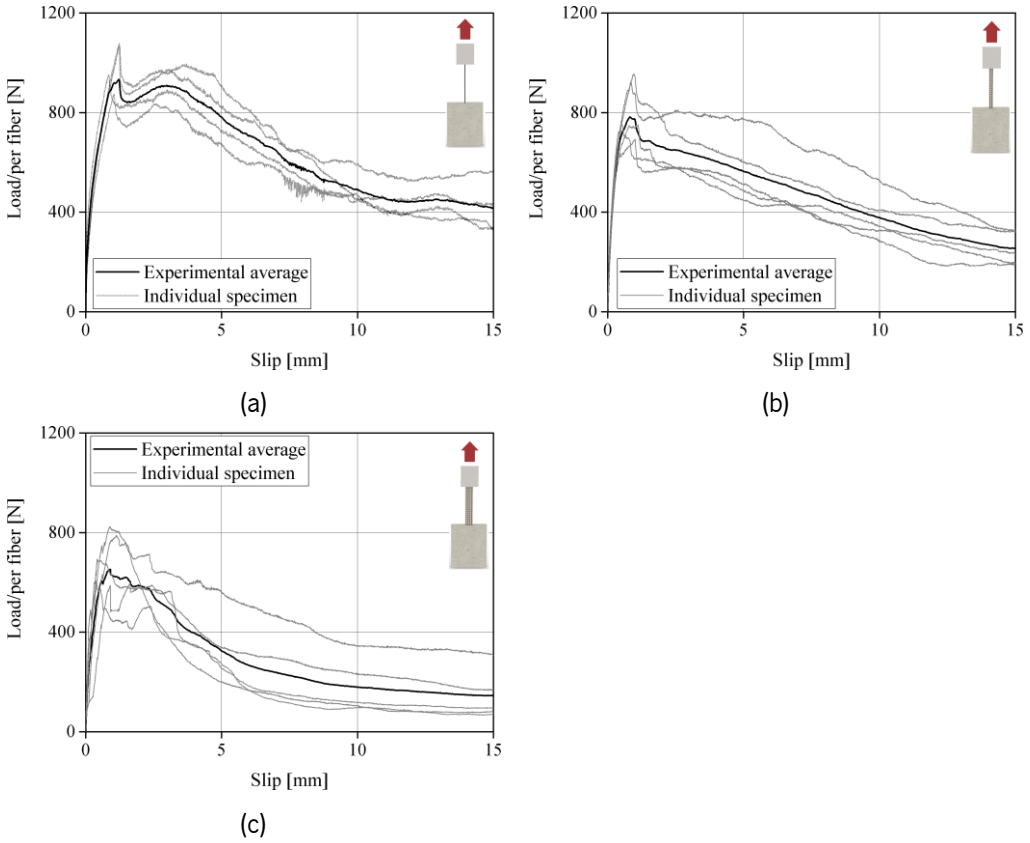

Fig. 5-10. Pull-out response of steel-based TRMs with different configurations: (a) single cord; (b) two cords; (c) four cords.

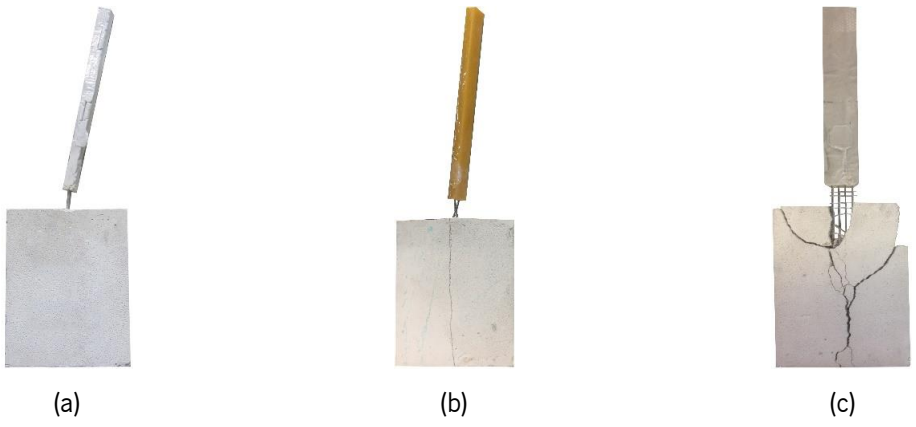

Fig. 5-11. Failure modes of steel-based TRMs with different configurations: (a) single cord; (b) two cords; (c) four cords.

Fig. 5-12a illustrates a comparison among the average pull-out responses in different configurations, and Fig. 5-12b presents the calibrated load-slip curves based on the number of cords. It can be observed that by increasing the number of cords, the load carried by each cord decreases due to the so-called fiber volume fraction effect [209–211] and the change of failure modes. Table 5-4 clearly shows that by increasing the number of cords, the peak load (P_P), and the slip corresponding to the peak load (s_P), the toughness (E_{deb}) and initial stiffness (K) of the load-slip curves decrease. Moreover, by increasing the number of cords, the energy absorption decreases that due to the change of the failure mode from pull-out to mortar cracking, as presented in Fig. 5-12b.

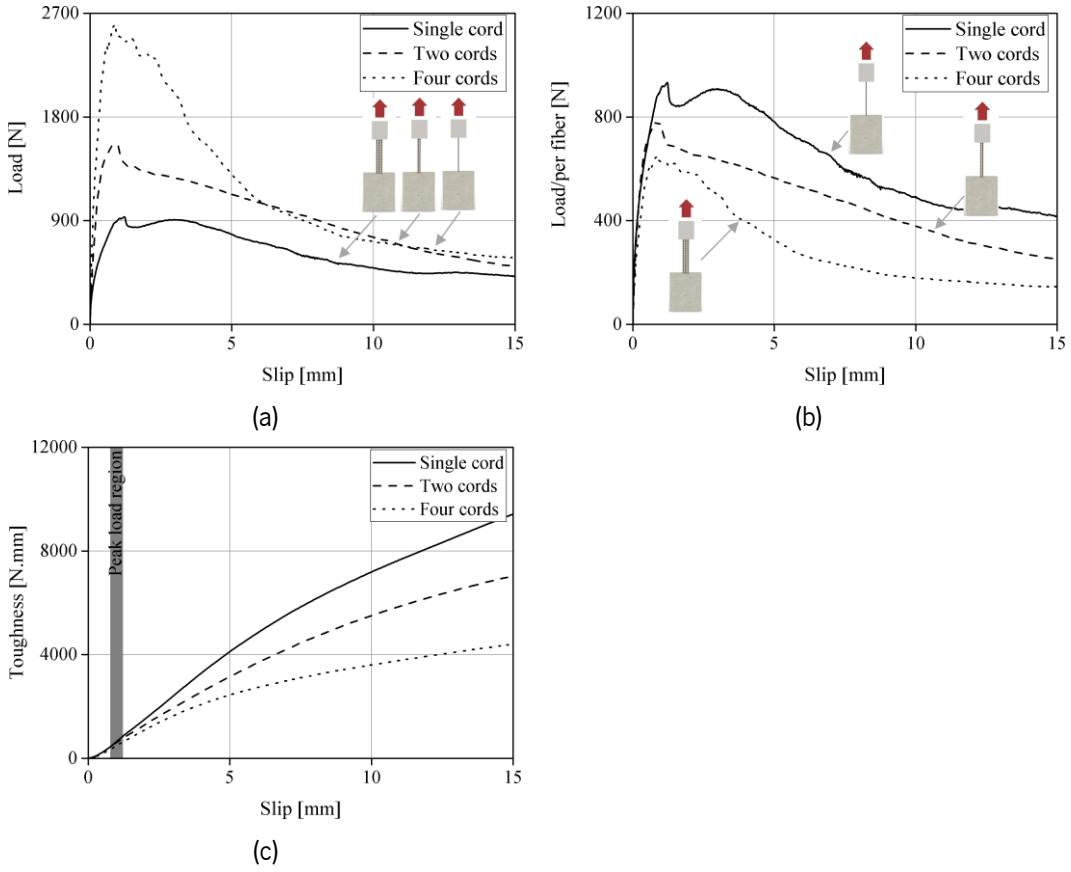

Fig. 5-12. (a) The average pull-out curves; (b) the average pull-out curves per fiber; (c) the cumulative absorbed energy of steel-based TRMs with different fiber configurations.

Table 5-4. Changes of bond properties in steel-based TRM with fiber configuration*.

Fiber configuration	Specimen	s_P [mm]	$P_{P,\ per\ fiber}$ [N]	$E_{deb,\ per\ fiber}$ [N.mm]	$K_{\ per\ fiber}$ [N/mm]
Single cord	1	1.03	874	603	3139
	2	1.23	1066	857	2972
	3	0.828	952	566	3662
	4	1.225	1079	895	3206
	average	1.08 (15)	992 (8)	730 (20)	3245 (8)
Two cords	1	0.96	956	651	2323
	2	1.01	695	556	2175
	3	0.86	922	538	2499
	4	0.51	752	271	3678
	5	1.12	750	673	3016
	average	0.89 (23)	815 (13)	538 (27)	2738 (20)
Four cords	1	0.41	693	168	3742
	2	0.86	823	491	3247
	3	0.90	589	286	2961
	4	0.39	607	162	3477
	5	1.12	789	592	3068
	average	0.74 (39)	700 (13)	340 (51)	3299 (9)

*CoV of the results is given in percentage inside parentheses; s_P: slip corresponding to peak load; P_P: peak load; E_{deb}: debonding energy; K: initial stiffness.

5.3.2. Glass-reinforced mortar

The average and envelope of the pull-out curves obtained from the glass-based TRMs with different configurations are shown in Fig. 5-13. The difference between the single-yarn and group fiber specimens is more significant in the latter, which can be attributed to the effect of transverse elements. The main parameters of the pull-out curves are also summarized in Table 5-5.

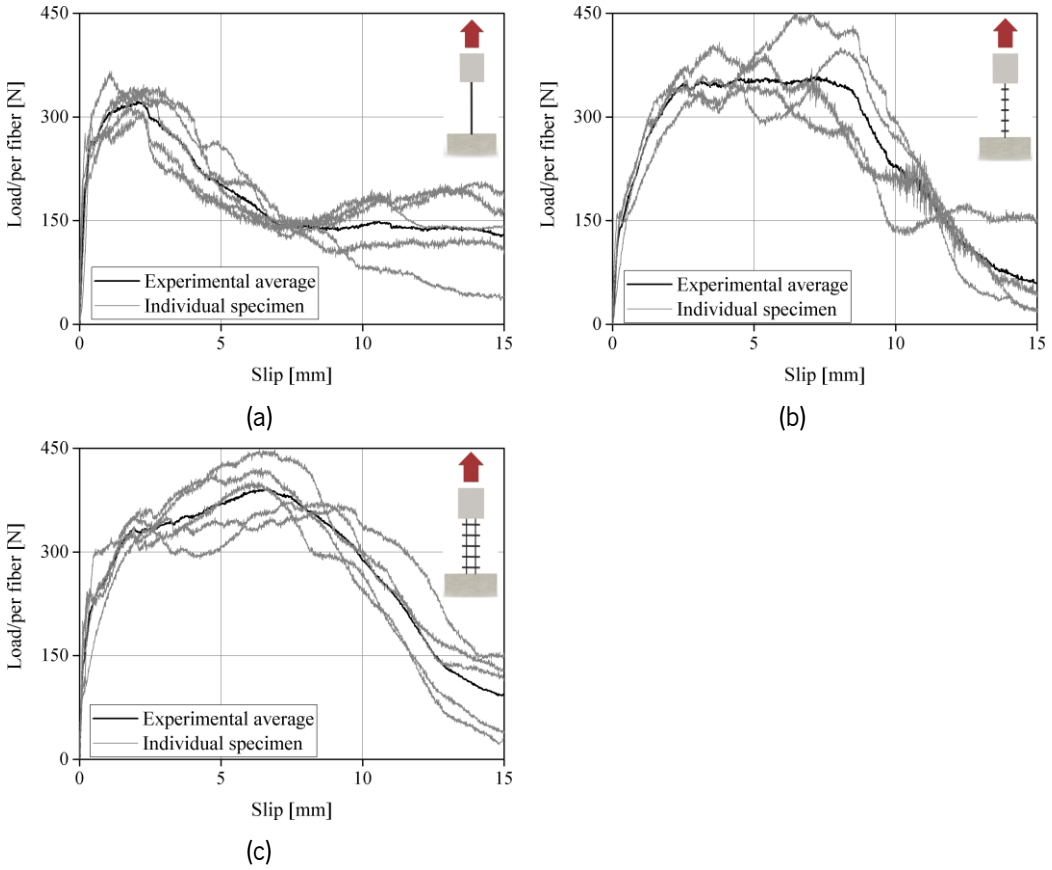

Fig. 5-13. Pull-out response of glass-based TRMs with different configurations: (a) single yarn; (b) single yarn+ transverse; (c) group (2 yarns).

In general, the specimens made of single yarns with 50 mm embedded length to show all the three conventional stages of the pull-out behavior [16,31,62,65,66], see Fig. 5-13a. On the other hand, the specimens made of "single+ transverse" and the group specimens do not have the typical drop of the pull-out load after the peak (Fig. 5-13b, c). On the contrary, the pull-out curves in these specimens show a slip hardening behavior and pseudo ductility before the final load drop. This strain hardening behavior can be attributed to the contribution of the transverse elements (weft yarns) to the bond response. It should also be reported that the slippage yarns in "single+ transverse" and the group specimens are followed by breakage of the transverse elements at the last stage of the tests.

The effect of transverse elements on the bond response has also been previously reported in [212] by comparing the bond behavior in the fabric and the single yarn polypropylene. The results illustrated that transverse elements increase clearly both the peak load and its corresponding slip. Meanwhile, in the current study, the presence of transverse elements has only caused an increment of slip hardening. This different observation shows that depending on the properties of the fiber and mortar, the effect of transverse elements on the bond response can be different. Therefore, it can be concluded that the transverse elements work as an anchorage, leading to enhanced strength and ductility.

Table 5-5. Changes of bond properties in glass-based TRM with fiber configuration*.

Fiber configuration	Specimen	s_P [mm]	$P_{P,\ per\ fiber}$ [N]	$E_{deb,\ per\ fiber}$ [N.mm]	$K_{per\ fiber}$ [N/mm]
Single yarn	1	2.26	347	641	945
	2	1.13	366	331	1706
	3	1.83	317	467	1469
	4	2.22	309	591	1392
	5	2.17	337	584	1009
	average	1.92 (22)	335 (6)	522 (21)	1304 (22)
Single yarn+ transverse	1	2.43	369	607	837
	2	3.12	341	729	786
	3	2.61	353	679	958
	4	3.56	405	1077	934
	average	2.93 (15)	367 (7)	773 (23)	879 (8)
Group (2 yarns)	1	6.35	449	2298	1002
	2	6.43	422	2208	1420
	3	7.22	374	2129	1247
	4	6.08	404	1941	1031
	5	9.15	372	2979	1562
	average	7.05 (16)	404 (7)	2311 (15)	1252 (17)

*CoV of the results is given in percentage inside parentheses; s_P: slip corresponding to peak load; P_P: peak load; E_{deb}: debonding energy; K: initial stiffness.

It seems that the slope of the slip hardening in the group specimens is higher than "single+ transverse," which is due to the higher stiffness of the transverse elements in these specimens, Fig. 5-14a. It can be observed in Table 5-5 that although a larger slip corresponding to the peak load (s_P) and debonding energy (E_{deb}) is obtained in the group and "single+ transverse" specimens compared to single yarn specimens, the peak load (P_P) and the initial stiffness (K) have negligible changes. The toughness, or the absorbed energy, is almost the same until the slip of 3.5 mm (Fig. 5-14b). Thereafter, the transverse elements cause the energy absorption to increase about 22 % and 36 % for the "single+ transverse" and the group specimens, respectively.

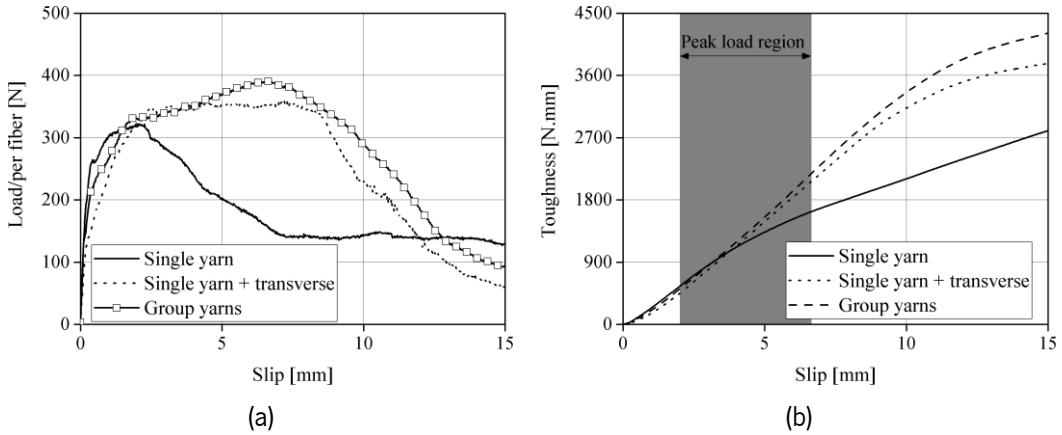

Fig. 5-14. (a) The average pull-out curves; (b) the cumulative absorbed energy of glass-based TRMs with different fiber configurations.

5.4. Effect of slip rate

Quasi-static tests were performed on specimens to study the influence of slip rate on bond behavior. Five different slip rates were considered, namely 0.2, 1.0, 5.0, 10.0, and 20.0 mm/min. Single steel and glass yarns were embedded in mortar M1 with bond lengths of 150 mm and 50 mm, respectively. A detailed description of the tests can be found in chapter 3.

5.4.1. Reliability and physical meaning of test outcomes

As explained before, the specimens prepared for pull-out tests consisted of a free yarn/cord length, which was embedded in an epoxy block resin to facilitate the gripping of the samples by the wedges of the testing machine. Nevertheless, as the tests were performed by imposing displacement rates on the hydraulic system, it was necessary to check the actual slip rates at the loaded end of the bonded area (upper surface of the mortar block), measured by the LVDTs.

Fig. 5-15 shows the changes in the actual slip rate versus slip for the different imposed (machine stroke) slip rates. The actual slip rate is computed by dividing the textile slip (measured by the LVDTs) into the experimental time. For better understanding, these changes are presented in the complete and enlarged scales for both the steel and glass-based TRM composites in Fig. 5-15a and Fig. 5-15b, respectively. For both systems, the slip rate reaches the expected value in the early stages of the tests, namely, at about 0.03 mm in the specimens tested at 0.2 mm/min and 1.0 mm/min rates, and about 0.4 mm for those tested at higher slip rates. In all steel and glass TRMs tested at 0.2 mm/min and 1.0 mm/min rates, these slip values are lower than the slip corresponding to the peak load (s_P), so the bond behavior is still in the elastic stage and no delamination has occurred. On the other hand, in glass TRMs tested with a slip rate equal to or higher than 5 mm/min, these slip values are larger than S_P, indicating the tests reach the intended slip rate after debonding had been initiated. These comparisons validate the experimental setup developed for the tests presented in this study and the slip rate selected for the first part of the cyclic tests. At the same time, they indicated the need to represent the results in terms of actually measured slip and actual slip rate (e.g., at peak load), instead of controlled machine stroke displacement and imposed sip rate, also in order to make test outcomes independent from test implementation details.

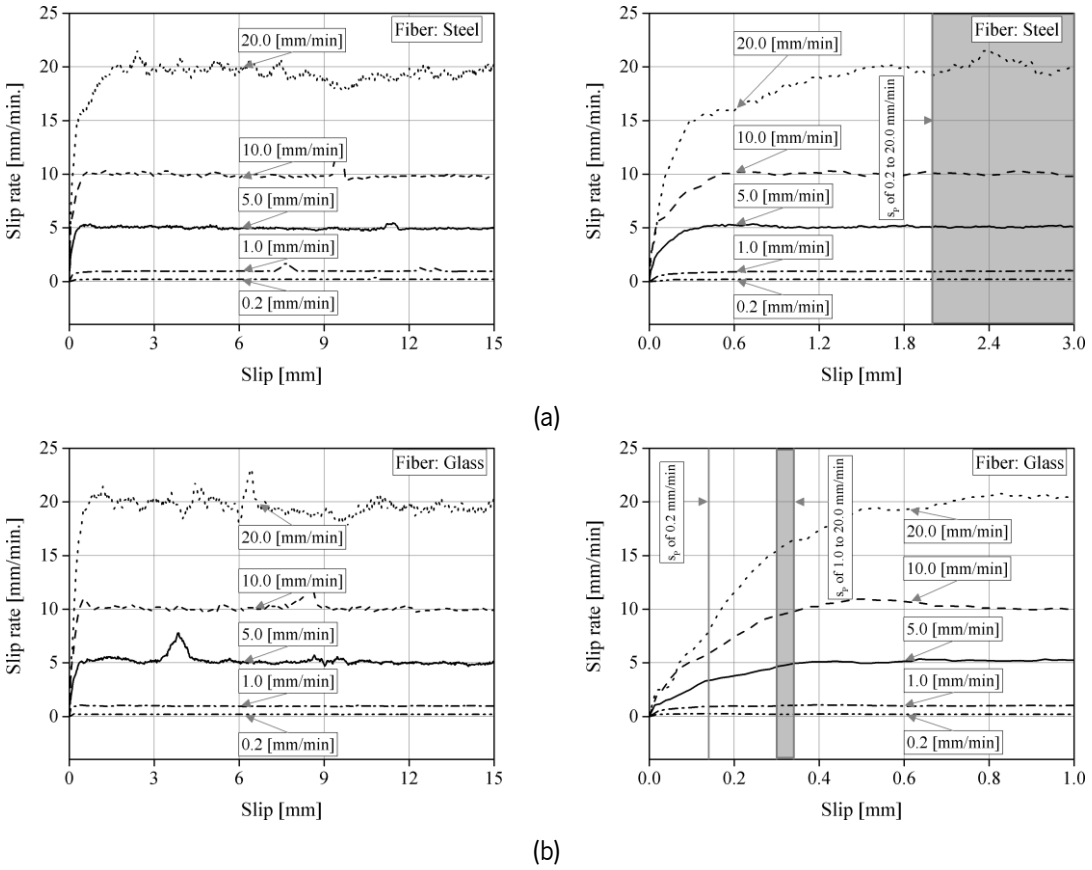

Fig. 5-15. Changes of slip rate vs. slip: (a) steel TRM; (b) glass TRM.

5.4.2. Steel-reinforced mortar

Fig. 5-16a to e show the individual and average curves obtained from the experiments on steel TRM composites, and Fig. 5-16f shows the five average curves together to compare the different slip rates. The first stage of the test is associated with a stiff branch of the response curves, in which the load transfer between the cord and matrix relies on both adhesion and interlocking, this latter arising by the high roughness of the cord surface. Then, the curves display a progressive reduction of the slope, up to the attainment of the load peak, followed by a post-peak softening phase with a nearly linear load reduction associated with the increase of slip. The transition between the first and second stages is smooth, and there are no sudden load drops associated with brittle failures, such that, in this case, a precise value of the loads corresponding to the loss of adhesion (P_F) and its residual value after the load drop (P_f) could not be identified.

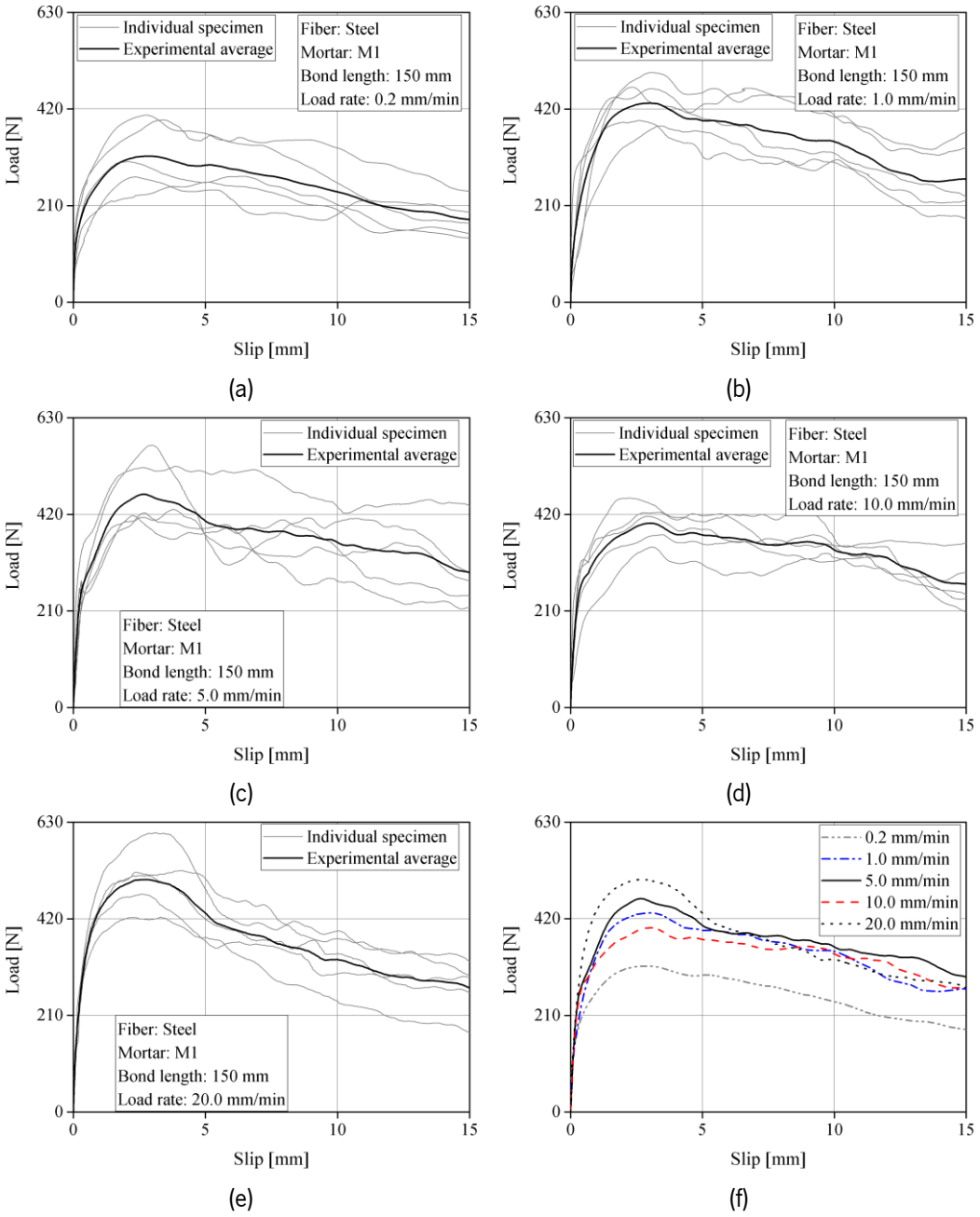

Fig. 5-16. Load-slip response curves of monotonic pull-out tests on steel TRM performed under different slip rates: (a) 0.2 mm/min; (b) 1.0 mm/min; (c) 5.0 mm/min; (d) 10.0 mm/min; (e) 20.0 mm/min; (f) average.

The peak load (P_P), resulting from the contributions of adhesion, interlocking, and friction, increases from 328 N (at 0.2 mm/min slip rate) to 507 N (20 mm/min), without a clear trend with the increase of slip rate (Fig. 5-17a). The strength at the slowest rate (0.2 mm/min), however, confirms itself as the lowest one. The pull-out behavior is affected by the slip rate at the lowest rates considered in this investigation. The bond capacity at 0.2 mm/min resulted lower than those obtained at all the other rates. On the other hand, the differences amongst such higher rates (from 1 mm/min to 20 mm/ min) are of the same order of magnitude of the scatter, so no clear trends emerged (Table 5-6).

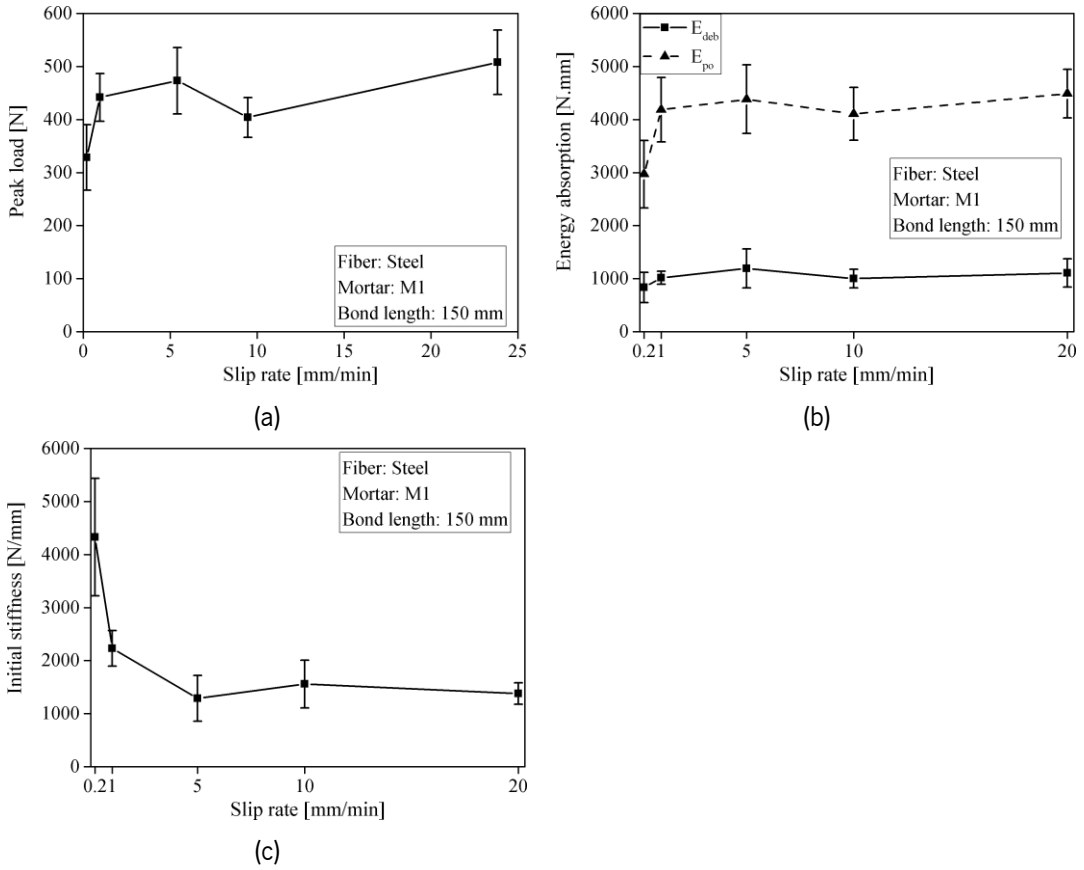

Fig. 5-17. Effect of the slip rate on bond parameters of steel TRM in monotonic pull-out tests: (a) peak loads; (b) pull-out and debonding energy; (c) initial stiffness.

The debonding energy (E_{deb}) in the steel TRM system is, in general, significantly higher than the pull-out energy (E_{po}), as shown in Fig. 5-17b. The pull-out energy is defined as the area under the load-slip curve from the peak load (P_P) until the end. Both debonding and pull-out energies show slight variations with the slip rate beyond 0.2 mm/min. Finally, the initial stiffness (K) decreases until a slip rate of 5 mm/min, and then it does not change. This output should be further investigated, also considering other types of steel cords.

Table 5-6. Results of monotonic pull-out tests on steel TRM: average value*.

Slip rate [mm/min]	Specimens	P_P [N]	E_{deb} [N.mm]	E_{po} [N.mm]	K [N/mm]
0.2	1	396	1112	3783	5308
	2	272	484	2727	3401
	3	407	914	3470	6002
	4	261	1146	1947	3370
	5	306	511	2916	3557
	average	328 (19)	834 (34)	2969 (21)	4328 (26)
1.0	1	395	912	3557	2616
	2	499	1134	4834	1985
	3	499	1134	4834	1985
	4	468	869	4249	2150
	5	468	869	4249	2150
	average	442 (10)	1018 (12)	4183 (15)	2231 (15)
5.0	1	423	889	4325	1204
	2	570	1241	4712	773
	3	570	1241	3269	1389
	4	417	723	4361	1035
	5	524	1771	5244	2050
	average	473 (13)	1192 (31)	4382 (15)	1290 (33)
10.0	1	376	1081	3901	1391
	2	415	1067	3934	1102
	3	424	1255	4077	2420
	4	349	791	3573	1359
	5	455	812	5045	1516
	average	404 (9)	1001 (18)	4106 (12)	1558 (29)
20.0	1	474	1062	4219	1350
	2	607	1557	4880	1237
	3	514	1192	4674	1342
	4	521	969	4940	1194
	5	423	751	3725	1767
	average	508 (12)	1106 (24)	4488 (10)	1378 (15)

*CoV of the results is given in percentage inside parentheses; P_P: peak load; E_{deb}: debonding energy; E_{po}: pull-out energy; K: initial stiffness.

5.4.3. Glass-reinforced mortar

Fig. 5-18a to e show the individual and average curves obtained from the experiments on glass TRM composites, and Fig. 5-18f shows the five average curves together to compare the different slip rates. The average load values of the peak load (P_P), frictions load (P_f), and the peak load (P_P') due to the slip hardening effect are compared in Fig. 5-19a. The mean value of the P_P varies between 153 N (at 0.2 mm/min slip rate) and 340 N (at 10 mm/min), whereas the P_P' range, is between 144 N

(0.2 mm/min) to 386 N (at 10 mm/min), as listed in Table 5-7. It is worth noting that these peaks are of the same order of magnitude and that the former is not necessarily higher than the latter.

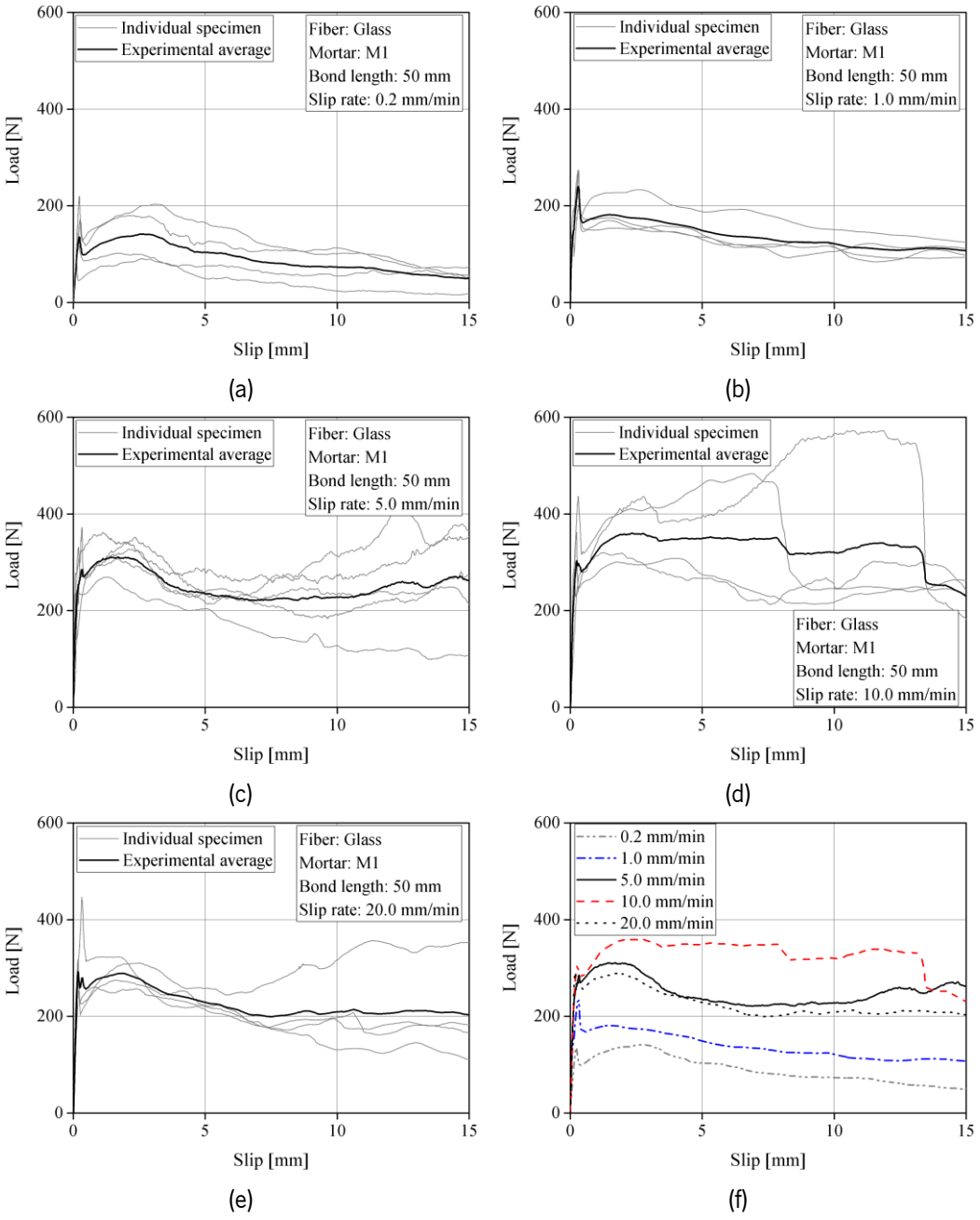

Fig. 5-18. Load-slip response curves of monotonic pull-out tests on glass TRM performed under different slip rates: (a) 0.2 mm/min; (b) 1.0 mm/min; (c) 5.0 mm/min; (d) 10.0 mm/min; (e) 20.0 mm/min; (f) average.

Pull-out tests revealed that the bond behavior in terms of peak load is affected by the slip rate. More specifically, for low rates when passing from 0.2 mm/min to 1.0 mm/min and to 5 mm/min, the higher the slip rate, the higher the first and second peak load. In contrast, a quasi-stabilization is found for the

higher rates (5 mm/min, 10 mm/min, and 20 mm/min). On the other hand, the load drop amount after full debonding (P_P – P_f) seems to be independent of the load rate.

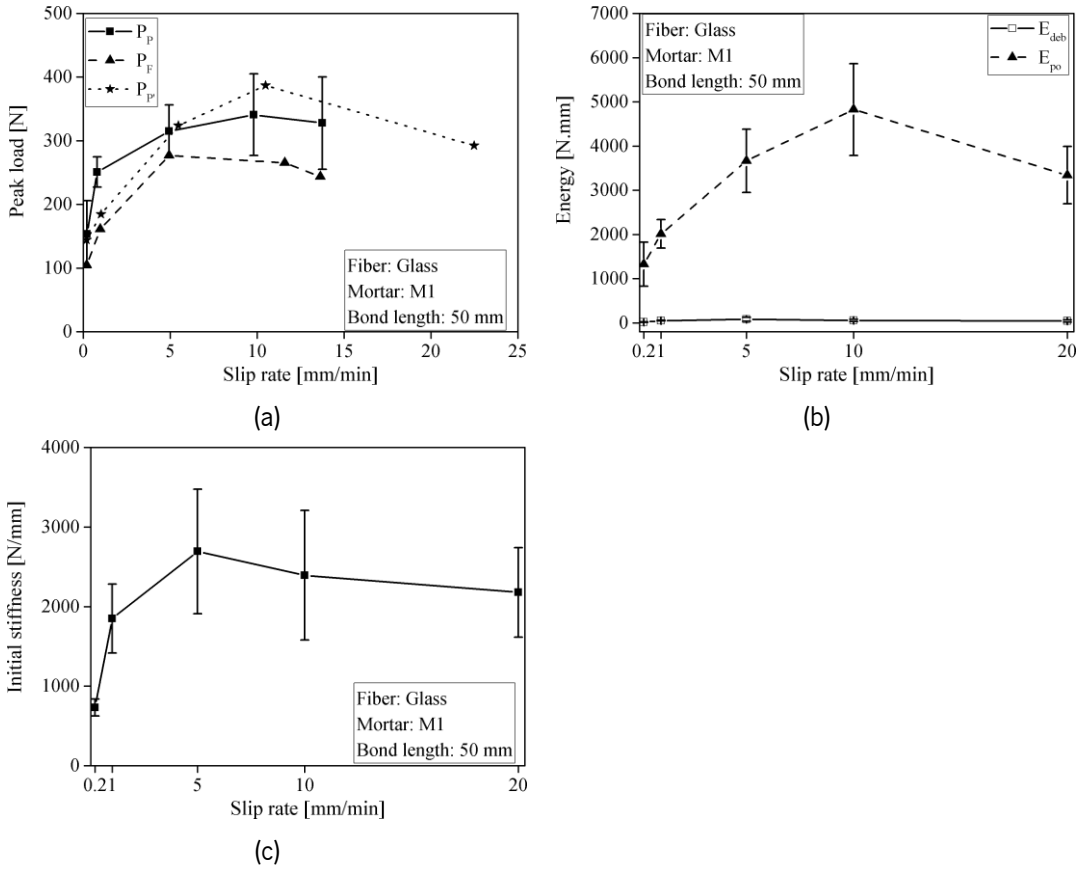

Fig. 5-19. Effect of the slip rate on the bond parameters of glass TRM in monotonic pull-out tests: (a) peak loads and frictional load; (b) toughness; (c) initial stiffness.

A similar trend is also found on the pull-out energy (E_{po}) and on the chemical bond energy (G_d), as shown in Fig. 5-19b. G_d is defined by Eq. 5-1, in which E_f is the modulus of elasticity of the glass textile and d_f is the diameter of the glass yarn (1.06 mm) [68,72,73].

$$\left\{ G_d = \frac{2\left(P_P - P_f\right)^2}{\pi^2 E_f d_f^3} \right\} \qquad \text{Eq. 5-1}$$

The debonding energy (E_{deb}) is smaller than the pull-out energy (E_{po}), and its changes with the increment of the slip rate are less significant. The initial stiffness (K) shows a large scatter but still follows a similar trend as the load peaks, as illustrated in Fig. 5-19c. By contrast, the values obtained under the slowest rates are always lower than the other ones, confirming that very slow tests may provide lower results.

Table 5-7. Results of monotonic pull-out tests on glass TRM: average value*.

Slip rate [mm/min]	Specimen	P_P [N]	P_F [N]	P_P' [N]	E_{deb} [N.mm]	E_{po} [N.mm]	G_d [J/mm^2]	K [N/mm]
0.2	1	141	86	102	14	1052	0.0079	622
	2	76	45	90	6	659	0.0025	725
	3	176	160	180	23	1691	0.0007	670
	4	220	127	203	24	1905	0.0221	907
	average	153 (34)	105 (41)	144 (34)	17 (43)	1327 (37)	0.0083 (101)	731 (15)
1.0	1	274	172	175	53	1821	0.0270	1628
	2	218	147	170	44	1798	0.0132	1544
	3	273	150	159	45	1858	0.0393	1629
	4	238	176	233	63	2573	0.0099	2594
	average	251 (9)	161 (8)	184 (16)	52 (14)	2013 (16)	0.0224 (52)	1849 (23)
5.0	1	292	289	308	152	3504	-	3166
	2	329	329	362	114	4315	-	3531
	3	372	265	353	60	3590	0.0300	1404
	4	332	269	327	44	4460	0.0103	2192
	5	249	233	269	38	2451	0.0007	3168
	average	315 (13)	277 (11)	324 (10)	81 (54)	3664 (20)	0.0137 (89)	2692 (29)
10.0	1	279	279	436	65	6417	-	1002
	2	285	228	320	21	4042	0.0084	2649
	3	362	239	308	53	3781	0.0393	2965
	4	436	315	484	84	5061	0.0377	2959
	average	341 (19)	265 (13)	387 (19)	56 (41)	4825 (21)	0.0285 (50)	2394 (34)
20.0	1	253	202	310	27	4432	0.0066	1495
	2	294	225	275	33	3102	0.0122	1971
	3	316	231	261	25	2716	0.0190	2200
	4	447	315	323	88	3114	0.0451	3046
	average	328 (22)	243 (18)	292 (9)	43 (60)	3341 (19)	0.0207 (71)	2178 (26)

*CoV of the results is given in percentage inside parentheses; P_P: peak load; P_F: frictional load; P_P': peak load corresponding to slip-hardening effect; E_{deb}: debonding energy; E_{po}: pull-out energy; G_d: chemical bond energy; K: initial stiffness.

In summary, based on the results of the pull-out tests performed on the glass TRM system investigated in this work, and limited to the experimental setup used and the slip rate range considered, the influence of the slip rate is negligible between 5 mm/min and 20 mm/min. In contrast, it leads to a reduction of the bond strength for lower rates (below 5 mm/min).

5.5. Effect of cyclic loading

The cyclic pull-out tests were conducted on steel and glass yarns embedded in mortars M1 and M2. The maximum (target) slip was progressively increased between 0.3 mm and 20 mm during loading-unloading cycles. Detailed information about the tests is provided in chapter 3.

5.5.1. Steel-reinforced mortar

Pull-out cyclic parameters including peak loads, strength degradation, and stiffness are defined in Fig. 5-20. The first two peaks (Peak-1 and Peak-2) are followed by an unloading phase, whereas the third one (Peak-3) is attained during a longer loading phase, which ends at the following target slip (see the cyclic test protocol in section 03.4.5). The strength degradation is calculated (in percent) at each cycle (i.e., at each target slip) as the reduction of Peak-2 with respect to Peak-1 (Cycle-1) and that of Peak-3 with respect to Peak-2 (Cycle-2), see Fig. 5-20. Finally, the stiffness is detected in cycles 2 and 3 with respect to that of the previous cycle. The stiffness corresponding to the secant modulus of elasticity of the loading branch between its first point and the target slip is defined as follows (Eq. 5-2):

$$\left\{\Delta K_1 = \left(1 - \frac{K_1^i}{K_{1,max}}\right) \times 100\right\}$$
$$\left\{\Delta K_2 = \left(1 - \frac{K_2^i}{K_{2,max}}\right) \times 100\right\} \qquad \text{Eq. 5-2}$$

Where K_i^1 and $K_{1,max}$ are the slop of the first load cycle at the slip "i," and the slop corresponding to the maximum stiffness of the same test group, respectively. The same function is employed for the second cycle.

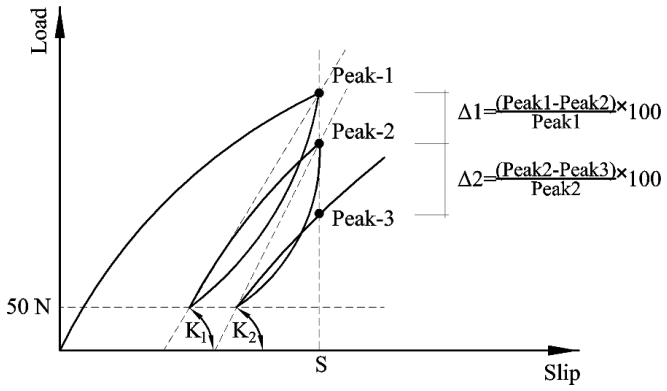

Fig. 5-20. Pull-out cyclic parameters.

Fig. 5-21 to Fig. 5-24 show the cyclic response of steel TRM composites, namely, load versus slip response curves in subplots (a), peak loads at target slips (b), strength degradation (c), and stiffness degradation (d). The cyclic curves displayed narrow cycles with small energy dissipated by hysteresis. Moreover, the monotonic curves could be considered as envelopes of the cyclic ones. Cyclic loading leads to a strength degradation, which is higher after the first cycle (10- 35%) than after the second cycle (5- 20%, with only a few exceptions), suggesting that a residual bond strength could be attained with few more cycles. The stiffness degradation in the two cycles is comparable and comprised between 10- 30% at small slips (below 3 mm) and 50- 75% at the end of the test (15 mm slip).

The comparisons amongst different configurations show the role of embedded length and type of mortar, confirming the outcomes of previous monotonic studies [15,17,31]. The maximum load attained by a single cord in mortar M2 with 50 mm bond length, L_b, (246.5 N, Fig. 5-21b) is much lower than that exhibited with mortar M1 (519.1 N, Fig. 5-21b), clearly showing the role of mortar properties on the bond performance. Mortar M1, despite a similar compressive strength and elastic modulus, shows a larger flexural strength compared to mortar M2. The better flexural tensile strength of this mortar, which can be due to the presence of short fibers in the mix and differences in the chemistry of these mortars, appeared as a good indicator for the bond performance with the textile. In addition, the enhancement of the bond response when the embedded length is increased from 50 mm to 150 mm is different. In contrast to the specimens with mortar M2, the bond behavior does not show a significant improvement when the embedded length is increased in specimens with mortar M1, which could be attributed to the differences in the effective embedded length in these two systems.

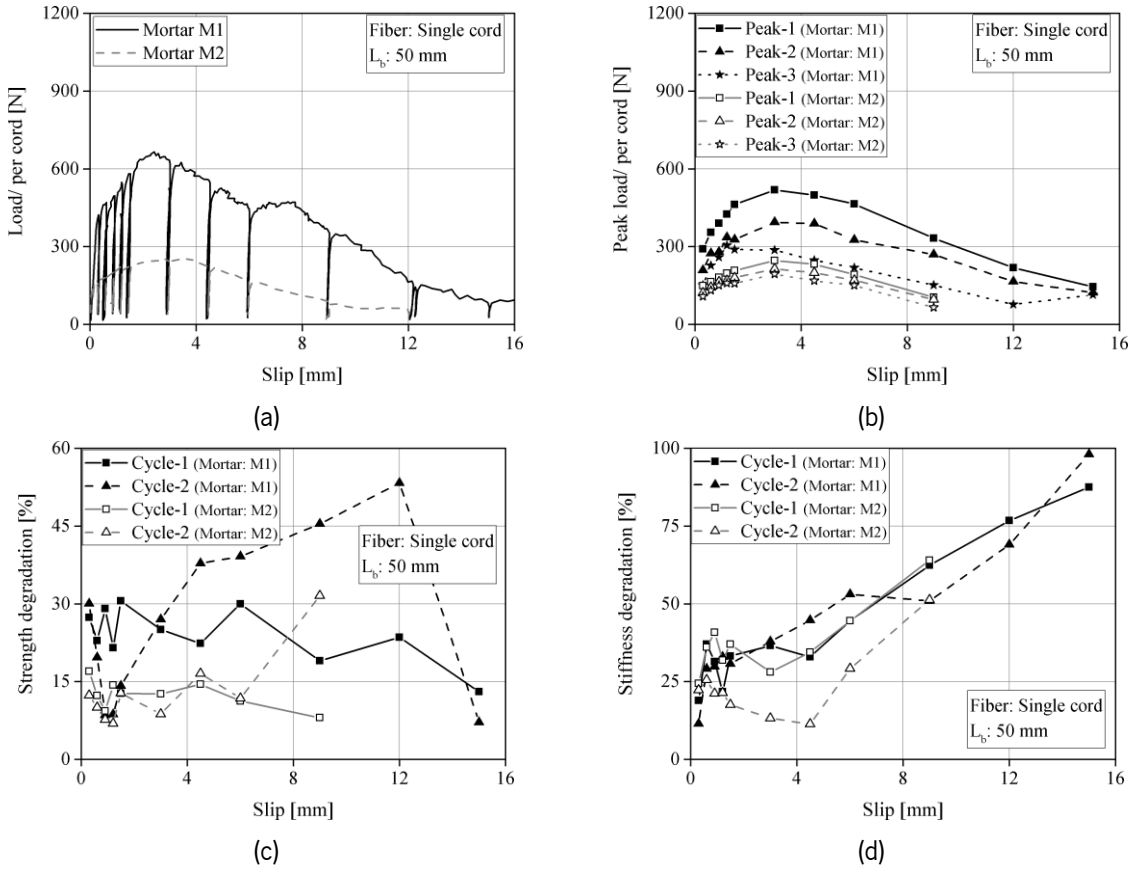

Fig. 5-21. Cyclic pull-out behavior of the single steel cord and mortars M1 and M2 with L_b=50 mm: (a) load-slip curve; (b) peak loads; (c) strength degradation; (d) stiffness degradation.

Since the steel mesh is unidirectional, the effect of the number of cords is expected to be insignificant. Nevertheless, the peak loads per cord with mortar M1 are 611.9 N with one cord (Fig. 5-22b), 783.6 N with two cords (Fig. 5-23b), and 983.8 N with four cords (Fig. 5-24b), showing an increase in the load-bearing capacity by each cord when the number of cords increases. In contrast, in samples with mortar M2, the peak load difference is insignificant (819 N with one cord (Fig. 5-22b) and 907 N with two cords (Fig. 5-23b), (in all cases, bond length, L_b, is 150 mm). Indeed, the interaction between cords is much weaker due to the absence of weft (transversal) elements with respect to that experienced by bidirectional meshes and, therefore, the beneficial effects observed with the groups of glass yarns (discussed in the next section) are much less pronounced in this case. Finally, the energy absorption levels are smaller in cyclic tests with respect to monotonic tests.

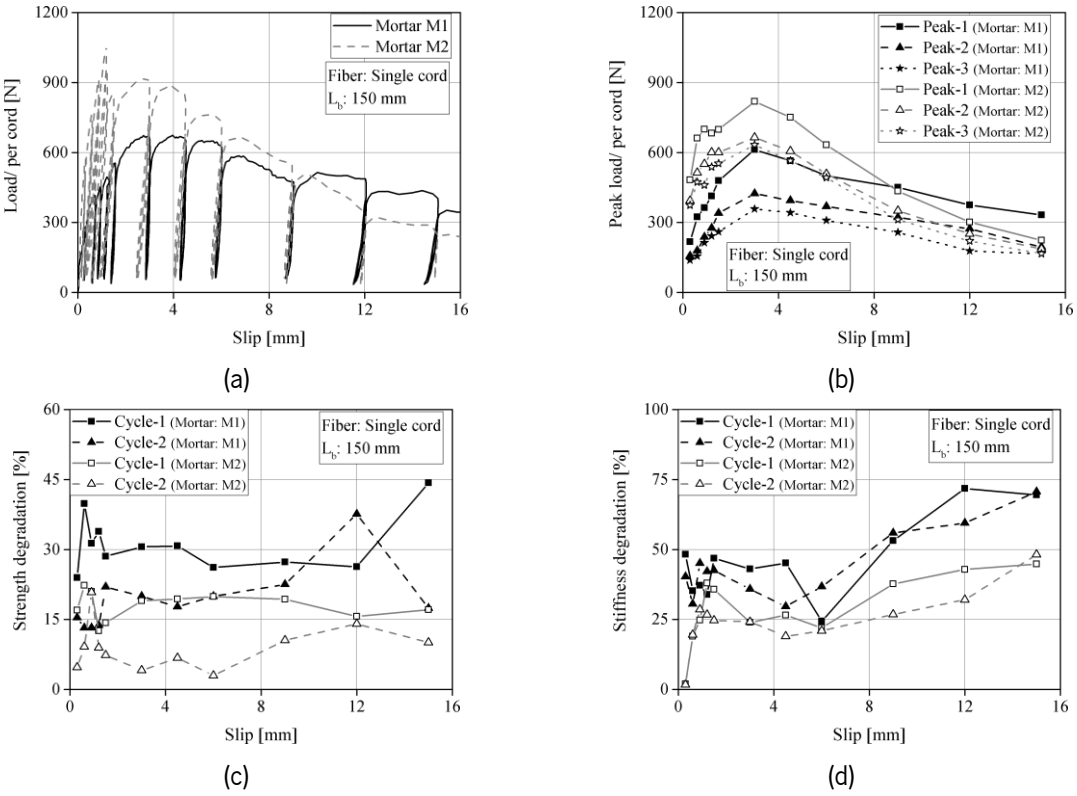

Fig. 5-22. Cyclic pull-out behavior of the steel cord and mortars M1 and M2 with L_b=150 mm: (a) an example load-slip curve; (b) peak loads; (c) strength degradation; (d) stiffness degradation.

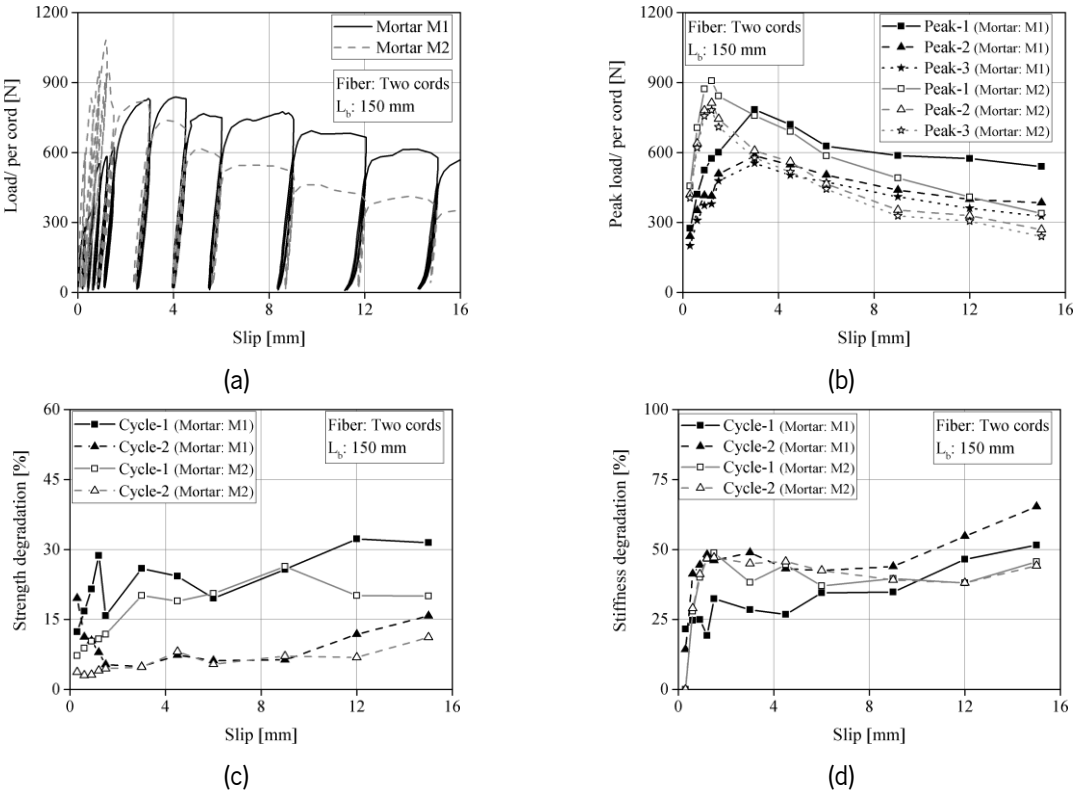

Fig. 5-23. Cyclic pull-out behavior of the group of 2 steel cords and mortars M1 and M2 with L_b=150 mm: (a) load-slip curve; (b) peak loads; (c) strength degradation; (d) stiffness degradation.

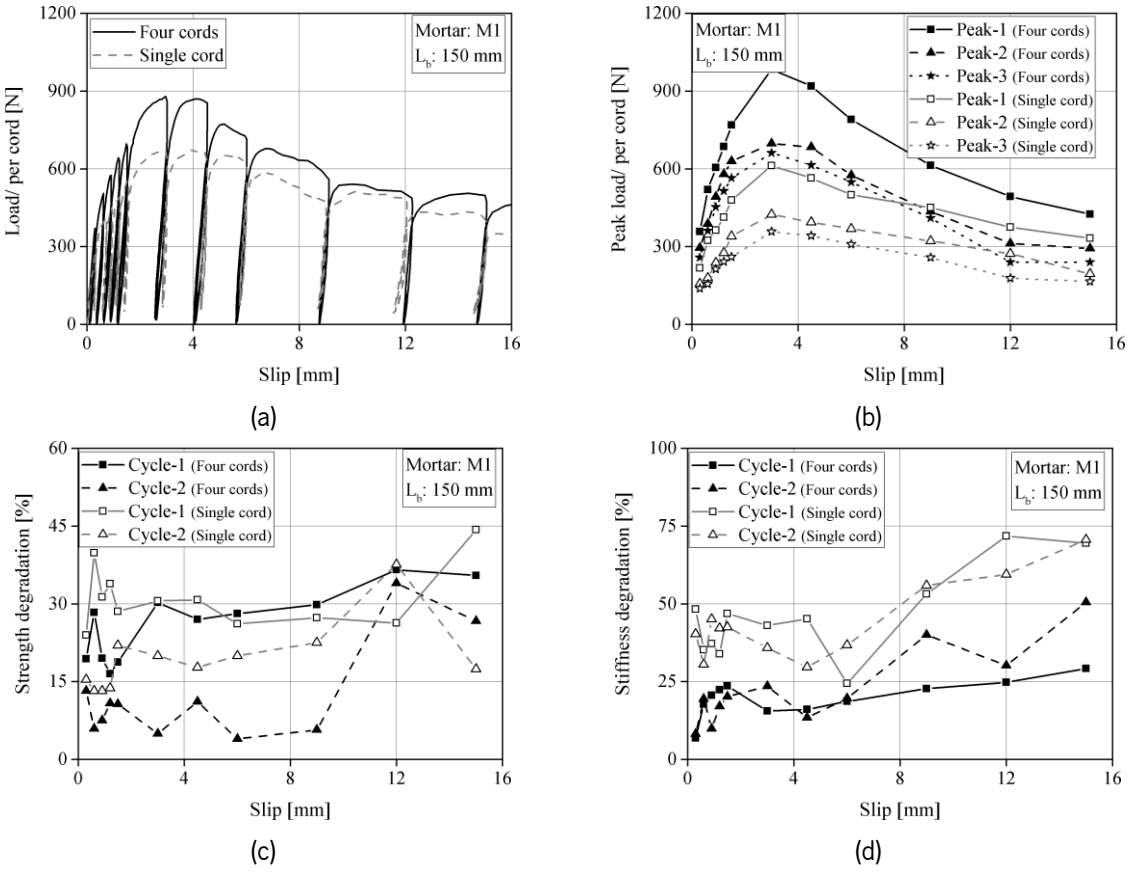

Fig. 5-24. Cyclic pull-out behavior of the single cord and the group of 4 steel cords and mortar M1 with L_b=150 mm: (a) load-slip curve; (b) peak loads; (c) strength degradation; (d) stiffness degradation.

5.5.2. Glass-reinforced mortar

Fig. 5-25 to Fig. 5-27 show the cyclic response of glass TRM composites, namely load versus slip response curves in subplots (a), peak loads at target slips (b), strength degradation (c), and stiffness degradation (d). Some common features emerged in all specimens, independently from their specific configuration. First, unloading-reloading cycles are very narrow, indicating a small amount of dissipated energy, and the cyclic test results are contained in the envelope of the monotonic one. Second, under repeated cycles at the same target slip, the peak load at the end of the first loading phase is not recovered after the cycles, i.e., a strength degradation resulted due to the irreversible loss of adhesion, especially in the first cycle. More precisely, the strength degradation after the first cycle, represented by the difference between Peak-1 and Peak-2 in subplots (b) and by the curve of Cycle-1 in subplots (c), is comprised between 15% and 45%. The peak loads after two cycles (Peak-3), instead, are similar to those after one cycle (Peak-2); the strength degradation curve of Cycle-2 is lower than that of Cycle-1 and comprised between 5% and 25%. On the other hand, for both Cycle-1 and Cycle-2, no clear correlation results between strength degradation

and slip. Finally, the stiffness degradation varied in the 5- 15% range at small slips (less than 1 mm), increased up to 50- 75% at 15 mm slip, and is similar in Cycle-1 and in Cycle-2, as shown in subplots (d). There are also some differences amongst the different configurations investigated. First, a higher maximum load is attained by the specimens with the single yarn with 75 mm bond length (L_b= 75 mm), as shown in Fig. 5-25a, b, with respect to L_b= 50 mm (Fig. 5-25a, b and Fig. 5-26a, b), indicating that a longer bond length leads to a higher pull-out strength, which, in its turn, may be due either to an effective bond length longer than 50 mm or to a higher contribution of friction activated over a longer embedded yarn (or to a combination of the two factors). At the same time, L_b= 75 mm shows a smaller strain (slip) capacity when compared to L_b= 50 mm (around 1/3) that is due to the early occurrence of the yarn rupture. These observations are also in line with the ones previously reported on the monotonic response of the same glass TRM system tested under different embedded lengths [15]. Also, the single yarn with L_b= 75 mm shows a smaller load degradation of Cycle-1 and Cycle-2, while similar stiffness degradation compared to L_b= 50 mm.

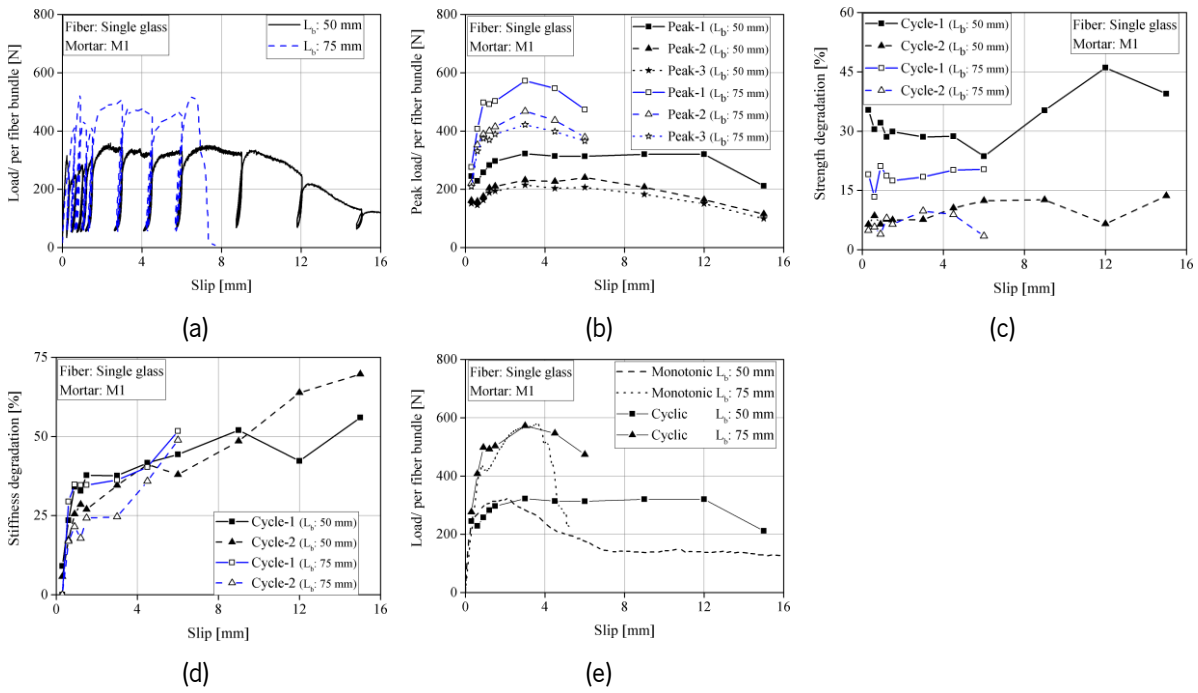

Fig. 5-25. Cyclic pull-out behavior of the single glass yarn with L_b= 50 mm and 75 mm: (a) load-slip curve; (b) peak loads; (c) strength degradation; (d) stiffness degradation; (e) comparison of monotonic and push of cyclic loading (Peak 1).

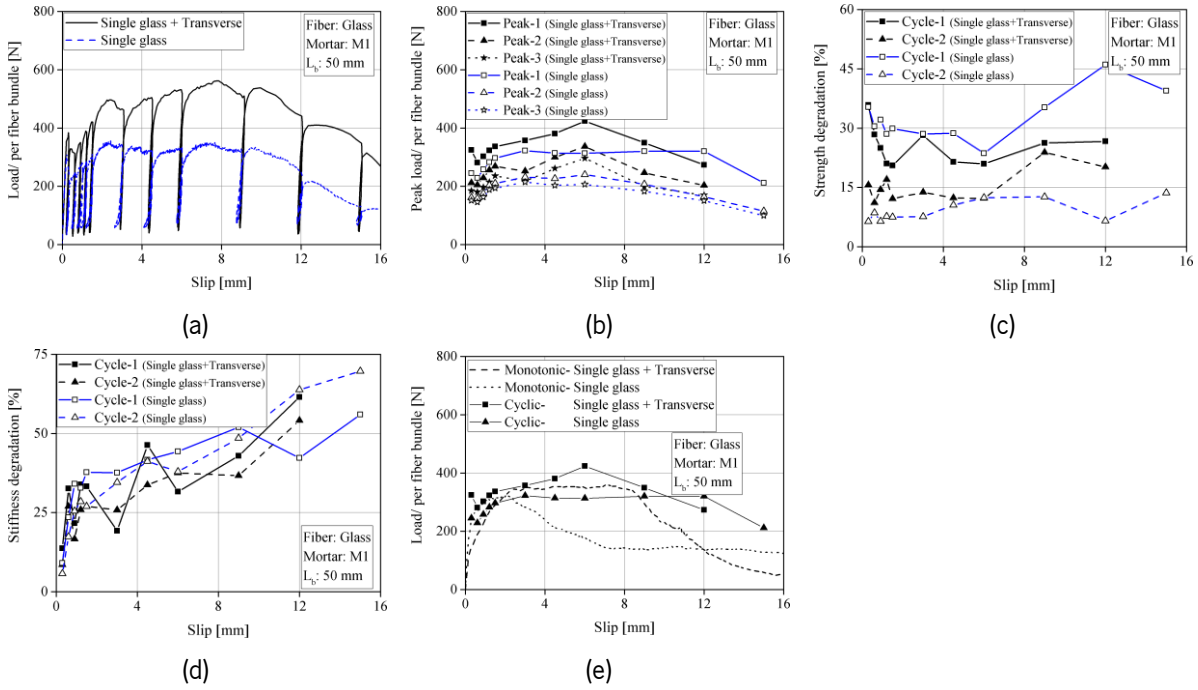

Fig. 5-26. Cyclic pull-out behavior of the single glass yarn with and without transverse elements and L_b= 50 mm: (a) load-slip curve; (b) peak loads; (c) strength degradation; (d) stiffness degradation; (e) comparison among monotonic and cyclic loading.

The role of transverse yarns on the cyclic response is also significant (Fig. 5-26). A clearly larger Peak-1, Peak-2, and Peak-3 are obtained in the specimens with transverse yarns when compared to those with a single longitudinal yarn. At the same time, single yarns show a larger strength degradation in both Cycle-1 and Cycle-2. A higher pull-out load/yarn is also obtained with two fiber yarns (Fig. 5-27a, b) with respect to one yarn (note that, as said before, the load is always indicated per yarn, i.e., the force recorded by the load cell is divided by the number of yarns to plot the results). This again shows the beneficial role of interaction between fiber yarns connected by weft elements, as also reported in [15].

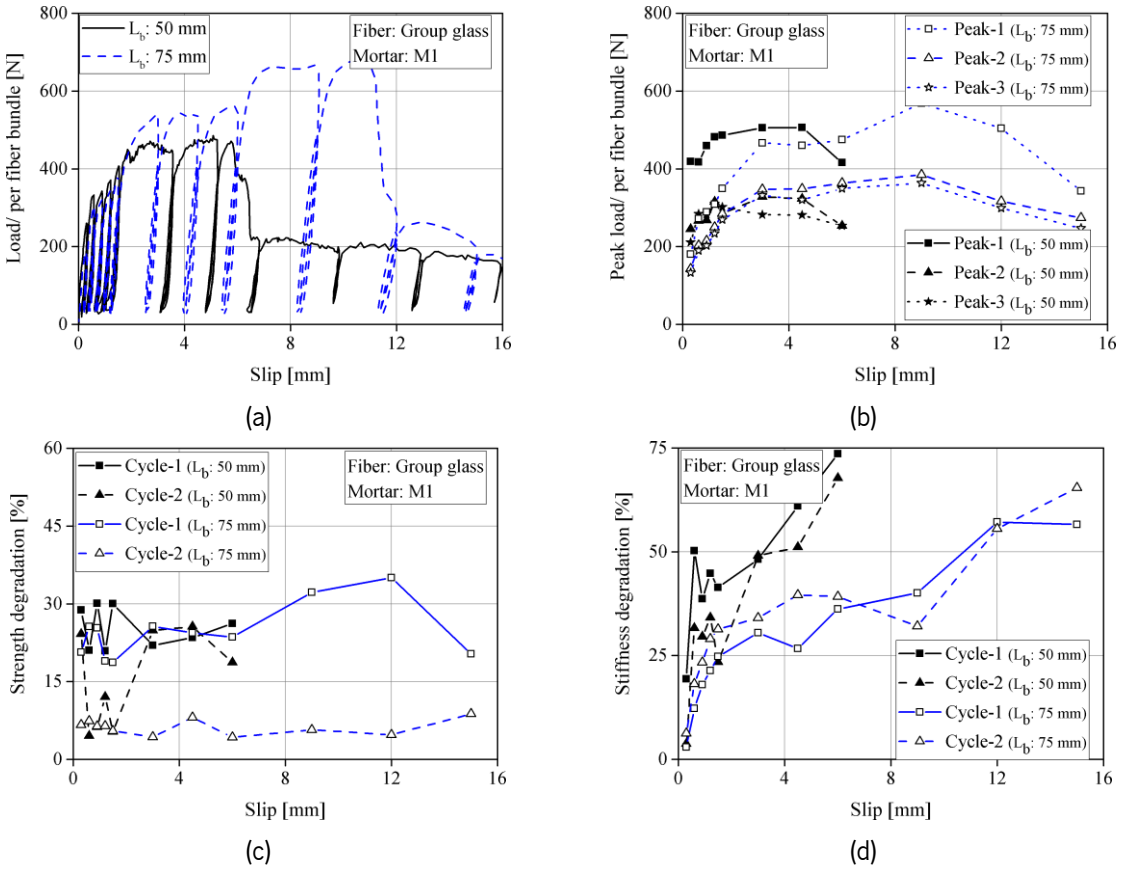

Fig. 5-27. Cyclic pull-out behavior of the group of 2 glass yarns with L_b= 50 mm and 75 mm: (a) load-slip curve; (b) peak loads; (c) strength degradation; (d) stiffness degradation.

5.6. TRM-to-substrate bond

In this section, a comprehensive investigation of the TRM-to-substrate bond behavior is performed. For this aim, the effect of bond length and surface treatment of the substrate is considered as variables. A comparison is also made between the results obtained from pull-out tests and conventional single-lap shear bond tests to highlight the differences/similarities between these two test methods. There is more information about the tests in section 3.6.

5.6.1. Effect of bond length and surface preparation

Two groups of single-lap samples were prepared with 100 mm bonded length. In one group, the original brick surface was used (method a), while in the second group, the brick surface was sandblasted to increase the surface roughness, here termed method b [119]. Besides, to investigate the effect of bond length, an additional embedded length of 150 mm was utilized with sandblasted bricks (method b). For each type of brick surface and embedded length, five specimens were constructed and named SL100-a

for the original brick and SL100-b and SL150-b for single-lap shear specimens constructed with the sandblasted brick.

A comparison among the results of SL100-a, SL100-b, and SL150-b specimens clearly shows the effect of sandblasting on the TRM-to-substrate bond behavior, see Fig. 5-28. The failure mode of the SL100-a samples is the delamination of the TRM from the substrate, while yarns slippage, followed by tensile rupture, is observed in the SL100-b samples. Additionally, in SL150-b specimens, all yarns ruptured by reaching the maximum load. The load-slip curves are also consequently different in these three sets of samples.

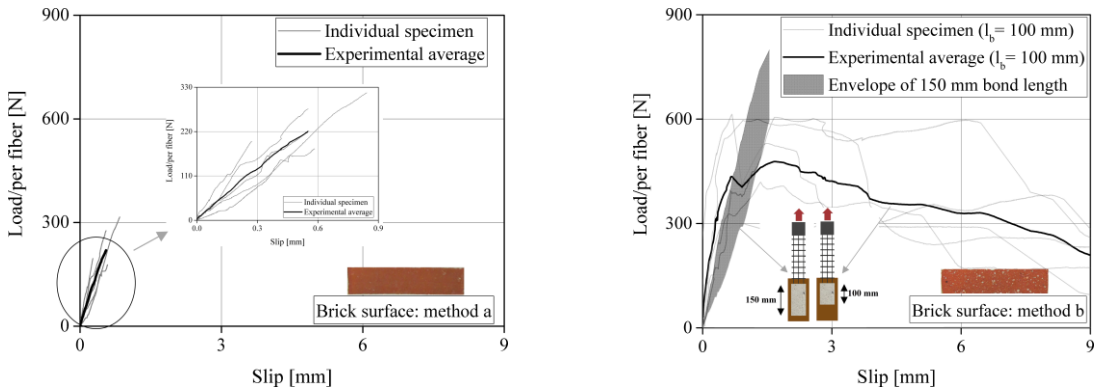

Fig. 5-28. TRM-to-substrate bond behavior: (a) original brick; (b) sandblasted brick.

The main experimental parameters, such as the peak load and its corresponding slip, the fabric stress, and the initial stiffness, are obtained for the tested samples and presented in Table 5-8. The stress is calculated by dividing the peak load by the cross-section area of the yarns (2.65 mm^2). It can be seen that sandblasting has a significant effect as SL100-b samples show a peak load and a corresponding slip around two times higher than those of SL100-a. In addition, the initial stiffness of SL100-b specimens is two times higher than the SL100-a samples. As expected, by increasing the embedded length, the peak load and its corresponding slip increased by 44% and 33% in SL150-b specimens compared to SL100-b specimens, respectively. The initial stiffness of SL150-b, however, decreases by 45%.

Table 5-8. TRM-to-substrate bond behavior based on surface treatment and bond length*.

Surface treatment	Bond length [mm]	Specimen	Peak load/per yarn [N]	Slip at the peak load [mm]	Stress [MPa]	Initial stiffness [N/mm]
original	100	SL100-a1	276	0.55	313	468
		SL100-a2	196	0.27	222	846
		SL100-a3	316	0.84	359	367
		SL100-a4	178	0.58	201	189
		SL100-a5	222	0.55	252	437
		Average	238 (22)	0.56 (32)	269 (22)	461 (47)
sandblasted	100	SL100-b1	605	1.71	687	446
		SL100-b2	299	0.99	339	844
		SL100-b3	419	1.34	475	662
		SL100-b4	614	0.68	696	1804
		SL100-b5	599	1.29	680	1123
		Average	507 (25)	1.20 (29)	575 (25)	976 (48)
sandblasted	150	SL150-b1	784	2.02	889	332
		SL150-b2	742	1.33	842	414
		SL150-b3	731	1.34	829	652
		SL150-b4	663	1.67	752	381
		Average	730 (6)	1.59 (18)	828 (6)	445 (28)

*CoV of the results is given in percentage inside parentheses

5.6.2. Comparison of pull-out and single-lap shear tests

Recent investigations on mechanical characterization of TRM-based composites have been mostly focused on mechanical tests for characterization of the tensile response of TRM composites or of the TRM-to-masonry bond behavior [14,31]. Single or double-lap shear bond tests have been extensively used for characterization of the TRM-to-substrate bond behavior, similar to that of FRP-strengthened masonry. However, the critical differences between these two composite materials in terms of the nonlinear response and failure modes suggest that these tests are not suitable for constitutive modeling and extraction of bond-slip laws. Fiber-to-mortar pull-out tests seem to be a more suitable testing method but have received very limited attention.

Consequently, in most of the available studies in the literature, the bond-slip laws proposed for TRM composites are based on the experimental results obtained from shear debonding tests. However, it should be noted that the bond response obtained from these tests is the resultant of several complex mechanisms, including the fiber-to-mortar bond behavior and the matrix-to-masonry bond behavior, as well as cracking of the mortar top layer (and possibly the bottom layer that is difficult to be observed).

This behavior leads to proposals of bond-slips law that are only able to reproduce the experimentally observed load-slip curves rather than actually considering the governing mechanisms, such as fiber pull-out, mortar cracking, debonding at the interface of masonry and TRM. Furthermore, the reproduction of the experimental curves in such conditions is also subjected to limitations and assumptions of the modeling approach on material properties and stress conditions. This limitation can therefore lead to erroneous predictions in numerical simulations if a different modeling strategy is adopted.

For simulating a strengthened masonry structure with a TRM system, one should model the bond behavior of components of TRMs (fiber-to-mortar and mortar-to-substrate) instead of using the results of the single-lap shear tests that express the general behavior of the system. Literature review showed that for the same experimental data, different bond-slip laws could be obtained following different approaches. To better clarify the importance of this issue, a comparison is made in this section between the load-slip curves obtained from the single-lap shear tests and pull-out tests. The average and envelope load-slip curves obtained from single-lap shear tests performed on specimens prepared and cured following the same procedure as of the specimens used for pull-out tests (in section 5.3.1) are shown in Fig. 5-29a. As it can be seen in Fig. 5-29b, the failure mode is cracking and splitting of the mortar top layer together with the sliding of the fibers. A comparison between the load-slip curves of the single-lap and pull-out tests shows that the response is similar in the elastic region in all the specimens (see Fig. 5-29a). However, the peak load and the post-peak response of the specimens are different. The main parameters of the load-slip curves, summarized in Table 5-9, can better clarify the observed differences. It seems that in the pull-out tests, by increasing the number of fibers, a decrease in the bond properties is observed. However, the single-lap shear tests results (that contain eight cords) show a higher peak load, higher slip corresponding to peak load, and higher toughness when compared to those of pull-out tests on specimens with four cords. This unexpected behavior can be due to the differences in the involved mechanisms and boundary conditions in these two test setups. In the pull-push tests, the mortar is fixed from the top, and a similar stress distribution exists on both mortar layers. Consequently, the mortar is under compressive load, and the fiber bear tensile load. On the other hand, in single-lap shear tests, the mortar is free, and only the substrate is fixed, causing different stress distributions in the top and the bottom mortar layers. Moreover, the type of test setup causes both the mortar and the fiber to be under tensile stress, but the brick bears the compressive stress, as reported in [119]. These observed differences in the load-slip curves suggest that a different bond-slip law will be obtained in each case, and therefore the application of these laws in numerical simulations should be made with special care and attention. While the stress distribution and the possible failure modes in the TRM system are similar to the results of the single-lap

shear test, the pull-out test is a suitable test for investigating the bond behavior between fiber and mortar. It is worth noting that the obtained results of pull-out tests only depend on the bond between fiber and mortar and the stress state in the mortar. In contrast, the load-slip curves obtained from single-lap shear tests are affected by other interacting factors, such as the mortar-to-substrate bond, cracking of the top layer of mortar, and unsymmetrical loading conditions on the mortar. Hence, for simulating the bond behavior of fiber-to-mortar in TRM systems, the bond-slip law extracted from the pull-out test is suggested.

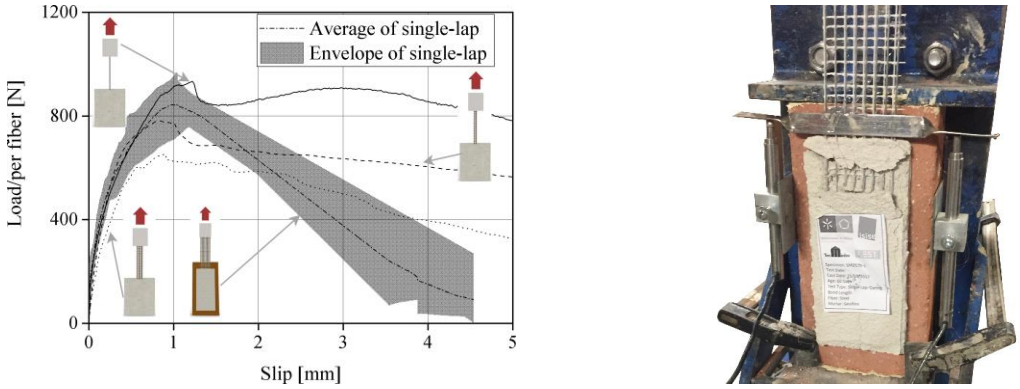

(a) (b)

Fig. 5-29. (a) Load-slip curve and (b) failure mode of steel-based TRMs under single-lap shear test.

Table 5-9. Changes of bond properties in steel-based TRM with fiber configuration*.

Test	Fiber configuration	s_P [mm]	$P_{P,\ per\ fiber}$ [N]	$E_{deb,\ per\ fiber}$ [N.mm]	$K_{\ per\ fiber}$ [N/mm]
Pull-out	Single cord	1.08 (15)	992 (8)	730 (20)	3245 (8)
	Two cords	0.89 (23)	815 (13)	538 (27)	2738 (20)
	Four cords	0.74 (39)	700 (13)	340 (51)	3299 (9)
Single-lap	Eight cords	1.05 (13)	875 (8)	674 (15)	2600 (31)

*CoV of the results is given in percentage inside parentheses; s_P: slip corresponding to peak load; P_P: peak load; E_{deb}: debonding energy; K: initial stiffness.

5.7. Effect of curing conditions

This section examined the effects of different mortar curing conditions and brick moisture content on fiber-to-mortar and TRM-to-substrate bond behavior. This was accomplished by initially curing specimens under three different conditions and then undergoing post-exposure tests (pull-out and single-lap shear tests) on the TRM composites. The pull-out specimens were prepared by embedding single glass yarns or steel cords into the mortars M1 and M2, respectively, where their bond lengths were 50 mm and 150 mm. Effect of mortar curing and brick moisture content was only investigated on steel-based TRM composites and mortar M2. The specimens are named X_Y_Z_Z′, in which X relates to the test type (P:

pull-out test, S: single-lap shear test). Y is connected to the curing condition of the mortar, and Z is linked to the brick moisture condition, which is used just for the single-lap shear specimens. Y and Z are defined in section 3.8. Z′ used only for the pull-out specimens are related to the fiber type (St: steel fiber, Gl: glass yarn).

5.7.1. Fiber-to-mortar bond

5.7.1.1. Steel-reinforced mortar

All steel-based TRM specimens failed due to fibers slippage from the mortar, resulting in a typical load-slip curve. Fig. 5-30 shows the individual and average load-slip curves of these specimens for each curing condition. The pull-out curves show a sudden drop in the load to a residual value P_f after reaching the peak load (P_P) due to the occurrence of debonding between the fiber and the mortar [18]. A slip hardening behavior follows this sudden drop by reaching the second peak load, resulting from friction between the fiber and the mortar. It can be observed that the slip hardening is smaller in the samples cured under PL-7 and RH-7 conditions compared to those cured under PL-1 conditions. Nevertheless, the curing conditions considered here do not affect the general form of the load-slip curves.

Table 5-10 presents the main characteristics of the experimental pull-out curves for each curing condition. The pull-out parameters include the first peak load (P_P), the dropped load or frictional load (P_f), the initial stiffness (K), the debonding energy (E_{deb}), and the pull-out energy (E_{po}). E_{deb} and E_{po} are the areas under the load-slip curve until the P_P and from the P_P until the end, respectively. In general, the specimens cured under PL-7 (seven days covered with damp cloths and a plastic sheet) and RH-7 (seven days stored in the chamber with 90% RH) show a much better bond performance than specimens cured under PL-1 (one day under the plastic sheet), as shown in Table 5-10. In other words, all bond parameters improve, but the post-peak energy absorption (E_{po}) does not change. The P_P, K, and E_{deb} of the P_PL-7_St specimens, the parameters explaining the fiber-to-mortar bond behavior before full debonding, are 41%, 168%, and 120%, respectively, higher than the P_PL-1_St specimens are. There is also a 9%, 112%, and 15% increase of these values in the P_RH-7_St specimens compared to P_PL-1_St specimens of 9%, 112%, and 15%, respectively. The increase in the mortar M2 strength under curing conditions PL-7 and RH-7 (Table 4-4) can be accounted for this improvement in the bond behavior.

Comparing P_PL-7_St and P_RH-7_St, it is evident that conserving moisture with plastic is more effective than curing under high humidity conditions (Table 5-10). For example, the P_P of P_PL-7_St specimens increases by 30%, compared to those of P_RH-7_St. Although mortar M2 has a similar mechanical strength under these two curing conditions (see Table 4-4), the DTA results show that the decarboxylation

level of the specimens cured in the PL-7 condition is higher than the condition RH-7. The results indicate a higher carbonation degree is achieved in samples cured under PL-7 conditions, leading to better bond performance even though the mechanical properties of the mortar M2 are not significantly different between PL-7 and RH-7.

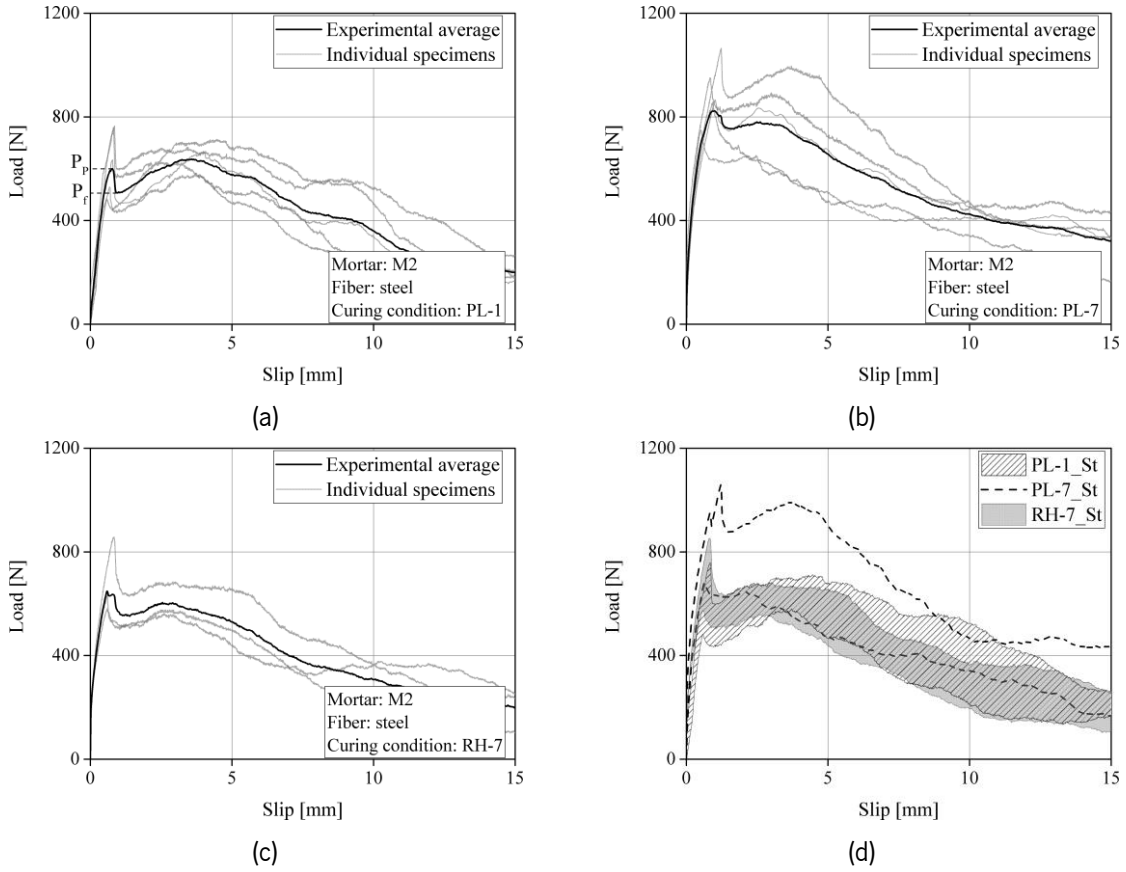

Fig. 5-30. Pull-out load-slip curves of steel-based TRM specimens: (a) P_PL-1_St; (b) P_PL-7_St; (c) P_RH-7_St; (d) Envelopes of the experimental results.

Table 5-10. Effect of different curing conditions on the fiber-to-mortar bond properties of steel-based TRM*.

Mortar curing condition	Specimen	s_P [mm]	P_P [N]	P_f [N]	E_{deb} [N.mm]	E_{po} [N.mm]	K [N/mm]
PL-1	P_PL-1_St_1	0.78	635	467	305	5594	1139
	P_PL-1_St_2	0.85	766	595	410	7395	1430
	P_PL-1_St_3	0.58	485	439	198	5451	1329
	P_PL-1_St_4	0.67	530	431	192	4998	942
	P_PL-1_St_5	0.81	759	565	342	7025	1110
	average	0.74 (14)	635 (18)	500 (14)	290 (29)	6093 (15)	1190 (14)
PL-7	P_PL-7_St_1	0.83	952	814	568	8573	3241
	P_PL-7_St_2	0.51	750	621	256	6633	3499
	P_PL-7_St_3	0.93	858	-	548	5861	2998
	P_PL-7_St_4	1.01	866	745	589	7747	3083
	P_PL-7_St_5	1.23	1066	872	852	8855	3151
	average	0.9 (26)	898 (12)	763 (12)	562 (34)	7534 (15)	3194 (5)
RH-7	P_RH-7_St_1	0.83	858	630	489	6653	2422
	P_RH-7_St_2	0.59	630	500	265	4742	2497
	P_RH-7_St_3	0.59	582	505	250	5766	2667
	average	0.7 (17)	689 (18)	544 (11)	334 (33)	5720 (14)	2528 (4)

*CoV of the results is given in percentage inside parentheses; s_P: slip corresponding to peak load; P_P: peak load; P_f: frictional load; E_{deb}: debonding energy; E_{po}: pull-out energy; K: initial stiffness.

5.7.1.2. Glass-reinforced mortar

The yarn slippage was the main failure mode of the glass-based TRM composites for all three curing conditions. Fig. 5-31 presents the average and individual load-slip curves for these specimens under different curing conditions. Similar to the steel-based TRM, the experimental results show the typical pull-out curves. In general, the curing conditions considered here do not affect the general form of the load-slip curve (Fig. 5-31d).

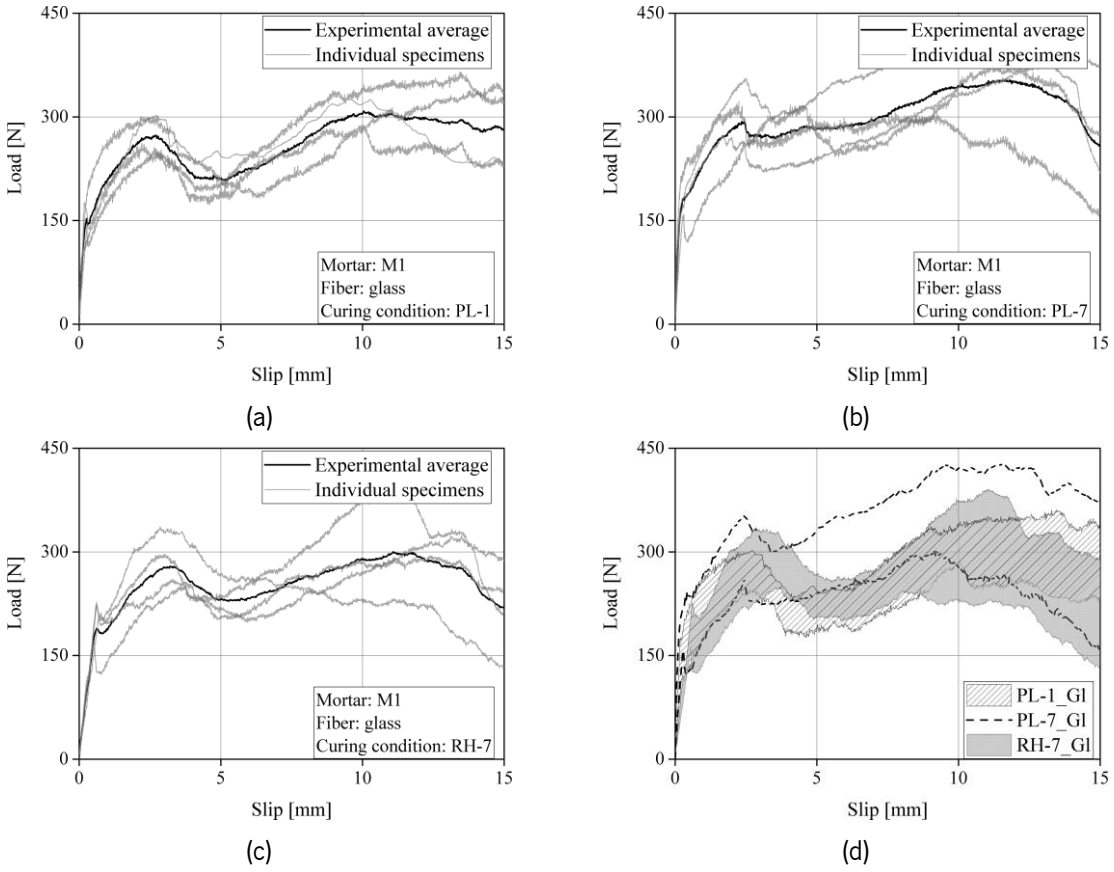

Fig. 5-31. Pull-out load-slip curves of steel-based TRM specimens: (a) P_PL-1_GI; (b) P_PL-7_ GI; (c) P_RH-7_ GI; (d) Envelopes of the experimental results.

Conservation of moisture during curing contributes considerably to the glass-to-mortar bond behavior. As reported in Table 5-11, P_P, K, and E_{deb} of the P_PL-7_GI specimens increased by 22%, 29%, and 42%, compared to the P_PL-1_GI specimens. These values are equal to 36%, 22%, and 274% for the P_RH-7_GI specimens compared to the P_PL-1_GI specimens. The other bond parameters also show a similar enhancement in the P_PL-7_GI and P_RH-7_GI specimens compared to the P_PL-1_GI specimens. Moreover, a comparison between the P_PL-7_GI and P_RH-7_GI bond parameters shows that plastic sealing is more effective than high humidity environments, which is in line with the steel-based TRM results.

Table 5-11. Effect of different curing conditions on the fiber-to-mortar bond properties of glass-based TRM*.

Mortar curing condition	Specimen	s_P [mm]	P_P [N]	P_f [N]	E_{deb} [N.mm]	E_{po} [N.mm]	K [N/mm]
PL-1	P_PL-1_GI_1	0.14	111	102	12	3476	891
	P_PL-1_GI_2	0.26	144	112	19	4102	750
	P_PL-1_GI_3	0.25	180	179	25	3921	800
	P_PL-1_GI_4	0.19	177	138	18	3893	985
	average	0.21 (23)	153 (18)	133 (22)	19 (26)	3848 (6)	857 (11)
PL-7	P_PL-7_GI_1	0.27	157	118	24	4267	1036
	P_PL-7_GI_2	0.19	215	206	26	3915	1290
	P_PL-7_GI_3	0.28	173	169	32	4363	951
	P_PL-7_GI_4	0.41	203	203	66	5188	1151
	average	0.25 (16)	187 (12)	193 (9)	27 (12)	4433 (11)	1107 (12)
RH-7	P_RH-7_GI_1	0.52	168	123	49	3548	1190
	P_RH-7_GI_2	0.62	223	193	73	4211	977
	P_RH-7_GI_3	0.62	228	201	74	3487	993
	P_RH-7_GI_4	0.76	212	196	87	3611	1008
	average	0.63 (14)	208 (11)	197 (2)	71 (19)	3714 (8)	1042 (8)

*CoV of the results is given in percentage inside parentheses; s_P: slip corresponding to peak load; P_P: peak load; P_f: frictional load; E_{deb}: debonding energy; E_{po}: pull-out energy; K: initial stiffness.

5.7.2. TRM-to-substrate bond

The main outputs of single-lap shear tests (load-slip curves, peak load (P_P), bond strength (σ_P), and failure mode of the specimens) are presented and discussed in this section [14,31,119]. Here, the bond strength is calculated by dividing the peak load by the fiber cross-section area. The ratio of the bond strength to the tensile strength of steel fiber (η) is also presented to investigate the effect of different curing conditions on the utilization of the tensile strength in the TRM systems.

5.7.2.1. Dry substrate

Fig. 5-32 and Table 5-12 show the load-slip curves and the summary of the S_PL-1_D, S_PL-7_D, and S_RH-7_D test results. The load-slip curves show a similar trend in all specimens comprising an elastic stage followed by a short nonlinear stage (see Fig. 5-32). Debonding at the TRM-to-substrate interface was the main failure mode of all the tested specimens (see failures in Fig. 5-32). This shows that the bond between the TRM and the substrate is weaker than the bond at the fiber-to-mortar interface in these specimens. Although the surface of the bricks was sandblasted to improve the mortar-to-substrate bond, using dry bricks led to a poor bond performance because of the suction of the mortar water towards the brick [213,214].

Interestingly, the specimens cured under PL-7 conditions (S_PL-7_D) show a lower peak load (P_P) than the specimens cured under the other conditions (S_PL-1_D and S_RH-7_D), as listed in Table 5-12. This observation contrasts with the pull-out results. This shows high drying shrinkage in those specimens, as reported before, has possibly led to the development of micro-cracks at the mortar-to-brick surface and reduction of its bond performance.

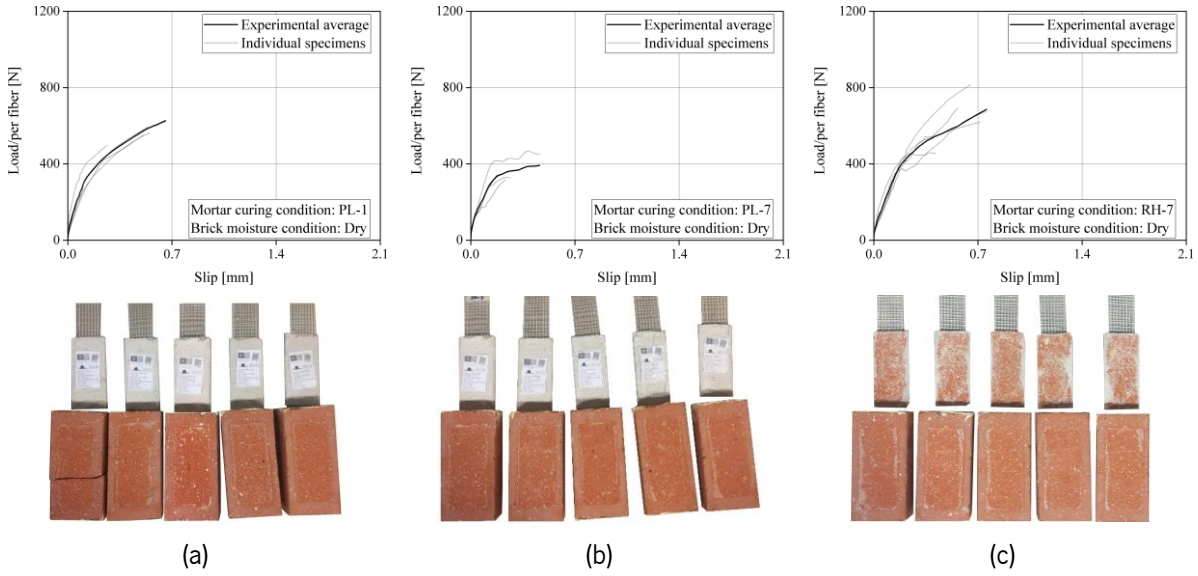

Fig. 5-32. Load-slip curves and failure mode of single-lap shear specimens with dry brick: (a) S_PL-1_D; (b) S_PL-7_D; (c) S_RH-7_D.

Table 5-12. Effect of different mortar curing conditions and dry brick on the TRM-to-substrate bond properties*.

Mortar curing condition	Specimen	Peak load/per yarn [N]	Stress [MPa]	η [%]
PL-1	S_PL-1_D_1	552	1025	34
	S_PL-1_D_2	621	1154	39
	S_PL-1_D_3	562	1045	35
	S_PL-1_D_4	498	926	31
	average	558 (19)	1038 (8)	35 (9)
PL-7	S_PL-7_D_1	344	639	21
	S_PL-7_D_2	316	588	20
	S_PL-7_D_3	330	613	21
	S_PL-7_D_4	469	871	29
	average	365 (17)	678 (17)	23 (17)
RH-7	S_RH-7_D_1	694	1289	43
	S_RH-7_D_2	675	1255	42
	S_RH-7_D_3	619	1151	39
	S_RH-7_D_4	458	852	29
	S_RH-7_D_5	815	1515	51
	average	652 (18)	1289 (15)	43 (15)

*CoV of the results is given in percentage inside parentheses; η: maximum bond strength to the tensile strength of steel fiber.

5.7.2.2. Semi-saturated substrate

These specimens showed a ductile load-slip curve (deformation ability after reaching the peak load), see Fig. 5-33. As opposed to the specimens prepared on dry substrate, the failure of all these specimens was fiber slippage followed by mortar cracking (Fig. 5-33) in these specimens. This indicates a better bond is formed between the mortar and the brick, in this case [33,195,215,216].

A comparison between the bond parameters of this group of specimens shows that S_PL-7_SS specimens have a better performance than two other series (Table 5-13). This can be due to the presence of sufficient moisture in these specimens, thus improving the fiber-to-mortar bond in a similar way to pull-out specimens (P_PL-7_S). Also, it seems that the bond performance in the specimens cured under high relative humidity conditions (P_RH_7_SS) does not differ much from the specimens cured under plastic for one day (P_PL_1_SS).

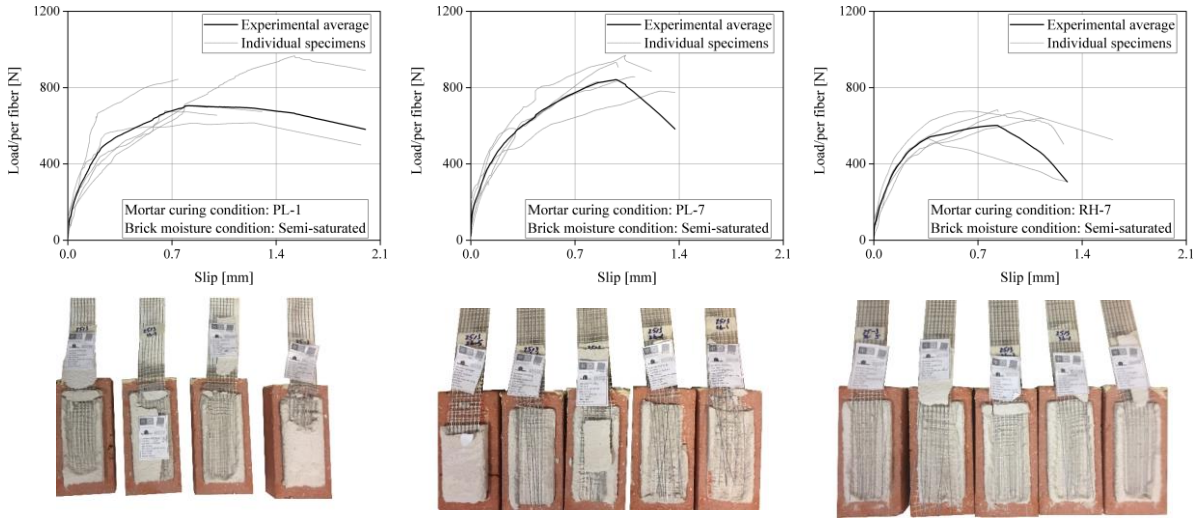

Fig. 5-33. Load-slip curves and failure mode of single-lap shear specimens with semi-saturated brick: (a) S_PL-1_SS; (b) S_PL-7_SS; (c) S_RH-7_SS.

Table 5-13. Effect of different mortar curing conditions and semi-saturation brick on the TRM-to-substrate bond properties*.

Mortar curing condition	Specimen	Peak load/per yarn [N]	Stress [MPa]	η [%]
PL-1	S_PL-1_SS_1	844	1569	53
	S_PL-1_SS_2	679	1261	42
	S_PL-1_SS_3	707	1314	44
	S_PL-1_SS_4	615	1144	38
	S_PL-1_SS_5	967	1798	60
	average	762 (17)	1322 (12)	44 (12)
PL-7	S_PL-7_SS_1	932	1733	58
	S_PL-7_SS_2	970	1803	61
	S_PL-7_SS_3	782	1454	49
	S_PL-7_SS_4	857	1594	54
	S_PL-7_SS_5	832	1546	52
	average	875 (8)	1646 (8)	55 (8)
RH-7	S_RH-7_SS_1	677	1259	42
	S_RH-7_SS_2	640	1190	40
	S_RH-7_SS_3	533	990	33
	S_RH-7_SS_4	684	1271	43
	S_RH-7_SS_5	678	1260	42
	average	642 (9)	1178 (10)	40 (10)

*CoV of the results is given in percentage inside parentheses; η: maximum bond strength to the tensile strength of steel fiber.

5.7.2.3. Saturated brick

Fig. 5-34 shows the load-slip curves of the S_PL-1_SA, S_PL-7_SA, S_RH-7_SA specimens. Compared with the dry bricks, these specimens demonstrate a higher ductility and bond strength. However, their load-slip curves lack the post-peak region observed in specimens prepared on semi-saturated bricks due to the type of failure mode that occurred in these specimens (combined fiber slipping and mortar cracking followed by detachment at the fiber-to-mortar interface, Fig. 5-34). As shown in Table 5-14, the S_PL-1_SA specimens have a better bond performance than the S_PL-7_SA and S_RH-7_SA specimens. This improvement in the bond behavior can be attributed to the water balance within the mortar during curing condition PL-1. It seems that the presence of high humidity (in PL-7 and RH-7) combined with a saturated substrate has led to an irreversible moisture expansion [217]. In contrast, as shown in section 4.3.1, higher humidity can affect the shrinkage behavior of the mortar.

A comparison between saturated and dry bricks shows an increase in the bond strength. According to Table 5-14, the η for the specimens prepared on saturated bricks is in the range of 41% to 59%. In contrast, this range falls between 23% and 41% for dry brick samples.

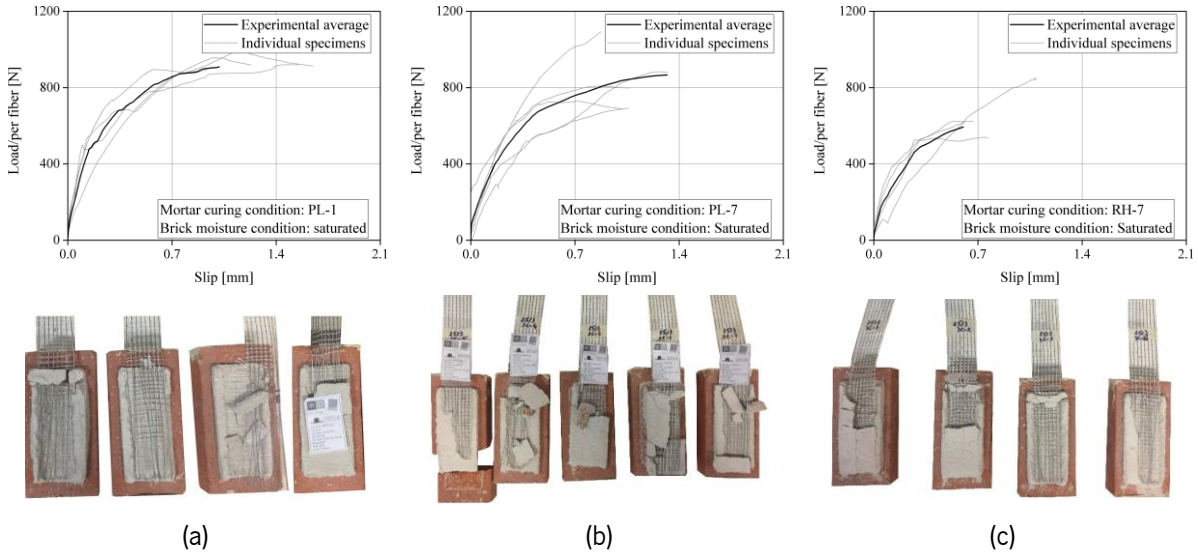

Fig. 5-34. Load-slip curves and failure mode of single-lap shear specimens with saturated brick: (a) S_PL-1_SA; (b) S_PL-7_SA; (c) S_RH-7_SA.

Table 5-14. Effect of different mortar curing conditions and saturated brick on the TRM-to-substrate bond properties*.

Mortar curing condition	Specimen	Peak load/per yarn [N]	Stress [MPa]	η [%]
PL-1	S_PL-1_SA_1	993	1845	62
	S_PL-1_SA_2	900	1672	56
	S_PL-1_SA_3	957	1780	60
	S_PL-1_SA_4	920	1710	58
	average	942 (4)	1845 (4)	62 (4)
PL-7	S_PL-7_SA_1	730	1357	46
	S_PL-7_SA_2	691	1285	43
	S_PL-7_SA_3	808	1502	51
	S_PL-7_SA_4	883	1642	55
	S_PL-7_SA_5	1094	2033	68
	average	841 (17)	1447 (9)	49 (9)
RH-7	S_RH-7_SA_1	616	1145	39
	S_RH-7_SA_2	850	1579	53
	S_RH-7_SA_3	624	1160	39
	S_RH-7_SA_4	540	1004	34
	average	657 (18)	1222 (18)	41 (18)

*CoV of the results is given in percentage inside parentheses es; η: maximum bond strength to the tensile strength of steel fiber.

5.7.2.4. Interaction of mortar curing and brick moisture conditions

The brick condition appears to have a significant impact on the TRM-to-substrate bond behavior. Comparing the exploitation ratio (η) of the samples S_PL-1_D, S_PL-1_SS, and S_PL-1_SA (dry, semi-, and saturated bricks with mortar curing condition PL-1), η has increased when the bricks have a higher initial moisture content (η=35%, 48%, and 59%, respectively). However, curing the mortar under high humidity conditions during the early ages (curing PL-7 and RH-7 in this study) can reduce the effect of substrate conditions on the bond performance. These findings are also corroborated by comparing the peak loads (P_P) of the pull-out and the single-lap shear tests. Under PL-1 curing conditions and semi-saturated or saturated substrate conditions (SS and SA conditions), the P_P of the single-lap shear tests is more than that of the pull-out test. For PL-7 conditions, the P_P of the pull-out and single-lap shear tests are in the same range (however, the P_P is smaller for the dry brick condition). Comparable results are also observed for RH-7 conditions. As a result, it is clear that the high moisture content in the mortar (due to either proper curing or lack of suction of mortar water by the substrate) results in a higher degree of hydration in the mortar and a better the bond performance.

5.8. Effect of aging of lime-based TRM

The experimental campaign investigated the changes in fiber-to-mortar bond behavior and the tensile response of TRM composites with time under indoor and outdoor environmental conditions. Single steel fiber was embedded in the mortar M2 in 150 mm bond length, and the single glass yarn was used with the mortar M1 with 50 mm bond length. More information about the tests can be found in section 3.9.1.

5.8.1. Steel fiber-to-mortar bond behavior

The failure mode for all the specimens is fiber slipping/pull-out from the mortar. The pull-out curves at all ages show the typical linear, nonlinear, and dynamic stages with a drop of the load after the peak load (see, for example, the results obtained for samples tested at 15 days in Fig. 5-35a). This sudden drop load shows the transition from chemical/frictional bond to frictional bond and indicates that the frictional bond is smaller than the adhesive bond in this system [67–69,72,73]. After this load drop, a slip hardening behavior (forming a second peak load) and then a softening response until the end of the tests is observed [68,69,72,75,77,218]. Comparing the load-slip curves of the samples tested at different ages under indoor conditions (Fig. 5-35b) shows that, in general, the bond behavior is improved with time even

until 920 days, although a slight decrement of bond performance may also be observed at some ages. This behavior is because of the increase of the mortar M2 strength.

The role of the mortar type seems to be significant for the bond performance of indoor aged samples, as shown in Fig. 5-35c. Specimens prepared with mortar M1 show a better bond performance at 90 days but a worse one at 920 days than specimens prepared with mortar M2. It seems that although pull-out samples prepared with mortar M1 gain higher strengths in early ages, bond deterioration or mortar shrinkage governs their performance at later ages. Besides, a comparison between the pull-out response of M1 mortar at 90 and 920 days shows (Fig. 5-35c) that the transition from the progressive debonding stage to the dynamic stage has changed from a smooth and upward trend to a sudden drop in the pull-out load.

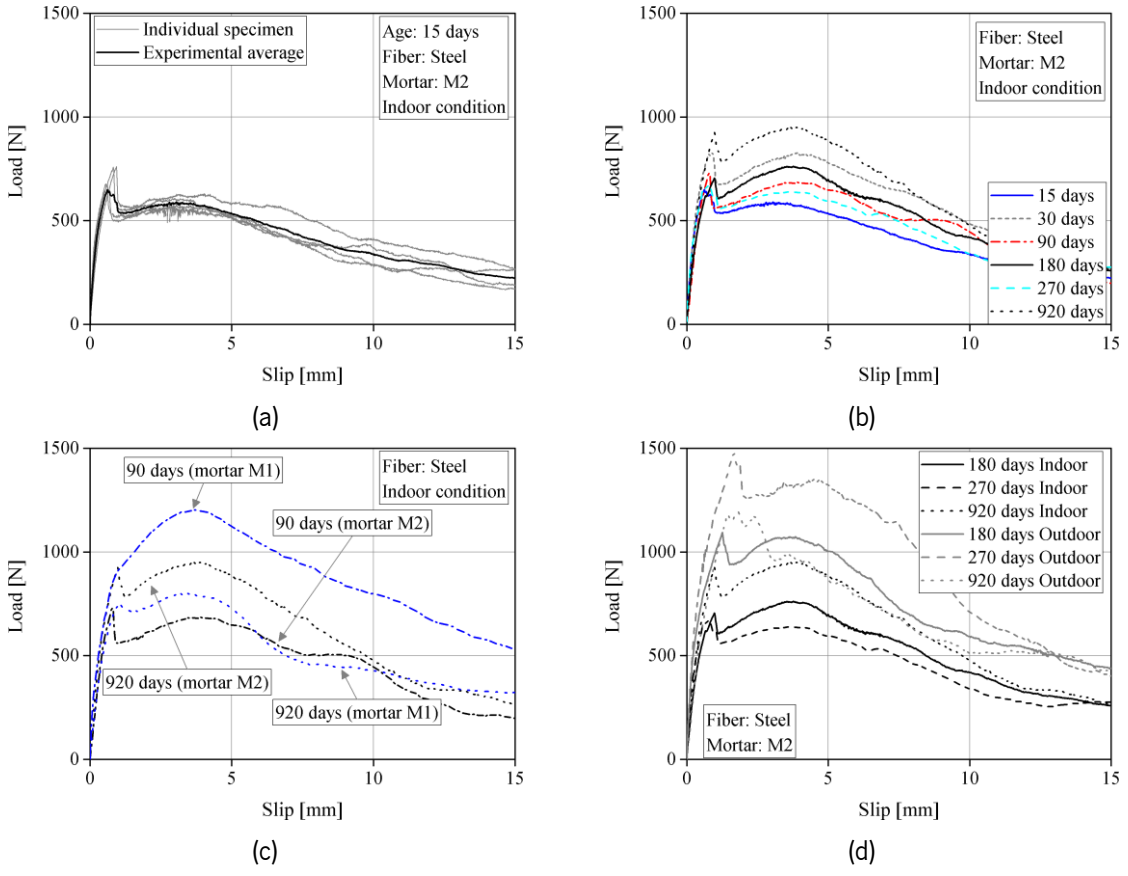

Fig. 5-35. Pull-out behavior of the steel-based TRM: (a) typical pull-out behavior; (b) effect of the mortar age; (c) effect of the mortar type; (d) effect of environmental condition.

Comparing the pull-out curves of indoor and outdoor aged samples (made of mortar M2), Fig. 5-35d shows that, generally, outdoor aged samples have a better bond performance. This observation can be due to a higher hydration degree achieved in the samples aged under outdoor conditions. Clearly, hydraulic lime-based mortars aged under indoor conditions have a considerably slower hydration degree

and thus lower bond performance. The peak load of samples aged at 920 days under outdoor conditions is 1125.9 N, which is 19% higher than samples aged under indoor conditions. It should also be noted that samples aged under outdoor conditions reached a peak load of 1550.3 N at 270 days showing a progressive deterioration mechanism afterward until 920 days.

To better understand the role of environmental conditions, the change in the key characteristics of the pull-out curves with time is presented in Fig. 5-36. Here, the individual sample results are presented together with a nonlinear regression line showing the general trend of the experimental results; however, a few experiments are not so well represented. The mean values of pull-out parameters of indoor and outdoor specimens are presented in Table 5-15 and Table 5-16. It can be observed that the peak load, the initial stiffness, the deboning energy, the chemical bond energy, and the pull-out energy show, in general, an incremental trend until 270 days, and then the values decreased until the end of the tests in outdoor aged samples. Meanwhile, in indoor aged samples, these properties reached their peak value at an early age and did not show a significant change with time after that, except for the chemical bond energy and initial stiffness, which are slightly decreased in the initial stage of exposure. As expected, the variation of the experimental results is also higher in the samples aged under outdoor conditions.

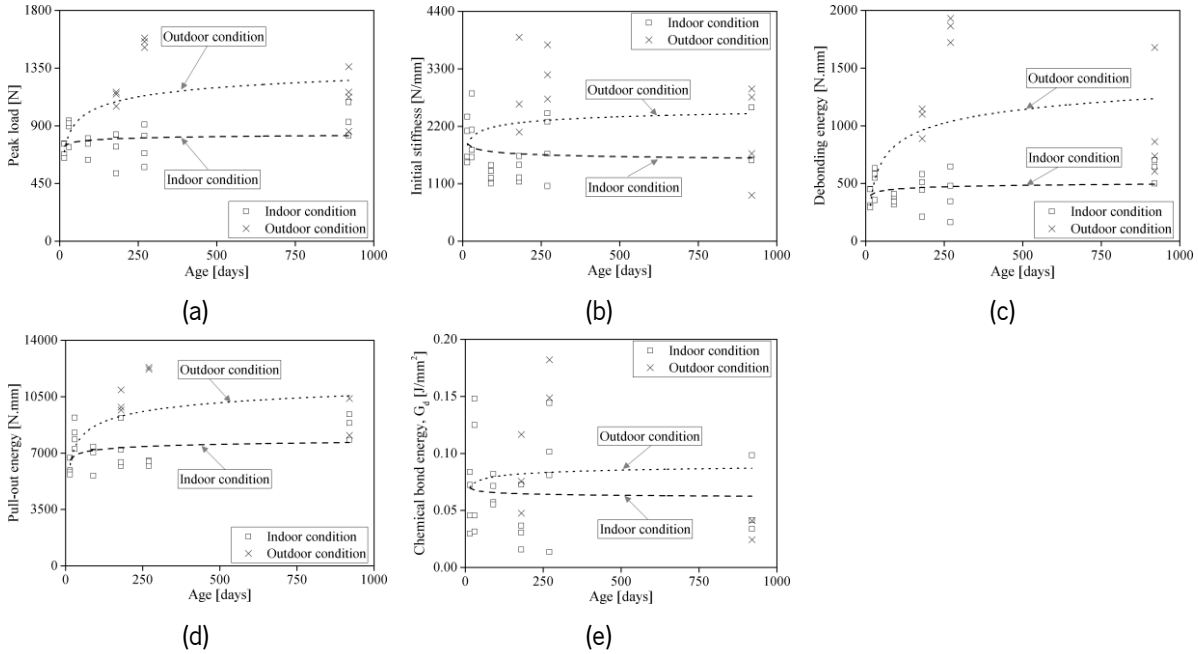

Fig. 5-36. Pull-out behavior parameters of the steel-based TRM: (a) peak load; (b) initial stiffness; (c) debonding energy; (d) pull-out energy; (e) chemical bond energy.

Table 5-15. Pull-out properties of the steel-based TRM aged under indoor conditions*.

Mortar	Age [days]	s_P [mm]	P_P [N]	E_{deb} [N.mm]	E_{po} [N.mm]	G_d [J/mm^2]	K [N/mm]
M2	15	0.8 (16)	711.1 (7)	376.0 (20)	6030.6 (7)	0.06 (37)	1902.6 (19)
	30	0.9 (9)	871.9 (9)	529.2 (20)	8132.8 (9)	0.09 (57)	2076.1 (23)
	90	0.8 (3)	740.6 (9)	364.5 (10)	6763.9 (10)	0.07 (16)	1277.4 (10)
	180	0.9 (16)	730.9 (17)	436.8 (32)	7253.0 (16)	0.04 (54)	1360.3 (14)
	270	0.8 (21)	747.9 (17)	408.4 (43)	6373.3 (2)	0.09 (55)	1865 (29)
	920	1.02 (6)	945.3 (11)	614.8 (14)	8691.6 (8)	0.06 (50)	1889.2 (25)
M1	90	1.0 (12)	916.6 (8)	599 (14)	12514.4 (16)	-	2657.8 (18)
	920	1.1 (19)	769.2 (8)	537.0 (28)	7358.8 (13)	0.01 (91)	1202.7 (6)

*CoV of the results is given in percentage inside parentheses; s_P: slip corresponding to peak load; P_P: peak load; E_{deb}: debonding energy; E_{po}: pull-out energy; G_d: chemical bond energy; K: initial stiffness.

Table 5-16. Pull-out properties of the steel-based TRM aged under outdoor conditions*.

Age [days]	s_P [mm]	P_P [N]	E_{deb} [N.mm]	E_{po} [N.mm]	G_d [J/mm^2]	K [N/mm]
180	1.3 (5)	1121.5 (4)	1045.0 (11)	10139.3 (5)	0.08 (35)	2871 (27)
270	1.7 (6)	1550.3 (2)	1839.2 (5)	12262.0 (1)	0.12 (56)	3222.3 (13)
920	1.3 (36)	1125.9 (16)	971.0 (43)	9243.7 (12)	0.03 (25)	2058.5 (40)

*CoV of the results is given in percentage inside parentheses; s_P: slip corresponding to peak load; P_P: peak load; E_{deb}: debonding energy; E_{po}: pull-out energy; G_d: chemical bond energy; K: initial stiffness.

5.8.2. Glass yarn-to-mortar bond behavior

The pull-out curves of the individual samples, the experimental average, and the analytical curves of the glass-based TRM are presented in Fig. 5-37. These specimens, in contrast to steel-based TRMs, do not show a sudden load drop after the peak load; thus, the transition from the progressive debonding to the dynamic stage is smooth. This behavior can be due to the insufficient curing condition of the mortar M1 at early ages, followed by the weak bond at the fiber-to-mortar interface. Comparing the pull-out curves tested at different ages and under indoor conditions (Fig. 5-37b), one shows that at early and later ages

(until 30 days and after 270 days), and the slip hardening is followed by a softening in the pull-out curves. However, at 90 and 180 days, the slip hardening is followed by a second slip hardening effect leading to significant absorption of energy. This change of final slip softening at early ages to slip hardening seems to be a result of further hydration of the mortar. Nevertheless, at later ages, it seems that a sort of bond deterioration or mortar shrinkage by forming micro-cracks at the bond interface has occurred, which led to a slip softening behavior.

Comparison of the indoor and outdoor aged samples indicates again that generally, outdoor aged samples show a better bond performance compared to indoor aged samples, see Fig. 5-37c. This behavior is in line with what is observed for the mortar M1 changes in indoor and outdoor conditions. As also observed in indoor aged samples, a degradation of the bond performance can also be observed in the samples aged under outdoor conditions at later ages.

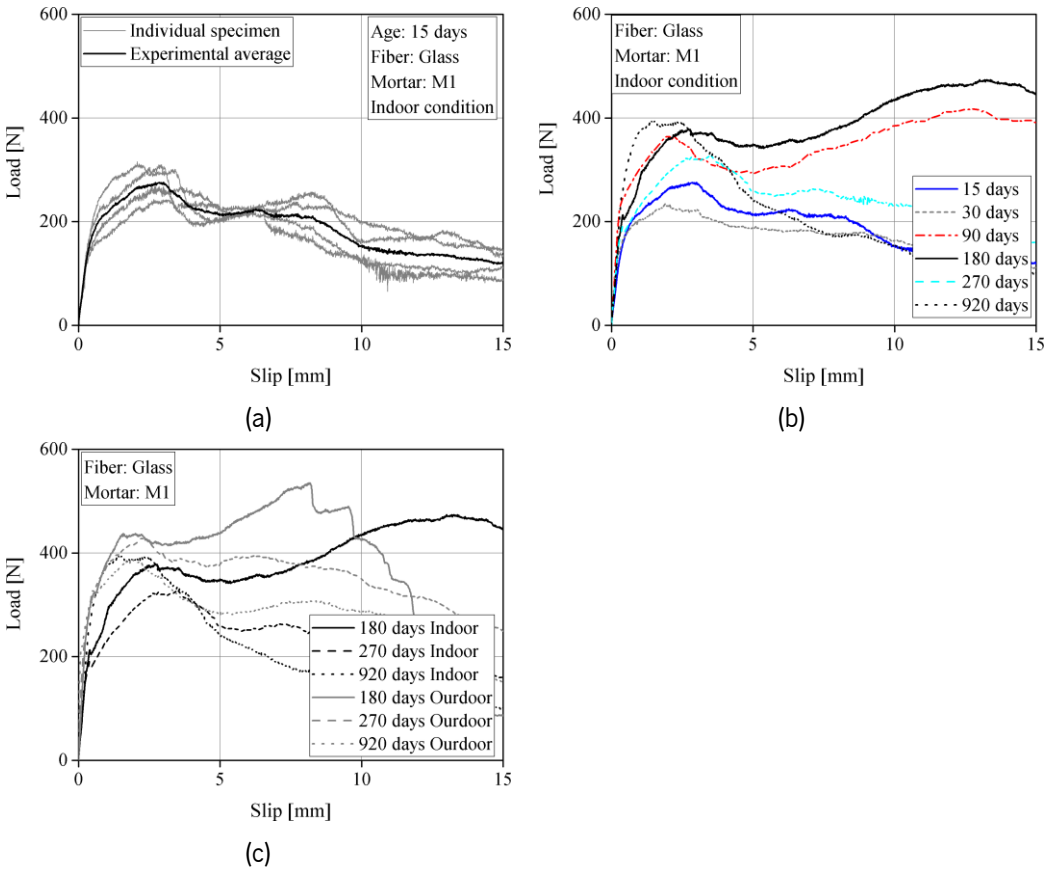

Fig. 5-37. Pull-out behavior of the glass-based TRM: (a) typical pull-out behavior; (b) effect of the mortar age; (c) effect of environmental conditions.

The key characteristics of the pull-out response, compared in Fig. 5-38, show that the peak load and debonding energy of outdoor samples are slightly higher than the corresponding specimens tested in the

indoor condition. However, both the peak load and debonding energy show a declining behavior from 270 days to 920 days in outdoor-aged samples. The initial stiffness of the outdoor aged samples is significantly higher than the indoor aged samples becoming more than three times at 920 days, owing to better curing conditions or higher hydration of the mortar M1. Moreover, both the debonding energy and the pull-out energy show an increasing trend for indoor aged samples while energy desorption is always smaller than that of outdoor aged samples up until the end of the tests, where they become close. Increasing the energy desorption at the early ages of outdoor exposure can be due to improving the bond of fiber-to-mortar. By increasing the exposure ages, the bond declined due to bond deterioration, shrinkage, or micro-cracks. Again, the experimental mean values are presented in Table 5-17 and Table 5-18.

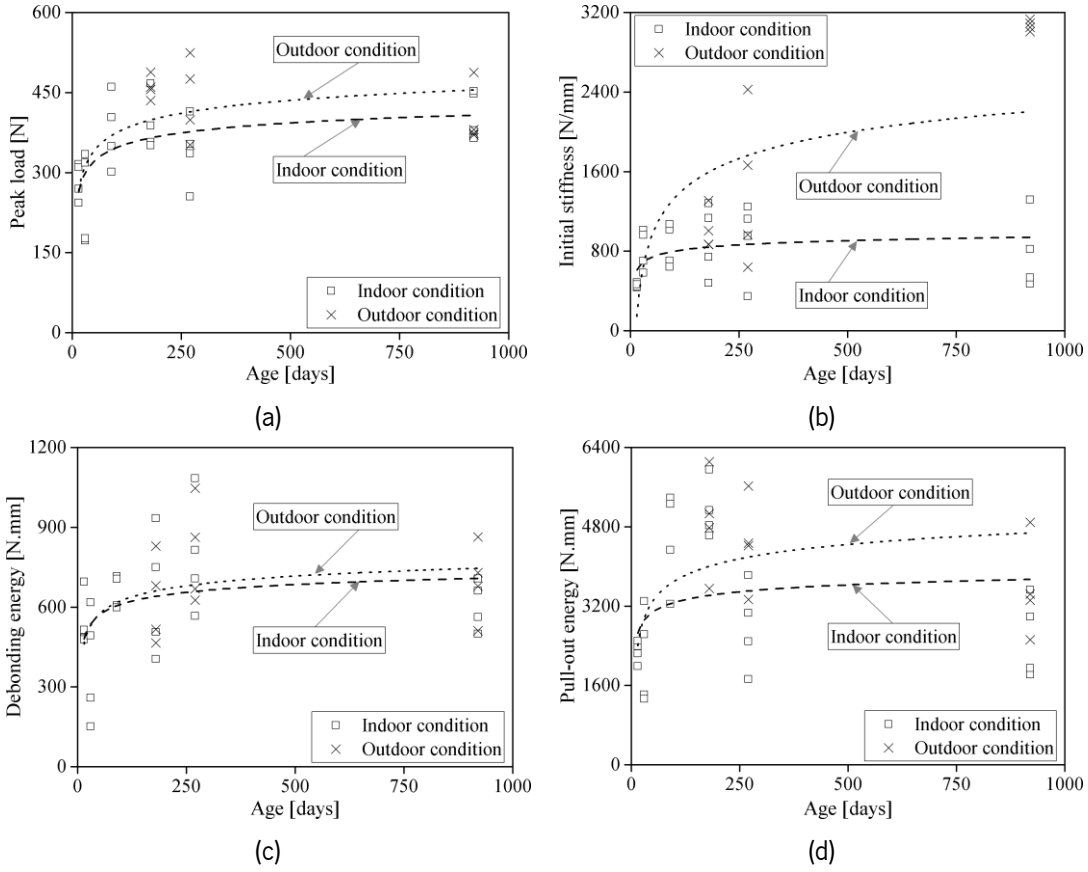

Fig. 5-38. Pull-out behavior parameters of the glass-based TRM: (a) peak load; (b) initial stiffness; (c) debonding energy; (d) pull-out energy.

Table 5-17. Pull-out properties of the glass-based TRM aged under indoor conditions*.

Age [days]	s_P [mm]	P_P [N]	E_{deb} [N.mm]	E_{po} [N.mm]	K [N/mm]
15	2.6 (12)	284.6 (10)	542.9 (16)	2279.0 (8)	456.1 (4)
30	1.9 (31)	250.5 (30)	380.2 (49)	2166.9 (38)	815 (22)
90	2.3 (13)	378.8 (16)	656.4 (8)	4554.6 (19)	857.8 (22)
180	2.3 (27)	390.8 (12)	648.4 (32)	5133.8 (10)	909.1 (35)
270	3.1 (13)	339.5 (17)	792.7 (24)	2775.7 (28)	917.3 (38)
920	1.9 (22)	410.9 (10)	607.6 (13)	2569.8 (28)	785.5 (43)

*CoV of the results is given in percentage inside parentheses; s_P: slip corresponding to peak load; P_P: peak load; E_{deb}: debonding energy; E_{po}: pull-out energy; K: initial stiffness.

Table 5-18. Pull-out properties of the glass-based TRM aged under outdoor conditions*.

Age [days]	s_P [mm]	P_P [N]	E_{deb} [N.mm]	E_{po} [N.mm]	K [N/mm]
180	1.8 (18)	459.7 (4)	622.8 (23)	4878.2 (19)	1012.7 (18)
270	2.2 (11)	437.6 (15)	801.0 (21)	4461.3 (18)	1423.0 (48)
920	2.1 (20)	403.2 (12)	695.9 (18)	3542.4 (24)	3069.2 (2)

*CoV of the results is given in percentage inside parentheses; s_P: slip corresponding to peak load; P_P: peak load; E_{deb}: debonding energy; E_{po}: pull-out energy; K: initial stiffness.

5.8.3. Tensile behavior of steel-based TRM

The typical tensile stress-strain response of individual steel-based TRMs at 90 days, together with their experimental average curves, are presented in Fig. 5-39a. In all specimens, fiber rupture is the governing failure mode. In addition to the three typical stages of the tensile response, explained previously, a final softening stage can be observed in the stress-strain curves. This final softening is probably due to the non-uniform distribution of the stresses among the cords or the step-by-step failure of steel wires. The cracking of the mortar can be clearly observed in the samples Fig. 5-39b. Many cracks have formed, showing the balance between the bond and mortar strength and suitable textile-to-mortar bond behavior in these samples.

At first glance, no significant differences are observed between the tensile responses of samples aged under indoor conditions (Fig. 5-39c) and outdoor conditions (Fig. 5-39d) with time (despite the final tension strength); however, the main characteristics of tensile response, shown in Fig. 5-40, show interesting trends. Only a slight increase can be observed in the first cracking stress (σ_1) in indoor aged samples. However, the cracking strength is increased until 270 days and then decreased until the end of the tests in the outdoor aged samples. At all ages, however, outdoor samples show higher cracking stress than indoor samples, which can be again attributed to a higher hydration degree of the mortar. These observations are in line with the observed changes in the mechanical properties of the mortars reported in previous sections. The stress corresponding to the end of stage II (σ_2) increases notably with time in both indoor and outdoor aged samples. Again, outdoor aged samples show a higher σ_2 than indoor aged ones. In contrast, stress at stage III (σ_3) shows an initial decrease and then an increase in both cases.

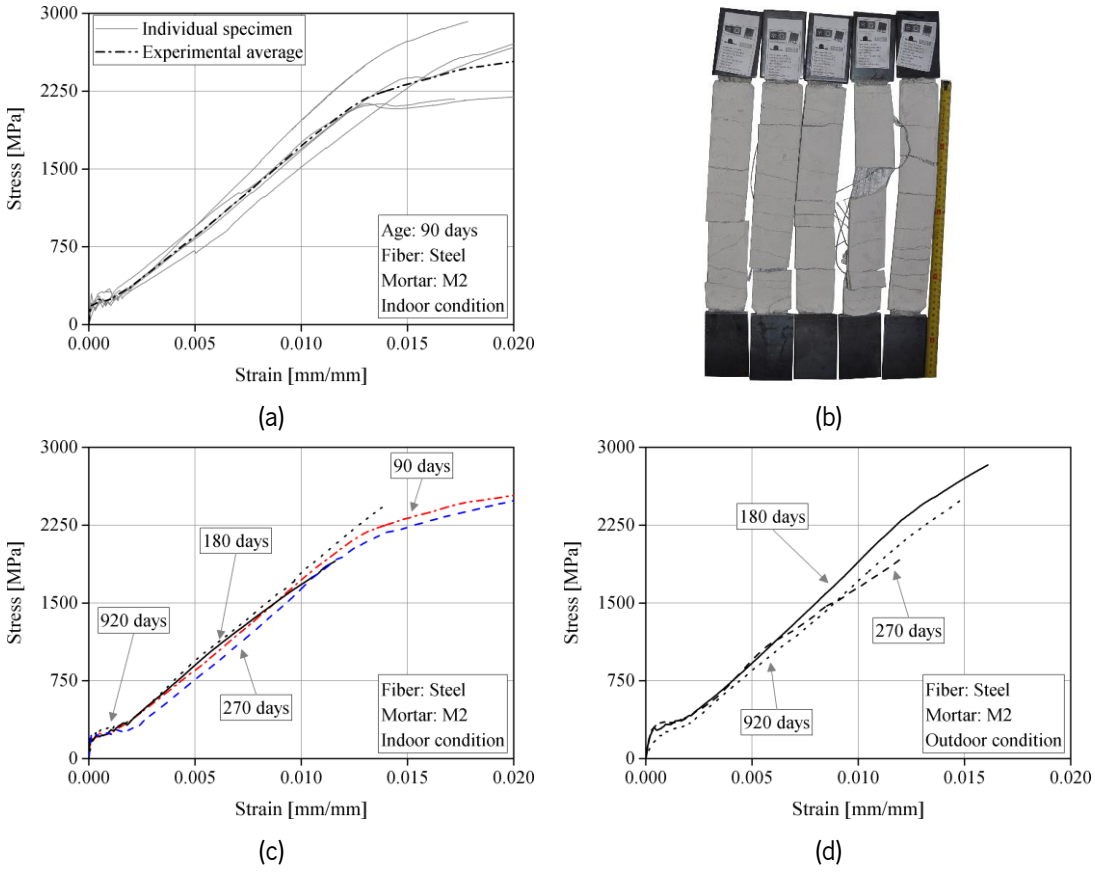

Fig. 5-39. Tensile response of the steel-based TRM: (a) typical tensile behavior; (b) saturated cracking stage at 90 days (indoor aged); (c) effect of the mortar age under indoor conditions; (d) effect of mortar age under outdoor conditions.

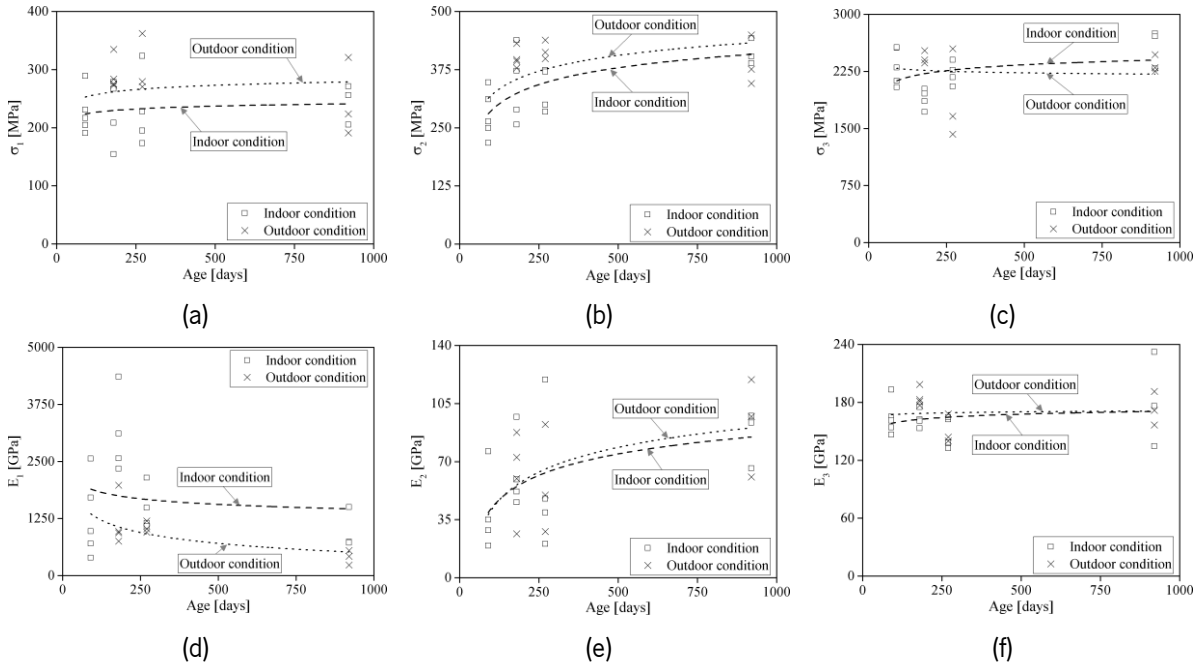

Fig. 5-40. Tensile response parameters of the steel-based TRM: (a) σ_1; (b) σ_2; (c) σ_3; (d) E_1; (e) E_2; (f) E_3.

As for stiffness, E_1 is increased initially and then decreased, E_2 increases, and E_3 does not show any significant changes with time. The saturation crack spacing of the samples gradually decreases over time, see Fig. 5-41a. The mean values are explicitly presented in Table 5-19 and Table 5-20.

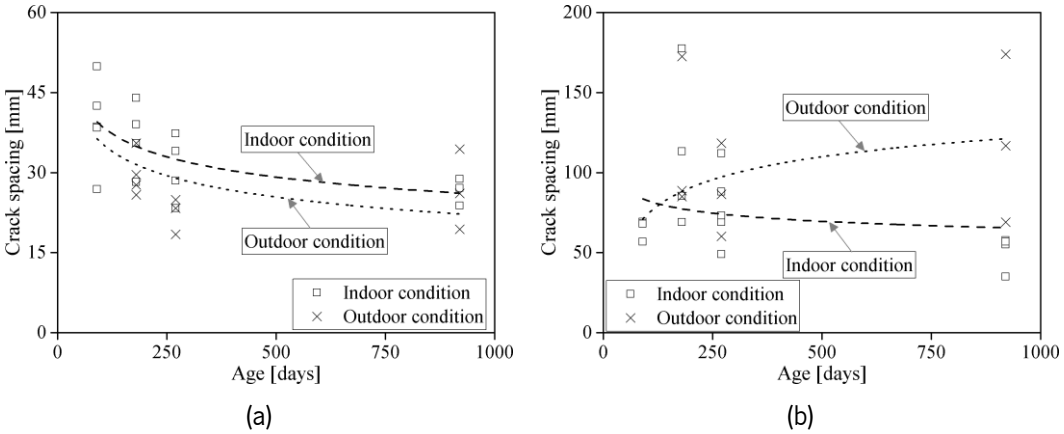

Fig. 5-41. Crack spacing under tensile test: (a) steel-based TRM; (b) glass-based TRM.

Table 5-19. Tensile parameters of the steel-based TRM aged under indoor conditions*.

Age [days]	E_1 [GPa]	E_2 [GPa]	E_3 [GPa]	ε_1 [%]	ε_2 [%]	ε_3 [%]	σ_1 [MPa]	σ_2 [MPa]	σ_3 [MPa]	Number of cracks	Distance between cracks [mm]
90	1266.3 (62)	37.5 (53)	163.9 (10)	0.03 (69)	0.15 (21)	1.40 (13)	226.2 (15)	277.8 (17)	2318.4 (9)	8	39
180	3094.3 (25)	63.4 (31)	162.8 (5)	0.01 (17)	0.19 (8)	1.14 (8)	227.1 (22)	339.0 (21)	1887.8 (6)	9	36.7
270	1464.7 (29)	56.7 (66)	149.4 (10)	0.02 (19)	0.21 (19)	1.49 (10)	229.9 (25)	332.0 (12)	2223.8 (6)	11	30.8
920	986.8 (37)	85.6 (16)	181.0 (22)	0.03 (37)	0.22 (4)	1.51 (25)	244.1 (12)	411.4 (6)	2582.8 (8)	13	26.1

*CoV of the results is given in percentage inside parentheses.

Table 5-20. Tensile behavior of the steel-based TRM aged under outdoor conditions*.

Age [days]	E_1 [GPa]	E_2 [GPa]	E_3 [GPa]	ε_1 [%]	ε_2 [%]	ε_3 [%]	σ_1 [MPa]	σ_2 [MPa]	σ_3 [MPa]	Number of cracks	Distance between cracks [mm]
180	1159.6 (41)	61.6 (37)	184.8 (4)	0.03 (32)	0.20 (4)	1.29 (5)	291.7 (9)	399.8 (5)	2411.7 (3)	11	29.6
270	1057.1 (10)	56.7 (47)	150.6 (8)	0.03 (22)	0.23 (10)	1.18 (20)	303.9 (14)	416.3 (4)	1877.5 (26)	15	20
920	400.4 (32)	92.4 (26)	173.1 (8)	0.08 (60)	0.24 (5)	1.37 (6)	245.1 (22)	390.2 (11)	2340.9 (4)	14	25

*CoV of the results is given in percentage inside parentheses.

5.8.4. Tensile behavior of glass-based TRM

The typical tensile stress-strain response of individual glass-based TRMs (at 90 days), together with their experimental average curves, are presented in Fig. 5-42a. Again, fiber rupture was the governing failure mode in all the specimens. Although the three stages of the tensile response are identified in the curves, no fluctuation in the crack developing stage can be observed, which is due to the small number of cracks formed in these samples and/ or the lower tensile strength of the glass fibers (Fig. 5-42b).

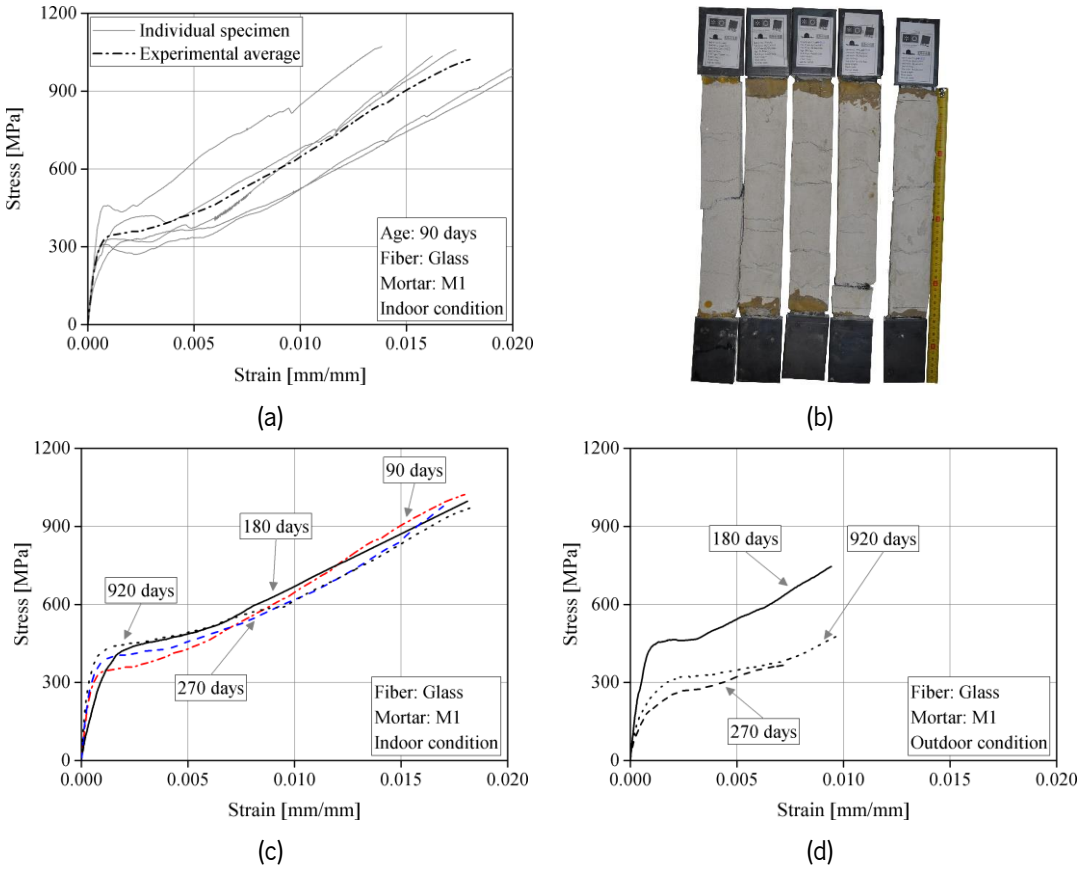

Fig. 5-42. Tensile response of the glass-based TRM: (a) typical tensile behavior; (b) saturated cracking stage at 90 days (indoor aged); (c) effect of the mortar age under indoor conditions; (d) effect of mortar age under outdoor conditions.

No significant change is observed in the tensile response of samples aged under indoor conditions, Fig. 5-42c, though the samples aged under outdoor conditions show that the tensile behavior declines by increasing the exposure, as presented in Fig. 5-42d. An in-depth look at the changes in the main characteristics of the tensile response (Fig. 5-43) shows some differences between the samples aged under indoor and outdoor conditions. As opposed to steel-based TRM, the first cracking stress, σ_1, decreases with time. This decrease is significantly higher in outdoor aged specimens in the first 270 days, which is then recovered to some extent until the end of the tests. The stress corresponding to the end of stage II, σ_2, increases with time in indoor aged samples but decreases in outdoor aged samples. In turn, σ_3 shows a slight decrease in indoor aged samples and a significant one in outdoor aged samples. This observation seems to indicate a non-negligible sensitivity of the glass fibers to outdoor environmental conditions, which has led to their mechanical degradation. As for stiffness, E_1 increases with time for indoor aged samples and decreases for outdoor aged samples, E_2increases in indoor aged samples, but it shows a decrease after 270 days in outdoor aged samples, and E_3 decreases in both cases. In contrast

to steel-based TRM, the crack spacing is decreased in indoor aged specimens but decreases in outdoor aged ones, Fig. 5-41b. The mean values are also explicitly presented in Table 5-21 and Table 5-22.

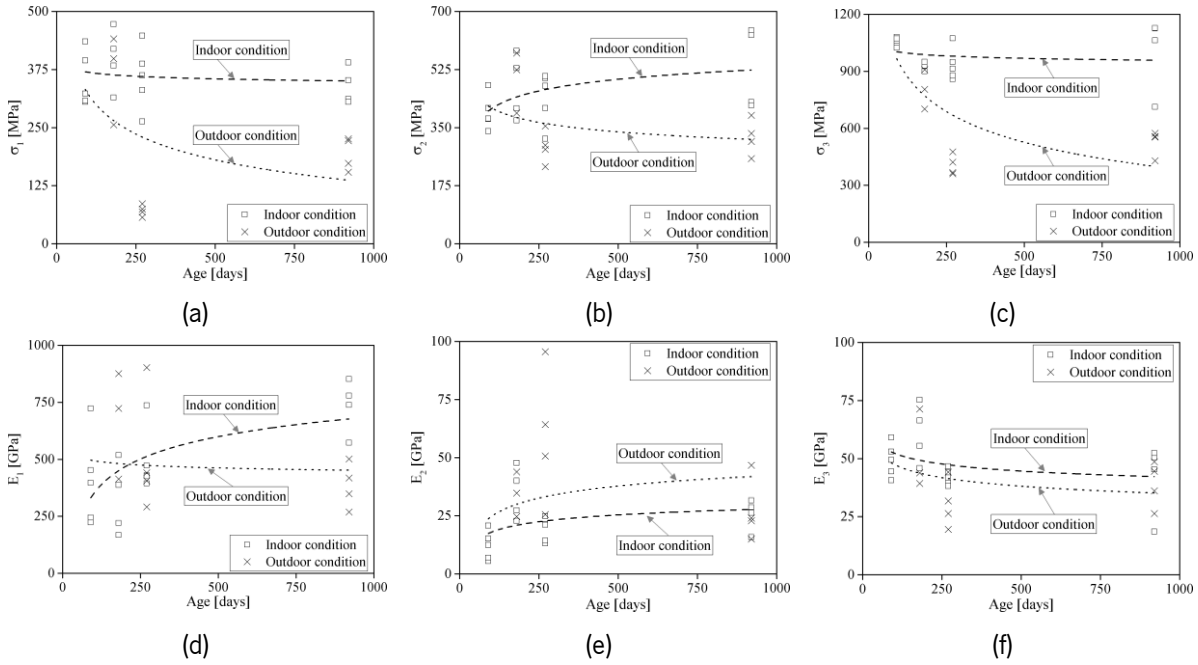

Fig. 5-43. Tensile response parameters of the glass-based TRM: (a) σ_1; (b) σ_2; (c) σ_3; (d) E_1; (e) E_2; (f) E_3.

Table 5-21. Tensile parameters of the glass-based TRM aged under indoor conditions*.

Age [days]	E_1 [GPa]	E_2 [GPa]	E_3 [GPa]	ε_1 [%]	ε_2 [%]	ε_3 [%]	σ_1 [MPa]	σ_2 [MPa]	σ_3 [MPa]	Number of cracks	Distance between cracks [mm]
90	408.1 (44)	12.2 (46)	49.3 (13)	0.10 (40)	0.47 (25)	1.83 (18)	353.1 (15)	395.6 (12)	1054.0 (2)	4	63.8
180	323.3 (43)	34.5 (29)	60.7 (18)	0.14 (38)	0.46 (32)	1.68 (8)	397.4 (14)	472.6 (18)	932.5 (2)	3	102.8
270	491.3 (25)	19.0 (24)	42.2 (7)	0.07 (12)	0.52 (33)	1.68 (12)	358.2 (17)	440.8 (16)	934.4 (8)	4	78.2
920	735.3 (14)	25.6 (23)	41.6 (33)	0.05 (10)	0.77 (24)	1.98 (10)	339.6 (10)	528.8 (20)	1006.9 (17)	6	46.9

*CoV of the results is given in percentage inside parentheses.

Table 5-22. Tensile behavior of the glass-based TRM aged under outdoor conditions*.

Age [days]	E_1 [GPa]	E_2 [GPa]	E_3 [GPa]	ε_1 [%]	ε_2 [%]	ε_3 [%]	σ_1 [MPa]	σ_2 [MPa]	σ_3 [MPa]	Number of cracks	Distance between cracks [mm]
180	670.7 (29)	34.5 (23)	51.5 (27)	0.06 (13)	0.44 (18)	1.07 (18)	365.1 (22)	497.6 (15)	804.7 (10)	2	115
270	509.9 (46)	59.0 (43)	30.5 (30)	0.02 (42)	0.45 (33)	0.82 (24)	71.4 (15)	292.1 (15)	406.5 (11)	4	88
920	384.0 (22)	27.2 (44)	38.9 (22)	0.05 (32)	0.55 (21)	1.10 (21)	193.8 (16)	320.9 (15)	528.0 (11)	2	119

*CoV of the results is given in percentage inside parentheses.

5.9. Effect of freeze-thaw conditions

This section investigates the effects of freeze-thaw conditions on TRM composites based on the experimental plan described in section 3.9.2. To this end, sections 5.8.1, 5.8.2, and 5.9.3 explain the effect of FT condition on the tensile, pull-out, and single-lap shear behavior of glass-based TRMs. Next, the effect of FT condition on fiber-to-mortar bond behavior of steel and glass-based TRM composites with different fiber embedded lengths and configurations are investigated.

Specimens are named XYZ, in which X is related to the type of TRM mechanical tests (T: Tensile test, P: Pull-out, S: Single-lap shear). Y is related to the control (C) or exposure (E) specimens, and Z is connected to the number of FT cycles. For example, PE360 is a pull-out specimen that received exposure to 360 FT cycles.

For the pull-out specimens with different bond lengths and fiber configurations, the UVW-YZ nomenclature is considered. Where U is related to the fiber type (S: steel, G: glass), and V is linked to the fiber configuration (S: single fiber, T: single yarn + transverse elements, G: two fibers, G′: four fibers). In addition, W is connected to the different embedded lengths (for glass fiber: 50, 75, and 100 mm, for steel fiber: 50, 150, 200, and 250 mm). For example, SS150-E60 is a steel-based TRM composite with a single yarn and 150 mm bond length exposed to 60 FT cycles.

5.9.1. Fiber-to-mortar bond

Fig. 5-44 shows the typical pull-out response of individual specimens at 0 cycles and their experimental average (of five samples) under the control and the FT conditions. In all cycles, the load-slip curves show the typical pull-out response. The failure mode for all the specimens is yarn slipping from the mortar with few exceptions in which the yarn raptures at the post-peak area. It can be observed that the pull-out response of the control specimens is enhanced until 180 cycles and then deteriorates until 360 days (Fig. 5-44b). A similar trend also was observed in the mortar age effect on the pull-out response of glass-based TRM (section 5.8.2). A similar enhancement of the pull-out response is also observed in the samples exposed to FT conditions under 120 cycles, followed by a declining trend until the end of the tests (Fig. 5-44c).

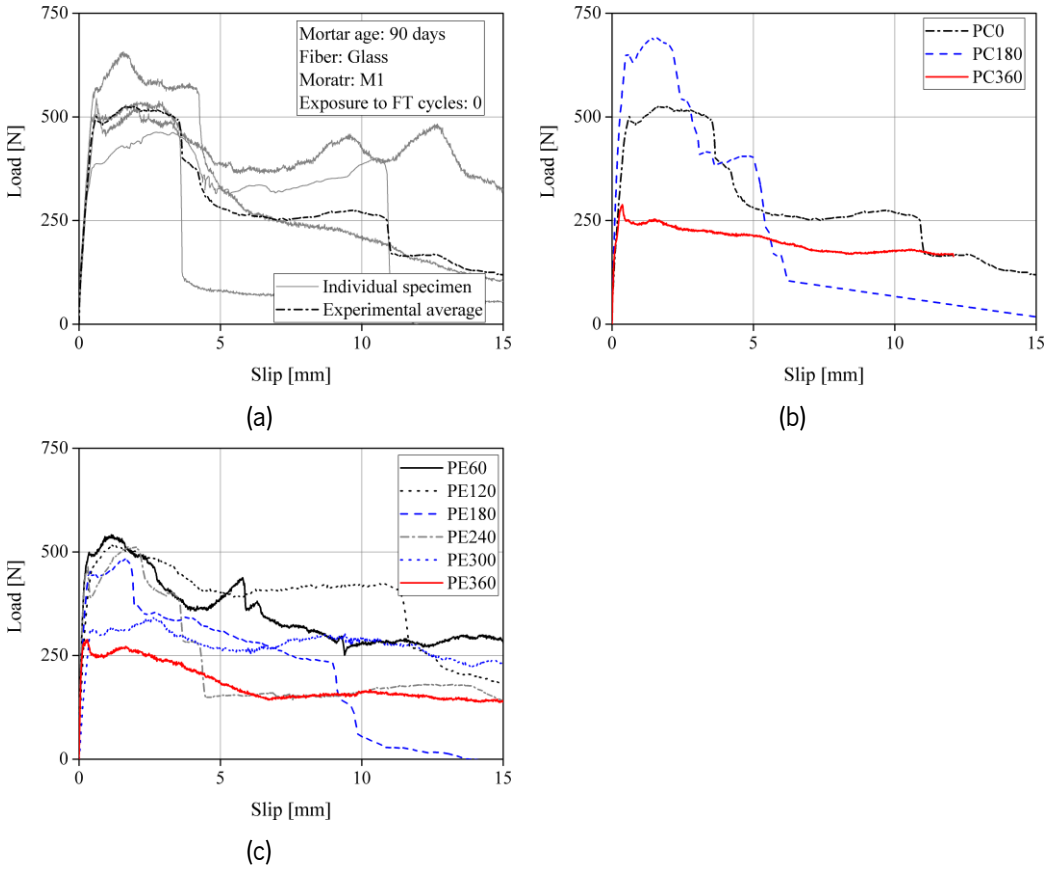

Fig. 5-44. Pull-out response: (a) typical pull-out behavior; (b) control specimens; (c) exposed specimens.

The peak load, debonding energy, and pull-out energy as the key characteristics of pull-out response are presented in Fig. 5-45 with a linear regression line to demonstrate the general trend of pull-out parameters (details presented in Table 5-23). The debonding energy and pull-out energy are defined as the area under the load-slip curve until the peak load and the area from the peak load until the end, respectively. In Table 5-23 and Fig. 5-45c, the pull-out energy of PE240 specimens is not presented and measured due to fiber rupture after reaching the peak load. The peak load, debonding energy, and pull-out energy of PE360 specimens (exposed specimens after applying 360 FT cycles) decrease by 39%, 85%, and 38%, respectively, compared to PC0 (control specimens at zero cycles). These values for PC360 specimens (control specimens corresponding to 360 FT cycles) are 39%, 70%, and 33%, respectively. These observations indicate that FT conditions do not affect bond behavior since the pull-out parameters decrease similarly under both conditions. Instead, bond deterioration seems to have other sources, which may be attributed to continued mortar hydration until the end of the test or shrinkage [161,219]. This output needs to be explored in more detail in future studies.

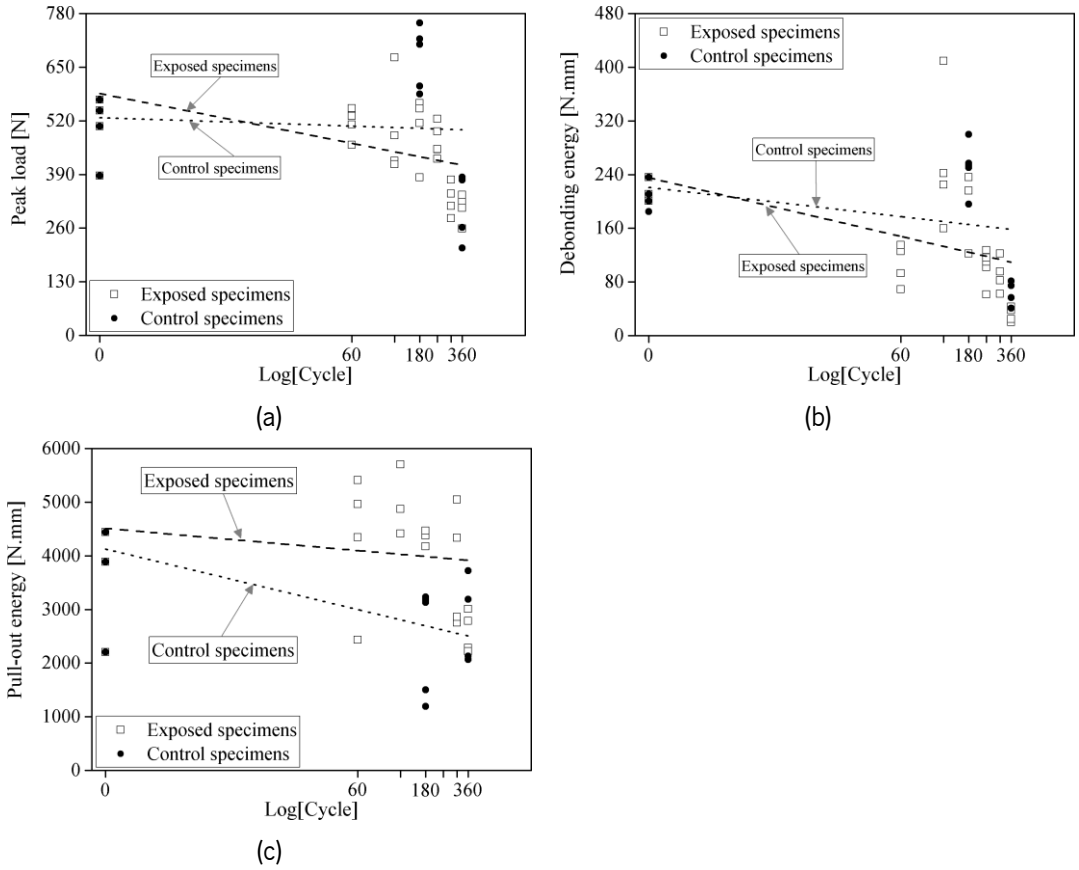

Fig. 5-45. Pull-out behavior parameters: (a) peak load; (b) debonding energy; (c) pull-out energy.

Table 5-23. Pull-out properties of glass-based TRM composite under freeze-thaw conditions*.

Name	s_P [mm]	P_P [N]	E_{deb} [N.mm]	E_{po} [N.mm]	K [N/mm]
PC0	0.63 (1)	502 (14)	208 (9)	4162 (34)	1829 (17)
PC180	0.56 (10)	674 (10)	252 (13)	2449 (37)	3509 (17)
PC360	0.32 (15)	308 (24)	63 (25)	2776 (25)	2419 (22)
PE60	0.28 (18)	514 (6)	106 (25)	4286 (27)	4738 (3)
PE120	0.70 (16)	499 (21)	259 (36)	5457 (17)	3069 (16)
PE180	0.47 (23)	502 (14)	191 (26)	4339 (3)	5828 (11)
PE240	0.34 (24)	470 (7)	103 (22)	-	4809 (17)
PE300	0.45 (23)	329 (11)	91 (24)	3748 (26)	971 (18)
PE360	0.17 (25)	308 (10)	32 (15)	2574 (13)	3606 (18)

*CoV of the results is given in percentage inside parentheses; s_P: slip corresponding to peak load; P_P: peak load; E_{deb}: debonding energy; E_{po}: pull-out energy; K: initial stiffness.

5.9.2. Tensile behavior

Fig. 5-46a and Fig. 5-46b show the typical tensile stress-strain response and crack pattern of TRMs at 0 cycles and their experimental average (of five samples) under the control and the FT conditions. The

experimental load is divided by the cross-section area of the yarns (2.645 mm^2) to calculate the stress. The strain equals the mean displacements from the two LVDTs divided by their base length (310 mm). A set of parallel and horizontal cracks followed by rupturing yarns are the governing failure mode in all the specimens under the control and the FT conditions, as shown in Fig. 5-46b. The linear, the crack development, and the post-cracking stages of the tensile response are identified in the tensile-strain curves. Fig. 5-46c shows no significant change in the stress-strain curves for specimens under the control conditions, while Fig. 5-46d displays that freeze-thaw action slightly decreases the tensile performance of glass-based TRM composite.

The tensile response parameters (elastic modulus and stress) of individual specimens are reported together with a linear regression line showing the general trend of the experimental results in Fig. 5-47 (and see Table 5-24 for exact values). In general, the stress and elastic modulus corresponding to the linear stage (σ_1 and E_1), as well as the stress of the crack development stage (σ_2), drops under the FT conditions (Fig. 5-47). The decrease is 42%, 12%, and 22% for σ_1, E_1, and σ_2 after 360 FT cycles (TE360 specimens) compared to the control samples at zero cycles (TC0). Nevertheless, the elastic modulus of the crack development stage (E_2) under the FT conditions shows an increasing trend (Fig. 5-47), so that E_2 at the last FT cycle (TE360) increases by 50% compared to TC0 specimens (Table 5-24). Control specimens behave differently in terms of tensile parameters so that σ_1 remains almost constant throughout the test and E_1 increases by 81% for TC360 specimens compared with TC0 specimens. At the crack development stage, both σ_2 and E_2 exhibit a decreasing trend under the control conditions. Compared with TC0 specimens, these parameters decrease by 14% and 62% at the end of the test. Besides, the crack spacing for both control and exposed specimens shows a slightly increasing trend, as shown in Fig. 5-48. These observations indicate that the proposed FT conditions degrade the tensile behavior of the glass-based TRM composites, particularly at the linear stage. This conclusion differs from the tensile behavior of mortar M1 (flexural and splitting results) under the FT conditions, which may be due to differences in specimen thicknesses and test setups.

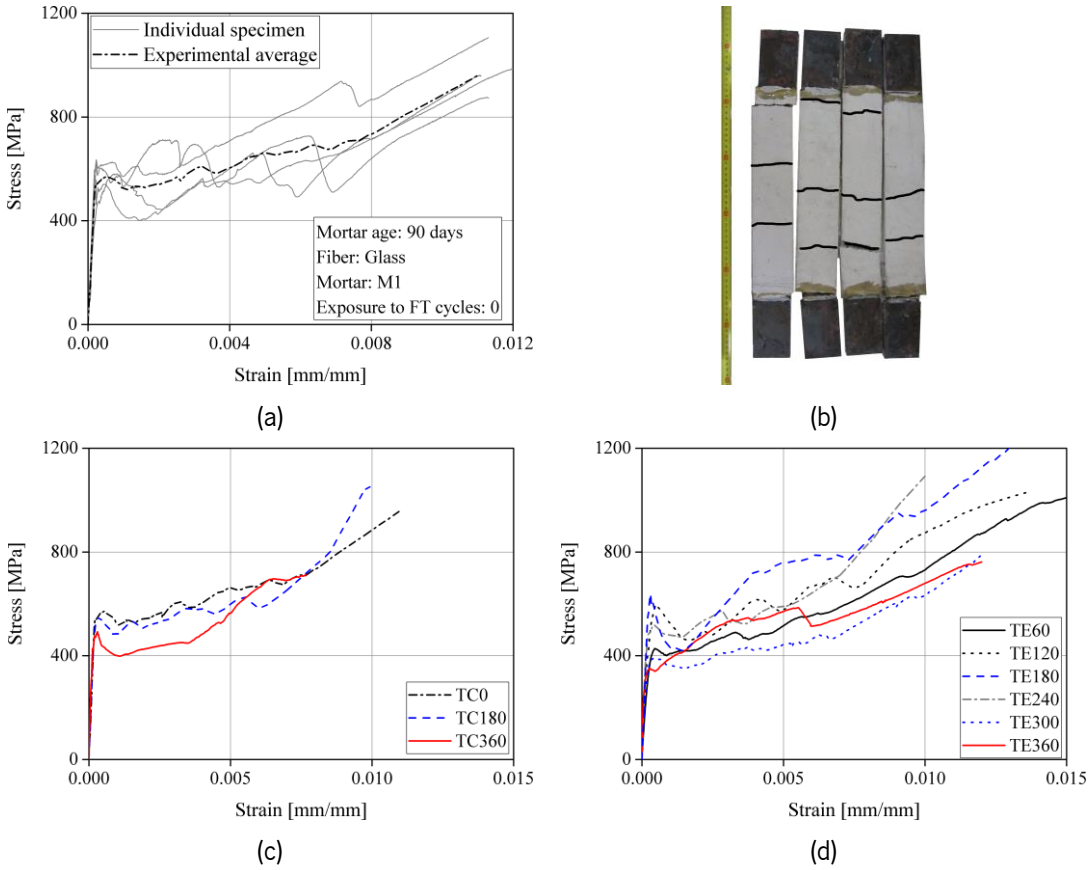

Fig. 5-46. TRM composite tensile response: (a) typical tensile behavior; (b) saturated cracking stage at 90 days (control specimens); (c) tensile response of control specimens; (d) tensile response of exposed specimens.

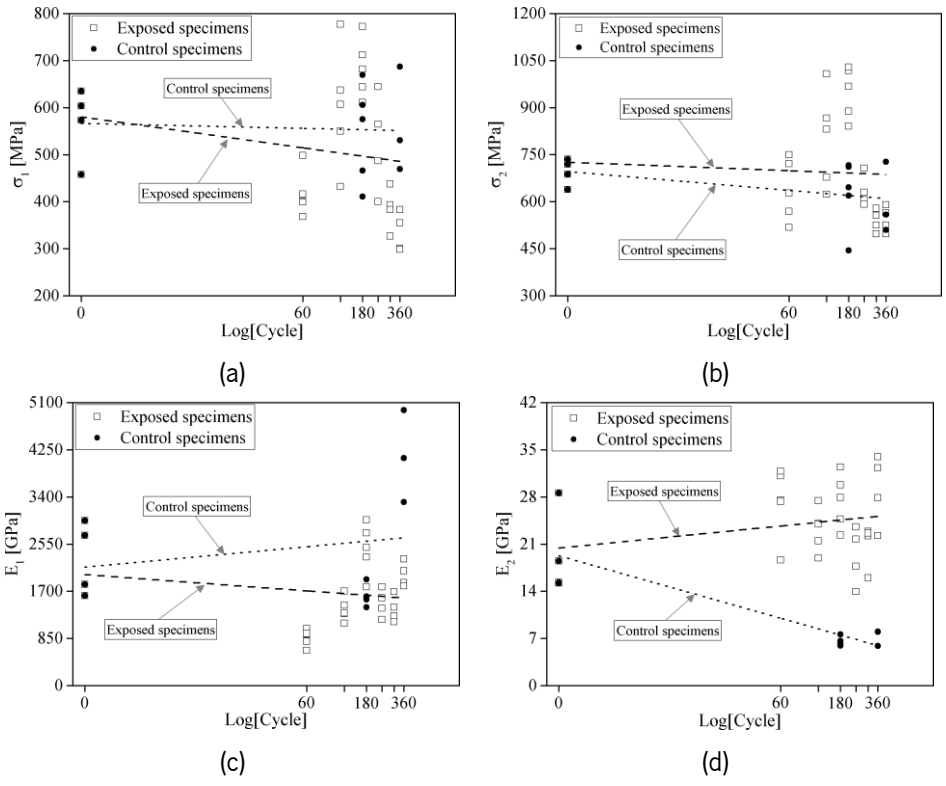

Fig. 5-47. Tensile response parameters of the TRM composite: (a) σ_1; (b) σ_2; (c) E_1; (d) E_2.

Table 5-24. TRM tensile behavior under freeze-thaw conditions*.

Name	E_1 [GPa]	E_2 [GPa]	E_3 [GPa]	ε_1 [%]	ε_2 [%]	ε_3 [%]	σ_1 [MPa]	σ_2 [MPa]	σ_3 [MPa]	Number of cracks	Distance between cracks [mm]
TC0	2280 (25)	19.4 (28)	62.7 (15)	0.03 (25)	0.68 (30)	1.19 (9)	567.5 (12)	695 (5)	995.6 (9)	3 (13)	101 (23)
TC180	1607.1 (12)	6.6 (10)	83.4 (13)	0.03 (17)	0.65 (18)	1.09 (15)	545.5 (17)	627.3 (16)	940.5 (8)	2 (32)	124 (21)
TC360	4124.3 (16)	7.3 (14)	53.5 (21)	0.01 (29)	0.54 (27)	0.82 (32)	562.4 (16)	598.9 (16)	736.8 (13)	2 (28)	133 (35)
TE60	863.9 (16)	27.3 (17)	59.1 (12)	0.05 (18)	0.84 (15)	1.66 (10)	419.2 (10)	637 (14)	1110.3 (5)	4 (23)	72 (20)
TE120	1375.1 (14)	23.2 (12)	63.7 (20)	0.04 (21)	0.92 (21)	1.21 (9)	600.5 (19)	801.1 (17)	1004.4 (10)	2 (20)	112 (11)
TE180	2463.8 (17)	27.4 (13)	69.6 (12)	0.03 (18)	0.98 (15)	1.2 (10)	684.3 (8)	948.8 (8)	1096.1 (5)	2 (18)	105 (15)
TE240	1485.8 (15)	19.2 (19)	70.0 (9)	0.04 (17)	0.45 (19)	0.91 (24)	524 (17)	633.4 (7)	833.6 (9)	2 (19)	101 (39)
TE300	1378.8 (15)	20.9 (14)	51.4 (22)	0.03 (20)	0.78 (20)	1.39 (18)	385.1 (10)	539.3 (6)	846.4 (11)	3 (0)	99 (25)
TE360	1999.9 (10)	29.1 (16)	47.6 (17)	0.02 (17)	0.75 (14)	1.51 (13)	334.3 (11)	544.2 (7)	907.1 (9)	2 (25)	140 (22)

*CoV of the results is given in percentage inside parentheses.

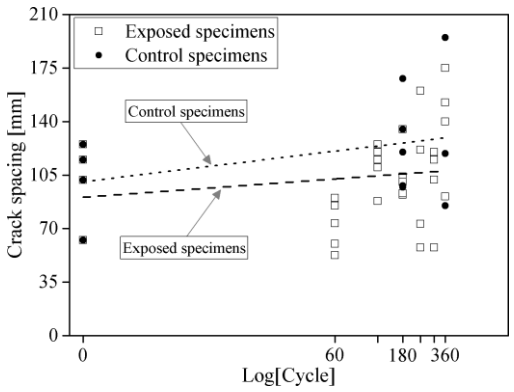

Fig. 5-48. Crack spacing of the tensile specimens.

5.9.3. TRM-to-substrate bond

Fig. 5-49 reports the typical load-slip curves of the individual TRM-to-substrate specimens at 0 cycles and the average load-slip curves of the control and the exposed specimens at all cycles. The curves in the figures are the average of five specimens. The load in these curves is divided into the number of yarns (3 yarns) to calibrate curves based on a yarn. Control samples fail because of yarns slippage, while exposed samples fail due to either yarns slippage or yarns slipping followed by tensile rupture (see Table 5-25). It

should be noted that no debonding has occurred at the TRM-to-substrate interface under both conditions due to the brick surface sandblasting and the equal CTE of the brick and the mortar M1. In general, the load-slip curves of the control specimens indicate that the single-lap shear response declines with age (Fig. 5-49b). In parallel, the load-slip curves of the exposed samples rise with increasing FT cycles up to 180 cycles. After this point, the load-slip curves show a declining trend, as shown in Fig. 5-49c. This observation is in agreement with the pull-out response.

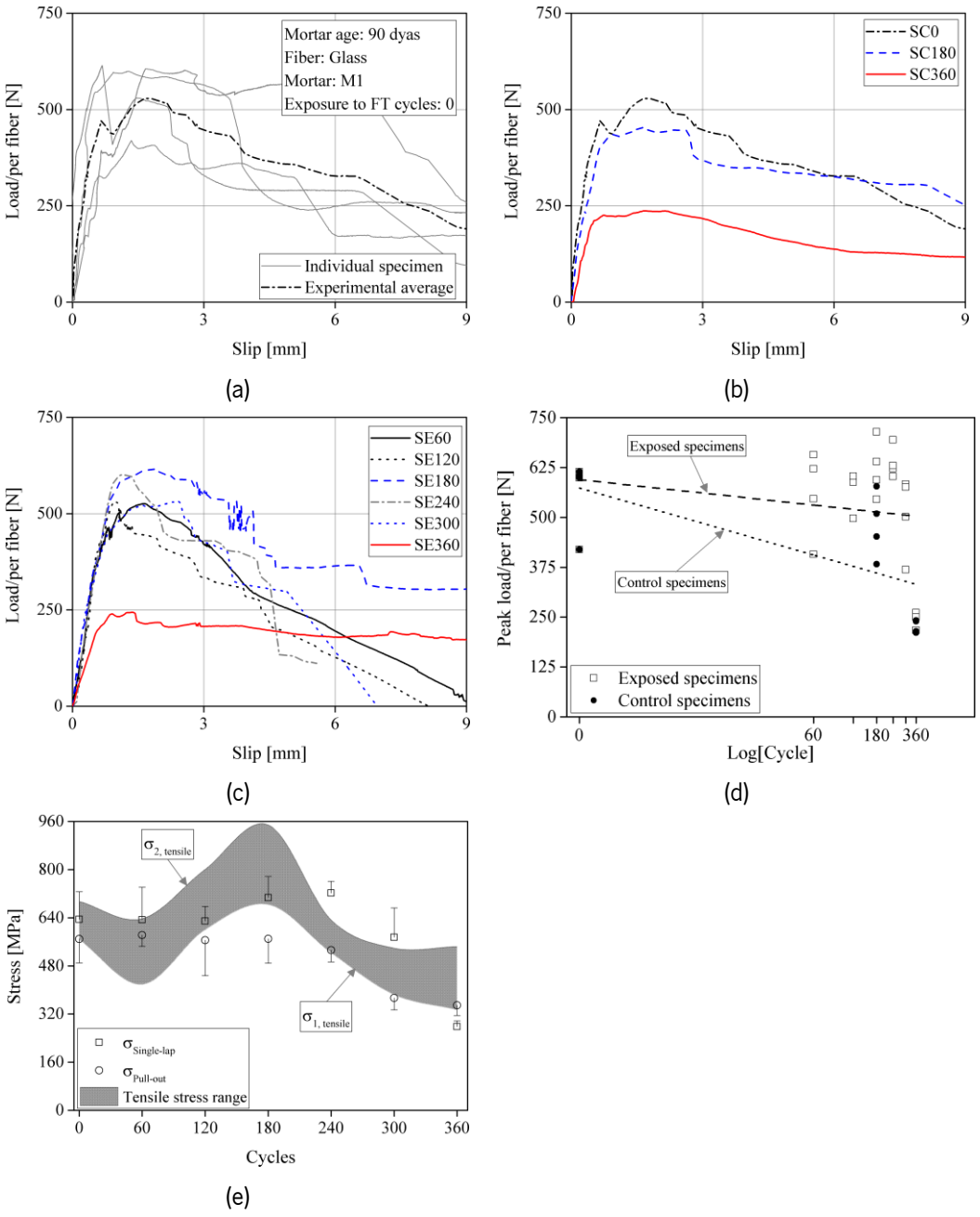

Fig. 5-49. TRM-to-substrate response: (a) typical load-slip curve; (b) control specimens; (c) exposed specimens; (d) peak load changes; (e) average stress at the exposed bond level specimens.

The changes in the single-lap shear peak load under both conditions are presented in Fig. 5-49d with a linear regression trending line for better understanding. Also, Table 5-25 reports the experimental mean values of the slip corresponding to peak load, the peak load, and initial stiffness (by computing the initial slopes of load-slip curves) in each cycle. As shown in Fig. 5-49d, the change in peak load under the FT conditions is generally decreasing. Therefore, the peak load of SE360 specimens (exposed to 360 FT cycles) decreases by 56% compared to the SC0 specimens. Meanwhile, the peak load of the control specimens displays a decreasing trend as well, by 59% for the SC360 specimens compared to the SC0 specimens. Since the peak load decreases similarly under both conditions, it indicates that FT does not affect the TRM-to-substrate bond behavior. In fact, bond deterioration may be due to ongoing hydration of the mortar or shrinkage. The effects of these conditions need to be explored further in future research.

Table 5-25. Glass-based TRM-to-substrate bond properties under freeze-thaw conditions*.

Name	Slip of the peak load [mm]	Peak load/per yarn [N]	Initial stiffness/ per yarn [N/mm]	Failure
SC0	1.25 (29)	559 (15)	342 (31)	slip
SC180	1.55 (39)	480 (15)	811 (24)	slip
SC360	0.58 (33)	227 (6)	729 (11)	slip
SE60	1.08 (30)	558 (17)	743 (15)	slip
SE120	1.21 (34)	555 (8)	775 (19)	slip- rupture
SE180	1.36 (32)	623 (10)	793 (5)	slip- rupture
SE240	1.15 (2)	637 (5)	952 (4)	rupture
SE300	1.07 (21)	507 (17)	531 (25)	slip- rupture
SE360	0.81 (17)	246 (7)	443 (14)	slip

*CoV of the results is given in percentage inside parentheses.

Fig. 5-49e also shows the average fabric stress of the pull-out ($\sigma_{pull\text{-}out}$) and the single-lap ($\sigma_{single\text{-}lap}$) specimens compared to the average tensile stress of the TRM composite at the end of the linear (σ_1) and the crack development stages (σ_2) under the FT conditions. As shown, $\sigma_{pull\text{-}out}$ and $\sigma_{single\text{-}lap}$ are close to the σ_1, indicating the bond strength of the whole system decreases before cracks appear in the mortar samples. However, in some points (240 and 300 cycles), $\sigma_{single\text{-}lap}$ is close to the σ_2 due to fiber rupturing in these samples. Moreover, comparison of $\sigma_{pull\text{-}out}$ and $\sigma_{single\text{-}lap}$ shows that these two stresses are equal up to 120 cycles, but after this point, $\sigma_{pull\text{-}out}$ is less than $\sigma_{single\text{-}lap}$. This can be attributed to the fact that the bond degradation effect on mesh fabric is less than that on single yarn. In addition, it is important to take into account that the bond length of pull-out specimens varies from those of single-lap specimens (50 mm versus 100 mm, respectively).

5.9.4. Steel-based TRM with different bond lengths

Fig. 5-50 shows the average load-slip curves of steel-based TRM with different embedded lengths under both the control and the FT conditions. Table 5-26 also presents the failure mode of these specimens. All SS50 and SS150 specimens show a fiber slipping/pull-out failure mode with the typical load-slip curves, including the linear, nonlinear, and dynamic stages. The linear stage exhibits a complete bond between fiber and mortar, while the nonlinear stage indicates debonding occurring at the fiber-to-mortar interface and continues until the peak load. Then, complete debonding occurs, and the fiber pulls out from the mortar (the dynamic stage). The failure mode in SS200 is a combination of the fiber rupturing (for SS200-E60, SS200-E180) and slipping (for SS200-E300/360 and SS200-C0/360), as listed in Table 5-26. The load-slip curves of the specimens with the fiber rupture show a linear and a partially nonlinear part until the peak load, followed by a sudden rupture of the fiber (Fig. 5-50). The failure of SS250 specimens is the fiber rupture (for SS250-C0 and SS250-E360) and fiber slipping (for SS250-E60/180/300 and SS250-C360) (see Table 5-26). The fiber rupture occurs at the loaded end (inside the mortar or at the mortar interface) due to reaching the applied load to the fiber tensile strength. Fiber rupturing shows that the bond strength at the interface of the fiber-to-mortar was higher than the tensile strength of the steel fibers and caused fiber failure. As listed in Table 5-26, the peak load of all steel-based TRM specimens with fiber failure is close to the tensile strength of the steel fiber (2819 MPa or 1517 N, as listed in Table 4-10).

In general, in all embedded lengths, the control samples show a deterioration of bond performance with time (comparing the load-slip curves of C0 with C360 in Fig. 5-50). The FT exposure, however, has different effects on specimens with different embedded lengths. For example, the load-slip curves of SS50-E and SS200-E specimens get flattered by increasing the number of cycles. In contrast, SS150-E and SS250-E show the opposite trend. Additionally, a few load-slip curves of steel-based TRM specimens (SS50-C360, SS150-C360, and SS200-E360) show a load drop after reaching peak load, followed by a slip-hardening (see Fig. 5-50). The fiber-to-mortar bond in a TRM composite with a high adhesion must be broken before the dynamic stage can begin. The load drop occurs when the load required to debond the fiber is higher than the frictional resistance after complete debonding, resulting in an unstable debonding. In addition, slip hardening occurs due to increasing friction stress between the fiber and the mortar at the dynamic stage.

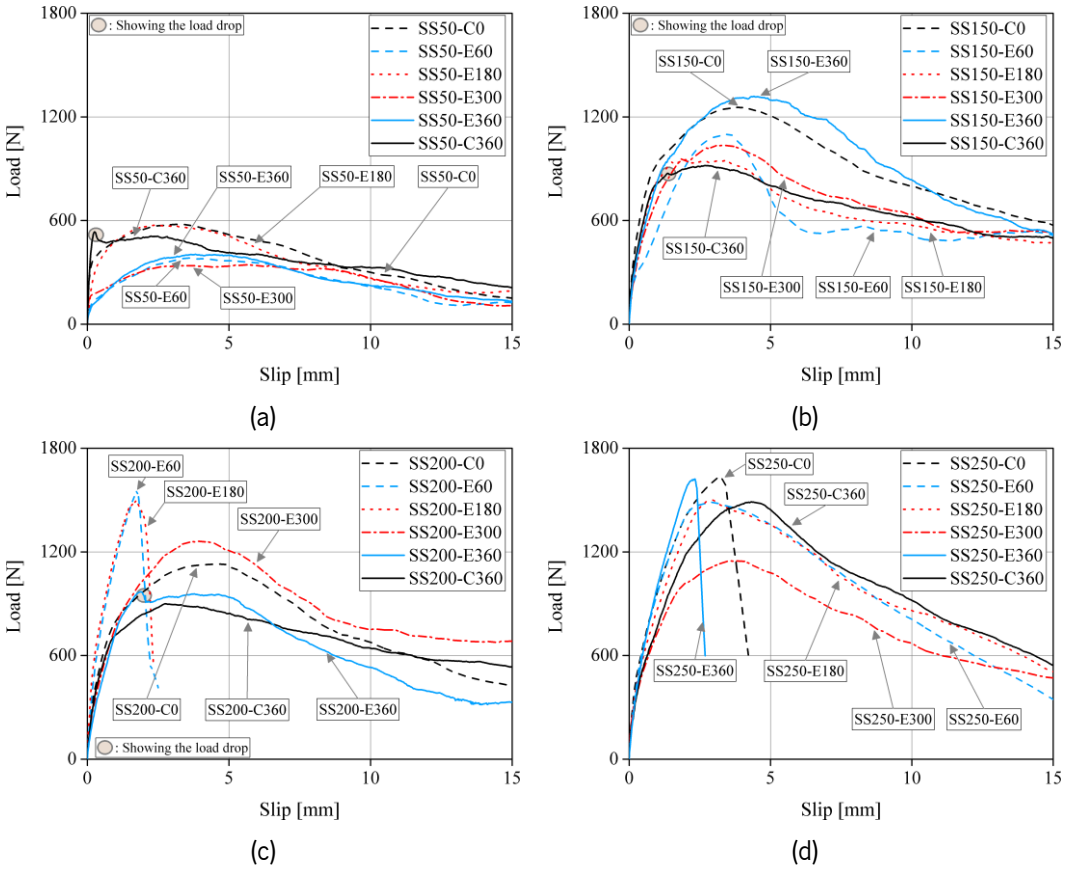

Fig. 5-50. Average of load-slip response of single steel fibers in different bond lengths: (a) SS50; (b) SS150; (c) SS200; (d) SS250.

The changes of the peak load (P_P), the debonding energy (E_{deb}), and the pull-out energy (E_{po}) with exposure are presented in Fig. 5-51(the average values are also reported in Table 5-26). E_{deb} and E_{po} are defined as the area under the load-slip curve until the peak load and from the peak load until the end, respectively. It should be mentioned that E_{po} is not calculated for SS250-E360 and SS250-C0 as the fibers failed at the peak load (see Fig. 5-50d). All pull-out parameters show, in general, a gradual decrement from 0 to 360 cycles under both the control and the FT conditions, as shown in Fig. 5-51. To understand better the effect of mortar age and FT conditions on the bond parameters, the difference (in percentage) between the average results at 360 cycles (C360 and E360) and the control specimens at 0 cycles (C0) are presented in Table 5-26. It can be inferred that the bond parameters are deteriorated equally under both conditions, showing the proposed FT condition was not harsh enough. It seems other parameters cause the bond degradation to occur in both conditions, such as the long-term shrinkage effect by forming micro cracks at the bond interface. Continuing hydration (as mentioned in section 4.5.1) may lead to chemical shrinkage due to a reduction in the hydration volume of anhydrous compounds. This output should be further investigated in future studies.

Table 5-26. Changes of bond properties in steel-based TRM with different embedded lengths and under FT conditions*.

Embedded length [mm]	Name	P_P [N]	$P_P/P_{P,C0}$-1 [%]	E_{deb} [N.mm]	$E_{deb}/ E_{deb,C0}$-1 [%]	E_{po} [N.mm]	$E_{po}/ E_{po,C0}$-1 [%]	Failure
50	SS50-C0	588 (14)	-	1546 (17)	-	4210 (14)	-	slip
	SS50-E60	413 (13)	-	1197 (38)	-	2495 (15)	-	slip
	SS50-E180	584 (22)	-	1102 (34)	-	4314 (23)	-	slip
	SS50-E300	350 (29)	-	799 (30)	-	3110 (30)	-	slip
	SS50-E360	420 (22)	-29	1169 (49)	-24	2860 (16)	-32	slip
	SS50-C360	536 (15)	-9	99 (30)	-94	5446 (14)	29	slip
150	SS150-C0	1280 (11)	-	3810.1 (25)	-	9816 (13)	-	slip
	SS150-E60	1301 (22)	-	2893 (11)	-	6755 (15)	-	slip
	SS150-E180	1033 (26)	-	1445 (39)	-	8503 (23)	-	slip
	SS150-E300	1087 (18)	-	2579 (25)	-	8186 (18)	-	slip
	SS150-E360	1389 (7)	9	3773 (42)	-1	10884 (25)	11	slip
	SS150-C360	875 (19)	-32	563 (40)	-85	9698 (10)	-1	slip
200	SS200-C0	1164 (26)	-	4033 (39)	-	7748 (21)	-	slip
	SS200-E60	1623 (2)	-	2051 (15)	-	-	-	rupture
	SS200-E180	1622 (1)	-	1995 (16)	-	-	-	rupture
	SS200-E300	1289 (13)	-	3759 (22)	-	9540 (13)	-	slip
	SS200-E360	981 (11)	-16	1021 (25)	-75	8616 (6)	11	slip
	SS200-C360	923 (12)	-21	3140 (38)	-22	7374 (14)	-5	slip
250	SS250-C0	1643 (3)	-	3874 (24)	-	-	-	rupture
	SS250-E60	1568 (7)	-	3743 (43)	-	11201 (2)	-	slip
	SS250-E180	1527 (4)	-	2799 (13)	-	12797 (9)	-	slip
	SS250-E300	1167 (11)	-	3447 (12)	-	8481 (3)	-	slip
	SS250-E360	1690 (2)	3	2456 (24)	-37	-	-	rupture
	SS250-C360	1507 (10)	-8	4541 (16)	17	11539 (7)	-	slip

*CoV of the results is given in percentage inside parentheses; P_P: Peak load; E_{deb}: Debonding energy; E_{po}: Pull-out energy.

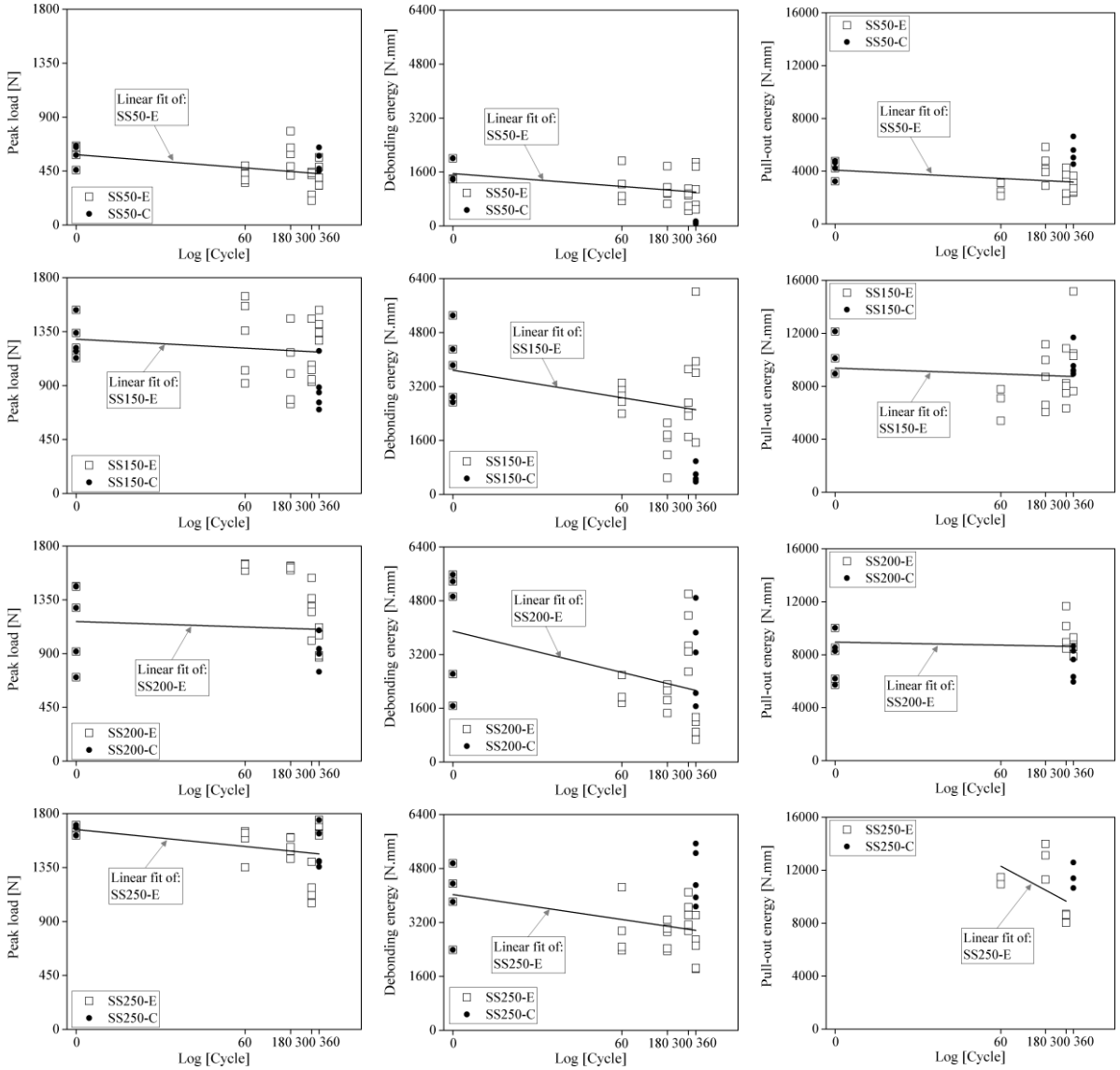

Fig. 5-51. Pull-out parameters of single steel-based TRM in different bond lengths: (a) peak load; (b) debonding energy; (c) pull-out energy.

5.9.5. Glass-based TRM with different bond lengths

The average of pull-out response curves obtained for the glass-based TRMs with different bond lengths is presented in Fig. 5-52. Besides, Table 5-27 presents the failure of these specimens. The load-slip curves of GS50 specimens include the linear and nonlinear part until reaching the first peak load, followed by slip hardening and then decreasing load. These specimens generally fail under yarn slipping/pull-out mode though tensile rupture of the yarns occurs in GS50-E60/180 and GS50-C0 specimens at the dynamic stage. The failure of GS75 specimens is yarn slipping followed by rupturing. This observation is also supported by their load-slip curves, where the yarn slipped until reaching peak load and then ruptured

at the dynamic stage. Meanwhile, GS100 samples are failed by fiber rupturing, so their load-slip curves only include the linear and nonlinear parts until a peak load is reached.

Load-slip curves show a decrease in bond performance of GS50 specimens. So, as the FT cycle or mortar age increases, the load-slip curve of GS50 specimens becomes flatter, and the slip hardening effect is reduced due to the decrease in the friction stress at the bond interface. In contrast, other glass-based TRMs (GS75 and GS100) appear to show better performance with an increase in mortar age, both under the control and the FT conditions. This observation finds that both conditions have an adverse effect on the glass-based TRM when the bond length is equal to or less than the effective bond length (50 mm based on section 5.2.2), where the load slip curve is flattened by increasing the number of cycles. However, the development length in tension does not decrease for longer embedded lengths (75 and 100 mm), as the load-slip curves increase after 360 FT cycles.

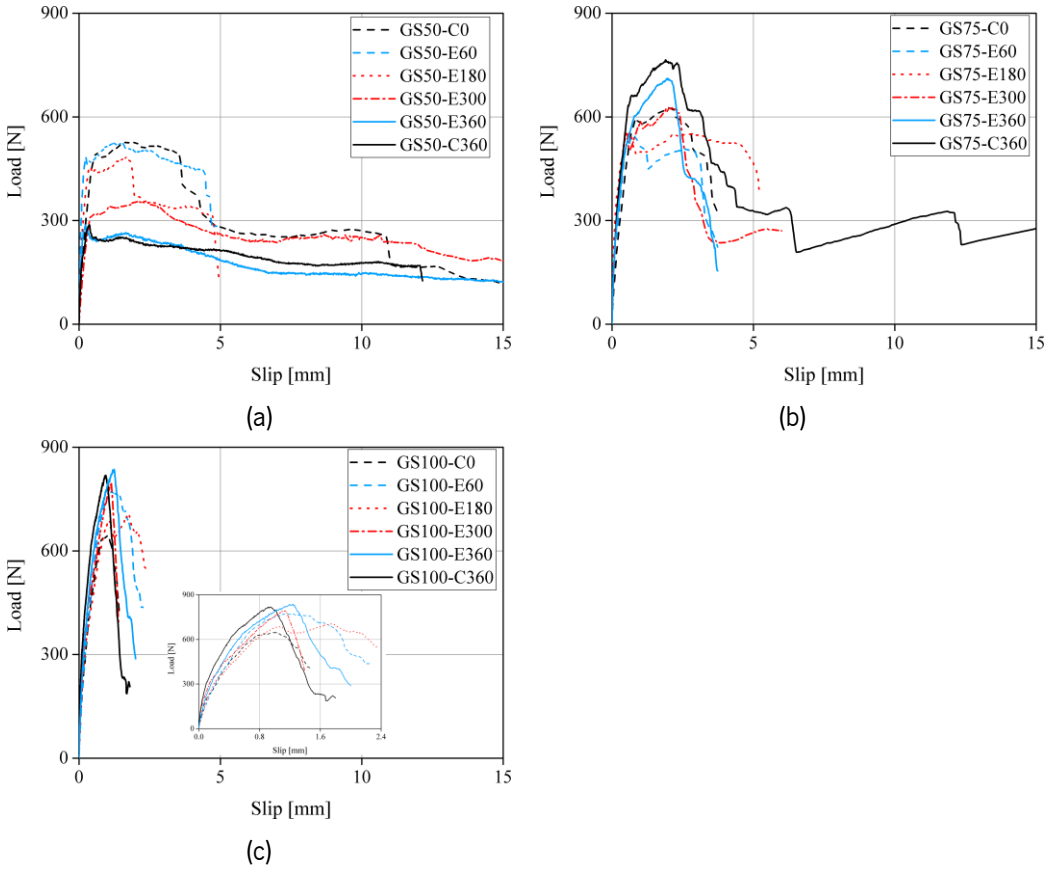

Fig. 5-52. Load-slip response of single glass fibers in different bond lengths: (a) 50 mm; (b) 75 mm; (c) 100 mm.

Fig. 5-53 shows the key parameters of the individual pull-out specimens with the regression line to show the general behavior of the glass-based TRM under the FT conditions. Since tensile rupture occurs at the peak load in GS75 and GS100 specimens, Epo is not presented for these specimens. In addition, Table

5-27 presents the difference between the FT and the control samples after 360 cycles with respect to the control conditions (C0) for a better analysis. The results show that the pull-out parameters of the GS50 specimens decrease under both conditions, compared to the GS75 and GS100 specimens showing an increase in the bond parameters. Due to the same decrease in pull-out parameters of GS50 specimens under both conditions, the proposed FT condition does not affect the bond behavior. Instead, it seems that a sort of bond deterioration by forming micro-cracks at the bond interface has occurred. One possible explanation is the negative impact of mortar hydration on the bond behavior of GS50 specimens, which continues until the end of the tests at both conditions (see section 4.5.1). This negative effect can manifest in the form of chemical shrinkage or notching of the yarn surface due to the formation of precipitates [161]. Future studies need to explore this output more thoroughly. On the other hand, the mortar hydration does not affect the pull-out parameters of GS75 and GS100 specimens, which can be due to the longer embedded length of these specimens than GS50 specimens.

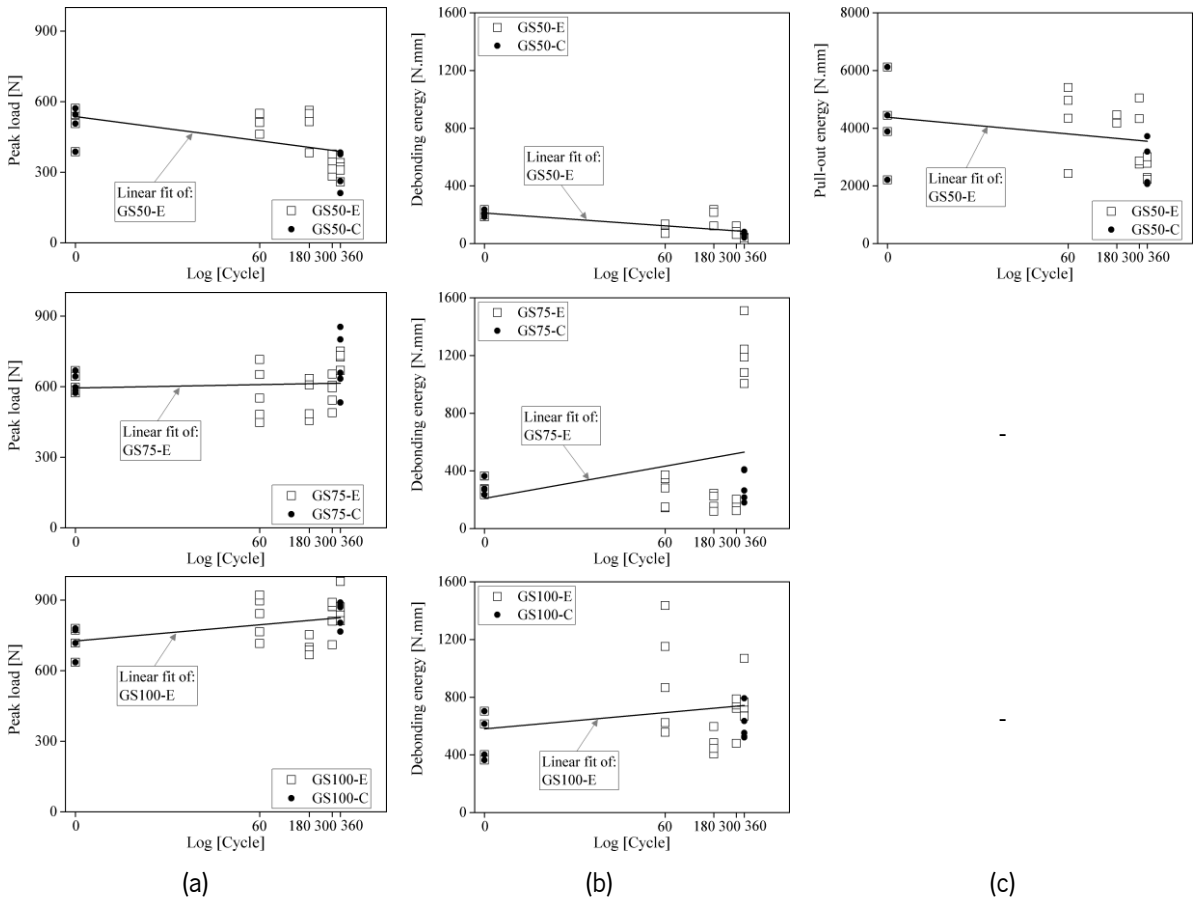

Fig. 5-53. Pull-out parameters of single glass-based TRM in different bond lengths: (a) peak load; (b) debonding energy; (c) pull-out energy.

Table 5-27. Changes of bond properties in glass-based TRM with different embedded lengths and under FT conditions*.

Embedded length [mm]	Name	P_P [N]	$P_P/P_{P,C0}$-1 [%]	E_{deb} [N.mm]	$E_{deb}/E_{deb,C0}$-1 [%]	E_{po} [N.mm]	$E_{po}/E_{po,C0}$-1 [%]	Failure
50	GS50-C0	502 (14)	-	208 (9)	-	4162 (34)	-	slip
	GS50-E60	514 (6)	-	106 (25)	-	4286 (27)	-	slip
	GS50-E180	502 (14)	-	191 (26)	-	4339 (3)	-	slip
	GS50-E300	329 (11)	-	91 (24)	-	3748 (26)	-	slip
	GS50-E360	308 (10)	-39	32 (15)	-85	2574 (13)	-38	slip
	GS50-C360	308 (24)	-39	63 (25)	-70	2776 (25)	-33	slip
75	GS75-C0	613 (6)	-	302 (17)	-	-	-	slip followed by rupture
	GS75-E60	569 (18)	-	258 (37)	-	-	-	slip followed by rupture
	GS75-E180	545 (14)	-	185 (27)	-	-	-	slip followed by rupture
	GS75-E300	577 (10)	-	171 (18)	-	-	-	slip followed by rupture
	GS75-E360	724 (4)	18	1206 (14)	300	-	-	slip followed by rupture
	GS75-C360	697 (17)	13	295 (32)	-2	-	-	slip followed by rupture
100	GS100-C0	723 (7)	-	593 (32)	-	-	-	rupture
	GS100-E60	828 (9)	-	926 (36)	-	-	-	rupture
	GS100-E180	702 (4)	-	483 (15)	-	-	-	rupture
	GS100-E300	831 (8)	-	700 (16)	-	-	-	rupture
	GS100-E360	871 (7)	21	786 (19)	32	-	-	rupture
	GS100-C360	841 (6)	16	605 (17)	2	-	-	rupture

*CoV of the results is given in percentage inside parentheses; P_P: Peak load; E_{deb}: Debonding energy; E_{po}: Pull-out energy.

To compare the behavior of steel and glass-based TRM under FT conditions, the results of SS50-E and GS50-E with equal bond lengths are selected. Generally, the steel-based TRMs (SS50-E) show a better performance than the glass-based TRMs (GS50-E) under the considered FT conditions. Comparing the load-slip curves of GS50 and SS50 specimens confirms this observation. In this way, glass-based TRMs show wide curves at the beginning of exposure, and by increasing the number of FT cycles, they become

narrow and flat. On the other hand, the steel-based TRMs show wide curves at all cycles and only decrease at the end of the exposure. Besides, Fig. 5-54 compares the pull-out parameters of SS50-E and GS50-E specimens, in which standard deviations are presented by the error bar. The results show that the peak load (P_P) and the pull-out energy (E_{po}) of both systems are approximately equal (by considering the error bar). However, the debonding energy (E_{deb}) of SS50-E is higher than the GS50-E one due to the different transitions between the nonlinear and dynamic stages at these specimens.

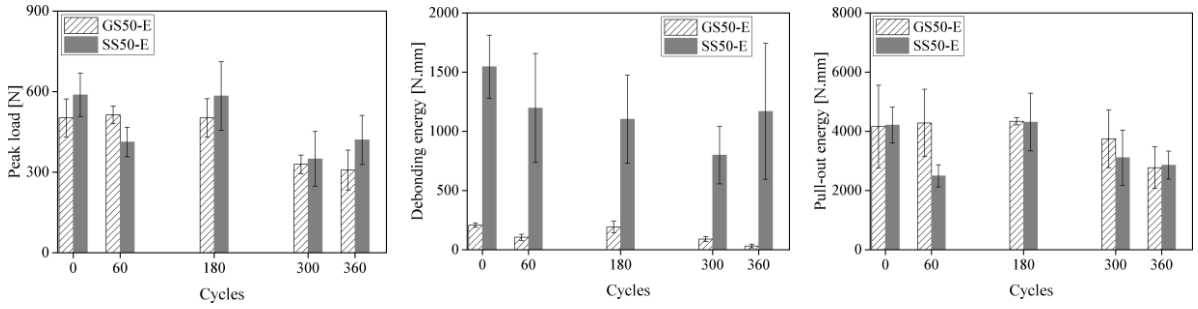

Fig. 5-54. Load-slip response of single glass fibers in different bond lengths: (a) 50 mm; (b) 75 mm; (c) 100 mm.

5.9.6. Steel-based TRM with different fiber configuration

The failure mode of SG150 specimens (with two cords) is generally fiber rupturing under the control and the FT conditions; however, SG150-C0 specimens show fiber slipping, as presented in Table 5-28. Besides, SG′150 specimens (with four cords) fail due to fiber slipping/pull-out under both conditions. The results also show that the failure modes of SG150 and SG′150 do not change from the control to the exposed specimens for the suggested period, like the single steel fiber specimens (SS150). The average load-slip curves of both SG150 and SG′150 specimens are presented in Fig. 5-55. The pull-out response of SG150 specimens includes the linear and nonlinear stages, and by reaching the peak load, the load drops suddenly due to the fiber rupturing. On the other hand, the load-slip curves of SG′150 specimens show a typical pull-out curve.

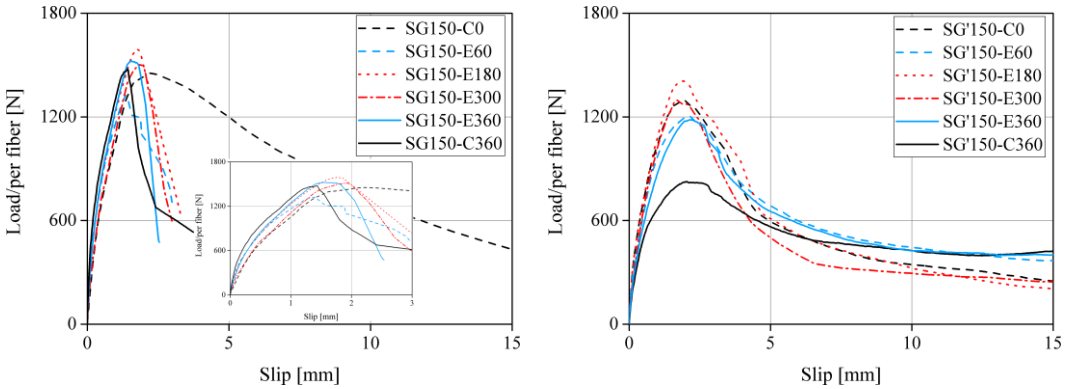

Fig. 5-55. Pull-out response of steel-based TRMs with different configurations and under FT condition: (a) two cords; (b) four cords.

Compared to SS150 specimens, the pull-out response of SG′150 samples (with four cords) shows the load decreasing with a steep slope after peak load under the control and the FT conditions. Increasing the number of fibers results in a decrease in the load carried by each fiber, which is due to the effect of the fiber volume fraction. In addition, the pull-out response of the SG′150-C and SG′150-E specimens decreases by increasing the mortar age or increasing the number of the FT cycles, as shown in Fig. 11. In contrast to SS150 and SG′150, there are no changes from the load-slip curve of the SG150-C to SG150-E specimens.

The pull-out parameters of the individual specimens under the control and the FT conditions are reported in Fig. 5-56, and their average values are presented in Table 5-28. Since tensile rupture occurs at the peak load in SG150 specimens, E_{po} is not presented for these specimens. The results display that the FT condition causes the pull-out parameters to decrease slightly in SG150-E and SG′150-E specimens (although the P_P of the SG150-E increases slightly). Under freeze-thaw conditions, bond parameters decrease less in the group fibers (SG150 and SG′150) than in single fibers (SS150). The difference of the bond parameters between the freezing-thawing exposure (E360) and the control specimens (C0), as well as between C360 and C0 specimens, shows that the FT condition does not affect the bond parameters of SG150 and SG′150 samples (see Table 5-28). Again, the effects of chemical shrinkage on bond degradation can be emphasized further here due to continuing mortar hydration, as shown in section 4.5.1.

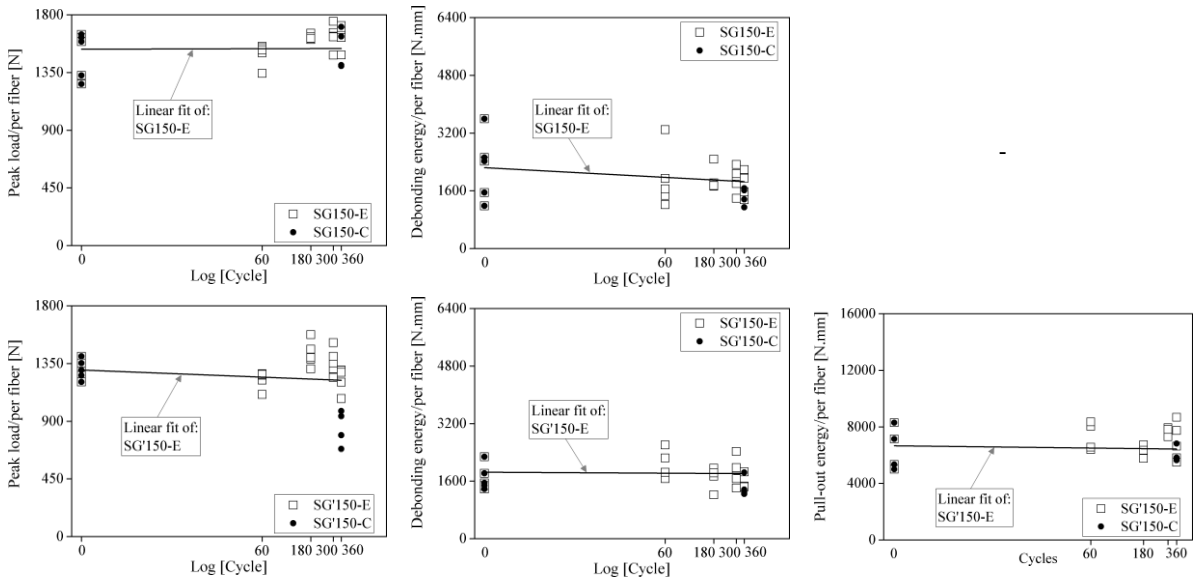

Fig. 5-56. Pull-out parameters of group steel-based TRM composite under FT conditions: (a) peak load; (b) debonding energy; (c) pull-out energy.

Table 5-28. Changes of bond properties in steel-based TRM with different fiber configurations and under FT conditions*.

Fiber configuration [mm]	Name	P_P [N]	$P_P/P_{P,C0}$-1 [%]	E_{deb} [N.mm]	$E_{deb}/E_{deb,C0}$-1 [%]	E_{po} [N.mm]	$E_{po}/E_{po,C0}$-1 [%]	Failure
Two cords	SG150-C0	1489 (11)	-	2253 (37)	-	-	-	slip
	SG150-E60	1494 (5)	-	1915 (38)	-	-	-	rupture
	SG150-E180	1625 (1)	-	1902 (15)	-	-	-	rupture
	SG150-E300	1631 (5)	-	1919 (16)	-	-	-	rupture
	SG150-E360	1627 (5)	9	1832 (17)	-19	-	-	rupture
	SG150-C360	1536 (9)	3	1447 (15)	-36	-	-	rupture
Four cords	SG'150-C0	1304 (5)	-	1700 (19)	-	6442 (21)	-	slip
	SG'150-E60	1225 (5)	-	2019 (18)	-	7176 (12)	-	slip
	SG'150-E180	1427 (6)	-	1721 (15)	-	6280 (6)	-	slip
	SG'150-E300	1364 (7)	-	1884 (18)	-	7683 (4)	-	slip
	SG'150-E360	1231 (7)	-6	1918 (23)	13	6868 (17)	7	slip
	SG'150-C360	848 (14)	-35	1435 (16)	-16	5999 (8)	-7	slip

*CoV of the results is given in percentage inside parentheses; P_P: Peak load; E_{deb}: Debonding energy; E_{po}: Pull-out energy.

5.9.7. Glass-based TRM with different fiber configuration

Fig. 5-57 shows the average load-slip curves of GT50 (with transverse yarns) and GG50 (2 group yarns) specimens under both the control and the FT conditions. In addition, Table 5-29 reports their failure mode. All GT50 specimens fail under yarn slipping/pull-out followed by rupturing. This observation is supported by their load-slip curves, including the linear, nonlinear, and partially dynamic stages. A similar failure mode also is observed for all GG50 specimens, except GG50-C360 failed by tensile rupture when the peak load was reached. A comparison among the load-slip curves of GT50, GG50, and GS50 illustrates the positive effect of transverse elements, so the pull-out curves of GT50 and GG50 do not show load decreasing after peak load (dynamic stage). The load-slip curves of the control specimens (GT50-C and GG50-C) show that the pull-out response improves by increasing the mortar age, in contrast with the GS50-C specimens. Like GS50-E, the FT condition slightly declines the load-slip curves of GT50-E and GG50-E.

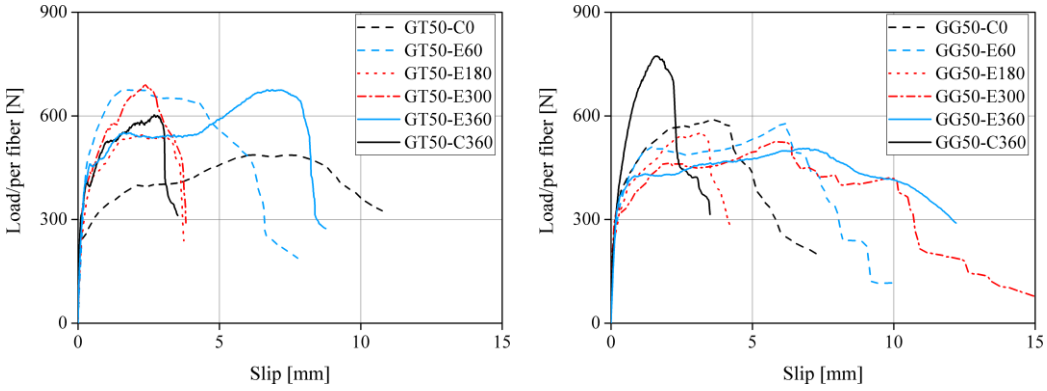

Fig. 5-57. Pull-out response of glass-based TRMs with different configurations and under FT condition: (a) single yarn+ transverse; (b) group yarns.

Table 5-29. Changes of bond properties in glass-based TRM with different fiber configurations and under FT conditions*.

Fiber configuration [mm]	Name	P_P [N]	$P_P/P_{P,C0}-1$ [%]	E_{deb} [N.mm]	$E_{deb}/E_{deb,C0}-1$ [%]	E_{po} [N.mm]	$E_{po}/E_{po,C0}-1$ [%]	Failure
Single yarn+ transverse elements	GT50-C0	273 (17)	-	28 (35)	-	4026 (42)	-	slip
	GT50-E60	717 (10)	-	855 (56)	-	2795 (37)	-	slip
	GT50-E180	573 (11)	-	1041 (39)	-	-	-	slip
	GT50-E300	459 (17)	-	124 (27)	-	2353 (38)	-	slip
	GT50-E360	456 (12)	67	80 (22)	183	4734 (14)	18	slip
	GT50-C360	449 (26)	65	82 (59)	190	1771 (71)	-56	slip
Two group yarns	GG50-C0	642 (8)	-	2252 (34)	-	-	-	slip
	GG50-E60	605 (6)	-	3363 (12)	-	-	-	slip
	GG50-E180	383 (21)	-	71 (51)	-	2073 (44)	-	slip
	GG50-E300	368 (3)	-	44 (21)	-	5268 (6)	-	slip
	GG50-E360	401 (11)	-38	90 (30)	-96	5091 (18)	-	slip
	GG50-C360	796 (13)	24	1085 (30)	-52	-	-	rupture

* CoV of the results is given in percentage inside parentheses; P_P: Peak load; E_{deb}: Debonding energy; E_{po}: Pull-out energy.

The key characteristics of the pull-out response of the individual GT50 and GG50 specimens are presented in Fig. 5-58 (see Table 5-29 for the average of the pull-out parameters at each cycle). Since tensile rupture occurs at the peak load in several GG50 specimens, Epo is not presented for these specimens in Fig. 5-58c. Under the control condition, P_P of the GT50-C and GG50-C shows an incremental trend by increasing the mortar age though other pull-out parameters decline. Besides, a comparison between the GT50-C and GG50-C shows that the key characteristics of GG50-C specimens are higher than the pull-out parameters of GT50-C specimens. This observation reveals that fabric mesh influences the yarn-to-mortar bond behavior more than the single yarn with the transverse elements, even at different mortar ages.

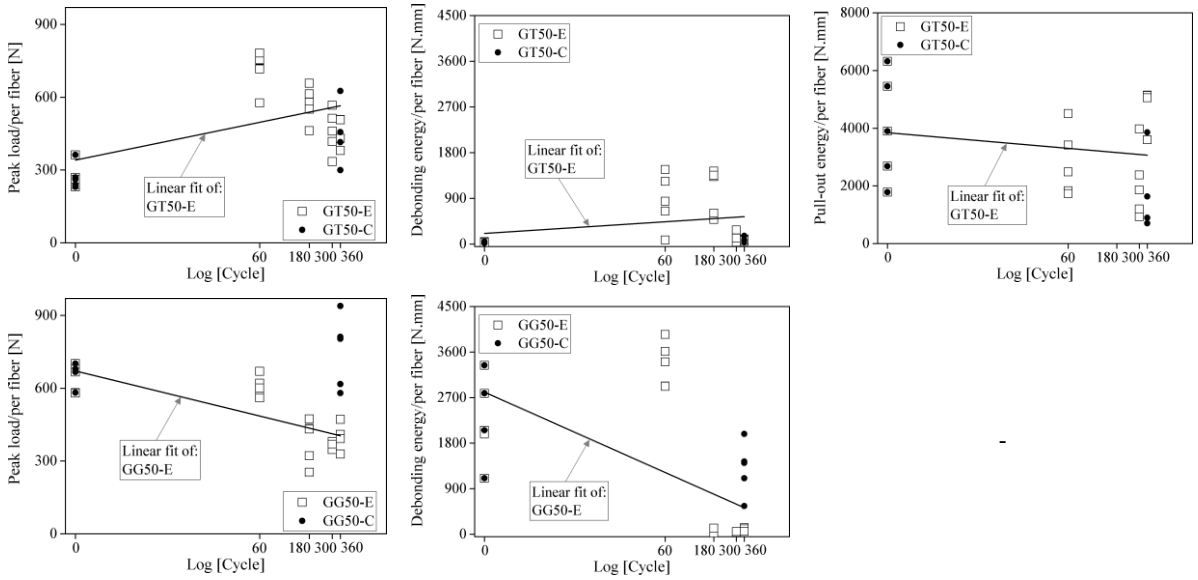

Fig. 5-58. Pull-out parameters of single+ transverse and group glass-based TRM composite under FT conditions: (a) peak load; (b) debonding energy; (c) pull-out energy.

Similar to the single glass-based TRM (GS50), the FT condition decreases the pull-out parameters in GG50-E, as shown in Fig. 5-58. However, GT50 specimens show an increasing trend under the FT conditions. Table 5-29 also presents the difference of the bond parameters between the freezing-thawing exposure (E360) and the control (C0) specimens, as well as C360 and C0 specimens. The outcomes illustrate that under both conditions, the bond properties of GT50 specimens improve. Meanwhile, the outcomes display that the FT conditions lead to a considerable decrement of all pull-out parameters in GG50-E360 specimens, in contrast to GG50-C360. As a result of this observation, it is apparent that glass fabric configuration affects the pull-out response, resulting in different bond behavior under FT conditions. Therefore, studying from single to mesh configurations of this type of fiber is crucial to understanding their behavior better.

5.10. Main conclusions

In this chapter, a comprehensive experimental evaluation of steel and glass-based TRM composites was presented. The pull-out response of TRM composites was investigated and discussed in terms of the test setup, embedded length, fiber configuration, slip rate, and cyclic loading. In addition, the interaction between the curing condition, mortar age effect, real environment effects, and freeze/thaw conditions to mechanical properties of TRM composites was examined. The following conclusions can be drawn from the analysis of the experimental results:

- The results showed that the pull-push test setup when the free length of the fiber was embedded in an epoxy resin (pull-push II setup) was the most reliable test setup and produced the lowest variation of the results (CoVs). In addition, the resin block facilitated the attachment of the LVDTs and prevented the premature failure of the fibers. It was also observed that the gripping of the mortar from the bottom in this configuration could lead to mortar cracking/crushing before performing the tests.
- Steel-based and glass-based TRMs had significantly different effective bond lengths. This value seemed to be in the range of 150 mm to 200 mm in steel-based TRM and in the range of 50 mm to 75 mm in glass-based TRMs used in the current study.
- Increasing the number of steel fibers changed the failure mode from pull-out to pull-out and mortar cracking. Furthermore, transverse elements at the glass-based TRM composites also improved the toughness at the nonlinear stage.
- The slip rate significantly affected bond strengths at low rates, while there was no significant difference in peak loads at faster rates. Similar trends were also observed for absorbed energy and stiffness, confirming the sensitivity to the slip rate in slow tests.
- Cyclic responses were narrow with few unloading-reloading cycles, indicating minimal hysteretic energy dissipation. The strength and stiffness of the pull-out deteriorated upon cycling. There was an effective interaction between fiber yarns in the bidirectional glass mesh, which was much less obvious in the steel fiber cords.
- Comparison of the pull-out and debonding (single-lap) shear tests indicated a significant difference in the obtained load-slip curves and failure modes. This difference, being significant even when the TRM-to-substrate bond was of high quality (when the surface was treated) due to the differences in the boundary conditions and stress distribution in these two test methods. While pull-out tests provided information for characterization of the fabric-to-mortar bond behavior, debonding tests provided information on the reliability of the strengthening system used.
- When the humidity was higher, the pull-out parameters showed an improving trend. The bond properties between TRM and substrate were fundamentally influenced by the water content of bricks. A dry brick could disrupt mortar chemical reactions, while the saturation brick could result in a weak bond between TRM and substrate.
- TRMs cracking behavior was found to be significantly influenced by the mortar type, both in the short and long-term. Indoor TRMs typically demonstrated a lower bond performance than outdoor TRMs. In addition, TRM composites exhibited different tensile behavior and cracking patterns

under indoor and outdoor conditions, which depended on the TRM type. During outdoor conditions, high humidity and rain increased the hydration rates of the hydraulic lime-based mortars, which in turn resulted in a stronger specimen.

- The TRM tensile behavior, the bond behavior at the yarn-to-mortar, and the TRM-to-substrate bond behavior also showed a decreasing trend in some parameters under the FT condition, in contrast to the control specimens at zero cycles.
- The pull-out response of the steel-based TRM with different bond lengths generally declined under both the control and the FT conditions. On the other hand, the glass-based TRM with different embedded lengths showed varied behavior. So that the bond strength deteriorated for 50 mm bond length while for 75 mm bond length, and enhancement of the bond strength was observed.
- Both the control and FT conditions resulted in improved bond performance for reinforced samples with two cords; however, these conditions had a detrimental effect on the reinforced samples with a single cord and four cords. Glass-based TRMs were also found to be influenced by yarn configuration. Under FT conditions, transverse yarn specimens showed enhanced bond behavior, but group yarn specimens exhibited deterioration similar to single yarn samples.

Chapter 6: Mechanical performance of TRM-strengthened masonry panels

The experimental results on the mechanical behavior of TRM-strengthened masonry panels are presented and discussed in this chapter. Accordingly, diagonal compression tests and flexural tests were performed to determine the in-plane behavior of unreinforced and strengthened masonry panels, as discussed in chapter 3. This chapter contains the following highlights:

- The effect of surface treatment on the in-plane and out-of-plane behavior of TRM-strengthened masonry panels is presented and discussed.
- The efficiency of glass-based TRM composites, as a strengthening system, on the mechanical performance of masonry panels is investigated.
- The mechanical behavior of unreinforced and strengthened masonry panels (with and without strengthening systems) under freeze-thaw conditions is presented and discussed.

6.1. Effect of surface treatment

The effect of masonry surface treatment (original surface vs. sandblasted surface) on the in-plane and out-of-plane behavior of TRM-strengthened masonry panels is presented here. Panels are labeled as VXY, where V represents whether the specimen is unreinforced (U) or strengthened (S); X is related to the type of panels (D for Diagonal compression wallets, P for out-of-plane failure parallel to bed joint, and N for out-of-plane failure normal to bed joint, respectively); Y represents the sample surface treatment (O: original brick, S: sandblasted bricks). For example, SPO is a strengthened out-of-plane panel loaded to fail parallel to the bed joints made with the original brick. Section 3.7.3 provides a detailed description of the test methods and procedures.

6.1.1. In-plane behavior

The average load-displacement (vertical and horizontal LVDT measurements) response of the unreinforced and strengthened panels is presented in Fig. 6-1a. The effect of strengthening on the strength of the masonry wallets is considerable (see Table 6-1). The strengthened panels show increases of 3.07 and 3.70 in the peak load in SDO (TRM-strengthened wallets built by original brick) and SDS wallets (TRM-strengthened wallets built by sandblasted brick), respectively, compared to UD specimens (unreinforced wallets). Also, sandblasting of the surface (in SDS) has led to a 19.8 % increment of the shear strength (compared to SDO wallets).

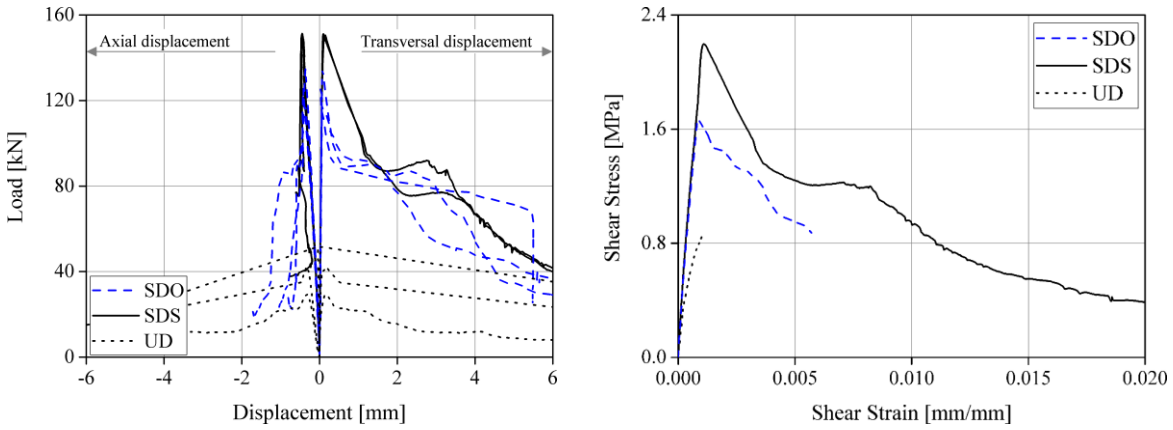

Fig. 6-1. Diagonal compression result: (a) load-displacement curves; (b) average shear stress-strain curves.

In the UD panels (unreinforced panels), the failure is brittle and composed of sliding along the mortar joint and cracking in masonry units with no considerable crack development before failure (see cracking

pattern at failure in Fig. 6-2a). While, in the SDO specimens, the TRM composite partially debonded from the masonry substrate before reaching the maximum load (Fig. 6-2b). A slightly different observation was made in the SDS wallets, in which two vertical cracks occur initially in the central region of the TRM composite, followed by tensile rupture of the yarns and further development of axial cracks (Fig. 6-2c). The distance between the cracks varied between 35 mm to 100 mm that is similar to the crack spacing observed in tensile tests (see the result of TC0 in section 5.9.2).

Table 6-1. Diagonal compression test results*.

Specimen	P_{max} [kN]	Failure	τ'_{max} [MPa]	γ_{max} [%]	γ_y [%]	γ_u [%]	$\mu_{diagonal}$	G [MPa]
UD-1	51.64	A	0.78	0.03	0.02	0.03	1.65	3764
UD-2	29.27	A	0.40	0.09	0.04	0.09	2.00	683
UD-3	42.21	B	0.61	0.11	0.05	0.11	2.25	998
average	41.04 (22)	-	0.60 (31)	0.07 (47)	0.04 (40)	0.07 (47)	1.97 (13)	1815 (76)
SDO-1	134.87	D & A	1.92	0.09	0.06	0.15	2.36	2564
SDO-2	117.71	D & A	1.72	0.09	0.06	0.23	4.13	2493
SDO-3	125.53	D & A	1.69	0.09	0.06	0.1	1.73	2148
average	126.04 (6)	-	1.78 (6)	0.09 (2)	0.06 (4)	0.16 (35)	2.74 (37)	2402 (8)
SDS-1	150.62	E & C	2.19	0.12	0.07	0.25	3.54	2516
SDS-2	151.39	E & C	2.21	0.11	0.07	0.24	3.38	2461
average	151.01 (0)	-	2.20 (1)	0.11 (3)	0.07 (2)	0.24 (1)	3.46 (2)	2488 (1)

*CoV of the results is given in percentage inside parentheses. A: combined sliding along mortar joint and cracking in the masonry units; B: sliding along mortar joint; C: cracking in the masonry units; D: TRM failure with debonding between TRM and the masonry; E: TRM failure.

(a) (b) (c)

Fig. 6-2. Diagonal compression failure mode: (a) UD; (b) SDO; (c) SDS.

In diagonal compression tests, the shear stress (τ') and strain (γ) in the center of the panels can be calculated according to ASTM- E 519-02 [184]. The shear stress (τ') can be expressed as:

$$\tau' = \frac{P\cos\theta}{A_n} \qquad \text{Eq. 6-1}$$

P and θ are the applied load and the angle between the bed joint and the main diagonal of the wallet, respectively. A_n, which is equal to 5400 mm^2, is the net area of the specimen calculated as follows:

$$A_n = \left(\frac{L' + H_w}{2}\right) t.n' \qquad \text{Eq. 6-2}$$

where L′, H_w, and t are the length, the height, and the thickness of the panel, respectively, and are equal to 540 mm, 540 mm, and 100 mm. n' is the percentage of the gross area of the unit that is solid, expressed as a decimal. The shear strain (γ) is calculated as follows:

$$\gamma = \frac{\Delta_v + \Delta_h}{L_g} \qquad \text{Eq. 6-3}$$

Δ_v, Δ_h, and g are the axial shortening, the transversal extension, and the axial gauge length, respectively. The average shear stress-strain curves of each series, obtained from the above formulations, are plotted in Fig. 6-1b. In addition, Table 6-1 reports the maximum shear stress (τ'_{max}) and its corresponding strain (γ_{max}), as well as the pseudo-ductility ratio ($\mu_{diagonal} = \gamma_u / \gamma_y$) and the shear modulus (G) of each specimen, which are the main parameters characterizing the shear behavior of the masonry wallets [220]. In this study, γ_u is the ultimate shear strain corresponding to a 20 % strength drop on the post-peak softening branch of the shear stress-strain curve [134,220–222]. γ_y is introduced as the shear strain at 75 % of the maximum shear stress [23,133,220,223]. Since the IU specimens show a brittle response, γ_u is considered equal to γ_{max} to calculate the pseudo-ductility ratio. Furthermore, G is defined as the secant modulus between 5% and 30% of the maximum shear stress [20,224].

A comparison between the UD and the strengthened wallets (SDO and SDS) illustrates that strengthening with TRM composites leads to a significant increment of all the parameters mentioned above, as shown in Table 6-1, which is also in line with previous studies [25,133,134,144]. Sandblasting of the masonry surface seems to have a significant effect on controlling the failure mode and, consequently, the mechanical performance of the strengthened wallets. From Table 6-1, τ'_{max}, γ_{max}, and μ of the SDS panels are 1.24, 1.22, and 1.26 times higher than for SDO wallets, respectively; however, sandblasting does not seem to have a significant influence on the shear modulus (G). This observation was expected as bond delamination in SDO panels occurred at later stages of the tests in this case.

Casacci et al. [134] also investigated the in-plane behavior of unreinforced and strengthened masonry panels using a similar TRM system as strengthening material. The panels were tested at 60 days' age, and the curing condition of TRM composite was 30 days in the laboratory environmental condition. The maximum shear strength of IU and reinforced wallets (strengthened at both sides) were 0.18 MPa and 0.87 MPa, respectively, while these values for UD and SDO panels tested in the present study are

significantly high (0.6 MPa and 1.78 MPa, respectively). These differences seem to highlight the significant and simultaneous effects of age and curing conditions on the in-plane behavior of panels constructed and strengthened using lime-based mortars.

6.1.2. Out-of-plane behavior

Fig. 6-3 shows the load-displacement curves and Fig. 6-4 failure modes of the panels with failure parallel (P) and normal (N) to the bed joint under out-of-plane loading. In both unreinforced wallet types (UP and UN), a sudden and brittle failure of masonry after the peak load was observed. In UP, a single crack across the panel and along the bed joint was formed (Fig. 6-4a), whereas, in UN wallets, the cracks initiated in the head joint and progressed around the units in alternate courses (Fig. 6-4b).

The failure mode of strengthened wallets is also sudden and occurs once the load reaches the tensile strength of the textile but at a much larger displacement and load capacity, as can be seen in Fig. 6-3a and Fig. 6-3b. The number of cracks for SP and SN (strengthened wallets with failure parallel and normal to bed joint, respectively) is two and one wide cracks, respectively, formed in the TRM composites at the constant moment region. Like unreinforced wallets, the SP wallets failed at the masonry bed joint (Fig. 6-5a), while the SN wallets failed through the masonry units (Fig. 6-5b), meaning that the presence of TRM composite influenced the failure mode of the NS wallets compared to the UN wallets. In contrast to diagonal compression wallets, no TRM-to-masonry detachment was observed in any of these wallets (with and without sandblasting). This behavior can be due to the differences in the stress states in the system compared to the in-plane tests. The average distance between cracks is 125 mm and 113 mm for SPO and SPS, respectively, slightly larger than the crack spacing observed in TRM tensile tests (see the result of TC0 in section 5.9.2). This difference can be due to the difference in the load application and boundary conditions in these two test methods.

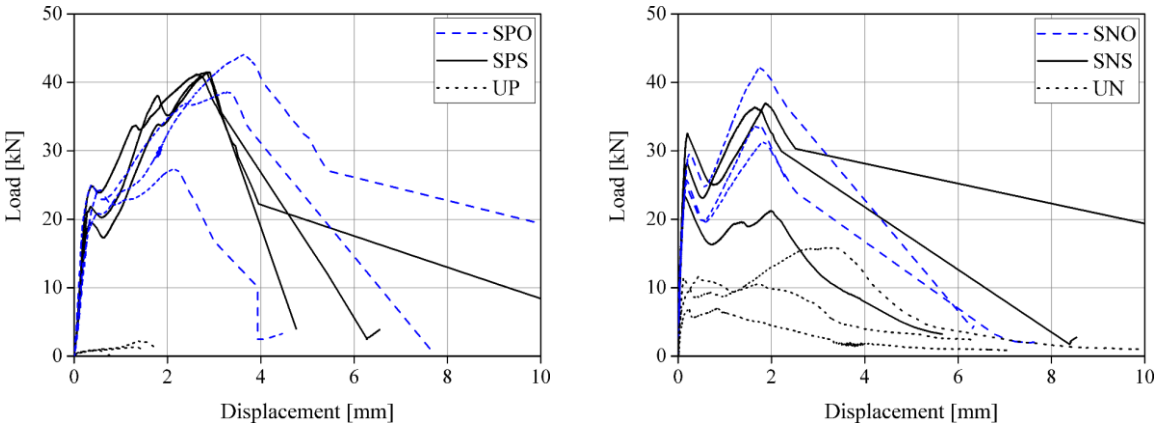

(a) (b)

Fig. 6-3. Load-displacement curves of the specimens tested under flexure tests: (a) failure parallel to bed joint; (b) failure normal to bed joint.

(a) (b)

Fig. 6-4. Failure mode of unreinforced flexural panels: (a) UP; (b) UN.

(a) (b)

Fig. 6-5. Failure mode of TRM-strengthened flexural panels: (a) SP; (b) SN.

Table 6-2 reports the main results of the out-of-plane behavior of the wallets tested parallel to the bed joint in terms of the cracking load (P_{cr}) and its corresponding deflection (Δ_{cr}), as well as the maximum load

(P_{max}) and its corresponding deflection (Δ_{max}). It can be observed that the application of the glass-based TRM system leads to a significant enhancement of the flexural strength of the panels (37 and 41 times for SPO and SPS, respectively). The deformation capacity of the system is also increased significantly. This parameter can be quantified through the definition of a ductility parameter ($\mu_{bending}$) as follows [144,225]:

$$\mu_{bending} = \frac{1}{2}\left(\frac{E_{max}}{E_{cr}} + 1\right) \quad \text{Eq. 6-4}$$

where E_{max} is the area under the load-displacement curve until the maximum load (P_{max}) and E_{cr} is the area until the cracking load (P_{cr}). It can be observed in Table 6-2 that the $\mu_{bending}$ of SPS wallets (sandblasted wallets) is 1.3 times higher than the ductility of the SPO wallets (wallets with no surface treatment). The role of TRM composite in improving the bending behavior of wallets is also significant in wallets tested normal to the bed joints (see Table 6-2). The maximum load is 3.3 and 2.9 times increased in SNO and SNS, respectively, compared with UN wallets. Sandblasting of the bricks does not show a considerable effect on the out-of-plane behavior. The ductility parameter, however, is higher by 14% in SNS in contrast to SNO.

The orthogonal strength ratio (OSR), a parameter about the anisotropy degree of masonry, is equal to the ratio of the gross area modulus of rupture (R) parallel to bed joints (R_P) to that of normal to bed joints (R_N) [138]. According to ASTM E518 [226], R is expressed as follows:

$$OSR = \frac{R_P}{R_N}, R = \frac{\left(P_{max} + 0.75P_s\right)L_s}{b_m t^2} \quad \text{Eq. 6-5}$$

in which P_s and L_s are the specimen weight and outer span length (420 mm). b_m and t correspond to the width and thickness of the panel (b_m= 420 for SP panels and 330 mm for SN panels). Since wallets are tested in the vertical position, the effect of self-weight on the flexural tensile strength is considered to be zero (P_s= 0). Table 6-2 shows that the OSR for URM wallets is equal to 9.5, which indicates the URM wallets have a high anisotropy degree. Nevertheless, for the SPO and SPS wallets, it is found to be 1.24 and 0.97, respectively, showing that the TRM composite has a crucial role in significantly decreasing the anisotropy degree.

Table 6-2. Flexural test results*.

Failure mode	Specimen	Δ_{cr} [mm]	P_{cr} [kN]	Δ_{max} [mm]	P_{max} [kN]	M_{max} [kN.m]	E_{cr} [kN.mm]	E_{max} [kN.mm]	$\mu_{bending}$	R [MPa]	OSR
Failure parallel to bed joint	UP-1			1.39	2	0.14	-	1.56	-	0.22	-
	UP-2			0.50	1	0.06	-	0.34	-	0.10	-
	UP-3			1.24	1	0.08	-	1.08	-	0.13	-
	average	-	-	1.05 (37)	1 (34)	0.09 (34)	-	0.99 (50)	-	0.15 (34)	9.50
	SPO-1	0.55	24.37	2.14	27.39	1.71	8.21	46.53	3.33	2.74	-
	SPO-2	0.38	24.97	3.29	38.75	2.42	6.24	99.14	8.44	3.87	-
	SPO-3	0.52	21.47	3.65	44.06	2.75	7.30	110.04	8.04	4.41	-
	average	0.48 (15)	23.60 (6)	3.02 (21)	36.73 (19)	2.30 (19)	7.25 (11)	85.23 (33)	6.60 (35)	3.67 (19)	1.24
	SPS-1	0.36	24.87	2.91	41.49	2.59	5.28	92.43	9.26	4.15	-
	SPS-2	0.36	19.46	2.83	41.37	2.59	4.23	77.26	9.64	4.14	-
	SPS-3	0.35	21.85	2.70	40.92	2.56	4.27	77.67	9.59	4.09	-
	average	0.36 (1)	22.06 (10)	2.81 (3)	41.26 (1)	2.58 (1)	4.59 (11)	82.45 (9)	9.49 (2)	4.13 (1)	0.97
Failure normal to bed joint	UN-1	0.23	7.03	0.85	6.98	0.44	1.14	5.00	2.70	0.89	-
	UN-2	0.43	11.61	3.25	15.87	0.99	3.74	39.37	5.76	2.02	-
	UN-3	0.11	11.50	1.76	10.63	0.66	0.71	16.34	12.06	1.35	-
	average	0.26 (51)	10.04 (21)	1.95 (51)	11.16 (33)	0.70 (33)	1.86 (72)	20.24 (71)	6.84 (57)	1.42 (33)	-
	SNO-1	0.19	25.86	1.86	31.35	1.96	3.31	44.81	7.28	3.99	-
	SNO-2	0.17	25.29	1.67	33.70	2.11	3.03	41.16	7.29	4.29	-
	SNO-3	0.25	29.60	1.77	42.14	2.63	5.16	54.53	5.78	5.36	-
	average	0.20 (18)	26.92 (7)	1.76 (4)	35.73 (13)	2.23 (13)	3.83 (25)	46.83 (12)	6.78 (10)	4.55 (13)	-
	SNS-1	0.20	32.56	1.88	36.95	2.31	4.36	54.20	6.71	4.70	-
	SNS-2	0.19	28.25	1.64	36.39	2.24	3.49	45.91	7.08	4.63	-
	SNS-3	0.14	23.33	1.98	21.23	1.33	2.04	37.05	9.56	2.70	-
	average	0.18 (13)	28.05 (13)	1.83 (8)	31.52 (23)	1.97 (23)	3.30 (29)	45.72 (15)	7.78 (16)	4.01 (23)	-

*CoV of the results is given in percentage inside parentheses.

6.2. Effect of freeze-thaw conditions

The effect of freeze-thaw conditions on the structural behavior of unreinforced and TRM-strengthened masonry panels is discussed here. Panels are labeled as VXYZ, where V represents whether the specimen is unreinforced (U) or strengthened (S); X is related to the type of panels (D for Diagonal compression wallets, P for out-of-plane failure parallel to bed joint, and N for out-of-plane failure normal to bed joint, respectively); Y represents whether the sample is a control specimen (C) or it was exposed to freeze-thaw conditions (E), and Z shows the number of cycles. For example, SPE360 is a strengthened out-of-plane panel loaded to fail parallel to the bed joints and was exposed to 360 FT cycles.

6.2.1. In-plane behavior

The most common failure mode for unreinforced panels (UD) under both the control and FT conditions is the sliding along with the mortar joint, and in a small number of cases, the sliding along the mortar joint is combined with cracking in the masonry units, as presented in Table 6-3 and Fig. 6-6a. As for the strengthened panels (SD), the failure is as follows: forming two vertical cracks in the center of the TRM composite, rupturing yarns under tensile, followed by developing the axial cracks (Fig. 6-6b). Besides, there is no debonding between the TRM composite and the substrate under the control and the FT conditions due to using sandblasted bricks and compatible materials (the brick and the mortar M1) with equal CTE.

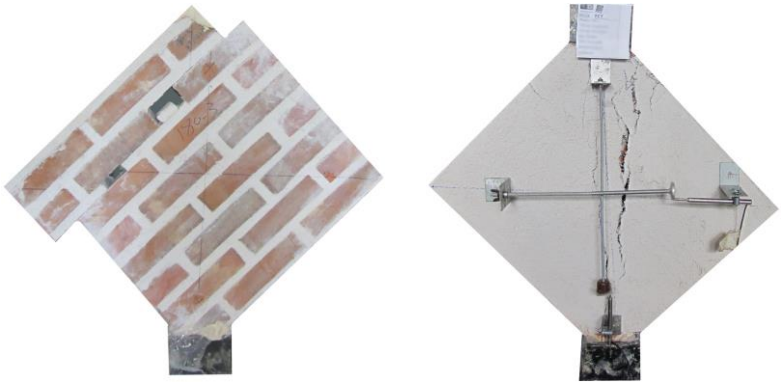

(a) (b)

Fig. 6-6. Diagonal compression failure mode under the control and FT conditions: (a) UD panels; (b) SD panels.

The average load-displacement (vertical and horizontal LVDT measurements) response of the unreinforced and strengthened panels is presented in Fig. 6-7. Also, Fig. 6-8 shows the average shear stress-strain curve of each series calculated according to ASTM- E 519-02 [184]. Reinforced masonry panels exhibit identical load-displacement curves under the control and the FT conditions, including linear, nonlinear until reaching a peak load, and then a decrease in load. Under both conditions, the curves of unreinforced panels only include linear and nonlinear parts. Based on this observation, the control and FT conditions do not affect the in-plane response (the shape of load-displacement curves) of reinforced and unreinforced panels (see Fig. 6-7). However, the shear stress-strain curves show that the diagonal tension strength of reinforced and unreinforced panels (SDE360, SDC360, UDE360, and UDC360) decreases under the control and the FT conditions in contrast to the panels at zero cycles (SDC0 and UDC0), as shown in Fig. 6-8.

The main characteristics values of the in-plane response are summarized in Table 6-3. Compared with unreinforced panels at zero cycles (UDC0), UDC360 and UDE360 panels show a significant decline in τ'_{max} by 70% and 62%, respectively. These values for G are 93% and 82%, respectively. Whereas γ_{max} increases considerably and $\mu_{diagonal}$ stays almost constant, as presented in Table 6-3. These results contrast with the changes in the mechanical properties of the brick and the mortar M3 under both conditions. It would seem that the mortar-to-brick bond (at the bed and head joints) is the factor reducing the in-plane behavior of the unreinforced masonry panels.

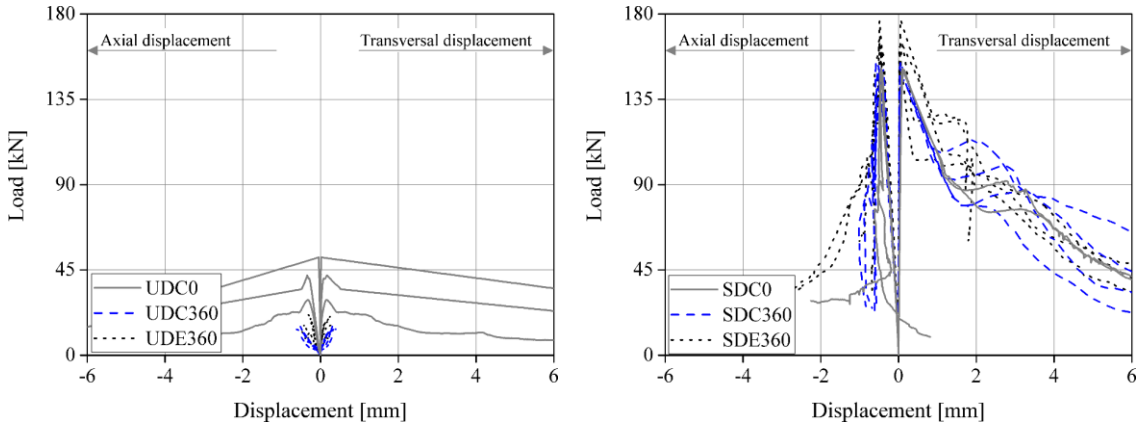

Fig. 6-7. Load-displacement curves of the diagonal compression tests under the control and the FT conditions: (a) UD panels; (b) SD panels.

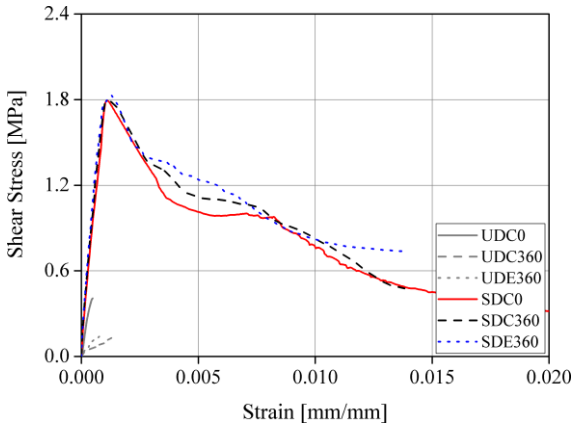

Fig. 6-8. Average shear stress-strain curves of the diagonal compression tests under the control and the FT conditions.

In strengthened panels, the τ'_{max} decreases by 17% and 13% for SDC360 and SDE360 panels under control and FT conditions compared to the strengthened panels at zero cycles (SDC0). However, other in-plane parameters (e.g., γ_{max}, G, and $\mu_{diagonal}$) do not change significantly, as listed in Table 6-3. The FT

conditions do not affect the in-plane behavior of strengthened panels at the test end (SDE360 specimens) and even slightly improve the panels' behavior compared to the SDC360 specimens. It can result from promoting mortar hydration in high humidity conditions present at the proposed FT cycles (90% RH). Accordingly, the obtained results agree with the mechanical behavior and the bond response of the glass-based TRM composite.

Table 6-3. Diagonal compression test results*.

Name	P_{max} [kN]	Failure	τ'_{max} [MPa]	γ_{max} [%]	γ_y [%]	γ_u [%]	$\mu_{diagonal}$	G [MPa]
UDC0-1	51.64	A	0.78	0.03	0.02	0.03	1.65	3764
UDC0-2	29.27	A	0.40	0.09	0.04	0.09	2.00	683
UDC0-3	42.21	B	0.61	0.11	0.05	0.11	2.25	998
Average	41.04 (22)	-	0.60 (31)	0.07 (47)	0.04 (40)	0.07 (47)	1.97 (13)	1815 (76)
UDC360-1	13.73	B	0.1835	0.16	0.10	0.16	1.51	160
UDC360-2	10.13	B	0.1351	0.19	0.12	0.19	1.57	92
UDC360-3	13.63	B	0.1830	0.20	0.12	0.20	1.70	135
UDC360-4	15.27	B	0.2051	0.17	0.11	0.17	1.53	128
Average	13.01 (14)	-	0.18 (14)	0.18 (9)	0.11 (6)	0.18 (9)	1.58 (5)	129 (19)
UDE360-1	12.08	B	0.21	0.14	0.06	0.14	2.47	275
UDE360-2	18.01	B	0.24	0.10	0.05	0.10	1.99	340
UDE360-3	21.38	B	0.29	0.13	0.06	0.13	2.35	470
UDE360-4	13.54	B	0.18	0.16	0.09	0.16	1.69	195
Average	17.64 (30)	-	0.23 (17)	0.13 (15)	0.06 (26)	0.13 (15)	2.12 (14)	320 (31)
SDC0-1	150.62	E & C	2.19	0.12	0.07	0.25	3.54	2516
SDC0-2	151.39	E & C	2.21	0.11	0.07	0.24	3.38	2461
Average	151.01 (0)	-	2.20 (1)	0.11 (3)	0.07 (2)	0.24 (1)	3.46 (2)	2488 (1)
SDC360-1	154.44	E & C	1.84	0.13	0.06	0.24	3.80	2309
SDC360-2	151.09	E & C	1.90	0.09	0.06	0.23	3.71	2303
SDC360-3	145.64	E & C	1.77	0.11	0.06	0.27	4.30	1905
SDC360-4	148.88	E & C	1.81	0.13	0.07	0.25	3.79	2226
Average	148.54 (2)	-	1.83 (3)	0.11 (15)	0.06 (3)	0.25 (6)	3.90 (6)	2186 (8)
SDE360-1	162.99	E & C	1.76	0.12	0.07	0.28	4.15	2098
SDE360-2	176.28	E & C	2.08	0.11	0.07	0.23	3.53	2582
SDE360-3	161.22	E & C	1.92	0.09	0.05	0.16	3.04	2453
SDE360-4	167.92	E & C	1.91	0.11	0.06	0.16	2.46	2459
Average	168.48 (4)	-	1.92 (6)	0.11 (11)	0.06 (9)	0.21 (24)	3.30 (19)	2398 (8)

*CoV of the results is given in percentage inside parentheses. A: combined sliding along mortar joint and cracking in the masonry units; B: sliding along mortar joint; C: cracking in the masonry units; E: TRM failure.

6.2.2. Out-of-plane behavior

Fig. 6-9 illustrates the failures of the out-of-plane panels. All unreinforced panels (UP and UN) show a brittle behavior and fail suddenly by reaching the peak load. A single crack crossing the panel develops in both the UP and UN specimens, except that in the UP panels, it occurs along the bed joint, but in the UN panels, it occurs around the units in alternate courses, as presented in Fig. 6-9.

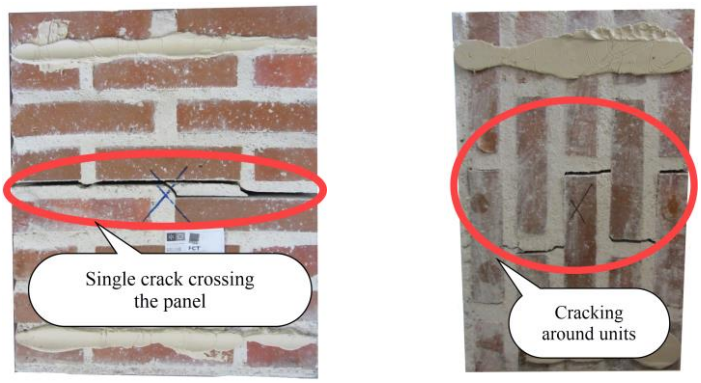

(a) (b)

Fig. 6-9. Out-of-plane failure mode: (a) UP panels; (b) UN panels.

Strengthened wallets (SP and SN) fail suddenly by reaching load to the tensile strength of the glass fibers at the constant moment region (Fig. 6-10). Two wide cracks occur in the SP panels in the TRM composite, and then panels fail at the masonry bed joint like the UP panels, as presented in Fig. 6-10a. One wide crack causes SN panels to fail through the masonry units (Fig. 6-10b), which contrasts with the failure of unreinforced panels (UN series). Additionally, no TRM-to-masonry detachment is observed in any of the strengthened panels under the control and the FT conditions. 113 mm, 135 mm, and 125 mm are the average crack spacing for SPC0, SPC360, and SPE360, respectively, which is slightly different from the crack spacing observed in TRM tensile tests (see tensile results in section 5.9.2). This difference can be due to the difference in the load application and boundary conditions in these two test methods.

Fig. 6-11 and Fig. 6-12 illustrate the load-displacement curves of the out-of-plane panels with failure parallel and normal to bed joints, respectively. In addition, Table 6-4 and Table 6-5 present the cracking load and maximum load (P_{cr}, P_{max}), their corresponding deflection (Δ_{cr}, Δ_{max}), ductility ($\mu_{bending}$), and orthogonal strength ratio (OSR), as the main characteristics values of the out-of-plane response.

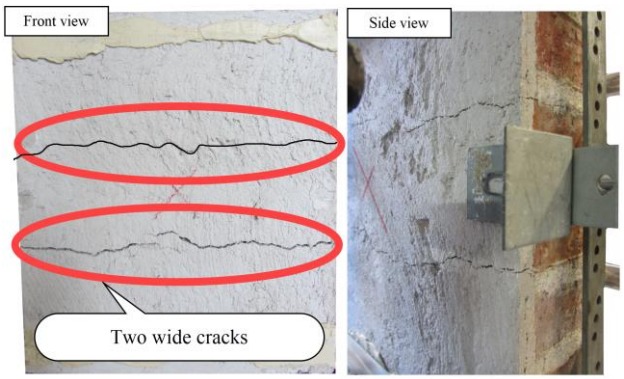

(a)

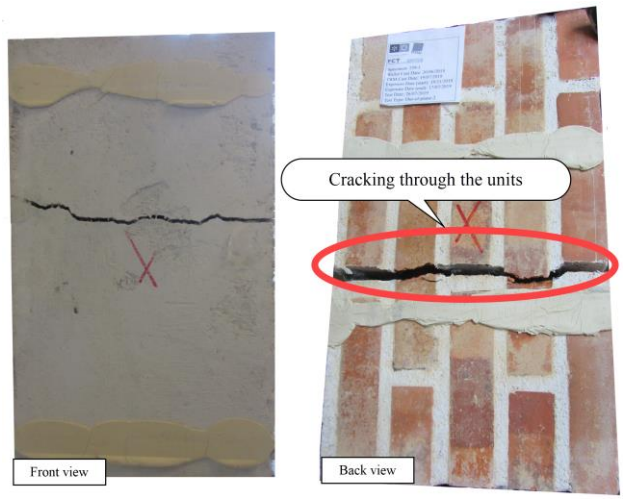

(b)

Fig. 6-10. Out-of-plane failure mode: (a) SP panels; (b) SN panels.

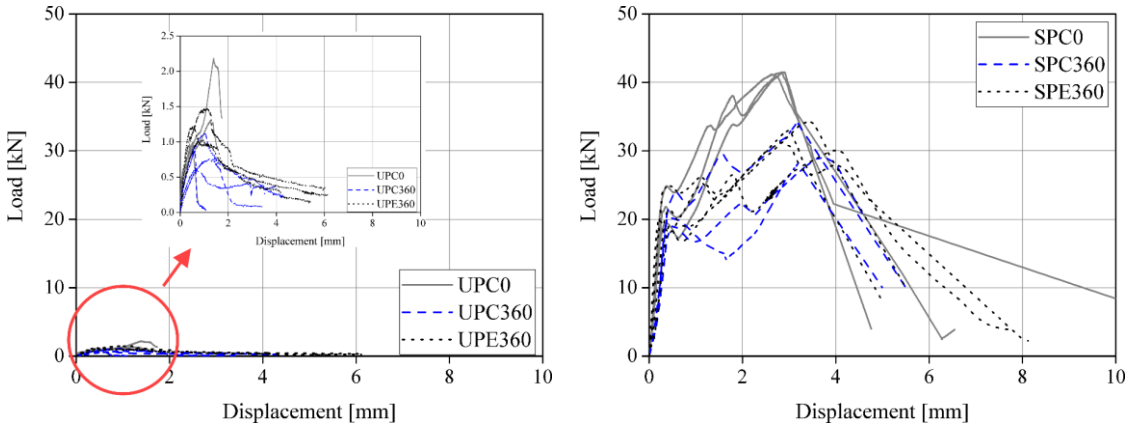

(a) (b)

Fig. 6-11. Out-of-plane response of panels under the control and FT conditions (failure parallel to bed joint): (a) UP; (b) SP.

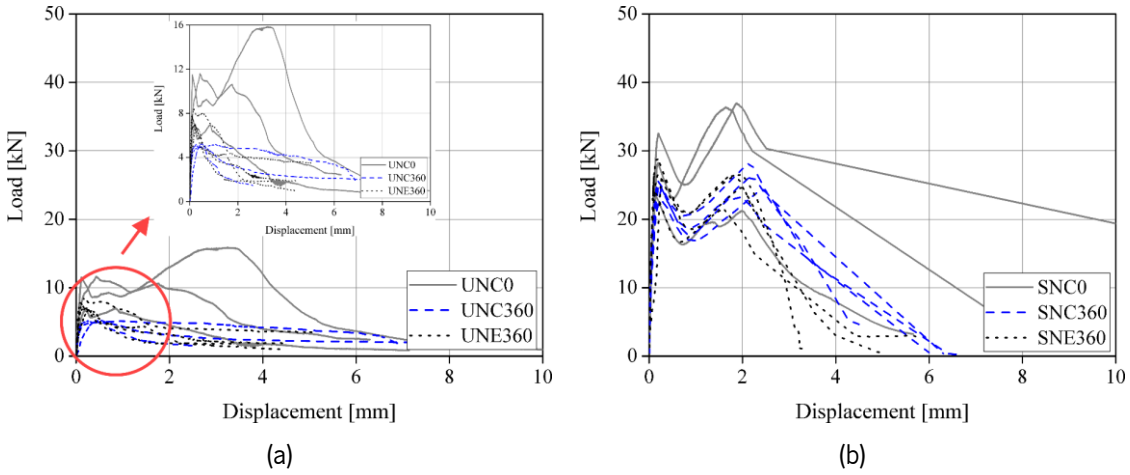

Fig. 6-12. Out-of-plane response of panels under the control and FT conditions (failure normal to bed joint): (a) UN; (b) SN.

According to Table 6-4 and Table 6-5, all out-of-plane parameters of unreinforced panels (for both failure parallel and normal to bed joints) decline under the control and the FT conditions, compared to the panels at zero cycles. This contrasts with the changes in the mechanical properties of the brick and the mortar M3 under both conditions. An influential factor in reducing out-of-plane response can be weakening the bond (at the bed and head joints) between the brick and mortar.

The out-of-plane response of strengthened panels (for both failure parallel and normal to bed joints) decreases under the control and the FT conditions, as presented in Table 6-4 and Table 6-5. This reduction in the out-of-plane response can result from a decline in the TRM composite tensile strength (as discussed in section 5.9.2) and a reduction in the flexural strength of masonry (as discussed in the previous paragraph) under both conditions. Furthermore, comparing the results of strengthened panels in the last stage of the experiment shows that out-of-plane parameters of panels are reduced equally under both conditions. Hence, the FT conditions do not affect reducing the flexural strength of the reinforced panels.

Table 6-4. Bending test results: failure parallel to bed joints*.

Name	Δ_{cr} [mm]	P_{cr} [kN]	Δ_{max} [mm]	P_{max} [kN]	M_{max} [kN.m]	E_{cr} [kN.mm]	E_{max} [kN.mm]	$\mu_{bending}$	R [MPa]	OSR
UPC0-1	-	-	1.39	2.2	0.14	-	1.56	-	0.22	-
UPC0-2	-	-	0.50	1.0	0.06	-	0.34	-	0.10	-
UPC0-3	-	-	1.24	1.3	0.08	-	1.08	-	0.13	-
Average	-	-	1.05 (37)	1.5 (34)	0.09 (34)	-	0.99 (50)	-	0.15 (34)	9.50
UPC360-1	-	-	1.36	0.8	0.05	-	0.72	-	0.08	-
UPC360-2	-	-	1.06	1.1	0.07	-	0.83	-	0.11	-
UPC360-3	-	-	0.63	0.6	0.04	-	0.25	-	0.06	-
UPC360-4	-	-	0.61	0.9	0.06	-	0.34	-	0.09	-
Average	-	-	0.91 (34)	0.9 (21)	0.05 (21)	-	0.53 (46)	-	0.09 (21)	7.7
UPE360-1	-	-	0.51	1.21	0.08	-	0.42	-	0.12	
UPE360-2	-	-	0.76	1.03	0.06	-	0.49	-	0.10	
UPE360-3	-	-	1.00	1.48	0.09	-	1.02	-	0.15	
Average	-	-	0.76 (26)	1.24 (15)	0.08 (15)	-	0.64 (41)	-	0.12 (15)	7.64
SPC0-1	0.36	24.87	2.91	41	2.59	5.28	92.43	9.26	4.15	-
SPC0-2	0.36	19.46	2.83	41	2.59	4.23	77.26	9.64	4.14	-
SPC0-3	0.35	21.85	2.70	41	2.56	4.27	77.67	9.59	4.09	-
Average	0.36 (1)	22 (10)	2.81 (3)	41 (1)	2.58 (1)	4.59 (11)	82.45 (9)	9 (2)	4.13 (1)	0.97
SPC360-1	0.58	24	3.20	34	2.15	8.00	79.74	5.48	3.44	-
SPC360-2	0.47	20	3.20	28	1.76	5.10	57.33	6.12	2.82	-
SPC360-3	0.51	19	3.74	29	1.83	5.15	76.44	7.91	2.92	-
Average	0.52 (9)	21 (10)	3.38 (8)	31 (9)	1.91 (9)	6.09 (22)	71.17 (14)	6.50 (16)	3.06 (9)	1.06
SPE360-1	0.32	24	2.98	33	2.06	4.34	75.05	9.15	3.30	-
SPE360-2	0.44	21	2.87	31	1.95	5.44	64.47	6.42	3.12	-
SPE360-3	0.20	20	3.44	34	2.14	2.26	86.41	19.63	3.42	-
SPE360-4	0.44	19	4.00	30	1.88	4.06	88.99	11.45	3.01	-
Average	0.35 (29)	21 (9)	3.32 (13)	32 (5)	2.01 (5)	4.03 (28)	78.73 (12)	11.66 (42)	3.21 (5)	0.98

*CoV of the results is given in percentage inside parentheses.

Table 6-5. Bending test results: failure normal to bed joints*.

Cycles	Δ_{cr} [mm]	P_{cr} [kN]	Δ_{max} [mm]	P_{max} [kN]	M_{max} [kN.m]	E_{cr} [kN.mm]	E_{max} [kN.mm]	$\mu_{bending}$	R [MPa]
UNC0-1	-	-	0.85	6.98	0.44	-	-	-	0.89
UNC0-2	-	-	3.25	15.87	0.99	-	-	-	2.02
UNC0-3	-	-	1.76	10.63	0.66	-	-	-	1.35
-	-	-	1.95 (51)	11.16 (33)	0.70 (33)	-	-	-	1.42 (33)
UNC360-1	-	-	0.51	5.28	0.33	-	-	-	0.67
UNC360-2	-	-	0.48	4.99	0.31	-	-	-	0.63
UNC360-3	-	-	0.26	5.19	0.32	-	-	-	0.66
Average	-	-	0.42 (26)	5.15 (2)	0.32 (2)	-	-	-	0.66 (2)
UNE360-1	-	-	0.20	6.98	0.44	-	-	-	0.89
UNE360-2	-	-	0.12	7.75	0.48	-	-	-	0.99
UNE360-3	-	-	0.17	8.42	0.53	-	-	-	1.07
UNE360-4			0.24	6.58	0.41	-	-	-	0.84
Average	-	-	0.18 (25)	7.43 (10)	0.46 (10)	-	-	-	0.95 (10)
SNC0-1	0.20	32.56	1.88	36.95	2.31	4.36	54.20	6.71	4.70
SNC0-2	0.19	28.25	1.64	36.39	2.24	3.49	45.91	7.08	4.63
SNC0-3	0.14	23.33	1.98	21.23	1.33	2.04	37.05	9.56	2.70
Average	0.18 (13)	28.05 (13)	1.83 (8)	31.52 (23)	1.97 (23)	3.30 (29)	45.72 (15)	7.78 (16)	4.01 (23)
SNC360-1	0.28	22.57	2.43	24.36	1.52	4.84	47.82	5.44	3.10
SNC360-2	0.26	24.41	2.20	26.16	1.63	4.54	46.88	5.66	3.33
SNC360-3	0.19	25.57	2.15	28.10	1.76	3.52	49.49	7.52	3.58
SNC360-4	0.21	25.07	1.96	23.19	1.45	3.57	39.96	6.10	2.95
Average	0.24 (16)	24.41 (5)	2.18 (8)	25.45 (7)	1.59 (7)	4.12 (14)	46.04 (8)	6.18 (13)	3.24 (7)
SNE360-1	0.14	23.89	1.96	24.62	1.54	2.37	39.23	8.79	3.13
SNE360-2	0.17	28.78	1.82	26.41	1.65	3.50	42.87	6.63	3.36
SNE360-3	0.28	26.21	1.61	21.43	1.34	3.70	31.37	4.74	2.73
SNE360-4	0.21	26.56	1.94	26.52	1.66	4.26	44.92	5.77	3.38
Average	0.20 (27)	26.36 (7)	1.83 (8)	24.75 (8)	1.55 (8)	3.46 (20)	39.60 (13)	6.48 (23)	3.15 (8)

*CoV of the results is given in percentage inside parentheses.

6.3. Main conclusions

The purpose of this chapter was to provide a comprehensive experimental evaluation of the behavior of TRM-strengthened masonry. The effect of surface treatment and exposure to freeze-thaw conditions on the in-plane and out-of-plane behavior of masonry panels strengthened with a glass-based TRM system was investigated. Analyzing the experimental results lead to the following conclusions:

- Sandblasting of the masonry surface resulted in a significantly better bond between the TRM and the masonry substrate and hence better in-plane performance of the strengthened panels. However, this surface treatment did not have a significant effect on the out-of-plane performance of the strengthened panels.
- The application of a glass-based TRM layer on masonry panels had a significant influence on the out-of-plane and in-plane response. There was a significant increase in both load capacity and deformation capacity.
- The crack spacing of the strengthened panels under the diagonal compression tests at failure was similar to the saturated crack spacing observed in the tensile tests. In contrast, the out-of-plane test samples showed a larger crack spacing.
- The in-plane and out-of-plane behavior of the URM panels decreases under the control and the FT conditions. This can be caused by bond degradation at the interface of the bed joints and bricks due to mortar shrinkage and forming micro cracks.
- The strengthened panels showed a few degradations at the tensile stress. The durability of the TRM-strengthened panels under the FT condition was suitable so that their shear and flexural strength did not change.

Chapter 7: Analytical modeling

This chapter proposes a new bond-slip law and analytical model, which can be used to predict the bond behavior of TRM composites considering the slip hardening and softening effects observed in the experimental tests. In addition, the shear and flexural behavior of masonry panels are analytically investigated. In summary, the following outcomes are achieved in this chapter:

- Two different analytical pull-out modeling approaches are used, and their results are compared.
- With the aim of the analytical modeling approaches, bond-slip laws representing the textile-to-mortar bond behavior are extracted. The bond-slip laws are then used to predict the pull-out response of TRM composites.
- The modifications proposed in the bond-slip law allow the prediction of the slip hardening and softening effects in the pullout response of TRM composites.
- The effects of mortar age and freeze-thaw conditions on the bond-slip law parameters are investigated.
- Analytical modeling allows the prediction of saturated crack spacing in TRM composites.
- The shear and flexural strength of the TRM-strengthened masonry panels are analytically computed and compared with the experimental results.

7.1. Bond behavior

7.1.1. Bond-slip laws

In the literature, a variety of approaches have been proposed for simulating pull-out curves or determining the bond-slip laws from experimental pull-out curves, as discussed in section 2.2.3. Various multi-linear or nonlinear [65,66,85] and N-piecewise [84,86] bond-slip laws have been proposed, as shown in Fig. 7-1. In this study, both multi-linear (named method 1 in this study) and N-piecewise (named method 2 in this study) bond-slip laws were used to extract the bond parameters and analytical pull-out load-slip curves.

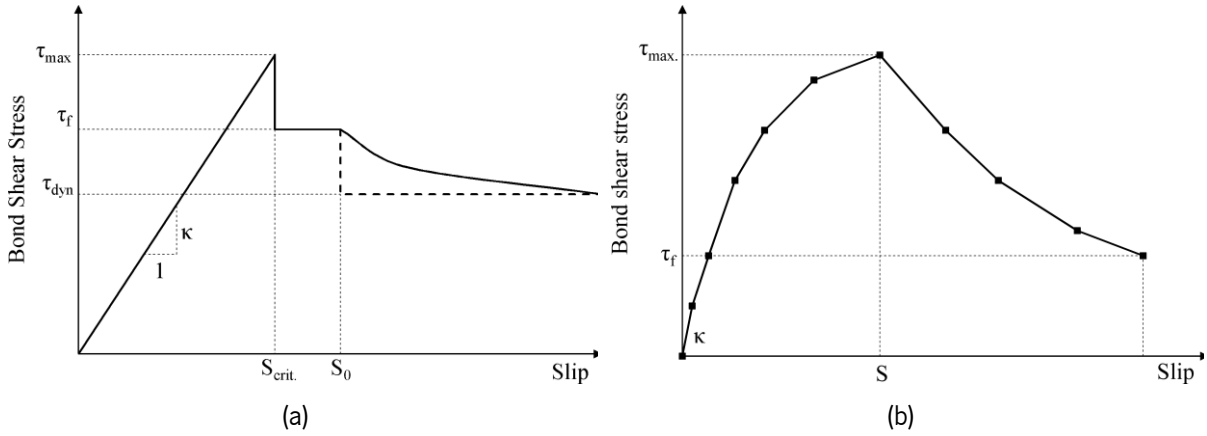

Fig. 7-1. Bond-slip law: (a) multi linear [65,66,85]; (b) N-piecewise [84,86].

7.1.2. Mathematical formulation of Method 1

Analytical modeling of the pull-out response is usually performed following the shear-lag model. In this model, it is assumed that the displacements and the tractions are continuous at the interface, and the slip is obtained from the frictional and the adhesive bond. In addition, it is assumed that sliding along a debonded interface is governed by a constant shear stress τ [227–229] while other models utilize Coulomb's friction law to study this problem [230]. This model has been extensively used for the analysis of pull-out problems in cementitious-based matrices [62,65,66,80,85,231] and is therefore also used in this study.

In this section, the bond-slip law is assumed multi-linear (see Fig. 7-1a) and is obtained indirectly from the experimental pull-out curves. Here, the formulation proposed by Naaman et al. [65,85] is used for the pull-pull test configuration (see appendix II for the details of the formulations). Nevertheless, Namman's formulations are modified here for the pull-push configuration, and the observed differences

are discussed in the next sections. The proposed model is based on the pull-out response observed in experimental results, in which the load-slip curve consists of three linear, nonlinear, and dynamic stages, as mentioned comprehensively in section 2.2.2.

7.1.2.1. Basic equations

The mathematical model of the pull-out behavior based on the stress criterion is expressed by two boundary conditions and a second-order differential equation. The equations are derived from the compatibility requirement and Hooke's law, assuming the mortar behaves as an elastic material [62,65,84]. The free-body diagram of the embedded length of the textile in the matrix, as shown in Fig. 7-2, leads to:

$$F + dF - F - \tau dx \psi = 0 \Rightarrow \frac{dF}{dx} = \tau \psi = t \qquad \text{Eq. 7-1}$$

where F is the local force in the fiber at distance x from the free end of the fiber, ψ is the perimeter of the fiber, τ and t are the shear stress and shear flow at the fiber-matrix interface, respectively. Furthermore, the static equilibrium in the pull-push tests requires that the sum of the local force in the fiber, F, and in the matrix, M, to be equal to zero (Fig. 7-2):

$$F + M = 0 \Rightarrow F = -M \qquad \text{Eq. 7-2}$$

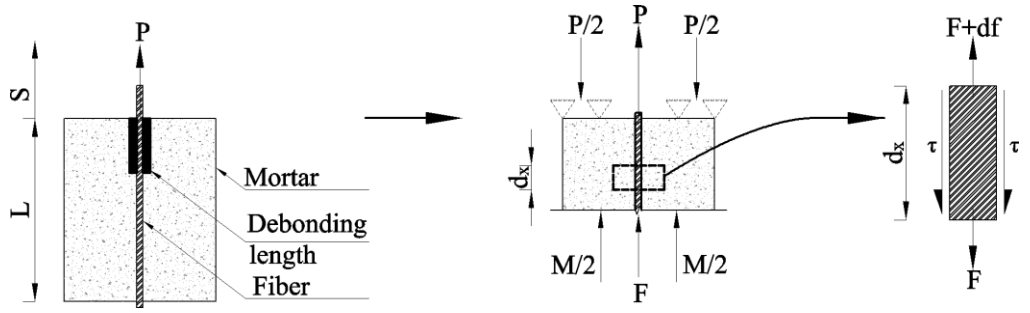

Fig. 7-2. Free-body diagram of a pull-push test, global force equilibrium, and infinitesimal segment of fiber.

According to Hook's law, the local force in the fiber and the matrix can be related to the local strain in the fiber, ε_f, and the mortar, ε_m, as follows:

$$F = A_f E_f \varepsilon_f \Rightarrow \varepsilon_f = \frac{F}{A_f E_f} \qquad \text{Eq. 7-3}$$

$$M = A_m E_m \varepsilon_m \Rightarrow \varepsilon_m = \frac{M}{A_m E_m} \qquad \text{Eq. 7-4}$$

where A is the cross-sectional area and E is Young's modulus. The subscripts f and m refer to the fiber and the matrix, respectively. During the elastic stage, the local shear stress, τ, follows a linear stress-slip relationship (Fig. 7-3a) and is related to the local slip, S, as follows:

$$\tau = \kappa S \qquad \text{Eq. 7-5}$$

where κ is the bond shear modulus (slope of the shear strength diagram in the elastic stage in Fig. 7-3a), and S is defined as:

$$S = \left(\delta_f - \delta_m\right) = \int_0^x \left[\varepsilon_f(x) - \varepsilon_m(x)\right] d_x \qquad \text{Eq. 7-6}$$

δ_f and δ_m are the elongations of the fiber and the matrix, respectively. Substituting Eq. 7-5 and Eq. 2-1 into Eq. 7-1 and taking the differentiation from x leads to:

$$\frac{d^2F}{dx^2} = \psi\kappa\left(\varepsilon_f - \varepsilon_m\right) \qquad \text{Eq. 7-7}$$

By considering Eq. 7-2 and replacing ε_f and ε_m from Eq. 7-3 and Eq. 7-4 in Eq. 2-1, one has:

$$\frac{d^2F}{dx^2} = \psi\kappa FQ \qquad \text{Eq. 7-8}$$

where

$$Q = \frac{1}{A_f E_f} + \frac{1}{A_m E_m} \qquad \text{Eq. 7-9}$$

Eq. 7-8 is a second-order differential equation and can be rewritten as:

$$\frac{d^2F}{dx^2} - \lambda^2 F = 0 \qquad \text{Eq. 7-10}$$

and

$$\lambda = \sqrt{\kappa\psi Q} \qquad \text{Eq. 7-11}$$

The general and particular solution of this nonhomogeneous-second order differential equation is:

$$F = A'e^{\lambda x} + B'e^{-\lambda x} \qquad \text{Eq. 7-12}$$

According to the test mechanism, the force boundary condition is equal to zero at the free end and equal to the applied pull-out load, P, at the loaded end:

$$F_{(0)} = 0 \qquad \text{Eq. 7-13}$$

$$F_{(P)} = L \qquad \text{Eq. 7-14}$$

Imposing these boundary conditions to Eq. 7-12, the force distribution along the embedded length and the interfacial shear flow, $t_{(x)}$, are obtained:

$$F = P\frac{\sinh(\lambda x)}{\sinh(\lambda L)} \qquad \text{Eq. 7-15}$$

$$t = \frac{dF}{dx} = P\lambda\frac{\cosh(\lambda x)}{\sinh(\lambda L)} \qquad \text{Eq. 7-16}$$

The corresponding shear stress can then be derived from Eq. 7-1 and Eq. 2-1:

$$\tau = \frac{P\lambda}{\psi} \times \frac{\cosh(\lambda x)}{\sinh(\lambda L)} \qquad \text{Eq. 7-17}$$

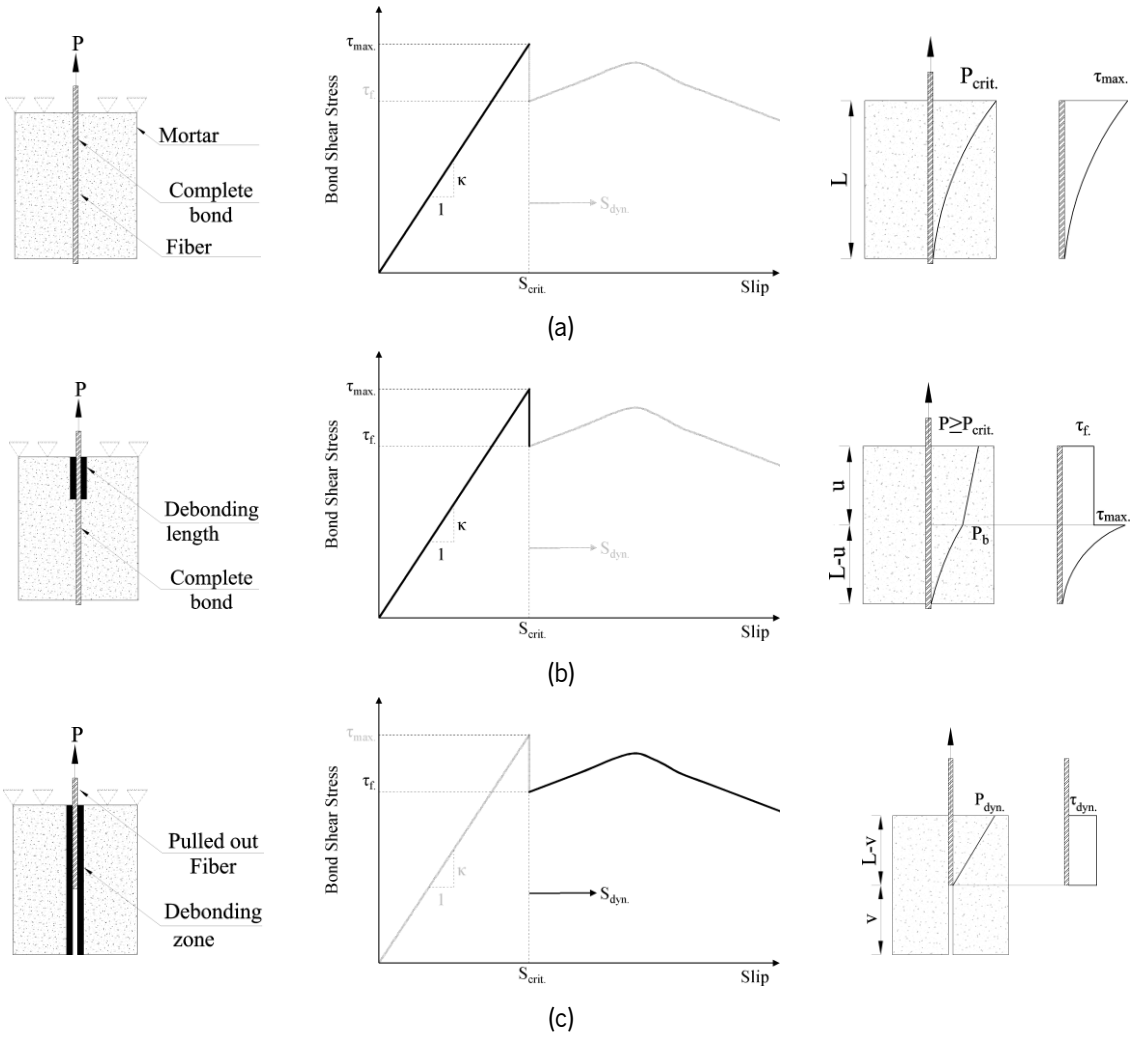

Fig. 7-3. Bond shear stress-slip and force distribution along with the fiber at the different stages: (a) linear; (b) nonlinear; (c) dynamic.

7.1.2.2. Elastic stage

If the shear stress at the interface is less than the maximum bond (shear) strength, τ_{max}, the applied load will be less than the maximum bonded load, and the textile and mortar will be fully bonded (see Fig. 7-3a).

By increasing the load, there will be a critical force, P_{crit}, which causes the shear stress at x=L to be equal to τ_{max}. To find the P_{crit}, the maximum shear stress at x=L is considered:

$$\tau_{max} = \tau_{(x=L)} = \frac{P\lambda}{\psi} \times \frac{\cosh(\lambda L)}{\sinh(\lambda L)} \quad \text{Eq. 7-18}$$

$$P_{crit} = \frac{\tau_{max}\psi}{\lambda} \tanh(\lambda L) \quad \text{Eq. 7-19}$$

The slip at the free end of the fiber can be evaluated by integrating Eq. 7-6 up to x=L:

$$S_{elastic} = \frac{QP}{\lambda \sinh(\lambda L)} \left(\cosh(\lambda L) - 1\right) \quad \text{Eq. 7-20}$$

The slip corresponding to this critical force is obtained by imposing the value of P_{crit} from Eq. 7-19 in Eq. 2-1.

7.1.2.3. Nonlinear stage

When the applied load, P, exceeds P_{crit}, debonding initiates at the loaded end and grows progressively towards the free end [65]. This means two different interfacial zones coexist along with the specimen at this stage. The first one is the debonded zone, in which the interfacial shear stress is equal to the frictional shear strength (or frictional stress, τ_f). The forces resisted in this zone are identified as the debonded force, P_d. The remaining zone is still perfectly bonded, as shown in Fig. 7-3b with the bond force equal to P_b. To satisfy the static equilibrium in the nonlinear stage, for any load larger than P_{crit} and less than the peak load one has:

$$P = P_b + P_d \quad \text{Eq. 7-21}$$

Along the debonded length, u, the normal force distribution in the fiber is linear owing to constant frictional shear strength. This force decreases at the rate of t_f (interfacial frictional shear flow) per unit length:

$$t_f = \tau_f \psi \quad \text{Eq. 7-22}$$

Therefore, P_d can be obtained as:

$$P_d = \tau_f \psi u = t_f u \quad \text{Eq. 7-23}$$

Over the bonded length, L-u, the shear-stress distribution is as explained in the elastic stage, except that the force is $P' = P - t_f \times u$ and the length is L-u, as shown in Fig. 7-3b. For finding the P_b, firstly, the fiber force in the nonlinear stage should be evaluated. In this stage, the force boundary condition is as follows:

$$F_{(x=0)} = 0 \quad \text{Eq. 7-24}$$

$$F_{(x=L-u)} = P - t_f u \quad \text{Eq. 7-25}$$

Imposing these two boundary conditions on Eq. 7-12, the force distribution and the interfacial shear flow are obtained as:

$$F = \left(P - t_f u\right)\frac{\sinh\left(\lambda x\right)}{\sinh\left(\lambda\left(L-u\right)\right)} \quad \text{Eq. 7-26}$$

$$t = \frac{dF_x}{dx} = \left(P - t_f u\right)\frac{\lambda\cosh\left(\lambda x\right)}{\sinh\left(\lambda\left(L-u\right)\right)} \quad \text{Eq. 7-27}$$

The maximum shear flow and the pull-out force in the nonlinear stage are equal to:

$$t_{(max)} = \frac{\left(P - t_f u\right)\lambda}{\tanh\left(\lambda\left(L-u\right)\right)} \quad \text{Eq. 7-28}$$

$$P = \frac{t_{(max)}}{\lambda}\tanh\left(\lambda\left(L-u\right)\right) + t_f u \quad \text{Eq. 7-29}$$

Eq. 2-1 includes two parts: bonded and debonded force. Therefore, the bonded force is:

$$P_b = \frac{t_{(max)}}{\lambda}\tanh\left(\lambda\left(L-u\right)\right) \quad \text{Eq. 7-30}$$

The slip can be obtained in the same way as in Eq. 7-20 considering the bonded and debonded regions as follows:

$$S = Q\left[\int_0^u \left(P - t_f x\right)d_x + \int_0^{L-u} P'\frac{\sinh\left(\lambda x\right)}{\sinh\left(\lambda\left(L-u\right)\right)}d_x\right] \quad \text{Eq. 7-31}$$

$$S_{nonlinear} = \frac{Qu}{2}\left(2P - t_f u\right) + Q\left(P - t_f u\right)\times\frac{\cosh\left(\lambda\left(L-u\right)\right)-1}{\lambda\sinh\left(\lambda\left(L-u\right)\right)} \quad \text{Eq. 7-32}$$

7.1.2.4. Dynamic stage

Once the debonding has occurred along all the embedded length (u=L), the dynamic stage starts. In this stage, with an increment of the rigid body displacement/slip of the fiber/yarn, v, the embedded length decreases to L-v (Fig. 7-3c), which is under frictional stresses [62,65]. The slip of the fiber at the onset of full debonding (S_0) is expressed as:

$$S_0 = \frac{QL^2}{2}t_f \quad \text{Eq. 7-33}$$

As a criterion, the dynamic pull-out slip, S_{dyn}, should be larger than the end slip of the fiber at the onset of full debonding, S_0, and less than the embedded length of the fiber [65]. S_{dyn}, which is equal to the total rigid body movement of the fiber plus the fiber elastic elongation, can be obtained as:

$$S_{dyn} = \frac{Qt_f}{2}\left(L - v\right)^2 + v \quad \text{Eq. 7-34}$$

The pull-out force at the dynamic stage can, therefore, be calculated as [65]:

$$P_{dyn} = \tau_f \psi (L - v) \quad \text{Eq. 7-35}$$

The load obtained from Eq. 7-35 is reduced linearly by increasing the rigid body displacement of the fiber/yarn (v). Namman's model at the dynamic stage was suitable for predicting the slip-softening effect after the peak load. As reported in [65], the pull-out force in the dynamic stage depends on the friction between the fiber and the matrix, the Poisson's effect, and the effect of decay in Misfit (deteriorates and decreases during the fiber pull-out):

$$P_{dyn} = \left(1 - \exp\left\{ \frac{-2\upsilon_f \mu x}{E_f r_f \left[\frac{(1+\upsilon_m)}{E_m} + \frac{(1+\upsilon_f)}{E_f} \right]} \right\} \right) \frac{\delta E_f \pi r_f}{\upsilon_f} \quad \text{Eq. 7-36}$$

where δ is the coefficient of fiber-matrix misfit and x is the embedded length of the fiber. Also, ν_f and ν_m are the Poisson's ratios for the fiber and the mortar, respectively. r_f is fiber radius, and μ is the friction coefficient assumed as 0.06. The formula for obtaining δ can be found in [65].

To determine an equivalent value for the dynamic shear strength, τ_{dyn}, for any given pull-out load in which slip is more than S_0, the following relation is suggested by Naaman et al. [65]:

$$\tau_{dyn} = \frac{P_{dyn}}{\psi L}, S \geq S_0 \quad \text{Eq. 7-37}$$

7.1.2.5. Pull-out simulation

Analytical modeling of the fiber pull-out response consists of a primary and a secondary problem [85]. In the primary problem, the bond-slip relationship is extracted from the experimental pull-out load-slip curves. Three main parameters, namely the peak load, P_P, the corresponding end slip, s_P, and the slope of the initial portion of the curve, P/S, have to be extracted from the pull-out curve for solving this problem. These parameters are used to obtain the key parameters of the characteristic bond-slip curves: κ, τ_f, τ_{max}, and S_0. In the secondary problem, the pull-out curve is predicted from the obtained bond-slip law.

Primary problem

Given an experimental pull-out load-slip curve, the local bond-slip law can be theoretically obtained for a given fiber by calculating the κ, τ_{max}, and τ_f. The bond modulus, κ, is determined as follows:

$$\kappa = \frac{\lambda^2}{\psi Q} \quad \text{Eq. 7-38}$$

where, Q can be obtained from Eq. 7-9 using the physical and mechanical properties of the fiber, and λ can be solved following an iterative approach from Eq. 7-20:

$$\left(\frac{P}{S}\right)=\frac{\lambda\sinh(\lambda L)}{Q(\cosh(\lambda L)-1)} \quad \text{Eq. 7-39}$$

P/S is the slope of the linear ascending portion of the experimental pull-out curve.

For obtaining the τ_{max} and the τ_f, the peak load and its corresponding end slip are extracted from the experimental pull-out response curves. As the peak load occurs under partial debonding conditions, its corresponding displacement, u_P, can be calculated from Eq. 7-29 as:

$$\left(\frac{dP}{du}\right)_{@u=u_p}=0\Rightarrow t_f-t_{(max)}\left(1-\tanh^2\left(\lambda\left(L-u_P\right)\right)\right)=0 \quad \text{Eq. 7-40}$$

If using P_P, s_P, and u_p instead of P, S, and u, respectively, in Eq. 7-29 and Eq. 7-32, the following equations will be obtained:

$$P_P=\frac{t_{(max)}}{\lambda}\tanh\left(\lambda\left(L-u_p\right)\right)+t_f u_p \quad \text{Eq. 7-41}$$

$$S_P=\frac{Qu_P}{2}\left(2P_P-t_f u_P\right)+Q\left(P_P-t_f u_P\right)\times\frac{\cosh\left(\lambda\left(L-u_P\right)\right)-1}{\lambda\sinh\left(\lambda\left(L-u_P\right)\right)} \quad \text{Eq. 7-42}$$

This leads to a system of three nonlinear equations (Eq. 7-40, Eq. 7-41, and Eq. 7-42) and three unknowns (t_f, t_{max}, and u_p) that can be solved to obtain the unknown parameters. Once t_f, t_{max}, and u_p are obtained, the τ_f and τ_{max} can be calculated as follow:

$$\tau_f=\frac{t_f}{\psi} \quad \text{Eq. 7-43}$$

$$\tau_{max}=\frac{t_{max}}{\psi} \quad \text{Eq. 7-44}$$

The accurate answer is obtained if the three following conditions are reached: i: solving three equations Eq. 7-40, Eq. 7-41, and Eq. 7-42, ii: having u_p less than embedded length (u_p<L), iii: having slip corresponding to τ_{max} less than the relative slip of the fiber/yarn under conditions of full debonding (S_0). With the four basic parameters κ, τ_{max}, τ_f, and S_0 known, the whole bond-slip relationship can be constructed.

Secondary problem

The procedure for modeling the pull-out behavior from a given bond-slip relationship can be summarized as follows [65]:

a) In the elastic stage, assume P_i and calculate the slip from Eq. 7-20. Keep increasing the P_i until it reaches P_{crit} (Eq. 7-19).

b) In the nonlinear stage, keep imposing the debonded length u, calculate the corresponding pull-out force (Eq. 7-29) and end slip (Eq. 7-32). The value of u is taken between zero and the embedded length of the fiber, L. As a snap back is not observed in a fiber pull-out experiment, this stage is terminated when the slip decreases or becomes larger than the fully debonded slip (Eq. 7-41).

c) In the dynamic stage, v is assumed, and S_{dyn} is calculated from Eq. 7-34. For each value of the end slip S_{dyn} ($S_0 \leq S_{dyn} \leq L$), the load can be obtained from Eq. 7-36. v is increased, and the calculation is repeated to obtain a full-range response.

7.1.3. Mathematica formulation of Method 2

In this section, the bond-slip law is assumed N-piecewise (see Fig. 7-1b) and is obtained indirectly from the experimental pull-out curves following the model proposed by Banholzer et al. [84,86]. In this model, which is a cohesive-based method, the experimental load-slip curve is divided into n steps. From the experimental test, the pull-out load, P_n, and its corresponding fiber slip, ω_n, are known for each load step. The parameters γ and q, defined as the relative compliance and the normalized pull-out force, respectively, are obtained as follows:

$$\gamma = \frac{1}{A_f E_f} + \frac{1}{A_m E_m} \qquad \text{Eq. 7-45}$$

$$q = \gamma P \qquad \text{Eq. 7-46}$$

where A is the cross-sectional area and E is Young's modulus. The subscripts f and m refer to the fiber and the matrix, respectively. The bond stress, τ_s, and its corresponding slip, S, are normalized for simplicity in terms of T_s, which is calculated as:

$$T_s = m_i \left(S - S_{i-1}\right) + T_{i-1} = \pi d \gamma \tau_s \qquad \text{Eq. 7-47}$$

where S_{i-1} is the slip at the lower bound of an interval i of the piecewise-defined normalized shear flow versus slip relation. T_{i-1} and d are the normalized shear flow corresponding to the slip S_{i-1} and the fiber diameter, respectively. m_i is the slope of the N-piecewise linear normalized shear flow-slip relation in an interval i and is equal to:

$$m_i = \frac{T_i - T_{i-1}}{S_i - S_{i-1}}, \; T_0 = S_0 = 0 \qquad \text{Eq. 7-48}$$

The procedure is to find the shear stress distribution, τ_n, or the normalized shear flow, T_n, along the bonded length in each step. T_n has to be found in an iterative procedure for a given slip $\omega = S$ at $x = L$ and a given pull-out force $P = \gamma^{-1} q$. For each load step, n, the introduced slip, and its corresponding pull-out

load are known from the experimental tests. The procedure for finding the bond-slip laws can be summarized as follows:

a) At n= 1, P_1 and S_1 are known from the experimental results; thereby, T_1 can be calculated from the following equation:

$$L = \frac{1}{\sqrt{m_k}} \ln\left[\frac{\sqrt{m_k}q_k + T_k}{\sqrt{T_k^2 - m_k q_k^2}}\right] = \frac{1}{\sqrt{m_1}} \ln\left[\frac{\sqrt{m_1}q_1 + T_1}{\sqrt{T_1^2 - m_1 q_1^2}}\right] \quad \text{Eq. 7-49}$$

L and q are the embedded length of the fiber and normalized force in the fiber at location x ($q_1 = \gamma P_1$), respectively. Based on Eq. 7-48, m_1 depends on T_1 that is the only unknown parameter in Eq. 7-49. The subscript k refers to the point at which the force in the fiber is zero [84].

b) To determine T_2, a value should be initially assumed. Then from Eq. 7-48, the value of m_2 is calculated. By obtaining m_2, the following equation can be solved:

$$q_{i-1}^2 = q_i^2 - m_i\left(S_i - S_{i-1}\right)^2 - 2T_{i-1}\left(S_i - S_{i-1}\right) \Rightarrow q_1^2 = q_2^2 - m_2\left(S_2 - S_1\right)^2 - 2T_1\left(S_2 - S_1\right) \quad \text{Eq. 7-50}$$

If the obtained value of Eq. 7-50 is negative, the assumed value is correct, and one can proceed to the next step. Otherwise, the value of T_2 must be changed so that the amount of Eq. 7-50 becomes negative. Therefore, this recursive determination of the fiber forces guarantees that there is a point at which the fiber load is zero [84].

c) The accurate value for T_2 is obtained by solving the following equation:

$$L = \overline{\Delta x} + \sum_{i=k+1}^{n} \Delta x_i \quad \text{Eq. 7-51}$$

where $\overline{\Delta x}$ and Δx_i can be determined as follows:

$$\overline{\Delta x} = \frac{1}{\sqrt{m_k}} \ln\left[\frac{\sqrt{m_k}q_k + T_k}{\sqrt{T_k^2 - m_k q_k^2}}\right], \quad m_k > 0$$

$$\overline{\Delta x} = \frac{1}{\sqrt{-m_k}} \arcsin\left[\frac{\sqrt{-m_k}\left(-q_k\sqrt{T_k^2 - m_k q_k^2}\right)}{T_k^2 - m_k q_k^2}\right], \quad m_k < 0 \quad \text{Eq. 7-52}$$

$$\overline{\Delta x_i} = \frac{1}{\sqrt{m_i}} \ln\left[\frac{\sqrt{m_i}q_i + T_i}{\sqrt{m_i}q_{i-1} + T_{i-1}}\right], \quad m_i > 0$$

$$\overline{\Delta x} = \frac{1}{\sqrt{-m_i}} \arcsin\left[\frac{\sqrt{-m_i}\left(Tq_{i-1} - T_{i-1}q_i\right)}{T_{i-1}^2 - m_k q_{i-1}^2}\right], \quad m_i < 0 \quad \text{Eq. 7-53}$$

In fact, by solving Eq. 7-50, the precise point of the embedded length in which the fiber load is equal to zero is obtained [84].

d) Having T_2, the shear stress is calculated by Eq. 7-47.

e) This procedure is then repeated for the next steps (n= 3, 4,...).

The main input parameters required for this problem are the elastic modulus of the fiber and the mortar that is usually known from the experimental tests and the mortar load carrying area. This latter has not been determined explicitly in the literature [62,65,66,80,86,232]. The effect of this parameter on the bond-slip laws is discussed in the next section.

7.1.4. Evaluation of proposed bond-slip law methods

Here, the proposed models are compared with experimental results to determine their accuracy based on different pull-out test setups. First, the multi-linear bond-slip law (method 1) will be performed, and the bond parameters, load-slip curves, and the effect of the mortar area (A_m) will be examined. Next, bond-slip law and load-slip curve derived from method two will be extracted. Finally, a comparison will be made between these two methods. In this section, the experimental results of test setup effects are used to verify the analytical models, where the experimental results are presented in section 5.1.

7.1.4.1. Method 1

A comparison is made here between the obtained experimental results and analytical simulations for all the considered test setups. The input parameters for these simulations are mechanical and geometrical properties of the fiber and the mortar, as well as the experimental load-slip curves. The modulus of elasticity of the steel fiber and the mortar M2 is equal to 174.87 GPa (obtained from experimental tests) and 9.23 GPa (given in the technical datasheets), respectively. The Poisson's ratio of the fiber and the mortar is taken as 0.3 and 0.2, respectively. The parameters P_P, s_P, and P/S, are obtained from the experimental load-slip curves as explained in section 7.1.2. The effective area of the mortar, A_m, is usually assumed as 100 times the fiber ($A_m = \alpha A_f$, $\alpha = 100$, and $A_f = 0.538$ mm^2) [85]. However, a survey of the literature indicated that the effective load carrying area of the matrix had not been determined explicitly [84]. The effect of this parameter on the analytical results is therefore discussed in the next paragraphs. Having the above-mentioned properties, the key parameters of the bond-slip curve (λ, κ, τ_{max}, τ_f, S_0) are calculated by solving Eq. 7-40, Eq. 7-41, and Eq. 7-42. With the aim of the obtained bond-slip curves, the secondary problem is then solved to predict the pull-out load-slip curves.

Fig. 7-4 shows the analytical load-slip curves and bond-slip laws obtained for all the test setups considering different values for the effective mortar area (by changing the value of α). It should be mentioned that a load of the dynamic stage in this section was calculated based on Naaman's model (Eq. 2-1). It can be instantly seen that α has a significant effect on the obtained results. As explained before, obtaining an accurate answer for the differential equations presented in section 7.1.2.5 requires satisfaction of all

three Eq. 7-40, Eq. 7-41, and Eq. 7-42, as well as having the obtained u_p and S_{max} less than the embedded length and the S_0, respectively.

Here, in the pull-push, I tests, although almost all α values (from 50 to 3700) produce acceptable pull-out curves with respect to the experimental envelope, Fig. 7-4a, and show small changes in the bond-slip laws, Fig. 7-4b, the convergence criteria are fell-field only for α values larger than 500. On the other hand, all the considered α values fulfill the convergence criteria in pull-push II and pull-pull configurations, Fig. 7-4c-f, but only α values of 55 and 100 produce acceptable results (similar to the value proposed in [85]) in comparison to the experimental envelope (best results are for α= 55 in pull-push II and α= 100 in pull-pull configurations).

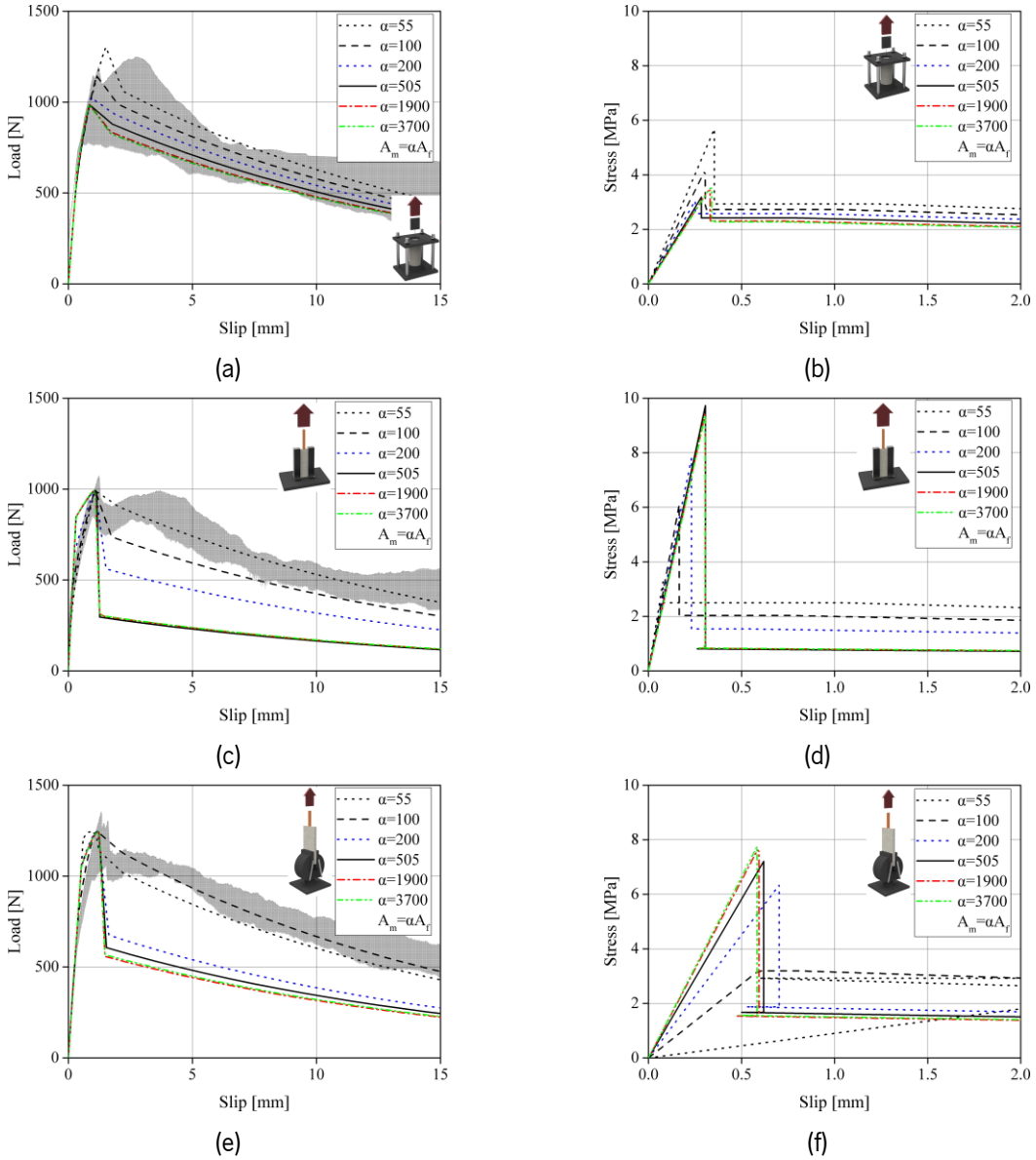

Fig. 7-4. The results of analytical modeling based on changing mortar area, A_m: (a) and (b) pull-push I; (c) and (d) pull-push II; (e) and (f) pull-pull.

The effect of α on the bond-slip laws seems significant in pull-push II and pull-pull configurations. This is clearer in Fig. 7-5, where the changes of bond-slip law parameters with α are presented. It can be observed that by increasing α (and correspondingly A_m), the τ_{max} increases while the τ_f decreases in both test configurations until 500<α<1900 where these values do not change anymore with the change of α. The effect of α on the bond modulus is contrary in pull-push II and pull-pull tests, i.e., its increase leads to increment of bond modulus in pull-push II and its decrement in pull-pull configuration. It should also be noted that the τ_{max} and τ_f are in the same range in both pull-push II and pull-pull tests for α<500, after which these values converge significantly.

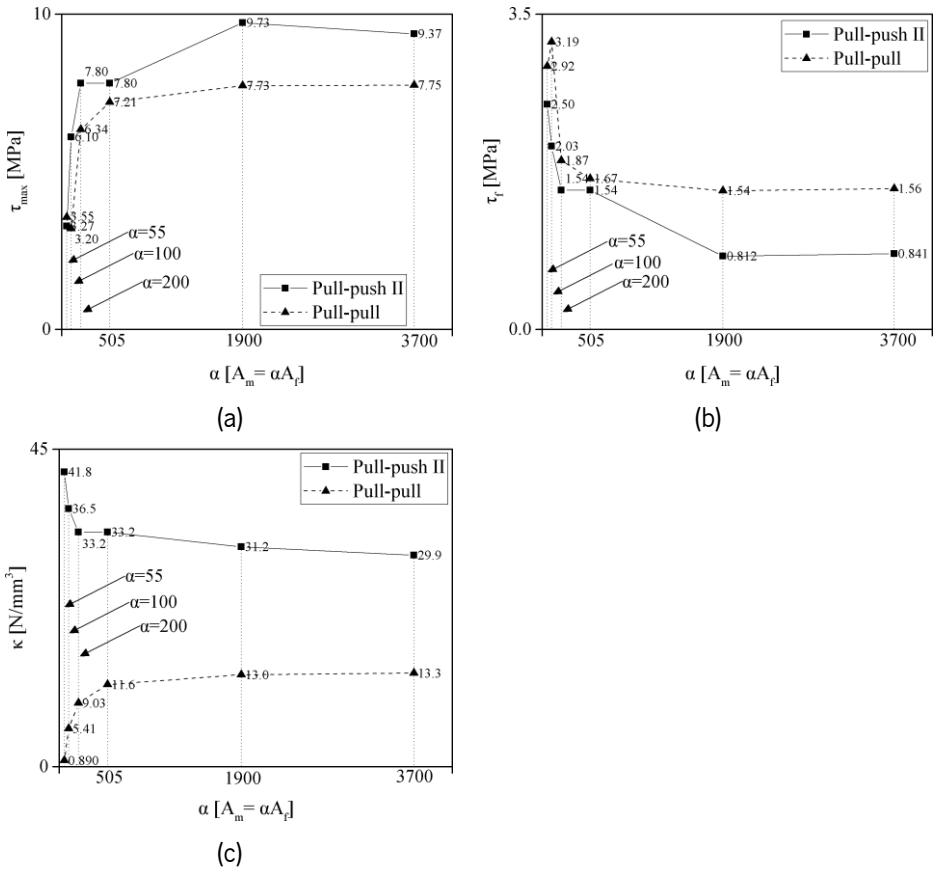

Fig. 7-5. Effect of mortar area (A_m) on the bond properties: (a) maximum stress; (b) friction stress; (c) bond modulus.

Banholzer et al. [86] reported that if the ratio of the mortar stiffness (A_mE_m) to the fiber (A_fE_f) is larger than 10 (A_mE_m/ A_fE_f >10), the difference the pull-pull and pull-push tests are negligible, and the same formulations can be used. In this study, if the mortar area is equal to 200 times the fiber area (assuming α= 200), the stiffness ratio of mortar and fiber becomes larger than 10. Comparison between the analytical results of both pull-push and pull-pull configurations, however, shows that the bond properties

and their corresponding load-slip curves are not similar to each other, see Fig. 7-4 and Fig. 7-5. Although, it should be noted that the input values (the ones that are taken from the experimental load-slip curves) for the simulations are also different in these cases, and this may be the reason for the observed differences in the pull-pull and pull-push configurations.

For this reason, a new analysis is performed considering the same input values, but different α, and the bond-slip laws and pull-out curves are produced for both pull-push and pull-pull configurations, see Fig. 7-6. It can be observed that even when the input values are similar, in both cases of α= 55 (corresponding to an A_mE_m/ A_fE_f= 2.90) and α= 200 (corresponding to an A_mE_m/ A_fE_f= 10.56), the results obtained from pull-pull and pull-push configurations are different. On the other hand, if the simulations are performed on experimental results produced by Naaman et al. [85] (specimen H2SL with mortar compressive strength and elastic modulus of 60.2 MPa and 21 GPa, respectively), Fig. 7-7, it can be seen that the results from pull-pull and pull-push simulations are similar when an α= 100 (corresponding to an A_mE_m/ A_fE_f= 10) is used while they are different when this value is changed to 50 (corresponding to an A_mE_m/ A_fE_f= 5). These results show that the A_mE_m/ A_fE_f ratio is not a sufficient criterion for evaluating the applicability of pull-pull formulations in the pull-push test configuration. Indeed, it seems that the ratio of A_m/A_f and E_m/E_f have to be evaluated separately with different criteria.

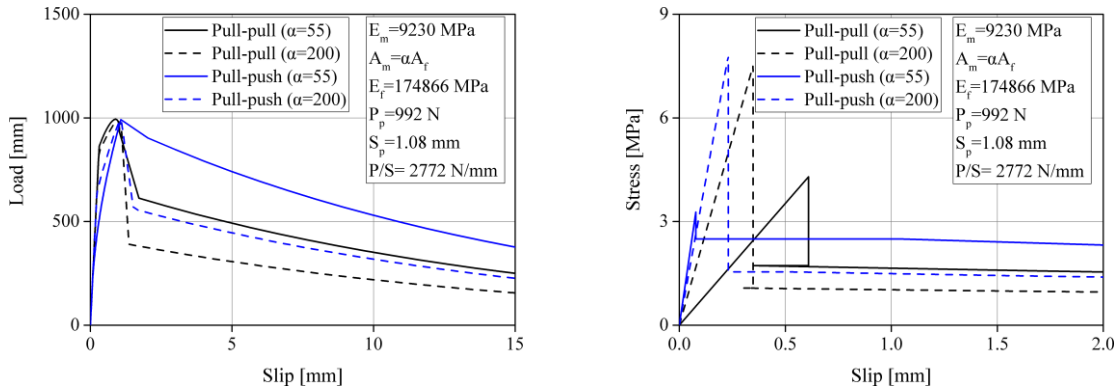

(a) (b)

Fig. 7-6. The effect of pull-pull and pull-push configuration when similar input values are used.

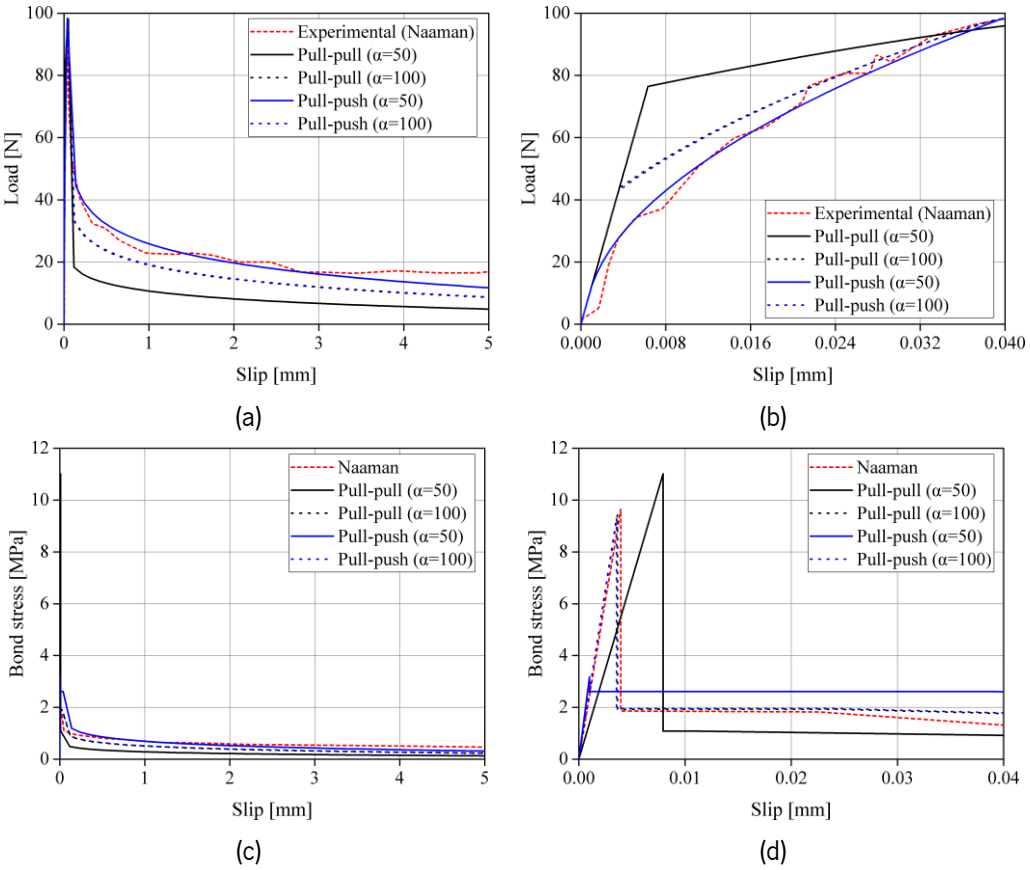

Fig. 7-7. Analytical modeling of experimental tests performed by Naaman et al. [85]: (a) full scale of the load-slip curve; (b) ascending branch of the load-slip curve; (c) full scale of the bond-slip curve; (d) enlarge the scale of the bond-slip curve.

Having considered the above-mentioned issues, the effect of test setup on the extracted bond-slip laws are summarized in Table 7-1 and Fig. 7-8, where α is equal to 200, 55, and 100 for pull-push I, pull-push II, and pull-pull test setups. A comparison between the experimental and analytical results of pull-push I and II illustrates that increment of the initial stiffness of the pull-out curves (as is the main difference between these two tests) leads to increment of the bond modulus in pull-push II tests. Meanwhile, the τ_{max} and τ_f are approximately equal in both pull-push I and II tests. On the other hand, in the pull-pull configuration, the bond modulus is lower than, the τ_f is higher than, and the τ_{max} is similar to the pull-push configuration results.

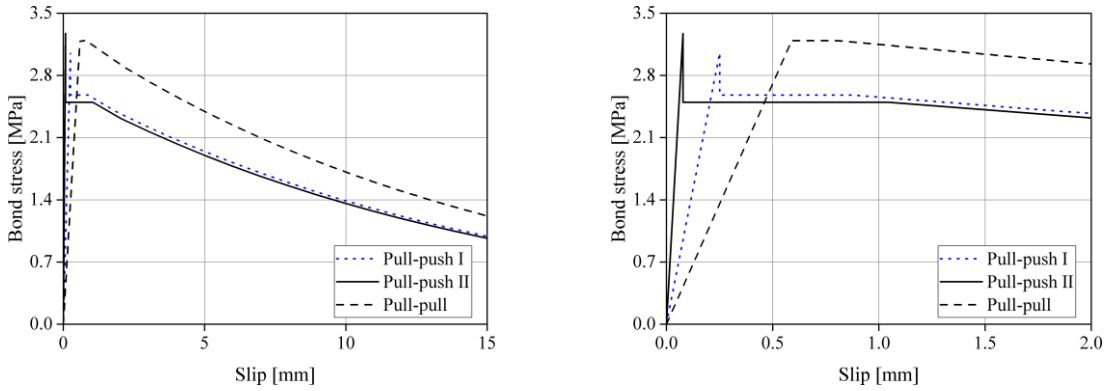

Fig. 7-8. Bond-slip law diagrams extracted with method 1: (a) full scale; (b) enlarge scale.

Table 7-1. Bond-slip parameters for each test setup based on method 1.

Specimen	P/S [N/mm]	P_P [N]	s_P [mm]	λ	κ [N/mm³]	τ_f [MPa]	τ_{max} [MPa]	S_0 [mm]
pull-push I	1762	987	0.78	0.0163	9.252	2.424	3.18	0.782
pull-push II	2772	992	1.08	0.0394	41.777	2.499	3.27	1.045
pull-pull	2032	1245	1.33	0.0133	5.408	3.192	3.2	0.804

For further verification of the observed response and drawn conclusions on the pull-out behavior in different test setups, finite element (FE) simulations are performed next. For simulations, 8-node solid elements and 2-node truss elements (with a 5 mm mesh size) are utilized to model the mortar and the fiber, respectively. Interface elements are also used to simulate the bond behavior between the mortar and the fiber, in which the bond-slip laws obtained from the analytical modeling are employed, see Fig. 7-9.

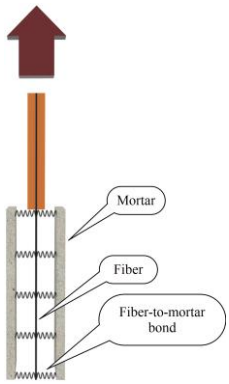

Fig. 7-9. Sketch of numerical modeling.

The independence of the results to the mesh size is also investigated. The distributions of stresses in the mortar at the peak load in pull-pull and pull-push configurations are presented in Fig. 7-10. It can be observed that most of the mortar in the pull-push configuration is under compressive stresses, caused due to the tensile load in the fiber, and only a small region near the loaded end is under tensile stresses, Fig. 7-10a. On the other hand, the mortar is completely under tensile stresses in the pull-pull configuration (Fig. 7-10b). These observations confirm the assumptions made for the development of the analytical formulations. A comparison between the numerical and analytical results is presented in Fig. 7-11 and Table 7-2 for all the considered test setups. The outcomes, besides a slight difference between numerical and analytical results, illustrate a good agreement between these modeling strategies. In addition, the pull-out properties of numerical modeling are shown in Table 7-2. It should be noted that the abrupt changes after the peak load are owing to the sudden change of the nonlinear stage to the dynamic stage. This observation has also been reported by other researchers [62,66,85].

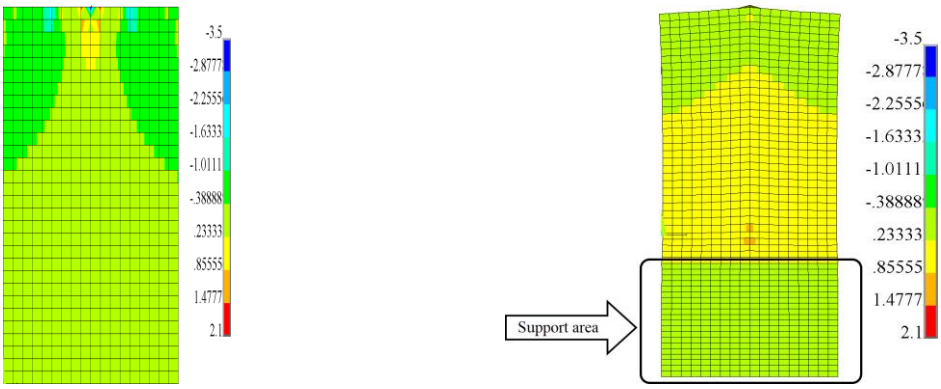

Fig. 7-10. Stress [MPa] distribution in the mortar along with the tensile applied load: (a) pull-push; (b) pull-pull.

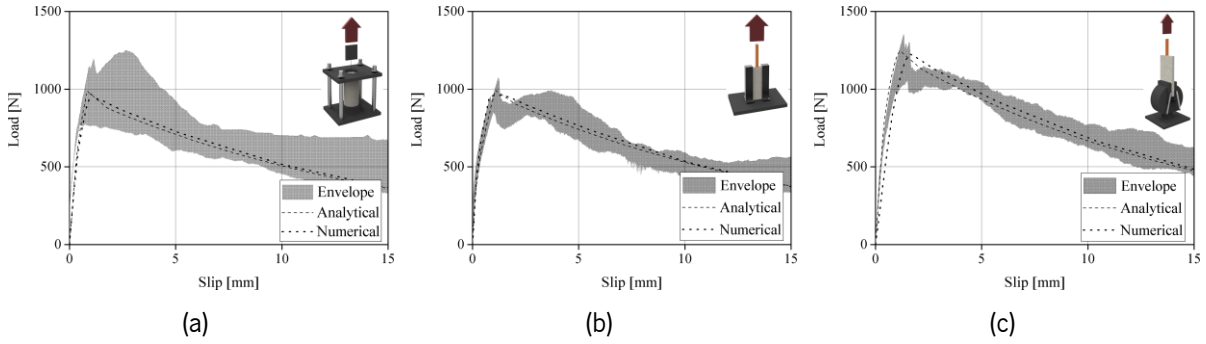

Fig. 7-11. Experimental pull-out curve versus analytical and numerical pull-out curve: (a) pull-push I; (b) pull-push II; (c) pull-pull.

Table 7-2. Comparison between analytical and numerical results.

Modeling	Specimen	s_P [mm]	P_P [N]	E_{deb} [N.mm]	K [N/mm]
analytical	pull-push I	0.84	986	501	1758
	pull-push II	1.08	992	694	2772
	pull-pull	1.18	1245	1001	2032
numerical	pull-push I	1.0	969	611	1688
	pull-push II	1.0	961	677	2301
	pull-pull	1.6	1228	1208	1103

s_P: slip corresponding to peak load; P_P: peak load; E_{deb}: debonding energy; K: initial stiffness.

7.1.4.2. Method 2

With the aim of the analytical modeling approach proposed by Banholzer et al. [84,86], method 2, the fiber-to-mortar bond-slip laws are obtained from the experimental pull-out curves of different test setups. Fig. 7-12 and Table 7-3 presents the bond-slip law curves and parameters for each test setup, extracted from the average load-slip curves of pull-out experiments. In these results, the elastic modulus of the steel fiber (E_f) and the M2 mortar (E_m) is equal to 174.87 GPa and 9.23 GPa, respectively. In addition, the fiber area (A_f) is 0.538 mm^2, and the effective mortar area (A_m) is equal to α A_f. Similar to method 1, α is 200, 55, and 100 for pull-push I, pull-push II, and pull-pull test setups, respectively. As expected, the bond-slip laws show a higher initial stiffness, frictional stress, and bond strength in pull-pull tests compared to that of pull-push tests. Interestingly, the bond-slip laws extracted from the pull-push I and II test setups do not show any significant difference.

There is a difference between bond parameters calculated by both methods. Bond strength (τ_{max}) calculated with method 2 is greater than method 1, whereas frictional stress (τ_f) and bond modulus (κ) are opposites. In addition, Fig. 7-13 compares the analytical load-slip curves extracted from methods 1 and 2 with experimental envelope curves. Experimental results verify the linear and nonlinear stages of curves derived from method 1 as opposed to method 2. In the meantime, both methods could predict and verify the dynamic stage based on the experimental results. Using the numerical procedure and increasing the bond-slip law segments, it is possible to reduce discrepancies between experimental and method 2 results for both linear and nonlinear stages [84,86]. Hence, the fitting or optimization process for method 2 causes considerable difficulties due to the time-consuming process, in contrast with method 1.

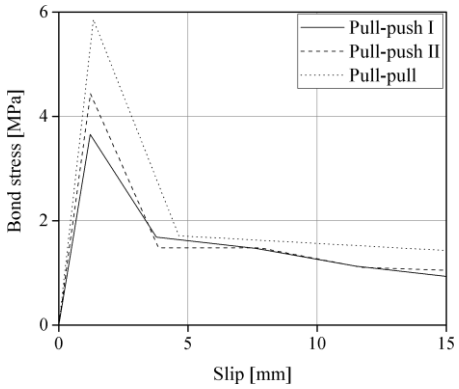

Fig. 7-12. Bond-slip law diagrams extracted with method 2.

Table 7-3. Bond-slip parameters for each test setup based on method 2.

Specimen	κ [N/mm^3]	τ_f [MPa]	τ_{max} [MPa]
pull-push I	3.01	1.69	3.65
pull-push II	3.64	1.48	4.44
pull-pull	4.36	1.71	5.85

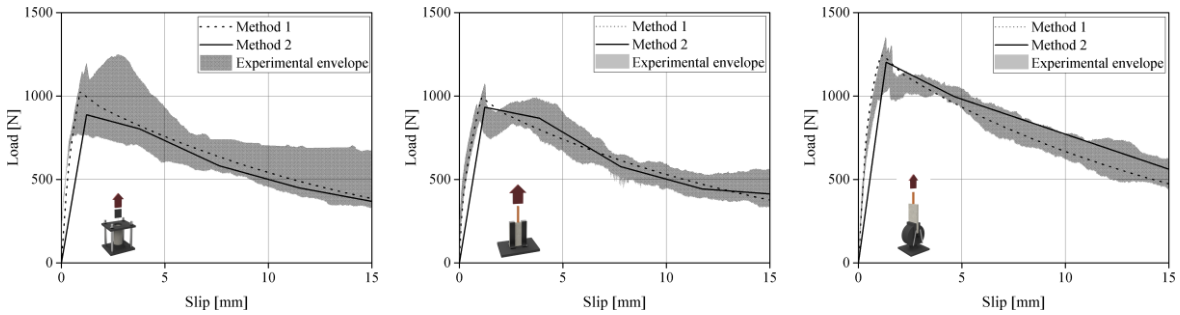

(a) (b) (c)

Fig. 7-13. Experimental pull-out curve versus analytical and numerical pull-out curve: (a) pull-push I; (b) pull-push II; (c) pull-pull.

7.1.5. Modified bond-slip law

Model 1 confirmed the linear and nonlinear stages of the experimental load-slip curves. However, the dynamic stage shows discrepancies between the results owing to the slip-hardening effect that occurs in the experiments. As mentioned in section 7.1.4.1, Naaman's formulation is useful for modeling the slip-softening effect. Thus, the method 1 model needs to be modified to produce better results. In addition, a few supplementary analyses, such as the efficiency of the model on different TRM composites and the embedded length effect, should be performed in this model to investigate its accuracy.

7.1.5.1. Effect of Slip-hardening

Method 1 was not suitable for predicting the slip hardening effect observed after the peak load in the tested TRM composites. To resolve that problem, a novel bond-slip law for lime-based TRMs is presented (though the proposed model can also be used for cement-based mortars), which allows predicting the full range of the pull-out response of those composites. This shape of bond-slip law, which is proposed based on Lin and Li [77] for short fibers (at the range of 13 mm), is presented in Fig. 7-14.

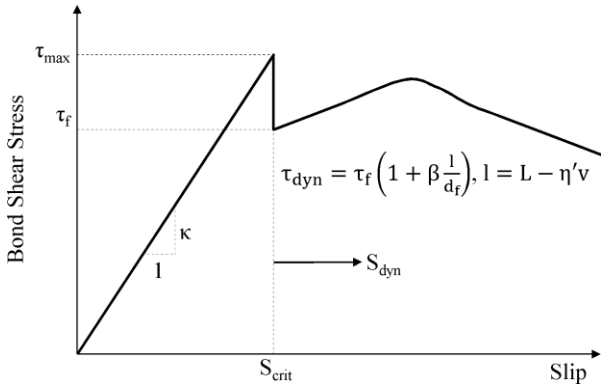

Fig. 7-14. Modified bond-slip law of method 1.

The linear and nonlinear stages of the modified model are similar to those described in section 7.1.2. To model the slip hardening effect at the dynamic stage, a simple two-parameter phenomenological model proposed by Lin and Li [77] is adopted. By considering suitable coefficients, it is possible to change the output of Eq. 7-35 from the linear curve to the nonlinear curve and model the slip hardening effect as follow:

$$P_{dyn} = \tau_f \left(L - \eta' v\right)\left(1 + \beta \frac{L - \eta' v}{d_f}\right)\psi \qquad \text{Eq. 7-54}$$

where η' reflects the changes in the slope of the pull-out curve, β is the slip hardening coefficient, and d_f is the fiber or yarn diameter. Both η' and β need to be determined by a curve fitting procedure to achieve the best match with the experimental load-slip curves. In Eq. 7-54, the η' sign is the opposite of the experimental load-slip curve slope, which means that if the slope in the load-slip curve is positive, the η sign is negative, and vice versa. The local force in the fiber at a distance x (from zero and L-v), therefore, can be calculated as:

$$F = \tau_f \left(L - \eta' v - x\right)\left(1 + \beta \frac{L - \eta' v - x}{d_f}\right)\psi \qquad \text{Eq. 7-55}$$

The total slip at the end of the fiber is defined as follow:

$$S = Q\int_0^{L-v} F_x \, dx \qquad \text{Eq. 7-56}$$

Replacing F_x from Eq. 7-55 into Eq. 7-56 gives the slip corresponding to the dynamic stage, S_{dyn}, as:

$$S_{dyn} = Q\tau_f \psi (L-v)\left\{L - \eta' v - \frac{L-v}{2} + \frac{\beta}{d_f}\left[(L-\eta' v)^2 + \frac{(L-v)^2}{3} - (L-\eta' v)(L-v)\right]\right\} \qquad \text{Eq. 7-57}$$

In a particular case, where no slip hardening is considered (β= 0.0 and η'= 1.0), Eq. 7-57 will be reduced to:

$$S_{dyn} = Q\tau_f \psi \frac{(L-v)^2}{2} \qquad \text{Eq. 7-58}$$

Eq. 7-58 is the same as proposed in Naaman et al. [65], Sueki et al. [62], and Mobasher [66] for calculating the slip corresponding to the dynamic stage. Thus, the total slip in the dynamic stage is [62,66]:

$$S_{measured} = S_{dyn} + S_{nonlinear,\,last} + v \qquad \text{Eq. 7-59}$$

where $S_{nonlinear,\,last}$ is the last slip calculated in the nonlinear stage.

7.1.5.2. The efficiency of method 1 on different TRM composites

In order to investigate the efficiency of the proposed model, the bond-slip laws are extracted from the pull-out response of two different TRM composites. The steel and glass-based fibers were embedded in the mortar M2 and mortar M1 in 150 mm and 50 mm bond length. The modulus of elasticity of the mortars M1 and M2 are 8 GPa and 9 GPa (taken from the technical datasheets), respectively. The modulus of elasticity for the glass yarn and the steel fiber is equal to 65.94 GPa and 189.34 GPa (obtained from experimental tests), respectively. The steel fiber and the glass yarn cross-section area (A_f) are equal to 0.538 mm^2 and 0.882 mm^2, respectively. The fiber/yarn perimeter and diameter are calculated from the cross-section area, assuming a circular cross-section.

The cross-section area of the mortar around fibers/yarns (A_m), which becomes active and participates in the debonding process, is a critical parameter in the analytical results. Since this parameter cannot be measured using conventional experimental testing methods, it is usually obtained based on a parametric study and considering the convergence of the numerical solution. As presented in section 7.1.4.1, it was found that the effective mortar area can be considered as $A_m = \alpha A_f = 55A_f$ for the steel-based TRM. For the glass-based TRM, α is considered as 7.5. These α values are derived by performing a try and error approach, where a primary value for α is considered, and the model is run. If an accurate answer is obtained, the effective mortar area will be accepted; otherwise, a new value will be considered for α. The exact answer can be obtained if the three conditions described in the primary problem are met. It should

be mentioned that the considerable difference between α values (55 and 7.5 for the steel and the glass fibers) results from both the fiber properties (E_f and A_f) and the obtaining accurate answer process as mentioned above.

Fig. 7-15 presents the experimental pull-out response envelope, obtained from four tested steel-based TRM specimens, together with the analytical extracted bond-slip laws and analytical predicted load-slip curves. The main parameters of the experimental pull-out curves and analytically extracted bond-slip laws are also presented in Table 7-4 and sP: slip corresponding to peak load; PP: peak load; K: initial stiffness.

Table 7-5. For the development of the analytical pull-out curves, the experimental pull-out curves of individual samples are initially used to extract the bond-slip laws using the analytical model adopted in this study. These bond-slip laws are then used for modeling the presented analytical pull-out curves.

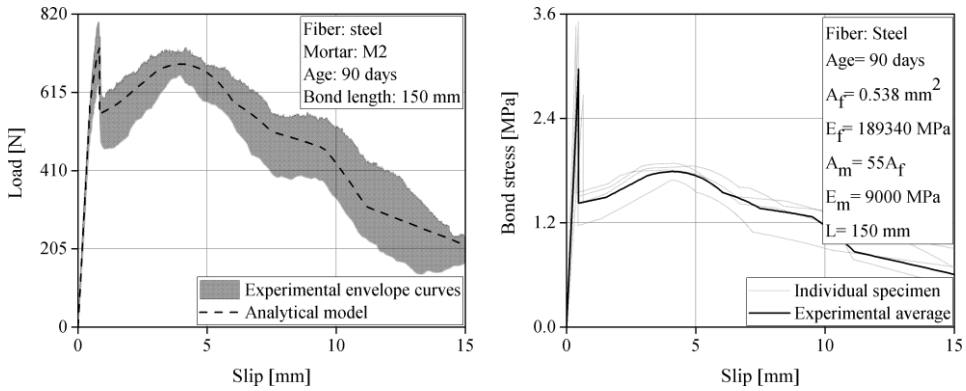

Fig. 7-15. Steel-based TRM with 150 mm embedded length (a) pull-out response; (b) analytical bond-slip law.

Table 7-4. Pull-out response parameters for steel-based TRMs (embedded length of 150 mm).

Specimen	s_P [mm]	P_P [N]	K [N/mm]	Debonding slip [mm]	Debonding load [N]
1	0.80	634.8	1210.8	0.80	634.8
2	0.80	802.5	1339.9	0.80	802.5
3	0.85	766.0	1455.6	0.75	729.3
4	0.81	759.0	1103.3	0.81	759.0
Average CoV (%)	0.81 (3)	740.6 (9)	1277.4 (10)	0.79 (3)	731.4 (8)

s_P: slip corresponding to peak load; P_P: peak load; K: initial stiffness.

Table 7-5. Analytical bond-slip laws and predicted debonding load/slip for steel-based TRM (embedded length of 150 mm).

Specimen	τ_{max} [MPa]	τ_f [MPa]	K [MPa/mm]	β	Debonding slip [mm]	Debonding load [N]	Error in debonding load prediction [%]
1	2.55	1.17	3.83	0.0003	0.74	626.5	1.3
2	3.51	1.51	6.05	0.0003	0.94	795.1	0.9
3	3.47	1.55	7.88	0.0003	0.87	761.4	-4.4
4	2.67	1.44	1.97	0.0003	0.85	745.8	1.7
Average CoV (%)	3.05 (15)	1.42 (10)	4.93 (45)	0.0003 (0)	0.85 (8)	732.2 (9)	-0.1

The agreement between the experimental and analytical pull-out curves of the steel-based TRM is clear (Fig. 7-15 and Fig. 7-16). The initial stiffness, post-peak slip hardening effect, and final deterioration of the bond strength are all simulated with great accuracy. It can also be observed that the proposed analytical model is suitably able to predict the slip at the free end of the samples (Fig. 7-16b). The experimental results show that the dynamic stage initiates near the peak load, Fig. 7-16b. This observation is also predicted with high accuracy (an error of less than 1%) with the proposed analytical model (see Table 7-5). This observation also shows that the dynamic stage initiation could be assumed to occur at the peak load with reasonable accuracy and previously considered in the literature [68,69,233]. The predicted load and slip (representative of the end of the nonlinear stage and beginning of the dynamic stage), as well as the difference among the results of analytical and experimental debonding loads, are presented in the last three columns of Table 7-5. It can be observed that the analytical predictions of the debonding load have a good agreement with the experimental results so that the average difference is equal to 0.1% (see Table 7-5).

The envelope of the experimental load-slip curves of the glass-based TRM specimens is shown in Fig. 7-17. The individual results obtained from each sample, together with the main extracted information from the experimental results, are also presented in Table 7-6. A more considerable variation in the experimental results is observed when compared to the steel-based TRM results, which may be attributed to the telescopic behavior of the glass yarn [179,234,235] and the abrasion effect [76,77] by breaking down layer by layer of filaments. The drop in the force after the peak load (corresponding to the lower frictional resistance compared to the adhesive resistance in this system) followed by a slip hardening behavior is also observed in this TRM system. Again, the analytical predictions have a perfect agreement with the experimental results regarding both loaded and free-end slip predictions (Fig. 7-18). Here also, complete debonding occurs near the peak load (Fig. 7-18, Table 7-6). The results show that the debonding load is also predicted with acceptable accuracy (an error of 0.2%, see Table 7-7).

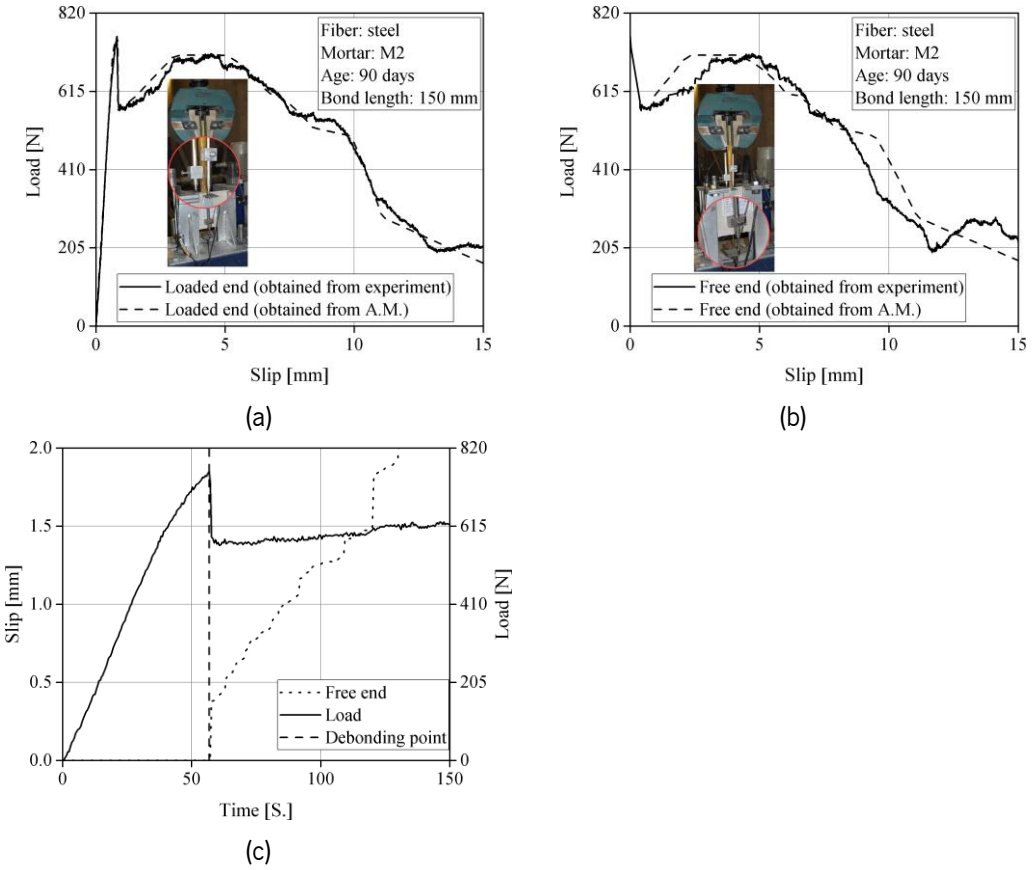

Fig. 7-16. The pull-out response of a steel-based TRM specimen: (a) loaded end slip curves; (b) free end slip curves (c) load-time vs. slip-time curves (A.M. stands for Analytical Modeling).

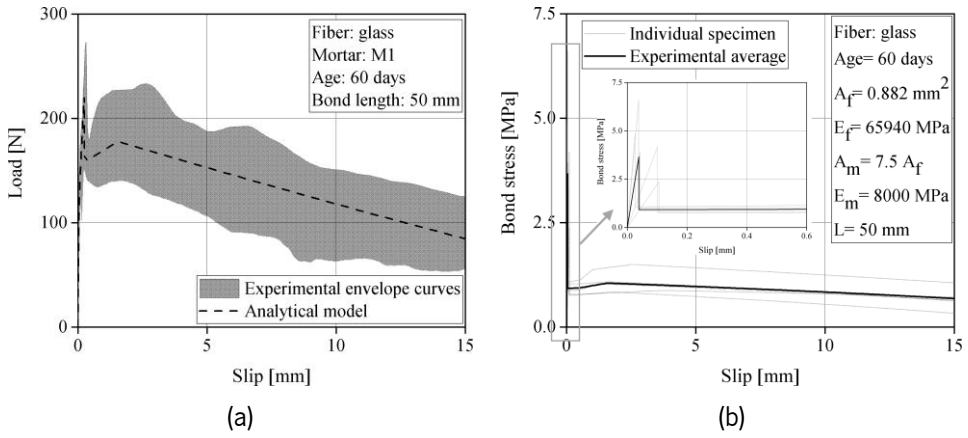

Fig. 7-17. Glass-based TRM with 50 mm embedded length (a) pull-out response; (b) analytical bond-slip law.

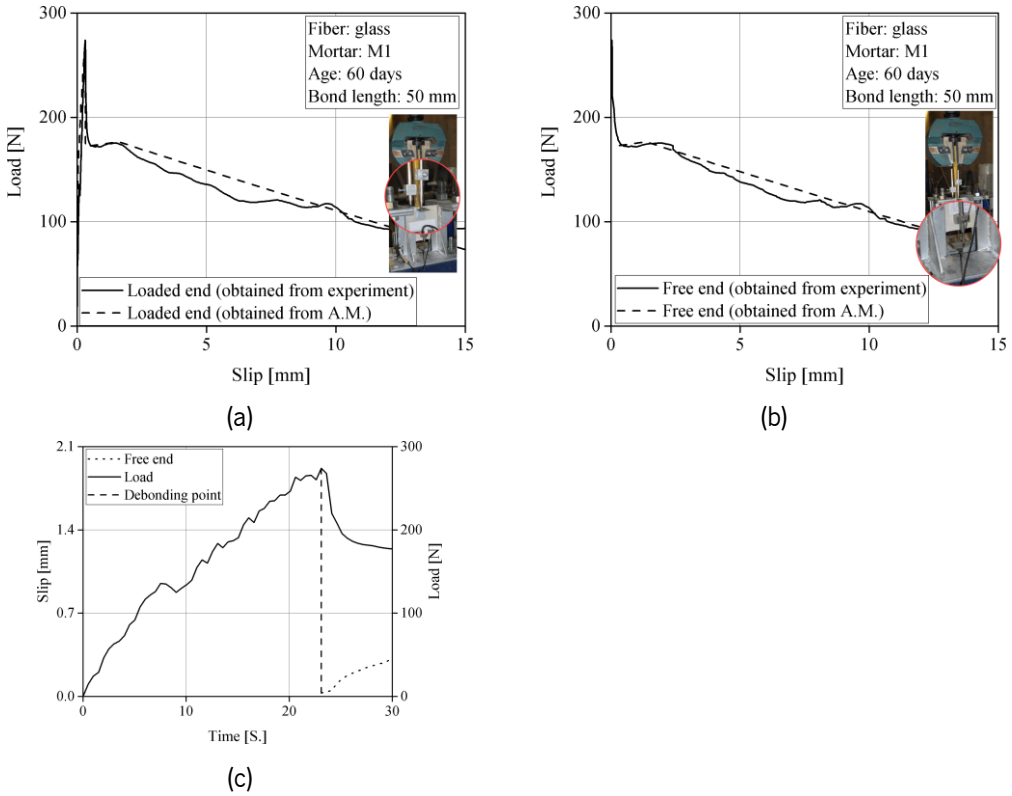

Fig. 7-18. The pull-out response of a glass-based TRM specimen: (a) loaded end slip curves; (b) free end slip curves (c) load-time vs. slip-time curves (A.M. stands for Analytical Modeling).

Table 7-6. Pull-out response parameters for glass-based TRMs (embedded length of 50 mm).

Specimen	s_P [mm]	P_P [N]	K [N/mm]	Debonding slip [mm]	Debonding load [N]
1	0.32	274.0	4015.4	0.32	274.0
2	0.34	218.3	2954.4	0.34	218.3
3	0.14	202.2	1639.3	0.14	202.2
4	0.28	273.0	2028.2	0.28	273.0
5	0.33	237.9	4166.3	0.33	237.9
Average CoV (%)	0.28 (26)	241.1 (12)	2659.3 (34)	0.28 (26)	241.1 (12)

s_P: slip corresponding to peak load; P_P: peak load; K: initial stiffness.

Table 7-7. Analytical bond-slip laws and predicted debonding load/slip for glass-based TRM (embedded length of 50 mm).

Specimen	τ_{max} [MPa]	τ_f [MPa]	K [MPa/mm]	β	Debonding slip [mm]	Debonding load [N]	Error in debonding load prediction [%]
1	6.61	1.03	174.36	0.0017	0.32	273.6	0.1
2	3.94	0.87	92.86	0.0044	0.25	218.2	0.0
3	2.38	0.76	22.48	0.0032	0.23	202.2	0.0
4	4.19	0.78	41.66	0.0031	0.36	272.6	0.1
5	4.86	1.08	187.79	0.0053	0.26	236.7	0.5
Average CoV (%)	4.4 (31)	0.90 (14)	103.83 (65)	0.0035 (34)	0.28 (17)	240.7 (12)	0.2

It is interesting to note that although the glass-based TRM specimens had a smaller embedded length, they show a mean value of the slip hardening coefficient (β=0.0031) of about ten times that of the steel fibers (Table 7-7 and Table 7-5).

7.1.5.3. Effect of embedded length

The proposed analytical model is used here to extract the bond-slip laws of the steel-based TRM samples with different bond lengths presented in section 5.2.1. It should be noted that these samples were tested at the 60-day curing ages and had embedded lengths of 50, 100, 150, and 200 mm. The pull-out parameters of these specimens are reported in section 5.2.1. The bond-slip laws are extracted from the individual samples and then averaged for each embedded length (see Fig. 7-19 and Table 7-8). These bond-slip laws are then used for predicting the load-slip curves following two different approaches (predicted load-slip curves are presented in Fig. 7-20, together with experimental envelopes), as follows: (i) The average bond-slip law corresponding to each embedded length is used to predict the load-slip curve of that embedded length; (ii) The average bond-slip law obtained from 150 mm embedded length samples (that is believed larger than the effective embedded length, as discussed in section 5.2) is used for predicting the load-slip curves of all embedded lengths. This second approach is followed to evaluate the accuracy of the hypothesis that the bond-slip laws obtained from pull-out tests performed on samples with embedded lengths higher than the effective bond length are sufficient for predicting the bond behavior in all other embedded lengths.

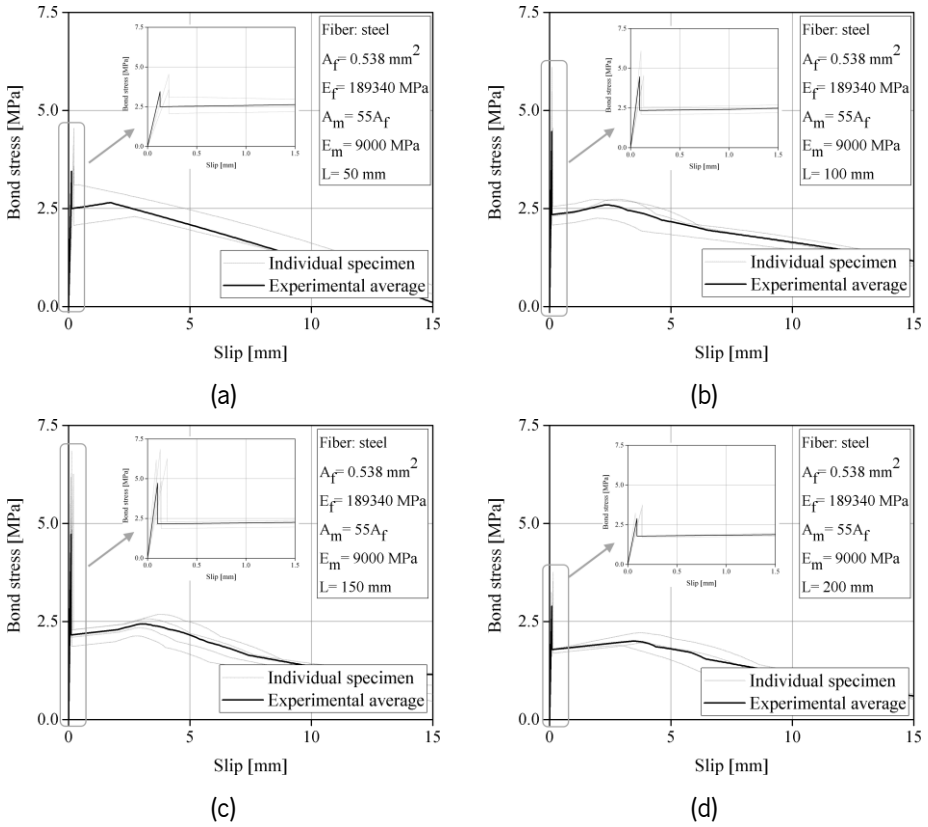

Fig. 7-19. The bond slip-law of the steel-based TRM at 60 days and in (a) 50 mm; (b) 100 mm; (c) 150 mm; (d) 200 mm bond length.

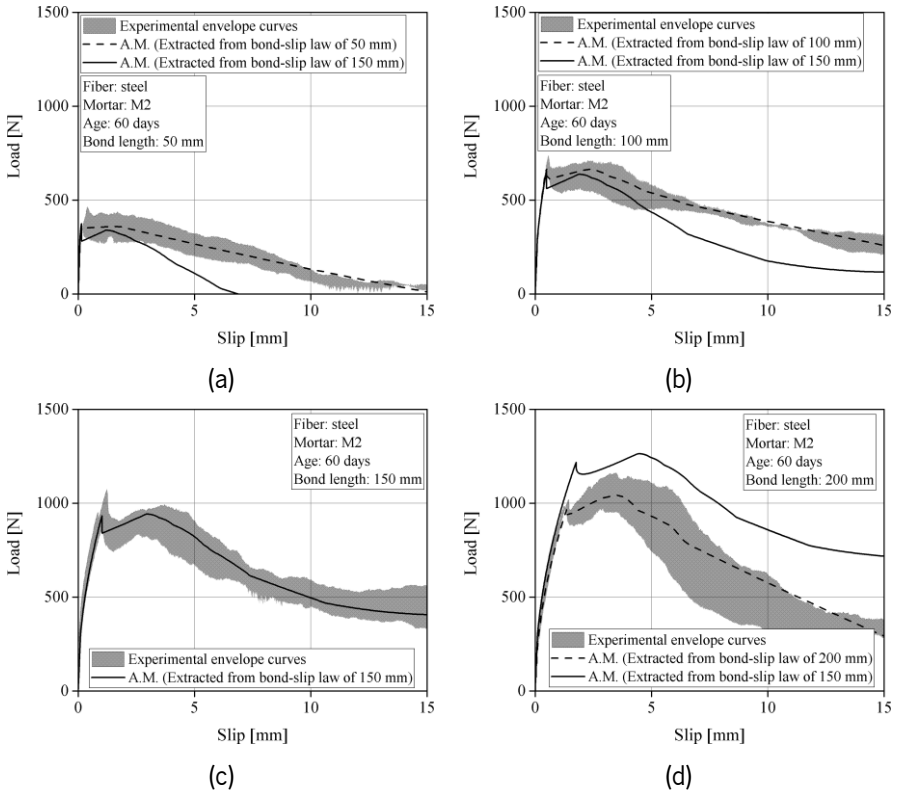

Fig. 7-20. The pull-out response of the steel-based TRM at 60 days: (a) 50 mm; (b) 100 mm; (c) 150 mm; (d) 200 mm bond length (A.M. stands for Analytical Modeling).

Table 7-8 reports the bond-slip laws for different embedded lengths (approach (i)). Table 7-8 shows that by increasing the embedded length, the frictional shear strength (τ_f) and the bond shear modulus (slope of the linear part, κ) decrease. Meanwhile, the slip hardening coefficient (β) and the bond strength (τ_{max}) increase. Specimens with 200 mm bond length show a decrement of bond strength owing to their different pull-out responses at the debonding point. A comparison among the load-slip curves of experimental results shows the intensity of the load drop in 200 mm bond length is the least, which means that the debonding load is slightly higher than the frictional resistance after debonding [73]. This hypothesis can be supported by investigating the strain distribution along the steel fibers, as shown in Fig. 7-21. From Fig. 7-21, the maximum strain of fiber with 200 mm bond length at the end of the linear and nonlinear stages is 0.206 % and 0.223 %, respectively, while for other bond lengths, it is between 0.255 and 0.300 %. Furthermore, Yamao et al. [236] reported that the bond stress-slip relationships in the short and long bond lengths are significantly different [237]. It can be deduced that the bond in the specimens with 200 mm embedded length is governed more by the friction stress rather than the bond strength.

The predictions of the pull-out curves when using the bond-slip laws from 150 mm embedded length are also in excellent agreement with the experimental results in most regions of the pull-out curves (the predictions are only slightly higher in 200 mm embedded length).

Table 7-8. Bond-slip law parameters for the steel-based TRM with different embedded lengths*.

Bond length [mm]	Specimen	τ_{max} [MPa]	τ_f [MPa]	κ [MPa/mm]	β
50	1	3.58	2.07	16.57	0.0001
	2	4.55	3.10	21.11	0.0001
	Average	4.07 (12)	2.59 (20)	18.84 (12)	0.0001 (0)
100	1	6.10	2.08	57.46	0.0002
	2	3.97	2.31	34.84	0.0002
	3	4.55	2.56	33.90	0.0002
	Average	4.87 (18)	2.32 (8)	42.07 (26)	0.0002 (0)
150	1	4.85	1.87	35.03	0.0003
	2	6.26	2.29	31.42	0.0003
	3	6.18	2.10	69.84	0.0003
	4	6.85	2.29	53.35	0.0003
	Average	6.04 (12)	2.14 (8)	47.41 (32)	0.0003 (0)
200	1	3.76	1.69	25.17	0.0004
	2	3.25	1.79	42.23	0.0008
	3	3.53	1.79	25.45	0.0003
	Average	3.51 (6)	1.76 (3)	30.95 (26)	0.0005 (43)

*CoV of the results is given in percentage inside parentheses

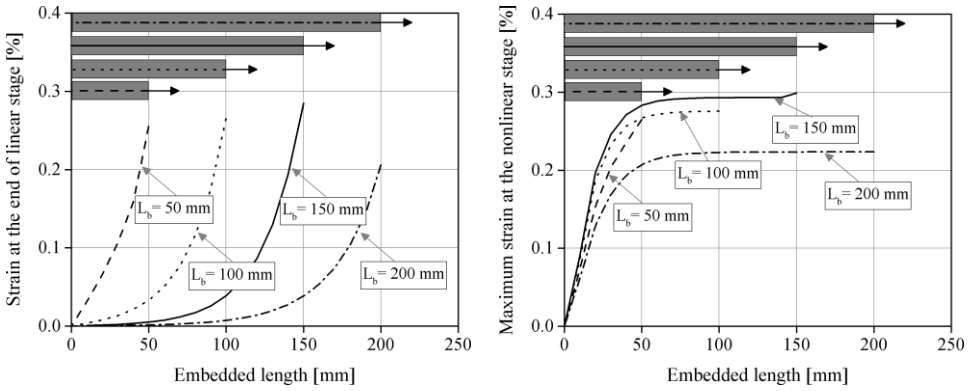

(a) (b)

Fig. 7-21. Fiber strain distributions along the embedded length of the steel-based TRM: (a) at the end of the linear stage; (b) at the nonlinear stage (L_b: bond length).

7.1.6. Effect of natural aging

The proposed analytical model 1 is also utilized to extract the bond-slip laws curves of the steel and the glass-based TRM samples at different mortar ages. The experimental results are presented in sections 5.8.1 and 5.8.2. Here the effect of mortar age (indoor) and the real environmental (outdoor) conditions on the bond-slip law parameters are discussed.

Fig. 7-22 and Fig. 7-23 show the bond-slip law curves of the steel-based TRM at different ages under indoor and outdoor conditions. In addition, the changes in the bond-slip law parameters at different mortar ages are presented in Fig. 7-24. Again, the bond strength, τ_{max}, (Fig. 7-24a), and the frictional strength, τ_f, (Fig. 7-24b) show an incremental trend in outdoor aged samples (bond strength decreases from 270 days to 920 days), while no significant changes can be observed in indoor aged samples. However, the bond modulus (κ) seems to increase significantly in outdoor aged samples but slightly decrease in the early ages in indoor aged samples (a high variation is observed in the results for this parameter), Fig. 7-24c. At the same time, the slip hardening coefficient (β) shows an increasing trend for both indoor and outdoor aged samples (Fig. 7-24d). Nevertheless, the indoor aged specimens show higher values in contrast to the outdoor aged specimens. A comparison between τ_f and β shows that the higher frictional stress, the lower the slip hardening coefficient. The mean values of the bond-slip laws for indoor and outdoor specimens are also presented in Table 7-9.

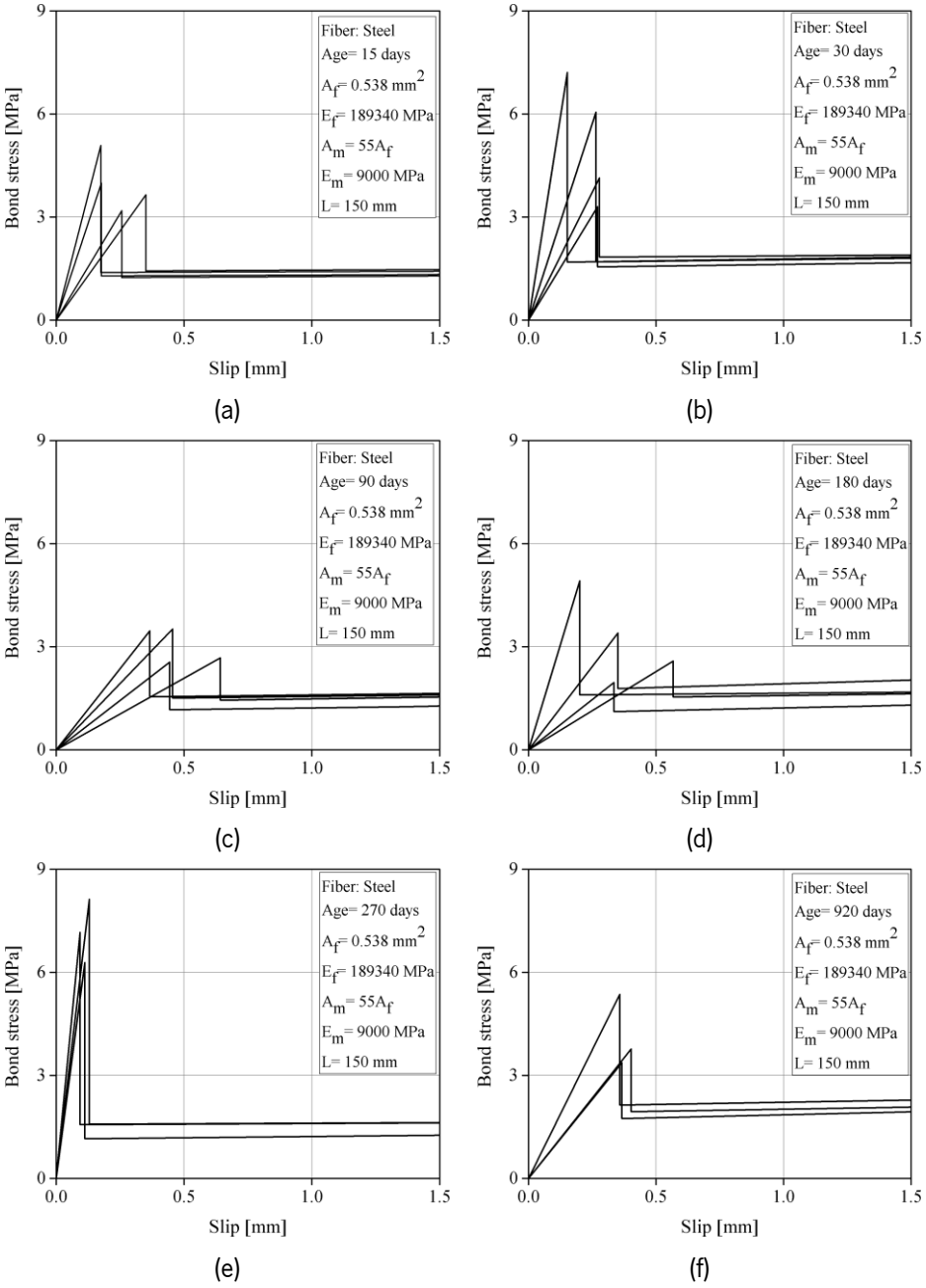

Fig. 7-22. Bond-slip law curves of the steel-based TRM at different mortar ages under indoor condition: (a) 15 days; (b) 30 days; (c) 90 days; (d) 180 days; (e) 270 days; (f) 920 days.

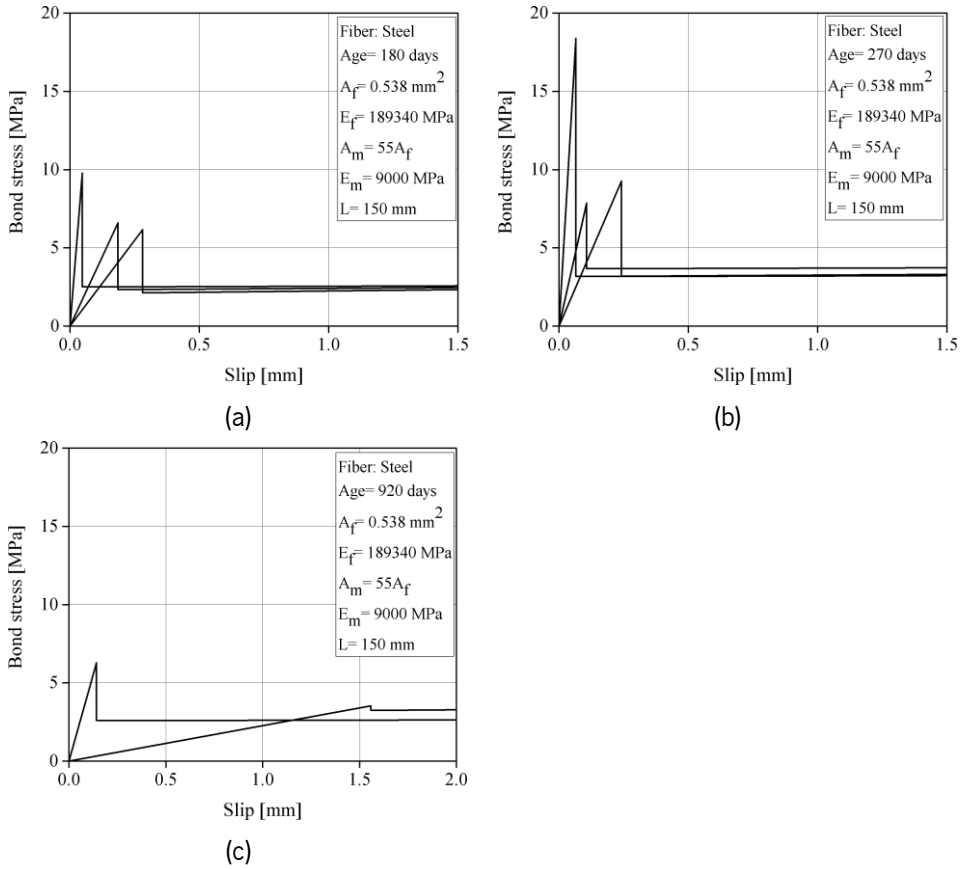

Fig. 7-23. Bond-slip law curves of the steel-based TRM at different mortar ages under the outdoor condition: (a) 180 days; (b) 270 days; (c) 920 days.

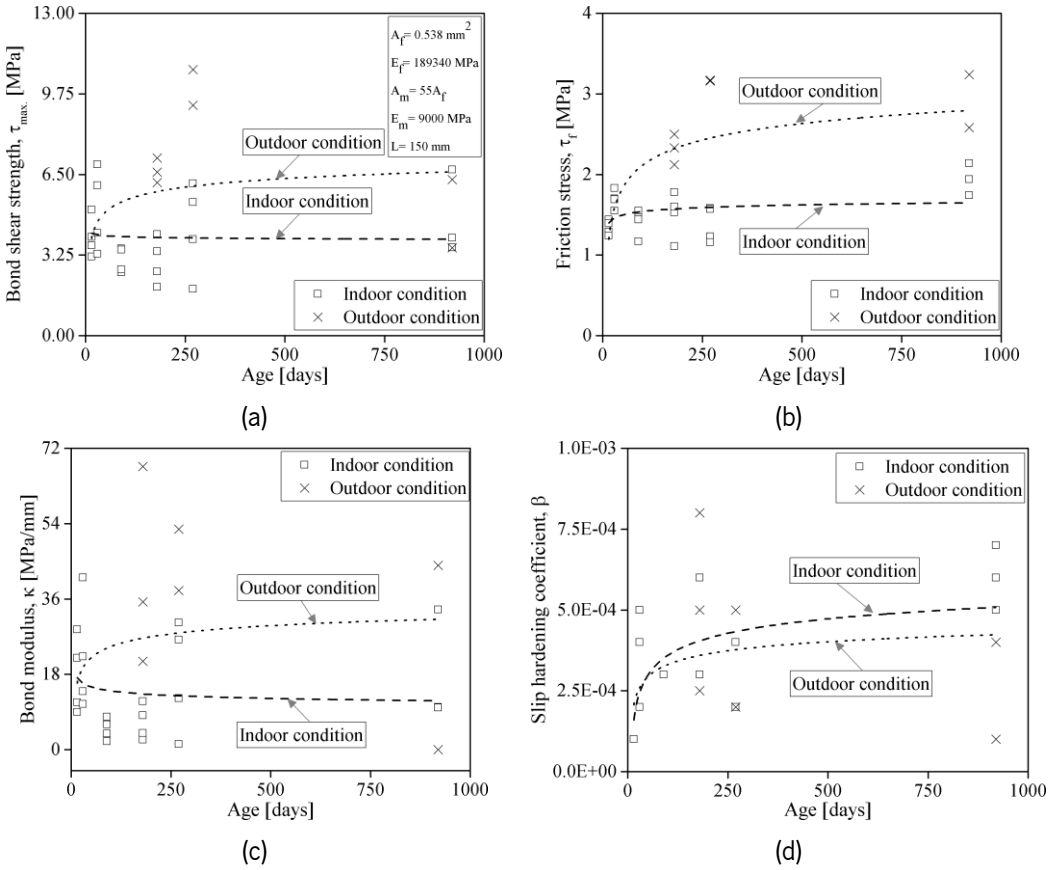

Fig. 7-24. Bond-slip law parameters of the steel-based TRM: (a) bond shear strength; (b) friction stress; (c) bond modulus; (d) slip hardening coefficient.

Table 7-9. Bond-slip laws of the steel-based TRM aged under indoor and outdoor conditions*.

Condition	Age [days]	τ_{max} [MPa]	τ_f [MPa]	κ [MPa/mm]	β
Indoor	15	3.97 (18)	1.34 (6)	17.72 (45)	0.0001 (0)
	30	5.10 (28)	1.69 (6)	22.06 (53)	0.0004 (29)
	90	3.05 (15)	1.42 (10)	4.93 (45)	0.0003 (0)
	180	3.01 (27)	1.51 (16)	6.52 (55)	0.0005 (33)
	270	4.32 (38)	1.39 (14)	17.56 (66)	0.0003 (33)
	920	4.73 (30)	1.94 (8)	17.92 (62)	0.0006 (14)
Outdoor	180	6.64 (6)	2.32 (7)	41.36 (47)	0.0005 (44)
	270	10.01 (7)	3.17 (0)	45.34 (16)	0.0004 (43)
	920	4.92 (28)	2.91 (11)	22.00 (100)	0.0003 (60)

*CoV of the results is given in percentage inside parentheses

Fig. 7-25 and Fig. 7-26 show the bond-slip law curves of the glass-based TRM at different ages under indoor and outdoor conditions. The changes in the bond-slip law parameters are shown in Fig. 7-27, Table 7-10. The bond strength, τ_{max}, is always higher in outdoor aged samples than indoor ones (almost twice at 920 days), as shown in Fig. 7-27a. On the other hand, the frictional stress, τ_f, shows an incremental

trend (with higher initial rates) in samples under indoor conditions, in contrast to the outdoor aged samples, in which a significant deterioration can be observed from 270 to 920 days. By contrast, the bond modulus, κ, and slip hardening coefficient, β, do not show a significant change in indoor aged samples but increase significantly with time in outdoor aged samples. These observations can show the effect of higher hydration of the mortar M1 on the parameters of the bond-slip law.

Table 7-10. Bond-slip laws of the glass-based TRM aged under indoor and outdoor conditions*.

Condition	Age [days]	τ_{max} [MPa]	τ_f [MPa]	κ [MPa/mm]	β
Indoor	15	1.97 (16)	1.03 (22)	6.46 (35)	0.009 (34)
	30	2.92 (28)	0.65 (34)	14.04 (49)	0.017 (51)
	90	5.38 (24)	0.86 (28)	18.57 (28)	0.028 (29)
	180	2.73 (24)	1.25 (11)	10.35 (69)	0.009 (76)
	270	2.88 (45)	0.91 (34)	11.70 (92)	0.014 (111)
	920	5.43 (37)	1.64 (12)	15.51 (63)	0.013 (58)
Outdoor	180	6.62 (32)	1.6 (12)	26.20 (48)	0.007 (38)
	270	8.94 (9)	1.37 (14)	51.17 (50)	0.013 (28)
	920	8.81 (6)	0.49 (14)	101.06 (3)	0.056 (21)

*CoV of the results is given in percentage inside parentheses

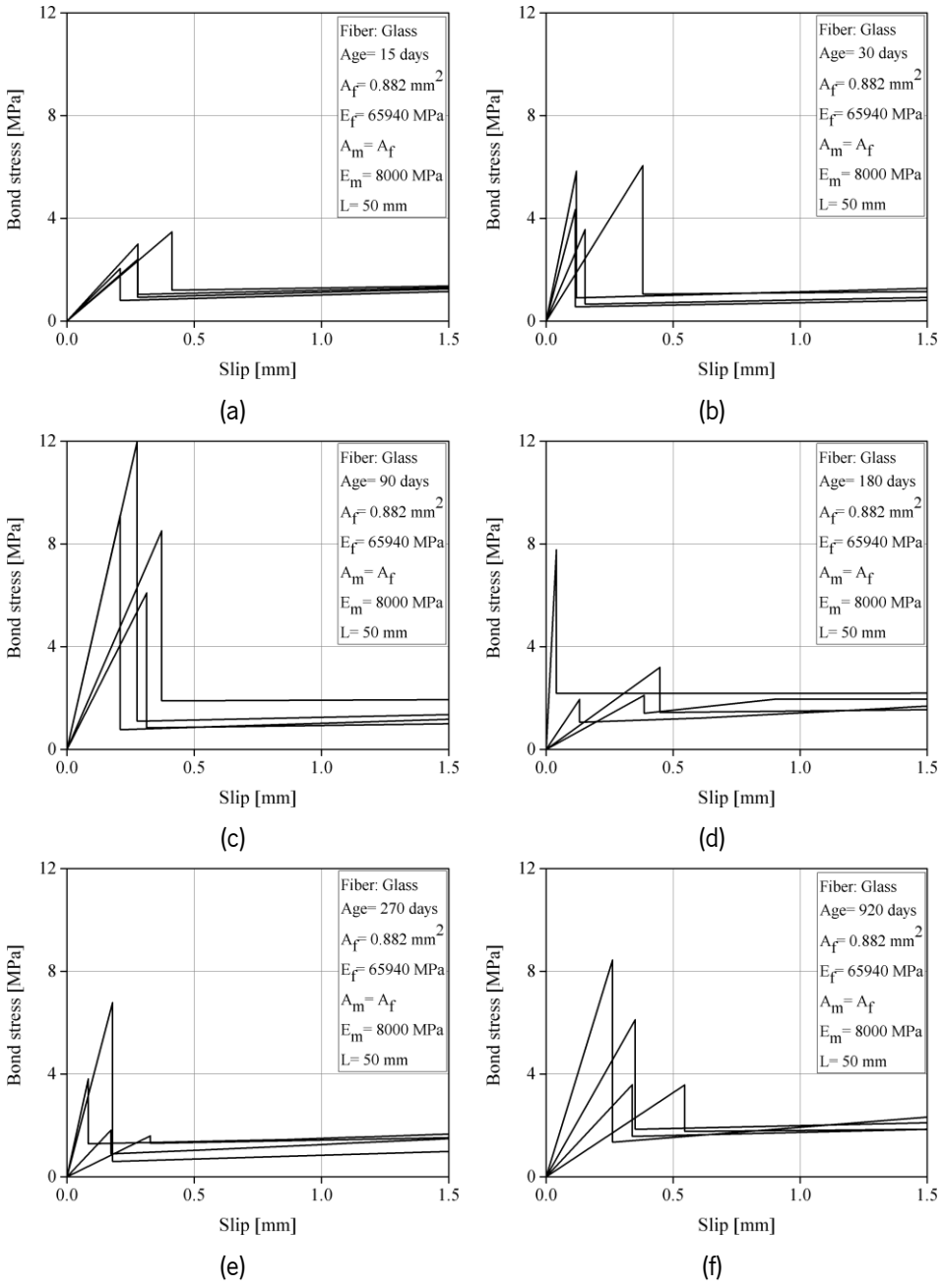

Fig. 7-25. Bond-slip law curves of the glass-based TRM at different mortar ages under indoor condition: (a) 15 days; (b) 30 days; (c) 90 days; (d) 180 days; (e) 270 days; (f) 920 days.

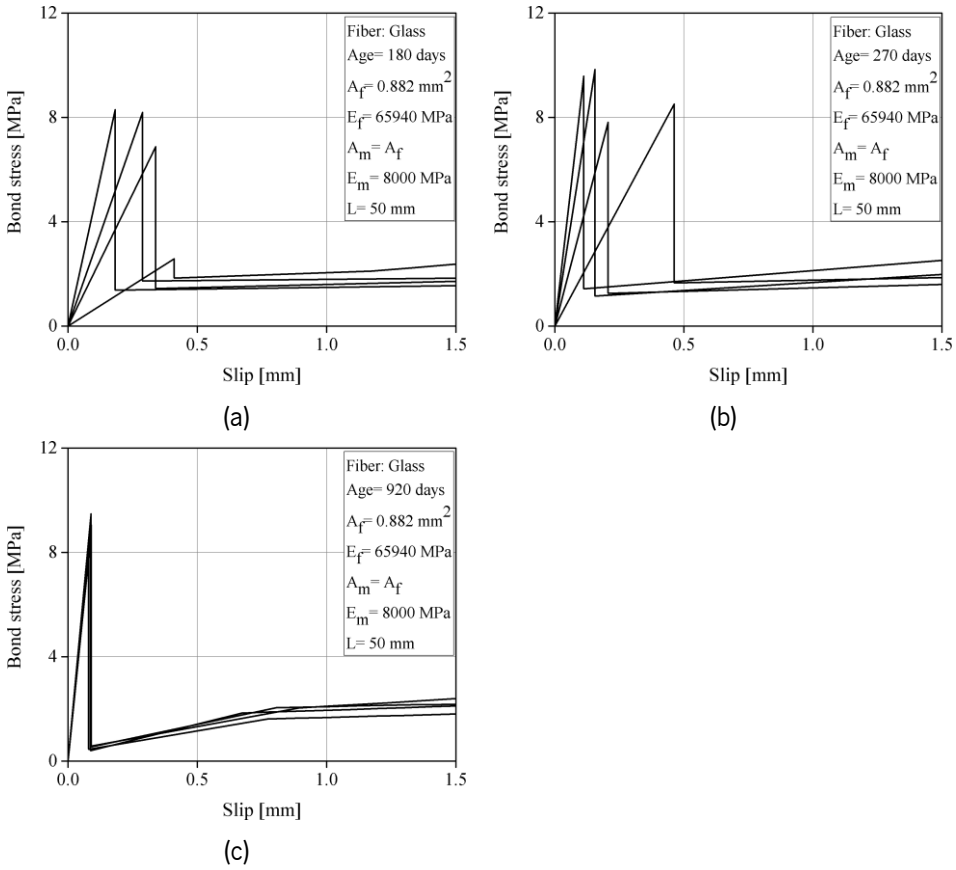

Fig. 7-26. Bond-slip law curves of the glass-based TRM at different mortar ages under the outdoor condition: (a) 180 days; (b) 270 days; (c) 920 days.

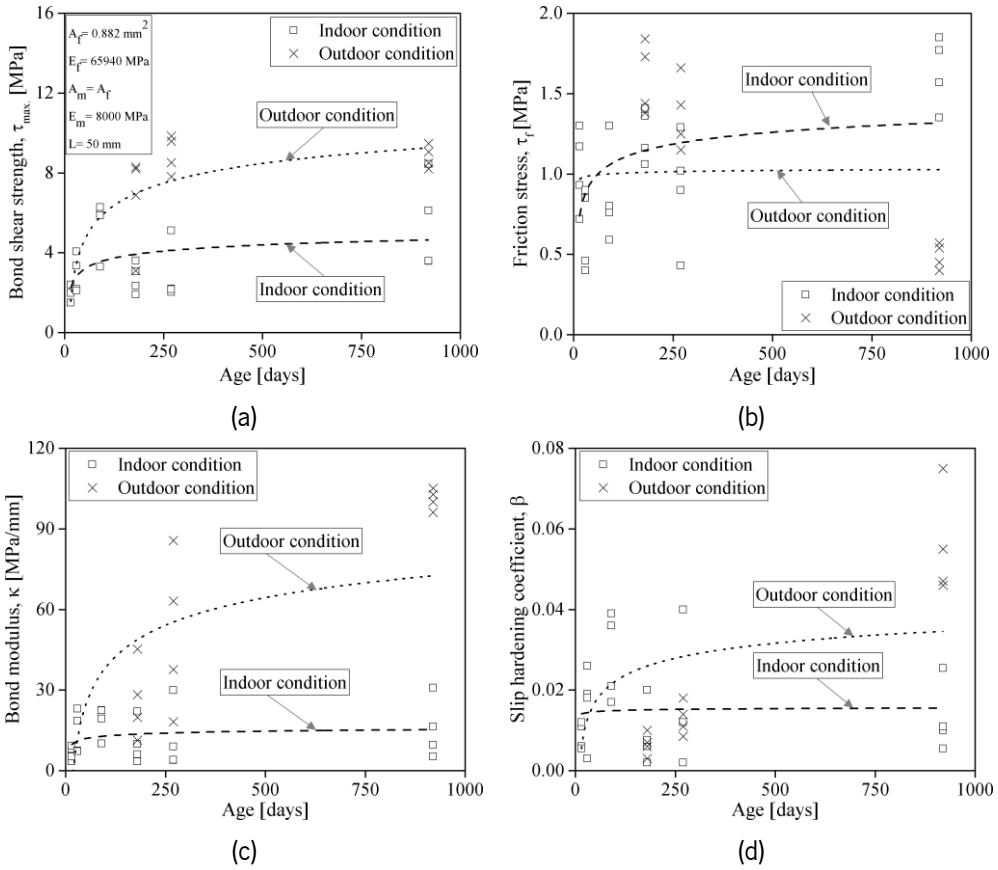

Fig. 7-27. Bond-slip law parameters of the glass-based TRM: (a) bond shear strength; (b) friction stress; (c) bond modulus; (d) slip hardening coefficient.

7.1.7. Effect of Freeze-thaw condition

The bond-slip laws are also derived using stress-based analytical modeling method 1 from the experimental load-slip curves of specimens under the FT conditions (section 5.9.1). Fig. 7-28a-d presents the changes in the bond-slip law parameters under the control and the FT conditions. Also, Table 7-11 reports the average of these parameters for each test series. By increasing the number of exposed cycles, the τ_{max}, κ, and β show an increasing trend, whereas the τ_f decreases. Since the bond parameters also show a decreasing trend (see section 5.9.1), it is possible to conclude that the glass-based TRM system is more responsive to the frictional shear strength than to the bond shear strength.

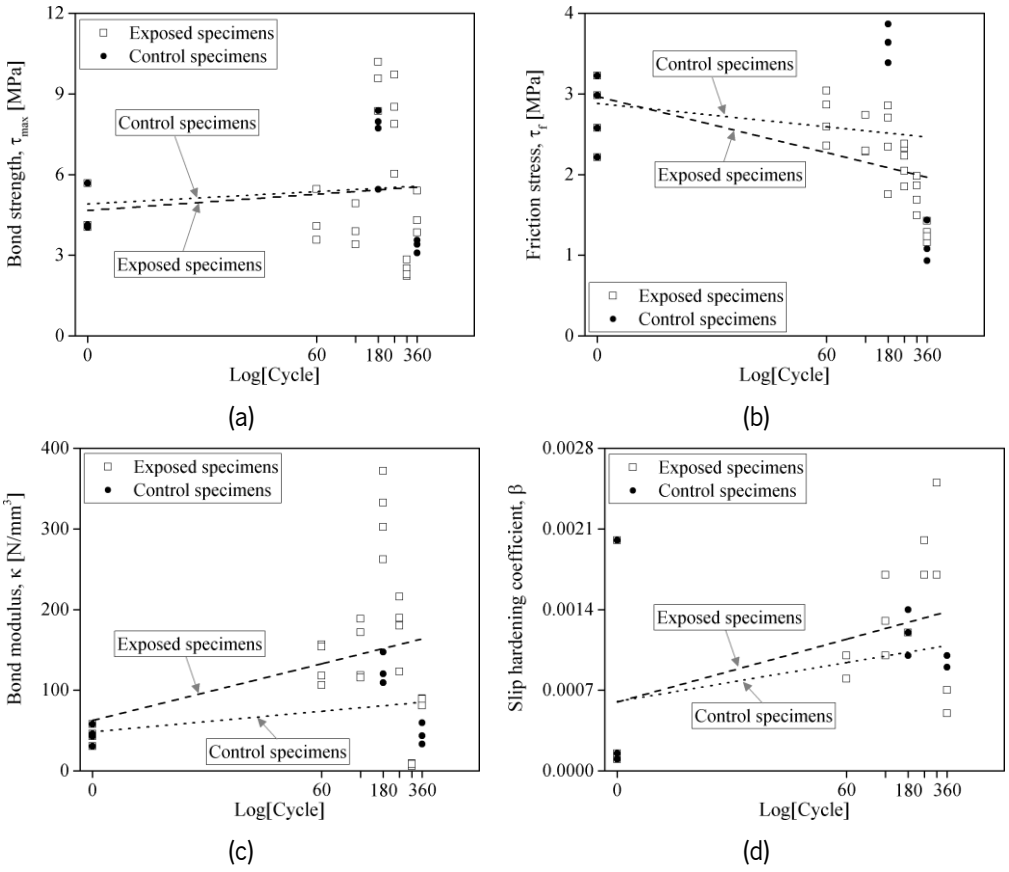

Fig. 7-28. The changes in bond-slip law parameters under the FT conditions (b) bond shear strength; (c) friction stress; (d) bond modulus; (e) slip hardening coefficient.

Table 7-11. Bond-slip laws of the glass-based TRM aged under the control and the FT conditions*.

Name	τ_{max} [MPa]	τ_f [MPa]	κ [N/mm^3]	β [-]
PC0	4.6 (16)	2.7 (14)	44.3 (22)	0.0006 (139)
PC180	7.4 (15)	3.6 (5)	125.7 (13)	0.0012 (14)
PC360	3.3 (6)	1.1 (18)	45.5 (24)	0.001 (4)
PE60	4.4 (18)	2.7 (11)	126 (16)	0.0009 (10)
PE120	4.1 (16)	2.4 (9)	148.5 (22)	0.0013 (19)
PE180	9.4 (8)	2.4 (18)	317.3 (13)	0.0012 (0)
PE240	8 (17)	2.2 (9)	177.1 (19)	0.0019 (8)
PE300	2.5 (10)	1.8 (10)	8 (20)	0.002 (19)
PE360	4.5 (14)	1.3 (8)	86.7 (5)	0.0006 (16)

*CoV of the results is given in percentage inside parentheses

7.2. Crack spacing prediction of TRM composites

This section utilizes the results of the tensile and pull-out tests (TC0 and PC0, respectively) performed under freeze-thaw conditions. The tests were performed on the glass-based TRM composites constructed with mortar M1. Sections 5.9.1 and 5.9.2 provide the experimental results.

The ACK (Aveston–Cooper–Kelly) theory is used here to calculate/predict the saturation crack spacing in the tensile specimens. Based on this model, the saturation crack spacing (X) can be obtained by expressing the force equilibrium along the loading axis of the yarns [238,239]:

$$X = 1.337 \frac{\upsilon_m r_f \sigma_{mu}}{\upsilon_f 2\tau_f} \qquad \text{Eq. 7-60}$$

υ_f and υ_m are the volumetric fractions of the yarns, and the mortar, respectively. υ_f is calculated as the ratio between the yarn area mesh and the average cross-section of the specimens (υ_f= 0.00335), while υ_m is equal to 1-υ_f. r_f is the yarn/cord radius equal to 0.5298 mm for glass yarns (assuming a circular section area). τ_f is the frictional shear strength at the yarn interface and the mortar obtained from the pull-out tests as 2.3 MPa. Finally, σ_{mu} is the direct tensile strength of the mortar. In the absence of experimental results, this value can be obtained from the compressive, flexural, or splitting strength [240], as calculated and presented in Table 7-12. It can be observed that the mortar tensile strength values calculated from these formulations are very similar. Having calculated the τ_f and σ_{mu}, Eq. 2-1 is used to calculate the saturation crack spacing, see Table 7-12. It can be observed that the crack spacing is predicted to be around 86-92 mm, which represents a 10-15% error with respect to the experimental results.

Table 7-12. Prediction of saturated crack spacing.

Calculating tensile strength by	σ_{mu} [MPa]	$X_{nom.}$ [mm]	$X_{nom.}/X_{exp.}$ [%]
compressive strength (f_{ck})	$0.3\left(f_{ck}\right)^{2/3} = 0.3\left(16.8\right)^{2/3} = 1.97$	91	90
flexural strength ($f_{ctm.fl}$)	$\frac{0.06h_b^{0.7}}{1+0.06h_b^{0.7}} f_{ctm.fl} = \frac{0.06\times 40^{0.7}}{1+0.06\times 40^{0.7}} 4.5 = 1.99$	92	91
splitting strength ($f_{ctm,sp}$)	$2.2\left(f_{cm}\right)^{-0.18} f_{ctm,sp} = 2.2\left(16.8\right)^{-0.18} \times 1.4 = 1.85$	86	85

7.3. Masonry panels

The nominal shear and flexural strength of masonry panels before and after strengthening with glass-based TRM composites are calculated here. For this aim, the nominal strengths are verified with the experimental results of panels used in section 6.1 (the effect of surface treatment). In the following sections, the mathematic formulations are presented.

7.3.1. Prediction of panels shear strength

The shear strength of IU panels can be computed based on the failure mode [139,141,144,241]: the shear sliding, the shear friction, the diagonal tension, and the toe crushing. Since sliding along the mortar joint was the failure mode of IU panels, their shear strength (V_{ss}) can be calculated as follows:

$$V_{ss} = \frac{\tau_0}{1-\mu_0 \tan\theta} A_n \qquad \text{Eq. 7-61}$$

where τ_0 is the shear bond strength obtained from the shear strength of masonry prisms at 28 days (τ_0= 0.26 MPa, based on [242]), and μ_0 is the coefficient of internal shear friction in mortar joint equal to 0.3 reported in other studies [139,144]. Other parameters (θ and A_n) are defined in section 6.1.1. Therefore, V_{ss} is equal to 20.06 kN, showing a 51% error to the experimental results. This difference can result from the μ_0 value. Paulay and Priestly [243] proposed that μ can be between 0.3 and 1.2. If μ is equal to 0.66, the V_{ss} will be 41.3 kN, equal to the experimental mean value of IU panels.

The nominal shear capacity (V_n) of TRM-strengthened panels, based on ACI 549.4R-13 [244], consists of the shear strength provided by the masonry (V_m) and the TRM composites (V_f), as shown in Appendix III:

$$V_n = V_m + V_f \qquad \text{Eq. 7-62}$$

Since all strengthened-masonry panels failed under diagonal tension, the masonry shear strength can be calculated as follows:

$$V_m = \frac{\tan\theta + \sqrt{21.16 + \tan^2\theta}}{10.58} f'_t A_n \left(\frac{L'}{H_w}\right) \qquad \text{Eq. 7-63}$$

where f'_t is the tensile strength of masonry and equal to $0.67\sqrt{f'_m}$, in which f'_m is the compressive strength of masonry (f'_m= 11.1) as reported by [139,141,144], and other parameters (θ, A_n, L', and H_w) are defined in section 6.1.1. Therefore, the masonry shear strength (V_m) is obtained as 65 kN, which is higher than V_{ss}, and the experimental result of IU panels is due to considering different failure modes.

The shear capacity provided by the TRM composites (V_f) can be calculated as [244]:

$$V_f = 2nA_f L' f_{fv} \quad \text{Eq. 7-64}$$

where n and A_f are the number of fabric layers (n= 1) and area of fabric per unit width in both directions (A_f= 0.07054mm²/mm). f_{fv} is the tensile strength in the TRM reinforcement, which is equal to:

$$f_{fv} = E_f \varepsilon_{fv}, \varepsilon_{fv} = \varepsilon_{fu} \leq 0.004 \quad \text{Eq. 7-65}$$

where E_f and ε_{fv} are the tensile modulus of elasticity of cracked TRM and the design tensile strain of TRM composites, respectively [244]. Based on ACI 549.4R-13 [244], ε_{fv} should be equal to the ultimate tensile strain of TRM composites (ε_{fu}= ε_3= 0.0119 from the first row of Table 5-24) and less than 0.004, as presented in Eq. 2-1. It seems this limitation is because of avoiding large cracks in the TRM composites [140]. By examining the tensile behavior of TRM composite in this study (see Fig. 5-46a and Table 5-24), it can be seen that ε_{fv} equal to 0.004 occurs precisely at the crack development stage. Having E_f= 62700 MPa from the average of the experimental tensile tests (see Table 5-24) and ε_{fv}= 0.004, f_{fv} can be obtained as 250.8 MPa. Replacing this value in Eq. 7-64 will lead to a V_f value of 19 kN. Adding Eq. 7-63 to Eq. 7-64 will lead to a total shear capacity of the strengthened panels of 84 kN, which is 33% and 44% lower than the experimental results of ISa and ISb panels, respectively (Table 7-13). This observation is also in agreement with the findings of other studies [139,140,144]. One possible reason for such a difference between the analytical and experimental results is the erroneous estimation of ε_{fv} in Eq. 2-1 and the fact that it is limited to 0.004. If ε_{fv} is considered equal to 0.0119, V_f and V_n will be equal to 56.8 kN and 121.8 kN, respectively, which shows a 3% and 19% error to the experimental results ISa and ISb panels, respectively.

Table 7-13. Prediction of the nominal shear (V_n) and flexural (M_n) capacity.

Model	f_{fv} [MPa]	V_f [kN]	V_n [kN]	V_n/P_{max} [%]		f_{fe} [MPa]	$M_{n,PS}$ [kN.m]	$M_{n,NS}$ [kN.m]	M_n/M_{max} [%]			
				ISa	ISb				PSa	PSb	NSa	NSb
ACI [244]	250.8	19.1	84.0	67	56	520.4	0.80	0.63	35	31	28	32
Combination of pull-out (50 mm) and tensile behavior	452.5	34.5	99.5	79	66	452.5	0.70	0.55	30	27	25	28
Combination of single-lap (SL100-b) and tensile behavior	486.8	37.1	102.1	81	68	486.8	0.75	0.59	33	29	26	30
Combination of pull-out (100 mm) and tensile behavior	793.3	60.4	125.4	99	83	793.3	1.21	0.95	53	47	43	48

Another method to determine f_{fv} is combining the results of the TRM-to-substrate bond and direct tensile tests performed on the yarn [245]. Such a combination, presented in Fig. 7-29, allows the calculation of the effective tensile capacity of the textile under more realistic boundary conditions. Here, the average pull-out load-slip curves obtained from samples with 50 mm and 100 mm bond length are also presented and used to calculate this load (values are presented in Table 7-13). In Fig. 7-29, more details about the single-lap (SL100-b), pull-out- 50 mm (GS50-C0), and pull-out- 100 mm (GS100-C0) are provided in sections 5.6.1 and 5.9.5. These three values are then used for predicting the TRM shear contribution (V_f) to obtain the total shear capacity, as presented in Table 7-13. In this method, the error in the prediction of V_n is less (1-21% for ISa panels and 17-34% for the ISb panels, in general). A comparison between the V_f obtained from the single-lap, and pull-out test results shows that although SL100-b specimens have a longer bond length than the pull-out specimens with 50 mm embedded length, they are similar tensile capacity and, consequently, V_f can be obtained from them. Also, the pull-out specimens with 100 mm embedded length show a higher utilization of tensile capacity than the single-lap samples with the same embedded length because of the difference in the boundary conditions in these two test setups. Overall, it appears that the single-lap test results are more suitable for calculating the tensile capacity of TRM systems due to the more realistic boundary conditions imposed on the samples in this test setup. However, it should also be noted that single-lap shear bond tests represent a specific case where the crack surface is perpendicular to the fabric direction. In reality, the cracks occur at an angle to the fabrics, leading to the involvement of transverse fabric in bidirectional grids. These, which can affect the utilized tensile capacity of the fabrics, are not considered when single-lap shear bond tests are used to calculate f_{fv}.

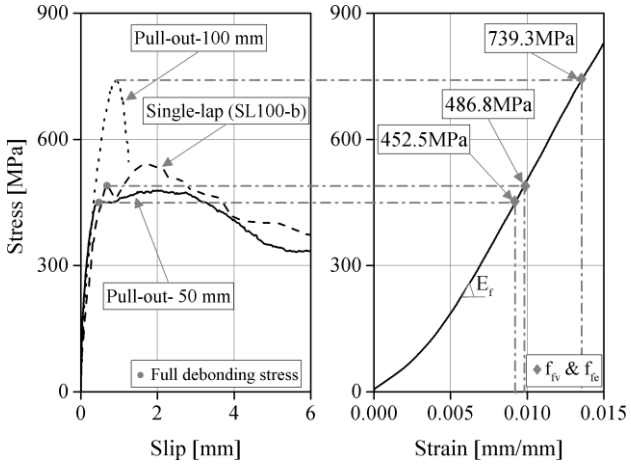

Fig. 7-29. Interaction between bond responses and tensile stress-strain of the yarn.

7.3.2. Prediction of panels flexural strength

The nominal flexural strength of unreinforced masonry panels can be calculated as follows [224]:

$$M_{Rd} = S_{modulus} f_{xk} \quad \text{Eq. 7-66}$$

where $S_{modulus}$ is the section modulus of un-crack wallets (7×10^5 mm^3 and 5.5×10^5 mm^3 for PU and NU panels, respectively). f_{xk} is the flexural strength of masonry and can be calculated based on the masonry unit type and the joint mortar compressive strength [224]. Since the flexural strength of masonry did not measure in this study, f_{xk} is used from what was proposed by EN 1996-1-1 [224]. Hence, f_{xk} is equal to 0.1 MPa and 0.4 MPa for PU and NU panels, respectively. Replacing S and f_{xk} in Eq. 2-1, M_{Rd} can be obtained for PU and NU panels as 0.07 kN.m and 0.22 kN.m, respectively, showing a 22% and 69% error, in contrast to the experimental results. This difference can be due to the estimated flexural strength of masonry (f_{xk}).

As for the TRM-strengthened masonry, the nominal flexural strength (M_n) can be calculated following ACI 549.4R-13 [244] formulations:

$$M_n = A_f b_m f_{fe}\left(t + \frac{t_c}{2} - \frac{\beta_1 c}{2}\right) \quad \text{Eq. 7-67}$$

$$f_{fe} = E_f \varepsilon_{fe}, \varepsilon_{fe} = 0.7\varepsilon_{fu} \le 0.012$$

where A_f is the fabric area per unit width (A_f= 0.03572 mm^2/mm), and f_{fe} is the effective tensile stress level in the TRM composite. Also, t and t_c, equal to 100 mm and 10 mm, are masonry wallet and TRM composite thicknesses. c is the depth of the effective compressive block (see Appendix IV), and β_1 is a stress block coefficient equal to 0.7. ε_{fe} is the effective tensile strain level in the TRM, and ε_{fu} is the ultimate tensile strain of TRM composites (Table 5-24, TC0). It should be mentioned that since the masonry compressive strength (f'_m) only was measured perpendicular to the flatwise surface of the brick, f'_m is considered the same value for both PS and NS panels. In Eq. 2-1, it is assumed that plane sections remain plane after loading, TRM has a linear behavior to failure neglecting its contribution before cracking, and the masonry tensile strength is neglected. Appendix IV presents the analytical predictions under both failure directions. M_n is equal to 0.80 kN.m and 0.63 kN.m for PS and NS, respectively, lower than the experimental results. Table 7-13 shows the proportion of M_n to the maximum flexural strength of PS and NS experiments representing a 65-72% error. This observation is also in agreement with the findings of other studies [139,144,246].

Based on the approach presented in section 7.3.1 (the combination of the bond response and the yarn tensile behavior), the effective tensile stress (f_{fe}) level in the TRM composite and the nominal flexural strength (M_n) of PS and NS are presented in Table 7-13. Combining the pull-out response with 50 mm

embedded length and the yarn tensile behavior shows a 70-75% error to the experimental results (see Table 7-13). The error resulted from the single-lap shear test (SL100-b), and the pull-out response in 100 mm bond length is 67-74% and 47-57%, respectively. It is obvious that all these methods produce a significant error in the prediction of the flexural capacity of TRM-strengthened masonry.

7.4. Main conclusions

In this study, a bond-slip law has been developed to help predict pull-out test results more accurately. In the proposed model, adhesives and friction bonds were taken into account. In addition, the nominal shear and flexural strength of the masonry panels without and with glass-based TRM composite were calculated and compared with experimental results. On the basis of the obtained results, it can be said that:

- In the analytical and numerical modeling, bond-slip laws were extracted from the experiments for each test setup. The optimum mortar effective area (A_m) was observed to have an important effect on the convergence of the results and on the obtained bond-slip law.
- The results of different test setups led to different bond-slip laws due to the differences in load-slip curves.
- By considering the slip hardening and softening effects observed in experimental results, the proposed bond-slip law and analytical solution may predict the pull-out behavior of a range of TRM composites.
- The analytical results showed that in both steel and glass-based TRMs, full debonding (corresponding to the initiation of the dynamic stage in the bond behavior) occurs at the peak load. This observation was verified with experimental results.
- It was also observed that the bond-slip laws extracted from pull-out tests performed on steel-based TRM samples with bond lengths higher than the effective embedded length (in this case, 150 mm embedded length) could be directly used for the prediction of the bond behavior in samples with other embedded lengths.
- Bond-slip law parameters of TRM composites at the indoor condition showed generally lower value compared to outdoor conditions. Meanwhile, the outdoor condition caused the bond-slip law parameter to improve.
- The ACK theory provided satisfactory predictions of crack spacing in tensile test samples when combined with pull-out results.

- To predict the capacity of strengthened panels, it was necessary to calculate the textile contribution to the load resistance of the whole system. Single-lap test results seem to be suitable for calculating the effective tensile capacity of TRM systems.

Chapter 8: Conclusions and future work

8.1. Experimental campaign

8.1.1. Material characterization

- Regarding brick moisture content, the results indicated that completely dry brick showed higher strength (compressive, flexural, and elastic modulus). The higher the moisture contents of the brick, the lower its strength.
- It was observed that extruded solid clay bricks show direction-dependent mechanical and transport properties. The capillary absorption coefficient and moisture absorption rate of the bricks in the widthwise direction was highest. This indicates that when fresh mortar is applied on the flatwise of the brick's surface (as is done in single-lap shear tests on TRM-strengthened bricks), the brick absorbs less water from the mortar compared to when it is applied on its widthwise (as is the case in real practice). The final bond performance will therefore be different, hence, questioning the suitability of single-lap shear tests when single bricks are used as the substrate.
- The mechanical and physical characterization tests performed on constituent materials showed the importance of curing conditions on the development of mechanical properties and pore structure of lime-based mortars. Although this importance varied in two mortars studies here, overall, the mechanical properties were improved when the samples were cured under higher humidity conditions (either under plastic or in high humidity rooms). The drying shrinkage, again dependent on the type of mortar, was also higher in specimens cured under plastic for seven days compared to those cured for only one day.
- It was examined the influence of indoor and outdoor aging on two lime-based mortars. The mechanical properties of the mortar were studied comprehensively through experimental investigation. The results indicated that in lime-based TRM composites, special attention needs to be given to the hydration degree of the mortar and its effects on the short-term and long-term performance of those composites. The 30 days curing testing age, as usually used for cementitious matrices, does not seem to be particularly a good reference for hydraulic lime-based TRMs. In addition, the large variety of the characteristics of the existing lime-based mortars makes it difficult to propose a specific representative age for the long-term behavior of those composites. The experimental results showed a good correlation between the changes in the textile-to-mortar bond behavior and the flexural strength of the mortar. Flexural strength is, therefore, proposed to be used as an indicator for evaluating the changes in the response of lime-based TRMs in the lack of more detailed results.

- The mechanical properties of the mortar M1 improved slightly under the considered FT conditions. Similar behavior was also observed for the control specimens. It can be deduced that the hardening process continued in the mortar even after 360 cycles (337 days). The detrimental effects of the FT conditions considered here were less than its effects on promoting the mortar hydration. This can be due to the fact that although 90% RH was considered in the FT exposure conditions, this might not have been sufficiently high for saturating the samples.
- The mechanical properties of the glass fibers were not affected by the FT conditions, as expected. However, the tensile strength of steel fibers decreased slightly.

8.1.2. Effect of the test setup

The obtained results from the effect of test setup on the bond behavior of textile-to-mortar showed the following conclusions:

- The results showed that the pull-push test setup when the free length of the fiber was embedded in an epoxy resin (pull-push II setup) was the most reliable test setup and produced the lowest variation of the results (CoVs). The embedment of the fibers in the free length with a resin block prevented the premature failure of the fibers. It also facilitated the attachment of the LVDTs for slip measurements during the tests. The advantage of using the block resin became even clearer when fibers with low axial stiffness or with a woven structure were under investigation. Installation of the specimens on the test setup when the fibers were not embedded in the epoxy resin (case of pull-push I in the current study) was also found very challenging and time-consuming. Application of a pre-loading was also necessary for these specimens before performing the tests to facilitate the LVDTs attachment.
- As for the preparation of the specimens, ensuring the straight alignment of the fibers in the mortar was also very complicated when cylindrical mortar specimens (case of pull-push I in the current study) were used. This was resolved by designing disk-shaped molds that allowed the application of the mortar in two layers parallel to the fiber embedment direction and the perfect alignment of the fibers (case of pull-push II and pull-pull configurations).
- The contribution of the mortar in resisting tensile forces in the pull-pull configuration led to larger experimental peak load and toughness in comparison to the pull-push configuration. It was also observed that the gripping of the mortar from the bottom in this configuration could lead to mortar cracking/crushing before performing the tests.

8.1.3. Effect of bond length

The effect of fiber embedded length on the fiber-to-mortar bond response in these composites was deeply investigated. The main focus was on the pull-out response of steel-based and glass-based TRMs as two common strengthening systems utilizing a pull-push test configuration. In general, the following was observed:

- The effect of embedded length was investigated by testing steel-based TRMs with 50, 100, 150, and 200 mm embedded length and glass-based TRMs with 50, 75, and 100 mm embedded length. In the steel-based TRMs, the failure mode was slippage in all embedded lengths. With an increment of the embedded length, the initial stiffness of the pull-out curves and the slip corresponding to the peak load increased independently from the embedded length. It was also observed that the peak load reached its maximum value at a bonded length of 150 mm. These results suggest that the effective bond length in this system is around 150 mm. In glass-based TRMs, the failure mode changed from fiber slippage (in 50 mm) to mixed slippage and yarn rupture (in 75 mm) and yarn rupture (in 100 mm). This suggests that the effective bond length in this system is between 50 mm and 75 mm.

8.1.4. Effect of fiber configuration

A qualitative and quantitative investigation of fiber configuration effects on fiber-to-mortar bond performance in TRM composites has been conducted. The obtained results can be summarized as follows:

- By increasing the number of steel fibers in pull-out tests, the failure mode changed from pull-out (for single fiber) to pull-out and mortar cracking (for group fibers). This change of failure mode could be avoided by increasing the mortar thickness.
- The bond behavior of the unidirectional and bidirectional glass fiber mesh, especially in the nonlinear region, was completely different. It means that transverse elements had a considerable effect on the bond behavior. The toughness was also increased dramatically due to the presence of transverse elements.

8.1.5. Effect of slip rate

Displacement controlled pull-out tests were carried out under monotonic loading to investigate the textile-to-matrix load transfer mechanism in glass and steel TRM composites. The experimental setup was

designed to control the rate of the relative displacement (slip) between yarn (or cord) and matrix at the first bonded section. From the experimental analysis, the following conclusions can be drawn:

- The bond strength was affected by the slip rate at low rates (it was lower below 1 mm/min than beyond this threshold), whereas no significant variation of peak load was detected in faster tests (up to 20 mm/min). Despite the scatter of test outcomes (due to the brittle nature of the mortar matrices and of the adhesion phenomena investigated), similar trends were also observed for absorbed energy and stiffness, confirming the sensitivity to the slip rate in slow tests. Clearly, other TRM materials may exhibit different sensitivity, and the results obtained in this investigation are hardly extendable to composites with different fabrics and mortars, as well as to different manufacturing and curing conditions. It was also observed that in the glass TRMs, the intended slip rate was reached only after the peak load in samples tested under high slip rates.

8.1.6. Effect of cyclic loading

The load transfer mechanism in steel and glass-based TRM composites was also studied under cyclic loading. The main findings were obtained:

- The cyclic response was characterized by narrow unloading-reloading cycles, indicating a small amount of hysteretic energy. The cyclic curve was contained in the envelope of the monotonic one. Cyclic loading led to a pull-out strength degradation, especially after the first cycle and in the order of 25-35%. Its reduction with the increase of performed cycles indicated that a residual strength could possibly be identified. The stiffness degradation, instead, varied in the 5-15% range at small slips (less than 1 mm) and increased up to 50-75% at 15 mm slip for both the first and the second load cycled performed in the tests. The bidirectional glass mesh exhibited an effective interaction between fiber yarns, which was much less pronounced in the cords of the steel fibers that are not provided with weft (transversal) elements.

8.1.7. TRM-to-substrate bond behavior

The experimental campaign consisted of the role of surface treatment and bond length on the TRM-to-substrate bond behavior. In addition, a comparison was made between the pull-out and single-lap shear results. In light of the obtained results, it is possible to draw the following conclusions:

- The effect of surface preparation on the TRM-to-substrate bond behavior was significant. The sandblasted specimens showed a perfect bond at the TRM-masonry interface, while delamination was observed in the samples prepared with no surface treatment.

- The results showed that the bond response obtained in pull-out tests could be different from the results from single-lap shear tests. This was due to the different stress states and boundary conditions in these two test setups.
- The obtained bond behavior from the single-lap shear tests was the result of several concurrent mechanisms, including the bond at the interface of TRM-to-masonry, textile-to-mortar bond, mortar cracking, and splitting and unsymmetrical boundary conditions. The focus was on the fiber-to-mortar bond response in the pull-put tests. The stress state in the TRM composite in single-lap shear tests was more similar to reality, but the interpretation of the experimental results should be performed with care. Meanwhile, the pull-out tests were more suitable for characterization of the fiber-to-mortar bond behavior and presented an opportunity for extraction of the bond-slip laws for use in numerical simulations.

8.1.8. Effect of curing conditions

An experimental investigation on the effect of preconditioning and curing on the bond performance of two conventional TRM composites used to strengthen masonry substrates (fiber-to-mortar and TRM-to-substrate bond performance) was presented. Three substrate moisture conditions (dry, semi-saturated, and saturated) and three different curing conditions (PL-1, PL-7, RH-7) were considered for this purpose. Following is a summary of key conclusions about the obtained data:

- Curing conditions had a significant effect on the development of mechanical properties of mortar and the fiber-to-mortar bond behavior. The pull-out response of both steel- and glass-based TRMs was enhanced when the specimens were cured under high humidity conditions (RH-7) or under plastic (PL-7) for seven days compared to when those were cured under the plastic only for one day (PL-1). However, the curing conditions considered did not affect the overall shape of the load-slip curves or the failure mode of the specimens.
- It was observed that the initial water content of the substrate is the most critical parameter on the TRM-to-substrate bond behavior. Dry substrates absorbed water from the mortar and disrupted the chemical reactions of the mortar. Consequently, a poor bond between the mortar and the brick was formed; hence, the single-lap shear test samples failed by debonding at the TRM-to-substrate interface. Nevertheless, semi- or full saturation of the bricks led to the formation of a strong bond.

- The results show that TRM composites show better performance if the masonry substrate is properly conditioned before application. Covering the mortar surface with damp cloths and storing it under plastic for seven days (PL-7 condition) is helpful for hydraulic lime-based TRM composites.

8.1.9. Effect of mortar age

The effect of indoor and outdoor aging on the micro- and macro-mechanical behavior of two lime-based TRM composites was examined. A comprehensive experimental study was performed to investigate the changes of the textile-to-mortar bond behavior and the TRM tensile response until 920 days of aging. Taking into account the results obtained, it can be concluded the following:

- As expected, the mortar type was found to have a significant influence on the short-term and long-term bond performance and therefore cracking behavior of TRMs.
- In both steel and glass-based TRMs, TRMs under indoor conditions typically exhibited a lower performance when compared to outdoor ones. This was more noticeable in the steel-based TRM, which showed a much lower bond strength when cured under indoor conditions than outdoor conditions. Advanced curing conditions may be useful for accelerating hydration, such as autoclave and steam. Outdoor conditions in both systems led to better mechanical performance and led to the deterioration in the long term. The degree of this deterioration, which was significant in some cases, was observed to be dependent on the TRM type (fiber-mortar combination).
- The difference between the tensile response and cracking behavior of the TRM composites under indoor and outdoor conditions was also noticeable and was observed to be dependent on the TRM type. In the steel-based TRM, aging led to the decrement of the crack spacing and no specific change in the final tensile strength. Meanwhile, in the glass-based TRM, the effect of outdoor exposure was significant in terms of crack spacing (increased) and tensile strength (decreased).
- Due to the high humidity and rain observed under outdoor conditions, the hydration rate of the hydraulic lime-based mortars was more significant, which increased the strength of the specimens. In contrast, owing to the constant humidity inside the laboratory, the mortars showed lower hydration rates.

8.1.10. Effect of freeze-thaw conditions

The effect of freeze-thaw (FT) conditions on the micro-mechanical response of steel and glass-based TRM composites was also examined. The research items included the bond performance as a function of

embedded length, number of cords, presence of transverse fibers, and age. In general, the following conclusions can be drawn:

- The TRM tensile behavior, the bond behavior at the yarn-to-mortar, and the TRM-to-substrate bond behavior also showed a decreasing trend in some parameters under the FT condition, in contrast to the control specimens (at zero cycles).
- The pull-out response of the steel-based TRM with different bond lengths generally declined under both the control and the FT conditions. However, the impact of the FT conditions on the 50 mm bonded length samples were the harshest, and its adverse effects decreased by increasing the bond length.
- The effect of FT conditions on the glass-based TRM varied with embedded lengths varied. While 50 mm embedded length samples showed deterioration of the bond strength, 75 mm samples showed an enhancement of the bond strength. A similar observation was also found for the specimens cured in the lab conditions.
- The effect of FT conditions on the pull-out response of the group steel-based TRM was significantly different from the single cord samples. Steel-based TRM composites with different numbers of fiber showed different behavior under FT conditions. While both control and FT conditions led to enhancement of the bond performance in the samples reinforced with two cords, those conditions caused deterioration in single and four cord samples. While this requires further investigations, it shows the importance of considering the group behavior in closely distanced fabrics.
- The yarn configuration was also found to be important in glass-based TRMs. While the bond behavior of the specimens with transverse yarns enhanced under the FT conditions, the samples with group yarns showed a considerable deterioration similar to the one observed in single yarn samples.
- These observations show the importance of considering the actual architecture of the fabrics in experimental specimens for evaluating the mechanical and durability performance of TRM composites. Also, consideration of other FT exposure conditions is suggested to be considered in future studies.

8.2. Structural behavior

8.2.1. Mechanical performance of masonry panels

An understanding of the mechanical behavior of un-strengthened and reinforced masonry wallets was obtained. The role of sandblasting on the masonry surface was also investigated. As general conclusions, it can be stated that:

- An important effect of surface preparation was observed on the mechanical performance of TRM-strengthened masonry panels. The sandblasting had a significant influence on the in-plane response of TRM-strengthened panels, in contrast to the samples prepared with no surface treatment. However, this influence was less important in out-of-plane tests because of the tension-compression stresses introduced in the TRM system under the test setup boundary conditions.
- Application of one layer of glass-based TRM, used in this study, was observed to influence significantly the in-plane and out-of-plane response of masonry panels. Both the load and deformation capacity increased significantly. The failure mode of the wallets also changed from brittle in URM walls to pseudo ductile (limited crack development stage followed by brittle failure) in TRM-strengthened masonry.
- Comparing the experimental results obtained in this study with the ones available in the literature that were performed on similar materials showed the significant and simultaneous effect of age and curing conditions on the structural response of strengthened panels. This significant influence is expected to be dependent on the type of mortar used.
- The crack spacing diagonal compression samples were similar to the saturated crack spacing observed in tensile tests. However, the put-of-plane test samples showed a larger crack spacing due to the differences in these samples' stress conditions, which affected the bond behavior as the main controlling mechanism for mortar crack spacing.

8.2.2. Effect of freeze-thaw

The durability performance of TRM-strengthened masonry panels under freeze-thaw conditions was investigated. A series of experimental tests were considered at the structural level included diagonal compression tests and out-of-plane bending tests. The tests were performed on the un-strengthened and strengthened panels. In light of the obtained results, it is possible to draw the following conclusions:

- The FT conditions decreased the diagonal tensile and flexural strengths of the unreinforced panels when compared to the control specimens (at zero cycles).

- The diagonal tensile strength of the URM panels decreases under both conditions. Also, the strengthened panels showed a few degradations at the tensile stress. The durability of the TRM-strengthened panels under the FT condition was suitable so that their diagonal tensile strength and flexural strength basically did not change.

8.3. Analytical findings

8.3.1. Textile-to-mortar bond behavior

A bond-slip law for better prediction of pull-out test results has been proposed in this study. The proposed bond-slip law was implemented in a shear lag analytical model for simulation of the pull-out response. The solution to the analytical model was also modified for better consideration of the pull-out response in the dynamic stage. Some parameters such as the effect of the test setup, slip-hardening effect, efficiency of the model on different TRM composites, the effect of bond length, mortar age, and freeze-thaw conditions effects. The following conclusions can be made based on the obtained results:

- The analytical modeling helped in the extraction of the bond-slip laws from the experimental results corresponding to each test setup. It was observed that the selected effective area of mortar (A_m) had a fundamental role in the convergence of the results. This value also had a significant effect on the obtained bond-slip law; so that by increasing A_m, the bond strength, in both pull-push II and pull-pull increased, while the frictional strength experienced an opposite trend. After a systematic parametric study, an optimum value for this parameter was obtained and proposed. It was observed that the differences in the load-slip curves obtained from different test setups led to different bond-slip laws.
- The proposed bond-slip law and analytical solution could predict the pull-out response of a range of TRM composites considering the slip hardening and softening effects observed in the experimental results.
- The experimental results showed that in both steel and glass-based TRMs, full debonding (corresponding to the initiation of the dynamic stage in the bond behavior) occurs near the peak load. This information is vital for the solution of the differential equations used for the extraction of the bond-slip laws when free-end measurements are not available. This observation proves the hypothesis that the dynamic stage starts when the embedded length is completely debonded (u= L).

- It was also observed that the bond-slip laws extracted from pull-out tests performed on samples with bond lengths higher than the effective embedded length could be directly used for the prediction of the bond behavior in samples with other embedded lengths. This observation is essential as it provides a base for designing test programs to evaluate the bond-slip laws in TRM composites.
- TRMs under indoor conditions, whether steel or glass-based, had generally lower bond strength, friction stress, and bond modulus than those in the outdoors. As a result of the outdoor conditions, the bond-slip law parameter improved in both systems but deteriorated over time.
- When combined with pull-out tests results, the ACK (Aveston–Cooper–Kelly) theory provided satisfactory predictions of the crack spacing in tensile test samples.

8.3.2. Structural behavior

The analytical shear and flexural strengths of the masonry panels were calculated and compared to the experimental results. In light of the obtained results, the following conclusions can be drawn:

- Analytical prediction of the capacity of strengthened panels required calculation of the textile contribution to the resistance of the whole system. The existing formulations use the tensile capacity of the textile as an input. Single-lap test results seem to be suitable for calculating the effective tensile capacity of TRM systems. However, it should also be noted that single-lap shear bond tests represent a specific case where the crack surface is perpendicular to the fabric direction. In reality, the cracks occur at a certain angle with respect to the fabrics, which can also lead to the involvement of transverse fabric yarns in bidirectional grids. These, which can affect the utilized tensile capacity of the fabrics, are not taken into account and require further investigation.

8.4. Future work

Despite the large and comprehensive experimental campaign carried out, encompassing the study of several variables, a number of critical gaps still need to be addressed due to the lack of information available on the durability of TRM-strengthened masonry. The following are a few important steps to follow.

- While this study served as a benchmark for hygrothermal exposure situations under new test conditions, future works are suggested to consider the following parameter in terms of hygrothermal effects, larger cooling, and heating range, and a larger number of cycles. It is

important to determine these parameters for multilevel TRM systems in order to study their effectiveness on TRM composites.

- A special emphasis is also placed on tests of durability regarding other exposure conditions. To reach this goal, it is needed to consider alkaline, saline, and acid solutions as degradation agents. It is also advisable to perform these tests in two different ways: by immersion and dry-wet methods. It is important to carry out water immersion tests using different temperatures as well.
- For establishing a reliable link between accelerated and real exposure conditions, performing real exposure tests in different environmental regions and conditions is also of great importance. In addition, the effect of sustained load and fatigue loading should be considered as basically no reliable information exists on this topic.
- All of the proposed durability tests should be applied to the micro and macro-scale of TRM composite (from the bond to the structural level) in order to reach a comprehensive picture of the durability of the TRM system. Obtaining these results will be crucial to the development of durability-based design relationships.
- An in-depth numerical investigation of TRM composites, including modeling of the degradation phenomena, is needed to develop design codes. By using numerical methods, it is also possible to model and predict the long-term behavior of TRM composites.

Reference

[1] ICOMOS/ISCARSAH Committee, ICOMOS charter - Principles for the analysis, conservation and structural restoration of architectural heritage, 2003.

[2] R. Marques, P.B. Lourenço, Structural behaviour and design rules of confined masonry walls: Review and proposals, Construction and Building Materials. 217 (2019) 137–155. https://doi.org/10.1016/j.conbuildmat.2019.04.266.

[3] S.M. Raoof, L.N. Koutas, D.A. Bournas, Textile-reinforced mortar (TRM) versus fibre-reinforced polymers (FRP) in flexural strengthening of RC beams, Construction and Building Materials. 151 (2017) 279–291. https://doi.org/10.1016/j.conbuildmat.2017.05.023.

[4] T. Trapko, The effect of high temperature on the performance of CFRP and FRCM confined concrete elements, Composites Part B: Engineering. 54 (2013) 138–145. https://doi.org/10.1016/j.compositesb.2013.05.016.

[5] P.K.V.R. Padalu, Y. Singh, S. Das, Cyclic two-way out-of-plane testing of unreinforced masonry walls retrofitted using composite materials, Construction and Building Materials. 238 (2020) 117784. https://doi.org/10.1016/j.conbuildmat.2019.117784.

[6] S. De Santis, G. de Felice, F. Roscini, Retrofitting of masonry vaults by basalt textile-reinforced mortar overlays, International Journal of Architectural Heritage. 13 (2019) 1061–1077. https://doi.org/10.1080/15583058.2019.1597947.

[7] M.R. Valluzzi, V. Modena, Claudio, G. de Felice, Current practice and open issues in strengthening historical buildings with composites, Materials and Structures. 47 (2014) 1971–1985. https://doi.org/10.1617/s11527-014-0359-7.

[8] T. D'Antino, C. Papanicolaou, Mechanical characterization of textile reinforced inorganic-matrix composites, Composites Part B: Engineering. 127 (2017). https://doi.org/10.1016/j.compositesb.2017.02.034.

[9] A. Younis, U. Ebead, Bond characteristics of different FRCM systems, Construction and Building Materials. 175 (2018) 610–620. https://doi.org/10.1016/j.conbuildmat.2018.04.216.

[10] F. Ferretti, C. Mazzotti, FRCM/SRG strengthened masonry in diagonal compression: experimental results and analytical approach proposal, Construction and Building Materials. 283 (2021) 122766. https://doi.org/10.1016/j.conbuildmat.2021.122766.

[11] C. Papanicolaou, T. Triantafillou, M. Lekka, Externally bonded grids as strengthening and seismic retrofitting materials of masonry panels, Construction and Building Materials. 25 (2011) 504–514. https://doi.org/10.1016/j.conbuildmat.2010.07.018.

[12] F.G. Carozzi, A. Bellini, T. D'Antino, G. de Felice, F. Focacci, Ł. Hojdys, L. Laghi, E. Lanoye, F. Micelli, M. Panizza, C. Poggi, Experimental investigation of tensile and bond properties of Carbon-FRCM composites for strengthening masonry elements, Composites Part B: Engineering. 128 (2017). https://doi.org/10.1016/j.compositesb.2017.06.018.

[13] M. Leone, M.A. Aiello, A. Balsamo, F.G. Carozzi, F. Ceroni, M. Corradi, M. Gams, E. Garbin, N. Gattesco, P. Krajewski, C. Mazzotti, D. Oliveira, C. Papanicolaou, G. Ranocchiai, F. Roscini, D. Saenger, Glass fabric reinforced cementitious matrix: Tensile properties and bond performance on masonry substrate, Composites Part B: Engineering. 127 (2017). https://doi.org/10.1016/j.compositesb.2017.06.028.

[14] S. De Santis, F. Ceroni, G. de Felice, M. Fagone, B. Ghiassi, A. Kwiecień, G.P. Lignola, M. Morganti, M. Santandrea, M.R. Valluzzi, A. Viskovic, Round Robin Test on tensile and bond behaviour of Steel Reinforced Grout systems, Composites Part B: Engineering. 127 (2017) 100–120. https://doi.org/10.1016/j.compositesb.2017.03.052.

[15] A. Dalalbashi, B. Ghiassi, D.V. Oliveira, A. Freitas, Fiber-to-mortar bond behavior in TRM composites: effect of embedded length and fiber configuration, Composites Part B: Engineering. 152 (2018) 43–57. https://doi.org/10.1016/j.compositesb.2018.06.014.

[16] A. Dalalbashi, B. Ghiassi, D.V. Oliveira, A. Freitas, Effect of test setup on the fiber-to-mortar pull-out response in TRM composites: experimental and analytical modeling, Composites Part B: Engineering. 143 (2018) 250–268. https://doi.org/10.1016/j.compositesb.2018.02.010.

[17] A. Dalalbashi, B. Ghiassi, D. V. Oliveira, Textile-to-mortar bond behaviour in lime-based textile reinforced mortars, Construction and Building Materials. 227 (2019) 116682. https://doi.org/10.1016/j.conbuildmat.2019.116682.

[18] A. Dalalbashi, B. Ghiassi, D. V. Oliveira, Textile-to-mortar bond behavior: An analytical study, Construction and Building Materials. 282 (2021) 122639. https://doi.org/10.1016/j.conbuildmat.2021.122639.

[19] A. Dalalbashi, S. De Santis, B. Ghiassi, D. V. Oliveira, Slip rate effects and cyclic behaviour of textile-to-matrix bond in textile reinforced mortar composites, Materials and Structures. 54 (2021). https://doi.org/10.1617/s11527-021-01706-w.

[20] X. Wang, C.C. Lam, V.P. Iu, Comparison of different types of TRM composites for strengthening masonry panels, Construction and Building Materials. 219 (2019) 184–194. https://doi.org/10.1016/j.conbuildmat.2019.05.179.
[21] M. Harajli, H. Elkhatib, J.T. San-jose, Static and cyclic out-of-plane response of masonry walls strengthened using textile-mortar system, Journal of Materials in Civil Engineering. 22 (2010) 1171–1181. https://doi.org/10.1061/(ASCE)MT.1943-5533.0000128.
[22] F.A. Kariou, S.P. Triantafyllou, D.A. Bournas, L.N. Koutas, Out-of-plane response of masonry walls strengthened using textile-mortar system, Construction and Building Materials. 165 (2018) 769–781. https://doi.org/10.1016/j.conbuildmat.2018.01.026.
[23] G. Marcari, M. Basili, F. Vestroni, Experimental investigation of tuff masonry panels reinforced with surface bonded basalt textile-reinforced mortar, Composites Part B: Engineering. 108 (2017) 131–142. https://doi.org/10.1016/j.compositesb.2016.09.094.
[24] M. Basili, F. Vestroni, G. Marcari, Brick masonry panels strengthened with textile reinforced mortar: experimentation and numerical analysis, Construction and Building Materials. 227 (2019) 117061. https://doi.org/10.1016/j.conbuildmat.2019.117061.
[25] M. Shabdin, M. Zargaran, N.K.A. Attari, Experimental diagonal tension (shear) test of Un-Reinforced Masonry (URM) walls strengthened with textile reinforced mortar (TRM), Construction and Building Materials. 164 (2018) 704–715. https://doi.org/10.1016/j.conbuildmat.2017.12.234.
[26] H. Maljaee, B. Ghiassi, P.B. Lourenço, D. V Oliveira, Moisture-induced degradation of interfacial bond in FRP-strengthened masonry, Composites Part B. 87 (2016) 47–58. https://doi.org/10.1016/j.compositesb.2015.10.022.
[27] H. Maljaee, B. Ghiassi, P.B. Lourenço, D. V Oliveira, FRP– brick masonry bond degradation under hygrothermal conditions, Composite Structures. 147 (2016) 143–154. https://doi.org/10.1016/j.compstruct.2016.03.037.
[28] B. Ghiassi, D. V Oliveira, P.B. Lourenço, Hygrothermal durability of bond in FRP-strengthened masonry, (2014) 2039–2050. https://doi.org/10.1617/s11527-014-0375-7.
[29] B. Ghiassi, G. Marcari, D. V Oliveira, P.B. Lourenço, Water degrading effects on the bond behavior in FRP-strengthened masonry, Composites Part B. 54 (2013) 11–19. https://doi.org/10.1016/j.compositesb.2013.04.074.
[30] G. de Felice, S. De Santis, L. Garmendia, P. Larrinaga, P.B. Lourenço, D. V Oliveira, C.G. Papanicolaou, Mortar-based systems for externally bonded strengthening of masonry, Materials and Structures. 47 (2014) 2021–2037. https://doi.org/10.1617/s11527-014-0360-1.
[31] B. Ghiassi, D. V Oliveira, V. Marques, E. Soares, H. Maljaee, Multi-level characterization of steel reinforced mortars for strengthening of masonry structures, Materials and Design. 110 (2016) 903–913. https://doi.org/10.1016/j.matdes.2016.08.034.
[32] F.G. Carozzi, C. Poggi, Mechanical properties and debonding strength of Fabric Reinforced Cementitious Matrix (FRCM) systems for masonry strengthening, Composites Part B: Engineering. 70 (2015) 215–230. https://doi.org/10.1016/j.compositesb.2014.10.056.
[33] S. Barr, W.J. McCarter, B. Suryanto, Bond-strength performance of hydraulic lime and natural cement mortared sandstone masonry, Construction and Building Materials. 84 (2015) 128–135. https://doi.org/10.1016/j.conbuildmat.2015.03.016.
[34] V. Pavlík, M. Uzáková, Effect of curing conditions on the properties of lime, lime–metakaolin and lime–zeolite mortars, Construction and Building Materials. 102 (2016) 14–25. https://doi.org/10.1016/j.conbuildmat.2015.10.128.
[35] J. Lanas, J.L. Perez Bernal, M.A. Bello, J.I. Alvarez, Mechanical properties of masonry repair dolomitic lime-based mortars, Cement and Concrete Research. 36 (2006) 951–960. https://doi.org/10.1016/j.cemconres.2005.10.004.
[36] C. Groot, RILEM TC 203-RHM: Performance requirements for renders and plasters, Materials and Structures. 45 (2012) 1277–1285. https://doi.org/10.1617/s11527-012-9916-0.
[37] J. Lanas, J.I. Alvarez, Masonry repair lime-based mortars: Factors affecting the mechanical behavior, Cement and Concrete Research. 33 (2003) 1867–1876. https://doi.org/10.1016/S0008-8846(03)00210-2.
[38] R.M.H. Lawrence, T.J. Mays, P. Walker, D.D. Ayala, Determination of carbonation profiles in non-hydraulic lime mortars using thermogravimetric analysis, Thermochimica Acta. 444 (2006) 179–189. https://doi.org/10.1016/j.tca.2006.03.002.
[39] S. Yin, L. Jing, M. Yin, B. Wang, Mechanical properties of textile reinforced concrete under chloride wet-dry and freeze-thaw cycle environments, Cement and Concrete Composites. 96 (2019) 118–127. https://doi.org/10.1016/j.cemconcomp.2018.11.020.
[40] A. Caggiano, H. Xargay, P. Folino, E. Martinelli, Experimental and numerical characterization of the bond behavior of steel fibers recovered from waste tires embedded in cementitious matrices, Cement and Concrete Composites. (2015). https://doi.org/10.1016/j.cemconcomp.2015.04.015.
[41] C. Caggegi, F.G. Carozzi, S. De Santis, F. Fabbrocino, F. Focacci, Ł. Hojdys, E. Lanoye, L. Zuccarino, Experimental analysis on tensile and bond properties of PBO and aramid fabric reinforced cementitious matrix for strengthening masonry structures, Composites Part B: Engineering. 127 (2017). https://doi.org/10.1016/j.compositesb.2017.05.048.

[42] T. D'Antino, L.H. Sneed, C. Carloni, C. Pellegrino, Influence of the substrate characteristics on the bond behavior of PBO FRCM-concrete joints, Construction and Building Materials. 101 (2015). https://doi.org/10.1016/j.conbuildmat.2015.10.045.
[43] S. De Santis, G. de Felice, Tensile behaviour of mortar-based composites for externally bonded reinforcement systems, COMPOSITES PART B. 68 (2015) 401–413. https://doi.org/10.1016/j.compositesb.2014.09.011.
[44] A. Bilotta, F. Ceroni, E. Nigro, M. Pecce, Experimental tests on FRCM strengthening systems for tuff masonry elements, Construction and Building Materials. 138 (2017) 114–133. https://doi.org/10.1016/j.conbuildmat.2017.01.124.
[45] G.P. Lignola, C. Caggegi, F. Ceroni, S. De Santis, P. Krajewski, P.B. Lourenço, M. Morganti, C. (Corina) Papanicolaou, C. Pellegrino, A. Prota, L. Zuccarino, Performance assessment of basalt FRCM for retrofit applications on masonry, Composites Part B: Engineering. 128 (2017) 1–18. https://doi.org/10.1016/j.compositesb.2017.05.003.
[46] K. Al-Lami, T. D'Antino, P. Colombi, Durability of fabric-reinforced cementitious matrix (FRCM) composites: A review, Applied Sciences (Switzerland). 10 (2020). https://doi.org/10.3390/app10051714.
[47] B. Ghiassi, Mechanics and durability of textile reinforced mortars: a review of recent advances and open issues, RILEM Technical Letters. 4 (2019) 130–137. https://doi.org/10.21809/rilemtechlett.2019.99.
[48] I.G. Colombo, M. Colombo, M. Prisco, Tensile behavior of textile reinforced concrete subjected to freezing-thawing cycles in un-cracked and cracked regimes, Cement and Concrete Research. 73 (2015) 169–183. https://doi.org/10.1016/j.cemconres.2015.03.001.
[49] E. Franzoni, C. Gentilini, M. Santandrea, S. Zanotto, C. Carloni, Durability of steel FRCM-masonry joints: effect of water and salt crystallization, Materials and Structures. 50 (2017) 1–16. https://doi.org/10.1617/s11527-017-1070-2.
[50] J. Donnini, Durability of glass FRCM systems: Effects of different environments on mechanical properties, Composites Part B. (2019) 107047. https://doi.org/10.1016/j.compositesb.2019.107047.
[51] E. Franzoni, M. Santandrea, C. Gentilini, A. Fregni, C. Carloni, The role of mortar matrix in the bond behavior and salt crystallization resistance of FRCM applied to masonry, Construction and Building Materials. 209 (2019) 592–605. https://doi.org/10.1016/j.conbuildmat.2019.03.059.
[52] B. Ghiassi, A. Dalalbashi, D.V. Oliveira, Single fibre-to-mortar bond characterization in TRM composites, in: Proceedings of 9th International Conference on Fibre-Reinforced Polymer (FRP) Composites in Civil Engineering, CICE 2018, Paris, 2018: pp. 284–289.
[53] P. Robins, S. Austin, P. Jones, Pull-out behaviour of hooked steel fibres, Materials and Structures. 35 (2002) 434–442. https://doi.org/10.1007/BF02483148.
[54] F. Isla, G. Ruano, B. Luccioni, Analysis of steel fibers pull-out. Experimental study, Construction and Building Materials. 100 (2015) 183–193. https://doi.org/10.1016/j.conbuildmat.2015.09.034.
[55] M. Krüger, H.-W. Reindhart, M. Fichtlscherer, Bond behaviour of textile reinforcement in reinforced and prestressed concrete, Otto Graf Journal. 12 (2001) 33–50.
[56] B. Ghiassi, A. Dalalbashi, D. V. Oliveira, Bond behaviour in lime-based textile reinforced mortars, in: 17th International Brick and Block Masonry Conference (IBMAC 2020), Taylor & Francis Group, Kraków, 2020. https://doi.org/10.1201/9781003098508-9.
[57] H.V. Le, D. Moon, D.J. Kim, Effects of ageing and storage conditions on the interfacial bond strength of steel fibers in mortars, Construction and Building Materials. 170 (2018) 129–141. https://doi.org/10.1016/j.conbuildmat.2018.03.064.
[58] J. Hegger, N. Will, O. Bruckermann, S. Voss, Load-bearing behaviour and simulation of textile reinforced concrete, Materials and Structures. 39 (2006) 765–776. https://doi.org/10.1617/s11527-005-9039-y.
[59] W. Brameshuber, ed., RILEM TC 201-TRC: Textile reinforced concrete- state-of-the-art, RILEM, Bagneux, 2006.
[60] M. Baena, L. Torres, A. Turon, M. Llorens, C. Barris, Bond behaviour between recycled aggregate concrete and glass fibre reinforced polymer bars, Construction and Building Materials. 106 (2016) 449–460. https://doi.org/10.1016/j.conbuildmat.2015.12.145.
[61] J. Shannag, R. Brincker, W. Hansen, Pullout behavior of steel fibers from cement-based composites, Cement and Concrete Research. 27 (1997) 925–936. https://doi.org/10.1016/S0008-8846(97)00061-6.
[62] S. Sueki, C. Soranakom, B. Mobasher, M. Asce, A. Peled, Pullout-slip response of fabrics embedded in a cement paste matrix, Journal of Materials in Civil Engineering. 19 (2007) 718–728. https://doi.org/10.1061/(ASCE)0899-1561(2007)19:9(718).
[63] L. Huang, Y. Chi, L. Xu, P. Chen, A. Zhang, Local bond performance of rebar embedded in steel-polypropylene hybrid fiber reinforced concrete under monotonic and cyclic loading, Construction and Building Materials. 103 (2016) 77–92. https://doi.org/10.1016/j.conbuildmat.2015.11.040.
[64] Y. Li, J. Bielak, J. Hegger, R. Chudoba, An incremental inverse analysis procedure for identification of bond-slip laws in composites applied to textile reinforced concrete, Composites Part B: Engineering. 137 (2018) 111–122. https://doi.org/10.1016/j.compositesb.2017.11.014.

[65] A.E. Naaman, G.G. Namur, J.M. Alwan, H.S. Najm, Fiber pullout and bond slip. i: analytical study, Journal of Structural Engineering. 117 (1991) 2769–2790. https://doi.org/10.1061/(ASCE)0733-9445(1991)117:9(2769).

[66] B. Mobasher, Mechanics of Fiber and Textile Reinforced Cement Composites, Taylor & Francis Group, London- New York, 2012.

[67] V.C. Li, H.C. Wu, Y.W. Chan, Interfacial property tailoring for pseudo strain- hardening cementitious composites, Advanced Technology for Design and Fabrication of Composite Materials and Structures. Engineering Applications of Fracture Mechanics. 14 (1995) 261–268. https://doi.org/10.1007/978-94-015-8563-7_18.

[68] Z. Lin, T. Kanda, V.C. Li, On interface property characterization and performance of fiber reinforced cementitious composites, Journal of Concrete Science and Engineering, RILEM. 1 (1999) 173–184.

[69] D.L. Naik, A. Sharma, R.R. Chada, R. Kiran, T. Sirotiak, Modified pullout test for indirect characterization of natural fiber and cementitious matrix interface properties, Construction and Building Materials. 208 (2019) 381–393. https://doi.org/10.1016/j.conbuildmat.2019.03.021.

[70] V.C. Li, H.-C. Wu, Y.-W. Chan, Effect of plasma treatment of polyethylene fibers on interface and ementitious composite properties, Journal of the American Ceramic Society. 79 (1996) 700–704. https://doi.org/10.1111/j.1151-2916.1996.tb07932.x.

[71] C. DiFrancia, T.C. Ward, R.O. Claus, The single-fibre pull-out test. 1: Review and interpretation, Composites Part A: Applied Science and Manufacturing. 27 (1996) 597–612. https://doi.org/10.1016/1359-835X(95)00069-E.

[72] C. Redon, V.C. Li, C. Wu, H. Hoshiro, T. Saito, A. Ogawa, Measuring and modifying interface properties of PVA fibers in ECC matrix, Journal of Materials in Civil Engineering. 13 (2001) 399–406. https://doi.org/10.1061/(ASCE)0899-1561(2001)13:6(399).

[73] W.P. Boshoff, V. Mechtcherine, G.P.A.G. van Zijl, Characterising the time-dependant behaviour on the single fibre level of SHCC: Part 2: The rate effects on fibre pull-out tests, Cement and Concrete Research. 39 (2009) 787–797. https://doi.org/10.1016/j.cemconres.2009.06.006.

[74] W.P. Boshoff, V. Mechtcherine, G.P.A.G. van Zijl, Characterising the time-dependant behaviour on the single fibre level of SHCC: Part 1: Mechanism of fibre pull-out creep, Cement and Concrete Research. 39 (2009) 779–786. https://doi.org/10.1016/j.cemconres.2009.06.007.

[75] K.H. Tsai, K.S. Kim, The micromechanics of fiber pull-out, Journal of the Mechanics and Physics of Solids. 44 (1996) 1147–1159. https://doi.org/10.1016/0022-5096(96)00019-1.

[76] Y. Wang, V.C. Lf, S. Backer, Modelling of fibre pull-out from a cement matrix, International Journal Of Cement Composites. 10 (1988) 143–149. https://doi.org/10.1016/0262-5075(88)90002-4.

[77] Z. Lin, V.C. Li, Crack bridging in fiber reinforced cementitious composites with slip-hardening interfaces, Journal of the Mechanics and Physics of Solids. 45 (1997) 763–787. https://doi.org/10.1016/S0022-5096(96)00095-6.

[78] Y. Wang, V.C. Li, S. Backer, Analysis of synthetic fiber pull-out from a cement matrix, Materials Research Society Symposia: Bonding in Cementitious Composites. 114 (1988) 159–166. https://doi.org/10.1557/PROC-114-159.

[79] M. Tuyan, H. Yazıcı, Pull-out behavior of single steel fiber from SIFCON matrix, Construction and Building Materials. 35 (2012) 571–577. https://doi.org/10.1016/j.conbuildmat.2012.04.110.

[80] J.M. Alwan, A. Naaman, W. Hansen, Pull-out work of steel fibers from cementitious composites : analytical investigation, Cement and Concrete Composites. 13 (1991) 247–255. https://doi.org/10.1016/0958-9465(91)90030-L.

[81] C.K.Y. Leung, Y. Geng, Effect of lateral stresses on fiber debonding/ pull-out, Composites Engineering. 5 (1995). https://doi.org/10.1016/0961-9526(95)00064-T.

[82] S.Y. Zhang, Debonding and cracking energy release rate of the fiber/matrix interface, Composites Science and Technology. 58 (1998) 331–335. https://doi.org/10.1016/S0266-3538(97)00073-0.

[83] T. Kanda, V.C. Li, Interface property and apparent strength of a high strength hydrophilic fiber in cement matrix, Journal of Materials in Civil Engineering. 10 (1998) 5–13. https://doi.org/10.1061/(ASCE)0899-1561(1998)10:1(5).

[84] B. Banholzer, Analytical simulation of pull-out tests- the direct problem, Cement and Concrete Composites. 27 (2005) 93–101. https://doi.org/10.1016/j.cemconcomp.2004.01.006.

[85] A.E. Naaman, G.G. Namur, J.M. Alwan, H.S. Najm, Fiber pullout and bond slip. ii: experimental validation, Journal of Structural Engineering. 117 (1991) 2791–2800. https://doi.org/10.1061/(ASCE)0733-9445(1991)117:9(2791).

[86] B. Banholzer, W. Brameshuber, W. Jung, Analytical evaluation of pull-out tests-The inverse problem, Cement and Concrete Composites. 28 (2006) 564–571. https://doi.org/10.1016/j.cemconcomp.2006.02.015.

[87] H. Stang, Z. Li, S.P. Shah, Pullout problem: stress versus fracture mechanical approach, Journal of Engineering Mechanics. 116 (1990) 2136–2150. https://doi.org/10.1061/(ASCE)0733-9399(1990)116:10(2136).

[88] S. Zhandarov, E. Mäder, An alternative method of determining the local interfacial shear strength from force-displacement curves in the pull-out and microbond tests, International Journal of Adhesion and Adhesives. 55 (2014) 37–42. https://doi.org/10.1016/j.ijadhadh.2014.07.006.

[89] P. Lawrence, Some theoretical considerations of fibre pull-out from an elastic matrix, Journal of Materials Science. 7 (1972) 1–6. https://doi.org/10.1007/BF00549541.

[90] A. Dalalbashi, B. Ghiassi, D. V. Oliveira, Analytical modeling of the bond behavior between textile and mortar based on pull-out tests, Key Engineering Materials. 817 (2019) 112–117. https://doi.org/10.4028/www.scientific.net/KEM.817.112.
[91] C. Pellegrino, J. Sena-Cruz, eds., Design procedures for the use of composites in strengthening of reinforced concrete structures- State-of-the-Art report of the RILEM technical committee 234-DUC, RILEM, Springer, 2016. https://doi.org/10.1007/978-94-017-7336-2 ISSN.
[92] P. Larrinaga, C. Chastre, H.C. Biscaia, J.T. San-José, Experimental and numerical modeling of basalt textile reinforced mortar behavior under uniaxial tensile stress, Materials and Design. 55 (2014) 66–74. https://doi.org/10.1016/j.matdes.2013.09.050.
[93] I.G. Colombo, A. Magri, Z. Giulio, M. Colombo, M. di Prisco, Textile Reinforced Concrete : experimental investigation on design parameters, Materials and Structures. (2013). https://doi.org/10.1617/s11527-013-0017-5.
[94] L. Mercedes, L. Gil, E. Bernat-Maso, Mechanical performance of vegetal fabric reinforced cementitious matrix (FRCM) composites, Construction and Building Materials. 175 (2018) 161–173. https://doi.org/10.1016/j.conbuildmat.2018.04.171.
[95] ACI Committee 549, ACI 549.6R-20 Guide to design and construction of externally bonded fabric-reinforced cementitious matrix (FRCM) and steel-reinforced grout (SRG) systems for repair and strengthening masonry structures, 2013.
[96] AC434 - Acceptance criteria for masonry and concrete strengthening using fiber-reinforced cementitious matrix (FRCM) composite systems, 2011.
[97] W. Brameshuber, RILEM TC 232-TDT: Test methods and design of textile reinforced concrete, Materials and Structures. 49 (2016) 4923–4927. https://doi.org/10.1617/s11527-016-0839-z.
[98] J. Hartig, F. Jesse, K. Schicktanz, U. Haußler-Combe, Influence of experimental setups on the apparent uniaxial tensile load-bearing capacity of Textile Reinforced Concrete specimens, Materials and Structures. 45 (2012) 433–446. https://doi.org/10.1617/s11527-011-9775-0.
[99] T. D'Antino, C.G. Papanicolaou, Comparison between different tensile test set-ups for the mechanical characterization of inorganic-matrix composites, Construction and Building Materials. 171 (2018) 140–151. https://doi.org/10.1016/j.conbuildmat.2018.03.041.
[100] R. Contamine, A.S. Larbi, P. Hamelin, Contribution to direct tensile testing of textile reinforced concrete (TRC) composites, Materials Science & Engineering A. 528 (2011) 8589–8598. https://doi.org/10.1016/j.msea.2011.08.009.
[101] D. Arboleda, F.G. Carozzi, A. Nanni, C. Poggi, Testing Procedures for the Uniaxial Tensile Characterization of Fabric-Reinforced Cementitious Matrix Composites, Journal of Composites for Construction. 1 (2016) 1–11. https://doi.org/10.1061/(ASCE)CC.1943-5614.0000626.
[102] G. Ferrara, B. Coppola, L. Di Maio, L. Incarnato, E. Martinelli, Tensile strength of flax fabrics to be used as reinforcement in cement-based composites: experimental tests under different environmental exposures, Composites Part B: Engineering. 168 (2019) 511–523. https://doi.org/10.1016/j.compositesb.2019.03.062.
[103] J. Donnini, V. Corinaldesi, A. Nanni, Mechanical properties of FRCM using carbon fabrics with different coating treatments, Composites Part B: Engineering. 88 (2016). https://doi.org/10.1016/j.compositesb.2015.11.012.
[104] C. Signorini, A. Nobili, E.I. Cedillo González, C. Siligardi, Silica coating for interphase bond enhancement of carbon and AR-glass Textile Reinforced Mortar (TRM), Composites Part B: Engineering. 141 (2018) 191–202. https://doi.org/10.1016/j.compositesb.2017.12.045.
[105] C. Caggegi, E. Lanoye, K. Djama, A. Bassil, A. Gabor, Tensile behaviour of a basalt TRM strengthening system: Influence of mortar and reinforcing textile ratios, Composites Part B: Engineering. 130 (2017) 90–102. https://doi.org/10.1016/j.compositesb.2017.07.027.
[106] O.A. Cevallos, R.S. Olivito, Effects of fabric parameters on the tensile behaviour of sustainable cementitious composites, Composites Part B: Engineering. 69 (2015). https://doi.org/10.1016/j.compositesb.2014.10.004.
[107] G. Ferrara, M. Pepe, E. Martinelli, R. Dias, Tensile behavior of flax textile reinforced lime-mortar : Influence of reinforcement amount and textile impregnation, 119 (2021). https://doi.org/10.1016/j.cemconcomp.2021.103984.
[108] J. Donnini, G. Chiappini, G. Lancioni, V. Corinaldesi, Tensile behaviour of glass FRCM systems with fabrics' overlap: Experimental results and numerical modeling, Composite Structures. 212 (2019) 398–411. https://doi.org/10.1016/j.compstruct.2019.01.053.
[109] C. Chiu, X. Wang, Z. Zhang, Y. Zhu, Experimental and numerical investigations of the tensile behaviour of steel-TRM prepared with recycled glass sands and lime, Construction and Building Materials. 280 (2021) 122512. https://doi.org/10.1016/j.conbuildmat.2021.122512.
[110] Z. Mesticou, L. Bui, A. Junes, A. Si Larbi, A.S. Larbi, Experimental investigation of tensile fatigue behaviour of Textile-Reinforced Concrete (TRC): Effect of fatigue load and strain rate, Composite Structures. 160 (2017) 1136–1146. https://doi.org/10.1016/j.compstruct.2016.11.009.

[111] M. De Munck, T. Tysmans, J. Wastiels, P. Kapsalis, J. Vervloet, M. El Kadi, O. Remy, Fatigue behaviour of textile reinforced cementitious composites and their application in sandwich elements, Applied Sciences (Switzerland). 9 (2019). https://doi.org/10.3390/app9071293.
[112] E. Bernat-Maso, L. Gil, L. Mercedes, C. Escrig, Mechanical properties of pre-stressed fabric-reinforced cementitious matrix composite (PFRCM), Construction and Building Materials. 191 (2018) 228–241. https://doi.org/10.1016/j.conbuildmat.2018.09.210.
[113] N. Trochoutsou, M. Di Benedetti, K. Pilakoutas, M. Guadagnini, Bond of flax textile-reinforced mortars to masonry, Construction and Building Materials. 284 (2021) 122849. https://doi.org/10.1016/j.conbuildmat.2021.122849.
[114] S.M. Raoof, L.N. Koutas, D.A. Bournas, Bond between textile-reinforced mortar (TRM) and concrete substrates: Experimental investigation, Composites Part B: Engineering. 98 (2016). https://doi.org/10.1016/j.compositesb.2016.05.041.
[115] C. Carloni, S. Verre, L.H. Sneed, L. Ombres, Loading rate effect on the debonding phenomenon in fiber reinforced cementitious matrix-concrete joints, Composites Part B. 108 (2017) 301–314. https://doi.org/10.1016/j.compositesb.2016.09.087.
[116] T. D'Antino, C. Carloni, L.H. Sneed, C. Pellegrino, Fatigue and post-fatigue behavior of PBO FRCM-concrete joints, International Journal of Fatigue. 81 (2015). https://doi.org/10.1016/j.ijfatigue.2015.06.008.
[117] A. D'Ambrisi, L. Feo, F. Focacci, Experimental and analytical investigation on bond between Carbon-FRCM materials and masonry, Composites Part B: Engineering. 46 (2013) 15–20. https://doi.org/10.1016/j.compositesb.2012.10.018.
[118] L. Ascione, G. De Felice, S. De Santis, A qualification method for externally bonded Fibre Reinforced Cementitious Matrix (FRCM) strengthening systems, Composites Part B: Engineering. 78 (2015) 497–506. https://doi.org/10.1016/j.compositesb.2015.03.079.
[119] A. Razavizadeh, B. Ghiassi, D. V. Oliveira, Bond behavior of SRG-strengthened masonry units: Testing and numerical modeling, Construction and Building Materials. 64 (2014) 387–397. https://doi.org/10.1016/j.conbuildmat.2014.04.070.
[120] C. Carloni, T. D'Antino, L.H. Sneed, C. Pellegrino, T. D'Antino, L.H. Sneed, C. Pellegrino, Role of the Matrix Layers in the Stress-Transfer Mechanism of FRCM Composites Bonded to a Concrete Substrate, Journal of Engineering Mechanics. 141 (2015) 1–10. https://doi.org/10.1061/(ASCE)EM.1943-7889.0000883.
[121] L.A.S. Kouris, T.C. Triantafillou, State-of-the-art on strengthening of masonry structures with textile reinforced mortar (TRM), Construction and Building Materials. 188 (2018) 1221–1233. https://doi.org/10.1016/j.conbuildmat.2018.08.039.
[122] P.D. Askouni, C.G. Papanicolaou, Experimental investigation of bond between glass textile reinforced mortar overlays and masonry: the effect of bond length, Materials and Structures. 50 (2017). https://doi.org/10.1617/s11527-017-1033-7.
[123] S. De Santis, G. de Felice, Steel reinforced grout systems for the strengthening of masonry structures, Composite Structures. 134 (2015) 533–548. https://doi.org/10.1016/j.compstruct.2015.08.094.
[124] F. Valvona, J. Toti, V. Gattulli, F. Potenza, Effective seismic strengthening and monitoring of a masonry vault by using Glass Fiber Reinforced Cementitious Matrix with embedded Fiber Bragg Grating sensors, Composites Part B: Engineering. 113 (2017) 355–370. https://doi.org/10.1016/j.compositesb.2017.01.024.
[125] A.H. Karimi, M.S. Karimi, A. Kheyroddin, A.A. Shahkarami, Experimental and numerical study on seismic behavior of an infilled masonry wall compared to an arched masonry wall, Structures. 8 (2016) 144–153. https://doi.org/10.1016/j.istruc.2016.09.012.
[126] A.S. Mosallam, Out-of-plane flexural behavior of unreinforced red brick walls strengthened with FRP composites, Composites Part B: Engineering. 38 (2007) 559–574. https://doi.org/10.1016/j.compositesb.2006.07.019.
[127] Ö. Anil, M. Tatayolu, M. Demirhan, Out-of-plane behavior of unreinforced masonry brick walls strengthened with CFRP strips, Construction and Building Materials. 35 (2012) 614–624. https://doi.org/10.1016/j.conbuildmat.2012.04.058.
[128] C.G. Papanicolaou, T.C. Triantafillou, M. Papathanasiou, K. Karlos, Textile reinforced mortar (TRM) versus FRP as strengthening material of URM walls: out-of-plane cyclic loading, Materials and Structures. 41 (2007) 143–157. https://doi.org/10.1617/s11527-007-9226-0.
[129] C.G. Papanicolaou, T.C. Triantafillou, M. Papathanasiou, K. Karlos, Textile-reinforced mortar (TRM) versus FRP as strengthening material of URM walls: in-plane cyclic loading, Materials and Structures. 40 (2007) 1081–1097. https://doi.org/10.1617/s11527-006-9207-8.
[130] T.L. Bui, A. Si Larbi, N. Reboul, E. Ferrier, Shear behavior of masonry walls strengthened by external bonded FRP and TRC, Composite Structures. 132 (2015) 923–932. https://doi.org/10.1016/j.compstruct.2015.06.057.
[131] D. Tripathy, S.M. Asce, P. Meghwal, V. Singhal, A.M. Asce, Strengthening of lime mortar masonry wallettes using fiber-reinforced cementitious matrix, 24 (2020). https://doi.org/10.1061/(ASCE)CC.1943-5614.0001086.

[132] C. D'Ambra, G.P. Lignola, A. Prota, E. Sacco, F. Fabbrocino, Experimental performance of FRCM retrofit on out-of-plane behaviour of clay brick walls, Composites Part B. 148 (2018) 198–206. https://doi.org/10.1016/j.compositesb.2018.04.062.
[133] F. Parisi, I. Iovinella, A. Balsamo, N. Augenti, A. Prota, In-plane behaviour of tuff masonry strengthened with inorganic matrix-grid composites, Composites Part B: Engineering. 45 (2013). https://doi.org/10.1016/j.compositesb.2012.09.068.
[134] S. Casacci, C. Gentilini, A. Di Tommaso, D. V. Oliveira, Shear strengthening of masonry wallettes resorting to structural repointing and FRCM composites, Construction and Building Materials. 206 (2019) 19–34. https://doi.org/10.1016/j.conbuildmat.2019.02.044.
[135] A. Dalalbashi, B. Ghiassi, D. V Oliveira, In-Plane behavior of clay brick masonry wallets Strengthened by TRM system, in: J. Sena-Cruz, L. Correia, M. Azenha (Eds.), Proceedings of the 3rd RILEM Spring Convention and Conference (RSCC 2020), RILEM Bookseries, Vol 34, Springer, Cham, Guimarães, 2020: pp. 1–9. https://doi.org/10.1007/978-3-030-76465-4_13.
[136] A. Martins, G. Vasconcelos, R. Fangueiro, F. Cunha, Experimental assessment of an innovative strengthening material for brick masonry infills, Composites Part B. 80 (2015) 328–342. https://doi.org/10.1016/j.compositesb.2015.06.012.
[137] G. Ferrara, C. Caggegi, E. Martinelli, A. Gabor, Shear capacity of masonry walls externally strengthened using Flax-TRM composite systems : experimental tests and comparative assessment, Construction and Building Materials. 261 (2020). https://doi.org/10.1016/j.conbuildmat.2020.120490.
[138] P.K.V.R. Padalu, Y. Singh, S. Das, Efficacy of basalt fibre reinforced cement mortar composite for out-of-plane strengthening of unreinforced masonry, Construction and Building Materials. 191 (2018) 1172–1190. https://doi.org/10.1016/j.conbuildmat.2018.10.077.
[139] S. Babaeidarabad, D. Arboleda, G. Loreto, A. Nanni, Shear strengthening of un-reinforced concrete masonry walls with fabric-reinforced-cementitious-matrix, Construction and Building Materials. 65 (2014) 243–253. https://doi.org/10.1016/j.conbuildmat.2014.04.116.
[140] M. Del Zoppo, M. Di Ludovico, A. Balsamo, A. Prota, Experimental in-plane shear capacity of clay brick masonry panels strengthened with FRCM and FRM composites, Journal of Composites for Construction. 23 (2019) 04019038. https://doi.org/10.1061/(ASCE)CC.1943-5614.0000965.
[141] T.T. a Li, N.N. b Galati, J.G. c G. Tumialan, A. Nanni, Analysis of unreinforced masonry concrete walls strengthened with glass fiber-reinforced polymer bars, ACI Structural Journal. 102 (2005) 569–577.
[142] S. Babaeidarabad, F. De Caso, A. Nanni, Out-of-plane behavior of URM walls strengthened with Fabric-Reinforced Cementitious Matrix Composite, Journal of Composites for Construction. 549 (2014). https://doi.org/10.1061/(ASCE)CC .1943-5614.0000457.
[143] B.P. Sinha, C.L. Ng, R.F. Pedreschi, Failure criterion and behavior of brickwork in biaxial bending, Journal of Materials in Civil Engineering. 9 (1997) 70–75. https://doi.org/10.1061/(ASCE)0899-1561(1997)9:2(70).
[144] S.L. Sagar, V. Singhal, D.C. Rai, P. Gudur, Diagonal Shear and Out-of-Plane Flexural Strength of Fabric-Reinforced Cementitious Matrix–Strengthened Masonry Walletes, Journal of Composites for Construction. 21 (2017). https://doi.org/10.1061/(ASCE)CC.1943-5614.0000796.
[145] V.M. Karbhari, J.W. Chin, D. Hunston, B. Benmokrane, T. Juska, R. Morgan, J.J. Lesko, U. Sorathia, D. Reynaud, Durability gap analysis for fiber-reinforced polymer composites in civil infrastructure, Journal of Composites for Construction. 7 (2003) 238–247. https://doi.org/10.1061/(ASCE)1090-0268(2003)7:3(238)#sthash.GisKiZcB.dpuf.
[146] M. Alma'aitah, B. Ghiassi, A. Dalalbashi, Durability of textile reinforced concrete: Existing knowledge and current gaps, Applied Sciences. 11 (2021) 1–10. https://doi.org/10.3390/app11062771.
[147] B. Ghiassi, Durability analysis of bond between composite materials and masonry substrates, University of Minho, 2013.
[148] D. Arboleda, S. Babaeidarabad, C.D. Hays, A. Nanni, Durability of fabric reinforced cementitious matrix (FRCM) composites, in: 7th. International Conference of FRP Composites in Civil Engineering (CICE 2014), Vancouver, 2014: pp. 1–6.
[149] J. Machovec, P. Reiterman, Influence of aggressive environment on the tensile properties of textile reinforced concrete, Acta Polytechnica. 58 (2018) 245–252. https://doi.org/10.14311/AP.2018.58.0245.
[150] F. Micelli, M.A. Aiello, Residual tensile strength of dry and impregnated reinforcement fibres after exposure to alkaline environments, Composites Part B. (2017). https://doi.org/10.1016/j.compositesb.2017.03.005.
[151] C. Tedeschi, S. Perego, P. Milano, Study on local effects of aggressive environmental conditions on masonry strengthened with FRCM, in: M.R.V. C. Modena, F. da Porto (Ed.), Brick and Block Masonry. Trends, Innovation and Challehgers, 1st Editio, CRC Press - Taylor & Francis Group, London, 2016: pp. 441–449. https://doi.org/10.1201/b21889-53.

[152] A. Nobili, Durability assessment of impregnated Glass Fabric Reinforced Cementitious Matrix (GFRCM) composites in the alkaline and saline environments, Construction and Building Materials. 105 (2016) 465–471. https://doi.org/10.1016/j.conbuildmat.2015.12.173.
[153] A. Nobili, C. Signorini, On the effect of curing time and environmental exposure on impregnated Carbon Fabric Reinforced Cementitious Matrix (CFRCM) composite with design considerations, Composites Part B. 112 (2017) 300–313. https://doi.org/10.1016/j.compositesb.2016.12.022.
[154] J. Donnini, F. Bompadre, V. Corinaldesi, Tensile behavior of a glass FRCM system after different environmental exposures, Processes. 8 (2020). https://doi.org/10.3390/pr8091074.
[155] D. Arboleda, S. Babaeidarabad, C.D. Hays, A. Nanni, Durability of fabric reinforced cementitious matrix (FRCM) composites, in: 7th. International Conference of FRP Composites in Civil Engineering (CICE 2014), Vancouver, 2014: pp. 1–6.
[156] J. Donnini, F. Bompadre, V. Corinaldesi, Tensile behavior of a glass FRCM system after different environmental exposures, Processes. 8 (2020). https://doi.org/10.3390/pr8091074.
[157] F. Micelli, M.A. Aiello, Residual tensile strength of dry and impregnated reinforcement fibres after exposure to alkaline environments, Composites Part B. (2017). https://doi.org/10.1016/j.compositesb.2017.03.005.
[158] C. Tedeschi, S. Perego, P. Milano, Study on local effects of aggressive environmental conditions on masonry strengthened with FRCM, in: M.R.V. C. Modena, F. da Porto (Ed.), Brick and Block Masonry. Trends, Innovation and Challehgers, 1st Editio, CRC Press - Taylor & Francis Group, London, 2016: pp. 441–449. https://doi.org/10.1201/b21889-53.
[159] J. Donnini, Durability of glass FRCM systems: Effects of different environments on mechanical properties, Composites Part B. (2019) 107047. https://doi.org/10.1016/j.compositesb.2019.107047.
[160] B.Y. Pekmezci, E. Arabaci, C. Ustundag, Freeze-thaw durability of lime based FRCM systems for strengthening historical masonry, Key Engineering Materials. 817 KEM (2019) 174–181. https://doi.org/10.4028/www.scientific.net/KEM.817.174.
[161] M. De Munck, M. El Kadi, E. Tsangouri, J. Vervloet, S. Verbruggen, J. Wastiels, T. Tysmans, O. Remy, Influence of environmental loading on the tensile and cracking behaviour of textile reinforced cementitious composites, Construction and Building Materials. 181 (2018). https://doi.org/10.1016/j.conbuildmat.2018.06.045.
[162] A. Dalalbashi, B. Ghiassi, D. V. Oliveira, Freeze-thaw durability of glass textile-reinforced mortar composites, in: 17th International Brick and Block Masonry Conference (IBMAC 2020), Taylor & Francis Group, Kraków, 2020. https://doi.org/10.1201/9781003098508-152.
[163] R. Snellings, J. Chwast, Ö. Cizer, N. De Belie, Y. Dhandapani, P. Durdzinski, J. Elsen, J. Haufe, D. Hooton, C. Patapy, O. Perebatova, M. Santhanam, K. Scrivener, D. Snoeck, L. Steger, S. Tongbo, A. Vollpracht, F. Winnefeld, B. Lothenbach, TC 238-SCM: Hydration stoppage methods for phase assemblage studies of blended cements– results of a round robin test, Materials and Structures. 5 (2018) submitted. https://doi.org/10.1617/s11527-018-1237-5.
[164] L.D. Mitchell, J.C. Margeson, The effects of solvents on C-S-H as determined by thermal analysis, Journal of Thermal Analysis and Calorimetry. 86 (2006) 591–594. https://doi.org/10.1007/s10973-006-7712-1.
[165] K. Van Balen, Carbonation reaction of lime, kinetics at ambient temperature, Cement and Concrete Research. 35 (2005) 647–657. https://doi.org/10.1016/j.cemconres.2004.06.020.
[166] K. Scrivener, R. Snellings, B. Lothenbach, A practical guide to microstructural analysis of cementitious materials, Taylor & Francis Group, 2016.
[167] ASTM C109/C109M-05, Standard test method for compressive strength of hydraulic cement mortars (Using 2-in. or [50-mm] Cube Specimens), 2005. https://doi.org/10.1520/C0109_C0109M-05.
[168] BS EN 1015-11, Methods of test for mortar for masonry. Determination of flexural and compressive strength of hardened mortar, 1999.
[169] ASTM C496/C496M- 04, Standard test method for splitting tensile strength of cylindrical concrete specimens, 2004. https://doi.org/10.1520/C0496_C0496M-04.
[170] BS EN 12390-13, Testing hardened concrete. Determination of secant modulus of elasticity in compression, 2013.
[171] ASTM C1314-03, Standard test method for compressive strength of masonry prisms, 2003. https://doi.org/10.1520/C1314-18.
[172] BS EN 1015-18, Methods of test for mortar for masonry- Determination of water absorption coefficient due to capillary action of hardened mortar, 2002.
[173] BS EN 772-11, Methods of test for masonry units. Determination of water absorption of aggregate concrete, autoclaved aerated concrete, manufactured stone and natural stone masonry units due to capillary action and the IRA of clay masonry units, 2011.
[174] ASTM C67-05, Standard test methods for smpling and testing brick and structural clay tile, 2005. https://doi.org/10.1520/C0067_C0067M-20.
[175] BS EN 1015-10, Methods of test for mortar for masonry- Determination of dry bulk density of hardened mortar, 1999.

[176] BS EN 1936, Natural stone test methods- Determination of real density and apparent density, and of total and open porosity, 2006.
[177] BS EN 12617-4, products and systems for the protection and repair of concrete structures. Test methods, Determination of Shrinkage and Expansion, 2002.
[178] ISO:8301, Thermal insulation: determination of steady state thermal resistance and related properties, heat flow meter apparatus, 1991.
[179] B. Banholzer, Bond of a strand in a cementitious matrix, Materials and Structures. 39 (2006) 1015–1028. https://doi.org/10.1617/s11527-006-9115-y.
[180] T. Abu-Lebdeh, S. Hamoush, B. Zornig, Rate effect on pullout behavior of steel fibers embedded in very-high strength concrete, American Journal of Engineering and Applied Sciences. 3 (2010) 454–463. https://doi.org/10.3844/ajeassp.2010.454.463.
[181] M. Xu, B. Hallinan, K. Wille, Effect of loading rates on pullout behavior of high strength steel fibers embedded in ultra-high performance concrete, Cement and Concrete Composites. 70 (2016) 98–109. https://doi.org/10.1016/j.cemconcomp.2016.03.014.
[182] Y. Tai, S. El-tawil, High loading-rate pullout behavior of inclined deformed steel fibers embedded in ultra-high performance concrete, Construction and Building Materials. 148 (2017) 204–218. https://doi.org/10.1016/j.conbuildmat.2017.05.018.
[183] A.J. Babafemi, W.P. Boshoff, Pull-out response of macro synthetic fibre from concrete matrix: Effect of loading rate and embedment length, Construction and Building Materials. 135 (2017) 590–599. https://doi.org/10.1016/j.conbuildmat.2016.12.160.
[184] ASTM E519-02, Standard test method for diagonal tension (shear) in masonry assemblages, 2002. https://doi.org/10.1520/E0519-02.
[185] BS EN 1052-2, Methods of test for masonry- Part2: Determination of flexural strength., 1999.
[186] I. Asadi, P. Shafigh, Z.F. Bin Abu Hassan, N.B. Mahyuddin, Thermal conductivity of concrete- A review, Journal of Building Engineering. 20 (2018) 81–93. https://doi.org/10.1016/j.jobe.2018.07.002.
[187] J. Lanas, J. Perez Bernal, M.A. Bello, J.I. Alvarez Galindo, Mechanical properties of natural hydraulic lime-based mortars, Cement and Concrete Research. 34 (2004) 2191–2201. https://doi.org/10.1016/j.cemconres.2004.02.005.
[188] G. Ye, X. Liu, G. De Schutter, A.-M. Poppe, L. Taerwe, Influence of limestone powder used as filler in SCC on hydration and microstructure of cement pastes, Cement and Concrete Composites. 29 (2007) 94–102. https://doi.org/10.1016/j.cemconcomp.2006.09.003.
[189] J.D.A.M. Filho, F.D.A. Silva, R.D. Toledo Filho, Degradation kinetics and aging mechanisms on sisal fiber cement composite systems, Cement and Concrete Composites. 40 (2013) 30–39. https://doi.org/10.1016/j.cemconcomp.2013.04.003.
[190] A. El-Turki, R.J. Ball, S. Holmes, W.J. Allen, G.C. Allen, Environmental cycling and laboratory testing to evaluate the significance of moisture control for lime mortars, Construction and Building Materials. 24 (2010) 1392–1397. https://doi.org/10.1016/j.conbuildmat.2010.01.019.
[191] R.J. Ball, G.C. Allen, Load-dependent deformation and shrinkage in hydraulic lime mortars, International Journal of Sustainable Engineering. 3 (2010) 40–46. https://doi.org/10.1080/19397030903191219.
[192] A. Duran, J.M. Fernández, J.I. Alvarez, Long-term mechanical resistance and durability of air lime mortars with large additions of nanosilica, Construction and Building Materials. 58 (2014) 147–158. https://doi.org/10.1016/j.conbuildmat.2014.02.030.
[193] O.S. Baghabra Al-Amoudi, S. Ahmad, M. Maslehuddin, S.M.S. Khan, Lime-activation of natural pozzolan for use as supplementary cementitious material in concrete, Ain Shams Engineering Journal. (2021). https://doi.org/10.1016/j.asej.2021.09.029.
[194] A. Izaguirre, J. Lanas, J.I. Álvarez, Ageing of lime mortars with admixtures: Durability and strength assessment, Cement and Concrete Research. 40 (2010) 1081–1095. https://doi.org/10.1016/j.cemconres.2010.02.013.
[195] S. Pavía, R. Hanley, Flexural bond strength of natural hydraulic lime mortar and clay brick, Materials and Structures. 43 (2010) 913–922. https://doi.org/10.1617/s11527-009-9555-2.
[196] Z. Zhou, Development of bond strength in hydraulic lime mortared brickwork, University of Bath, 2012.
[197] S.H. Kang, Y.H. Kwon, J. Moon, Controlling the hydration and carbonation in lime-based materials: Advantage of slow carbonation in CO2 curable construction materials, Construction and Building Materials. 249 (2020) 118749. https://doi.org/10.1016/j.conbuildmat.2020.118749.
[198] Ö. Cizer, K. Van Balen, D. Van Gemert, Competition between hydration and carbonation in hydraulic lime and lime-pozzolana mortars, Advanced Materials Research. 133–134 (2010) 241–246. https://doi.org/10.4028/www.scientific.net/AMR.133-134.241.
[199] A. Dalalbashi, B. Ghiassi, D. V. Oliveira, Aging of lime-based TRM composites under natural environmental conditions, Construction and Building Materials. 270 (2021). https://doi.org/10.1016/j.conbuildmat.2020.121853.

[200] A. Dalalbashi, B. Ghiassi, D. V. Oliveira, Effect of mortar age on the Textile-to-Mortar bond behavior, in: Proceedings of XV International Conference on Durability of Building Materials and Components, DBMC 2020, Barcelona, 2020: pp. 1165–1172. https://doi.org/10.23967/dbmc.2020.055.
[201] J. Lanas, R. Sirera, J.I. Alvarez, Study of the mechanical behavior of masonry repair lime-based mortars cured and exposed under different conditions, Cement and Concrete Research. 36 (2006) 961–970. https://doi.org/10.1016/j.cemconres.2005.12.003.
[202] J. Shannag, W. Hansen, P. Tjiptobroto, Interface debonding in fiber reinforced cement-matrix composites, Journal of Composite Materials. 33 (1999) 158–176. https://doi.org/10.1177/002199839903300203.
[203] M. Butler, V. Mechtcherine, S. Hempel, Experimental investigations on the durability of fibre-matrix interfaces in textile-reinforced concrete, Cement and Concrete Composites. 31 (2009) 221–231. https://doi.org/10.1016/j.cemconcomp.2009.02.005.
[204] E.-H. Yang, S. Wang, Y. Yang, V.C. Li, Fiber-bridging constitutive law of engineered cementitious composites, Journal of Advanced Concrete Technology. 6 (2008) 181–193. https://doi.org/10.3151/jact.6.181.
[205] N.W. Portal, I.F. Perez, L.N. Thrane, K. Lundgren, Pull-out of textile reinforcement in concrete, Construction and Building Materials. 71 (2014) 63–71. https://doi.org/10.1016/j.conbuildmat.2014.08.014.
[206] M.G. Alberti, A. Enfedaque, J.C. Gálvez, A. Ferreras, Pull-out behaviour and interface critical parameters of polyolefin fibres embedded in mortar and self-compacting concrete matrixes, Construction and Building Materials. 112 (2016) 607–622. https://doi.org/10.1016/j.conbuildmat.2016.02.128.
[207] B. Wang, H. Jin, T. Man, Q. Wang, Study on the mechanical property of textile reinforced self-stressing concrete sheets, Construction and Building Materials. 107 (2016) 1–10. https://doi.org/10.1016/j.conbuildmat.2015.12.167.
[208] X.B. Zhang, H. Aljewifi, J. Li, Failure behaviour investigation of continuous yarn reinforced cementitious composites, 47 (2013) 456–464. https://doi.org/10.1016/j.conbuildmat.2013.05.022.
[209] A. Pacios, C. Ouyang, S.P. Shah, Rate effect on interfacial response between fibres and matrix, Materials and Structures. 28 (1995) 83–91. https://doi.org/10.1007/BF02473175.
[210] S.P. Shah, C. Ouyang, Mechanical behavior of fiber-reinforced cement-based composites, Journal of the American Ceramic Society. 53 (1991). https://doi.org/10.1111/j.1151-2916.1991.tb06836.x.
[211] A.E. Naaman, S.P. Shah, Pull-out mechanism in steel fiber-reinforced concrete, Journal of the Structural Division. 102 (1976) 1537–1548.
[212] S. Sueki, An analytical and experimental study of fabric-reinforced, cement-based laminated composites, Arizona State University, 2003.
[213] R.J. Ball, A. El-Turki, W.J. Allen, J.A. Nicholson, G.C. Allen, Deformation of NHL3.5 and CL90/PC hybrid mortars, Proceedings of the Institution of Civil Engineers: Construction Materials. 162 (2009) 29–35. https://doi.org/10.1680/coma.2009.162.
[214] G. Allen, R. Ball, Mechanical properties of hydraulic lime mortars, in: 4th Portuguese Congress on Mortars and ETICS, 2012.
[215] B.V. Venkatarama Reddy, M.S. Latha, Mortar shrinkage and flexure bond strength of stabilized soil brick masonry, Journal of Materials in Civil Engineering. 30 (2018) 2–6. https://doi.org/10.1061/(ASCE)MT.1943-5533.0002280.
[216] K. Venu Madhava Rao, B. V Venkatarama Reddy, K.S. Jagadish, Flexural bond strength of masonry using various blocks and mortars, Materials and Structures. 29 (1996) 119–124. https://doi.org/10.1007/BF02486202.
[217] J.P. Forth, J.J. Brooks, S.H. Tapsir, The effect of unit water absorption on long-term movements of masonry, Cement and Concrete Composites. 22 (2000) 273–280. https://doi.org/10.1016/S0958-9465(00)00027-5.
[218] E.A. Schauffert, G. Cusatis, D. Pelessone, J.L. O'Daniel, J.T. Baylot, Lattice discrete particle model for fiber-reinforced concrete. II: Tensile fracture and multiaxial loading behavior, Journal of Engineering Mechanics. 138 (2011) 834–841. https://doi.org/10.1061/(asce)em.1943-7889.0000392.
[219] A. Dalalbashi, B. Ghiassi, D.V. Oliveira, Influence of freeze-thaw cycles on the pull-out response of lime-based TRM composites, Construction and Building Materials. 313 (2021). https://doi.org/10.1016/j.conbuildmat.2021.125473.
[220] X. Wang, C.C. Lam, V.P. lu, Experimental investigation of in-plane shear behaviour of grey clay brick masonry panels strengthened with SRG, Engineering Structures. 162 (2018) 84–96. https://doi.org/10.1016/j.engstruct.2018.02.027.
[221] H. Mahmood, J.M. Ingham, Diagonal compression testing of FRP-retrofitted unreinforced clay brick masonry wallettes, Journal of Composites for Construction. 15 (2011) 810–820. https://doi.org/10.1061/(ASCE)CC.1943-5614.0000209.
[222] N. Gattesco, I. Boem, Experimental and analytical study to evaluate the effectiveness of an in-plane reinforcement for masonry walls using GFRP meshes, Construction and Building Materials. 88 (2015) 94–104. https://doi.org/10.1016/j.conbuildmat.2015.04.014.

[223] S. Babaeidarabad, F. De Caso, A. Nanni, URM walls strengthened with fabric-reinforced cementitious matrix composite subjected to diagonal compression, Journal of Composites for Construction. 18 (2014) 1–9. https://doi.org/10.1061/(ASCE)CC.1943-5614.0000441.
[224] European Committee for Standardization, EN 1996-1-1: 2005, Eurocode 6- Design of masonry structures- Part 1-1: General rules for reinforced and unreinforced masonry structures, n.d.
[225] K. Galal, N. Sasanian, Out-of-plane flexural performance of GFRP-reinforced masonry walls, Journal of Composites for Construction. 14 (2010) 162–174. https://doi.org/10.1061/(ASCE)CC.1943-5614.0000061.
[226] ASTM E518-02, Standard test method for flexural bond strength of masonry, 2003. https://doi.org/10.1520/E0518-03.
[227] D.B. Marshall, Measurement of Interfacial Mechanical Properties in Fiber-Reinforced Ceramic Composites, Journal of the American Ceramic Society. 70 (1987) 542–548. https://doi.org/10.1111/j.1151-2916.1987.tb05702.x.
[228] C. Hsueh, Interfacial debonding and fiber pull-out stresses of fiber-reinforced composites, Materials Science and Engineering: A. 154 (1992) 125–132. https://doi.org/10.1016/0921-5093(92)90337-Z.
[229] D.B. Marshall, Analysis of fiber debonding and sliding experiments in brittle matrix composites, Acta Metallurgica et Materialia. 40 (1992) 427–441. https://doi.org/10.1016/0956-7151(92)90391-Q.
[230] J.W. Hutchinson, Models of fiber debonding and pullout in brittle composites with friction, Mechanics of Materials. 9 (1990) 139–163. https://doi.org/10.1016/0167-6636(90)90037-G.
[231] R.J. Gray, Analysis of the effect of embedded fibre length on fibre debonding and pull-out from an elastic matrix Part 2 Application to a steel fibre-cementitious matrix composite system, Journal of Materials Science. 19 (1984) 1680–1691. https://doi.org/10.1007/BF00563066.
[232] C. Sujivorakul, A.M. Wass, A.E. Naaman, Pullout response of a smooth fiber with an end anchorage, Journal of Engineering Mechanics. 126 (2000) 123–131. https://doi.org/10.1061/(ASCE)0733-9399(2000)126:9(986).
[233] J. Alwan, A.E. Naaman, P. Guerrero, Effect of mechanical clamping on the pull-out response of hooked steel fibers embedded in cementitious matrices, Concrete Science and Engineering. 1 (1999) 15–25.
[234] X. Shilang, L. He, Bond properties and experimental methods of textile reinforced concrete, Journal Wuhan University of Technology, Materials Science Edition. 22 (2007) 529–532. https://doi.org/10.1007/s11595-006-3529-9.
[235] A. J. Majumdar, A.J. Majumdar, The role of the interface in glass fibre reinforced cement, Cement and Concrete Research. 4 (1974) 247–266. https://doi.org/10.1016/0008-8846(74)90137-9.
[236] H. Yamao, L. Chou, J. Niwa, Experimental study on bond stress slip relationship, in: Japan Society of Civil Engineers, 1984: pp. 219–228.
[237] S. Hong, S.K. Park, Uniaxial bond stress-slip relationship of reinforcing bars in concrete, Advances in Materials Science and Engineering. 2012 (2012). https://doi.org/10.1155/2012/328570.
[238] J. Aveston, G. Cooper, A. Kelly, Single and multiple fracture, the properties of fibre composites., in: Proceedings of the Conference National Physical Laboratories., London: IPC Science and Technology Press Ltd., 1971: pp. 15–24.
[239] H. Cuypers, J. Wastiels, Stochastic matrix-cracking model for textile reinforced cementitious composites under tensile loading, Materials and Structures. 39 (2006) 777–786. https://doi.org/10.1617/s11527-005-9053-0.
[240] FIB- International Federation for Structural Concrete. fib Model Code for Concrete Structures 2010, 2013. https://doi.org/10.1002/9783433604090.
[241] ACI Committee 440, ACI 440.7R-10 Guide for design and construction of externally bonded FRP systems for strengthening unreinforced masonry structures, 2010.
[242] A. Dalalbashi, B. Ghiassi, D. V. Oliveira, A multi-level investigation on the mechanical response of TRM-strengthened masonry, Materials and Structures. 54 (2021). https://doi.org/10.1617/s11527-021-01817-4.
[243] T. Paulay, M.J.N. Priestely, Seismic design of reinforced concrete and masonry buildings, Wiley Interscience, 1992.
[244] ACI Committee 549, ACI 549.4R-13 Design and construction of externally bonded Fabric-Reinforced Cementitious Matrix (FRCM) systems for repair and strengthening concrete and masonry Structures, 2013.
[245] CNR DT 215/2018, Guide for the design and construction of externally bonded fibre reinforced inorganic matrix systems for strengthening existing structures, 2018.
[246] T. D'Antino, F.G. Carozzi, P. Colombi, C. Poggi, Out-of-plane maximum resisting bending moment of masonry walls strengthened with FRCM composites, Composite Structures. 202 (2018) 881–896. https://doi.org/10.1016/j.compstruct.2018.04.054.

Appendix I: Technical datasheets of the materials

Mortar M1:

WHERE TO USE
Smoothing and levelling layers on stone, brick and tuff surfaces.
For laying **Mapegrid G 120**, **Mapegrid G 220** and **Mapegrid B 250** basalt fibres glass fibre mesh in "reinforced" structural strengthening systems on facing walls, ceilings and masonry elements.

Some application examples
- Strengthening masonry facing walls, ceilings and general masonry work.
- Levelling and strengthening of structural elements in stone, brickwork and tuff.
- Laying and smoothing **Mapegrid G120**, a system for "localised" structural strengthening in the case of stresses induced by uneven substrates.
- Laying and smoothing **Mapegrid G 220** or **Mapegrid B 250** a system for "reinforced" structural strengthening against stresses induced by seismic activity.

TECHNICAL CHARACTERISTICS
Planitop HDM Restauro is a two-component, pre-blended, light-coloured mortar composed of hydraulic lime (NHL), Eco-Pozzolan, natural sand, special additives and synthetic polymers in water dispersion according to a formula developed in MAPEI's research laboratories. When the two components are mixed together (component A powder and component B liquid) they form a mix which is easy to spread, and which may be applied manually on vertical surfaces at a thickness of up to a maximum of 10 mm per coat. Thanks to its content of synthetic resin in water dispersion, **Planitop HDM Restauro** has high bonding strength and, once hardened, forms a tough and compact layer which is impermeable to water and aggressive gases present in the atmosphere, but permeable to vapour.
Planitop HDM Restauro is classified as an M15 type masonry mortar according to EN 998-2 European Standards and a category CS IV GP type render according to EN 998-1, in that it reaches a compressive strength of > 15 N/mm² (UNI EN 1015-11) even though it is a mortar composed of lime and Eco-Pozzolan.

RECOMMENDATIONS
- Do not apply **Planitop HDM Restauro** if the temperature is lower than +5°C.
- Do not add cement, aggregates or water to **Planitop HDM Restauro**.

APPLICATION PROCEDURE
Preparation of the substrate
To guarantee good adhesion, special care must be taken when preparing the substrate. It must be perfectly clean, sound and free of crumbling parts, dust, oil and old paintwork. Sandblasting, a vigorous cleaning cycle with high-pressure water jets are particularly suitable to eliminate efflorescence and soluble salts from the surface of the masonry. Clean the structure, therefore, with water.
If the product is applied on masonry, stone or tuff surfaces, any defects present must be repaired using **Mape-Antique Strutturale NHL**.

Preparation of the mortar
Planitop HDM Restauro must be prepared according to the application selected using a mixer or drum mixer

Planitop HDM Restauro

Application of the first layer of Planitop HDM Restauro by trowel on the outer face of a vaulted ceiling

Positioning Mapegrid G 220 alkali-resistant glass fibre reinforcement mesh

Application of the second layer of Planitop HDM Restauro by trowel on the outer face of a vaulted ceiling to cover the Mapegrid G 220 with an even coat

(for manual application) for large quantities or in the mixing unit of a rendering machine (for mechanical application).
For manual application, pour component B (liquid) into a suitable clean container and slowly add component A (powder) while stirring with a mechanical mixer. Carefully mix **Planitop HDM Restauro** for several minutes, making sure no powder remains attached to the sides or bottom of the container.
Keep mixing until the blend is completely homogenous (with no lumps). A low-speed mechanical mixer is recommended for this operation, to avoid too much air being entrapped in the mix.
If the mortar is applied by spray, on the other hand, a rendering machine with a separate mixing unit must be used.

Applying of the mortar when laying Mapegrid G 120, Mapegrid G 220 or Mapegrid B 250

1. Apply a uniform, 4-5 mm-thick layer of **Planitop HDM Restauro** using a flat, metal trowel (or with rendering machine).
2. While the product is still "fresh", insert the **Mapegrid G 120**, **Mapegrid G 220** or **Mapegrid B 250** by pressing it lightly with a flat trowel so that it adheres perfectly to the mortar.
3. Apply a second uniform layer of **Planitop HDM Restauro** approximately 4 mm thick in order to completely cover the mesh.
4. Smooth the surface while still "fresh" using a flat trowel.

Adjacent longitudinal and transversal strips of **Mapegrid G 120**, **Mapegrid G 220** or **Mapegrid B 250** must overlap by at least 5 cm at the junction points.

Finishing the mortar

After applying **Planitop HDM Restauro**, if a smooth finish is required, use a MAPEI product such as **Mape-Antique FC Ultrafine** or **Mape-Antique FC Civile** or **Mape-Antique FC Grosso** (cement-free mortars of different grain size, made from lime and Eco-Pozzolan).
Further protective coatings may be applied after complete hardening of the finishing layer. Use **Elastocolor Paint** (protective and decorative elastic paint based on acrylic resins in water dispersion) after applying a coat of **Elastocolor Primer** (solvent-based fixing primer with high penetration properties), or one of the silicate-based products from the **Silexcolor** range or one of the silicone resin-based products from the **Silancolor** range.
All covering materials are available in a wide range of colours, which may be created using the **ColorMap®** automatic colouring system.

Precautions to be taken during and after application

- No special precautions need to be taken when the temperature is around +20°C.
- In particularly dry, hot or windy conditions, **Planitop HDM Restauro** must be cured carefully; we recommend protecting the surface against quick evaporation of water.

Cleaning

Due to the high bonding strength of **Planitop HDM Restauro**, even on metals, we recommend that work tools are washed with water before the mortar sets. Once it has set, cleaning may only be carried out by mechanical means.

CONSUMPTION

1.9 kg/m² per mm of thickness.

PACKAGING

30 kg kits:
component A: 25 kg sacks;
component B: 5 kg cans.

STORAGE

Planitop HDM Restauro component A may be stored for up to 12 months when contained in its original packaging in a dry place.
The product complies with the conditions of Annex XVII to Regulation (EC) N° 1907/2006 (REACH), item 47.
Planitop HDM Restauro component B may be stored for up to 24 months.
Both components must be stored at a temperature of at least +5°C.

SAFETY INSTRUCTIONS FOR PREPARATION AND APPLICATION

Planitop HDM Restauro component A irritates eyes and skin. When handling the product use protective gloves and googles. For further and complete information about a safety use of our product please refer to our latest version of the Material Safety Data Sheet.

PRODUCT FOR PROFESSIONAL USE.

WARNING

While the indications and guidelines contained in this data sheet correspond to the company's knowledge and wide experience, they must be considered, under all circumstances, merely as an indication and subject to confirmation only after long-term, practical applications. Therefore, anybody who undertakes to use this product, must ensure beforehand that it is suitable for the intended application and, in all cases, the user is to be held responsible for any consequences deriving from its use.

Please refer to the current version of the Technical Data Sheet, available from our website www.mapei.com

All relevant references for the product are available upon request and from www.mapei.com

TECHNICAL DATA (typical values)

PRODUCT IDENTITY	
Comp. A	
Appearance:	powder
Colour:	light
Bulk density (kg/m³):	1,400
Max diameter of aggregate (mm): (UNI EN 1015-1):	1.5
Chloride content (EN 1015-17) (%):	< 0.05
Hazard classification according to EC 1999/45:	irritant. Before using refer to the "Safety instructions for preparation and application" paragraph and the information on the packaging and Safety Data Sheet
Comp. B	
Appearance:	fluid liquid
Colour:	white
Bulk density (kg/m³):	1.02
Dry solids content (%):	10
Chloride content (EN 1015-17) (%):	< 0.05
Hazard classification according to EC 1999/45:	none. Before using refer to the "Safety instructions for preparation and application" paragraph and the information on the packaging and Safety Data Sheet
APPLICATION DATA	
Mixing ratio:	1 25 kg sack of component A with 1 canister of component B
Consistency of mix:	fluid-trowable
Density of mix (UNI EN 1015-6) (kg/m³):	1,900
Thickness applied (mm):	from 3 to 10 mm per coat
Application temperature range:	from +5°C to +35°C
Pot life of mix:	approx. 1 hour
Setting time (start / finish):	10 hours / 20 hours

FINAL PERFORMANCE

Performance characteristic	Test method	Requirements according to EN 998-1	Requirements according to EN 998-2	Performance of product
Compressive strength after 28 days (N/mm²):	EN 1015-11	CS I (from 0.4 to 2.5)	from Class M 1 (> 1 N/mm²) to Class M d (> 25 N/mm²)	> 15 (Category CS IV) (Class M 15)
		CS II (from 1.5 to 5.0)		
		CS III (from 3.5 to 7.5)		
		CS IV (≥ 6)		
Bond strength to substrate (brickwork) (N/mm²):	EN 1015-12	declared value and failure mode (FP)	not required	> 0,8 Failure mode (FP) = A
Initial shear strength (f_{vk0}) (N/mm²):	EN 1052-3	not required	chart value	0.15
Compressive modulus of elasticity (GPa):	UNI EN 13412	not required	not required	8,000
Capillary action water absorption [kg/(m²·min$^{0.5}$)]:	EN 1015-18	from Category W 0 to Category W 2	declared value	Category W 2 ≤ 0.2
Coefficient of permeability to water vapour (μ)	EN 1015-19	declared value	chart value	≤ 60
Thermal conductivity ($\lambda_{10,dry}$) (W/m·K):	EN 1745	chart value	0,75	P - 50°C
Reaction to fire Euroclass:	EN 13501-1	value declared by manufacturer	value declared by manufacturer	Class E

Freshly-mixed Planitop HDM Restauro

Application of Planitop HDM Restauro by spray on a brick wall

Application of Planitop HDM Restauro system with Mapegrid G 220 on a brick wall

Mortar M2:

BUILDING RANGE / Natural geo-mortars for structural reinforcement of walls

GeoCalce®

Eco-friendly, certified natural breathable structural geo-mortar with pure natural NHL 3.5 lime and mineral geo-binder base, compressive strength class M15 under EN 998-2, for operations on highly breathable walls and concrete structures, ideal for use in GreenBuilding and Historical Restoration. Contains raw materials of only natural origin and recycled minerals. Low CO_2 emissions and very low volatile organic compound emissions. Provides natural ventilation to improve indoor air quality, natural bacteriostatic and fungistatic effect. Recyclable as an inert material at the end of its life.

GeoCalce® is an M15, CS IV and R1 resistance class geo-mortar, specifically for reinforcing and structural alterations in seismic zones in conjunction with the appropriate structural reinforcements. It is ideal for rendering, extrados reinforcement of vaults and roofs, the arrangement and pointing of load-bearing masonry, and protective plastering of brick, tufa, stone, and mixed masonry and concrete.

GREENBUILDING RATING®

GeoCalce®
- Category: Inorganic Natural Minerals
- Class: Natural geo-mortars for structural reinforcement of walls
- Rating: Bio 5

PRODUCT STRENGTHS

- **UNIVERSAL**. GeoCalce® is the revolutionary formula that combines the breathability qualities of pure natural NHL 3.5 with the resistance of mineral geo-binder to ensure a universally applicable product.
- **NHL 3.5 LIME AND MINERAL GEO-BINDER**. The use of pure natural NHL 3.5, mixed with the innovative mineral geo-polymer crystallization geo-binder makes it possible to achieve advanced levels of mechanical resistance. The GeoCalce® line respects and satisfies the characteristics of existing masonry in Historical Restoration of Environmental and Architectural Heritage buildings and the requirements of the structural planner for alterations involved in protecting against seismic events.
- **HEALTH AND SAFETY**. The GeoCalce® line, used in conjunction with GeoSteel structural reinforcement systems, makes it possible to create a new system, using the existing walls, that can increase the mechanical resistance of the walls (M15 - CS IV - R1 mortar compressive resistance class) to improve the structural safety of the building to ensure greater protection for its occupants. In interiors, it helps decrease concentrations of the leading indoor pollutants, improving the healthful parameters of the environments and increasing indoor liveability.

NATURAL INGREDIENTS

AREAS OF USE

Use
GeoCalce® is ideal for creating breathable, structural fine-grain concretes for internal and external use, in conjunction with structural mesh or textiles, on perimeter masonry structures and infill to repair damaged masonry facing, to reinforce stringcourses and flat or domed roofs. GeoCalce® can be used as a rendering mortar to build new walls in compliance with the mechanical performance required in seismic zones.
It is suitable for building substrates for laying glued covering materials, both on facades and interiors.
GeoCalce® is particularly well suited to provide static reinforcement of masonry structures in Edilizia del Benessere (Building for Wellness) in which the all-natural origin of its components guarantees compliance with the required levels of porosity, hygroscopicity and breathability.

Do not use
On substrates which are dirty, non-cohesive, powdery or on previous paint coats and finishing coats: remove salt scaling from surfaces. Where capillary moisture rising is present, complete the cycle with Biocalce® Rinzaffo® and Biocalce® Zoccolatura®.

INSTRUCTIONS FOR USE

Preparation of substrates
The substrate must be clean and solid, free from loose debris, dust and mould. Clean the surfaces using hydro-sandblasting or sandblasting followed by a pressure washer to remove all remaining traces of previous processes (lime putty coverings, old finishing coats, saline formations, etc.) that may impair adhesion. Remove inconsistent rendering mortars from between the stones. Use GeoCalce® and the fragment-filling and/or break-fill techniques to rebuild missing sections of the wall and restore an even surface. Always wet substrates before applying the product.

* ÉMISSION DANS L'AIR INTÉRIEUR Information sur le niveau d'émission de substances volatiles dans l'air intérieur, présentant un risque de toxicité par inhalation, sur une échelle de classe allant de A+ (très faibles émissions) à C (fortes émissions).

KERAKOLL
The GreenBuilding Company

00731GeoCalce® Code: 8851 2014/05 EN

INSTRUCTIONS FOR USE

Application
Manual application: to prepare GeoCalce®, mix one 25-kg bag using clean water, in the amount shown on the package, in a standard concrete mixer. Mix by pouring water into the clean cement mixer and then add the powder in one operation. Wait until the right consistency forms while mixing. In the first 1-2 minutes the product will seem dry; do not add water at this stage. Keep mixing for 4-5 minutes until a smooth, spongy and lump-free consistency is achieved. Use all of prepared mixture; do not reuse it in subsequent mixings. Use running water not subject to the influence of outside temperatures. Adding cement in any quantity would impair the quality of the geo-mortar which is guaranteed by its all-natural origins.
Mechanized application: GeoCalce® has the same plasticity of the best natural limes, making it ideal for applications using a plaster sprayer. Tests to prove the compliance of GeoCalce® were carried out using a plaster sprayer and the following accessories: Mixer, Stator/Rotor D6-3, 25x37-mm flexible hoses, 10-20 m long and spray gun.
GeoCalce® can be easily applied with a trowel or spray like a normal plaster/render. Prepare the substrate, filling in any fragments if necessary to create a flat, smooth surface. Create the levelling layers, and then wet the substrate until it is fully saturated yet dry, leaving no excess water on the surface.
Use GeoCalce® as a rough coat and allow the mortar to dry fully. Lay the plaster/render, and then flatten and float as the product hardens. GeoCalce® should be applied with precision, each coat being no more than 2 cm thick even though the product lends itself easily to form thicker coats. This traditional system of application prevents the formation of micro-cracks. Only apply patch layers on rough or previous coats when the lower has hardened. Allow the hardened product to cure and keep it moistened during the first 24 hours during warm periods.

For reinforced, structural patching, first apply an initial coat of GeoCalce® that is thick enough to ensure that the surfaces are corrected. Then, over the GeoCalce® while it is still wet, apply the appropriate structural reinforcement mesh, making sure that it is completely enveloped in the GeoCalce® layer by pressing gently with a flat spreader. Next, create a second layer with GeoCalce®, making sure that the entire reinforcement system is fully covered; it should lay halfway through the overall thickness of the mortar. If no reinforced structural reinforcements will be created, on new masonry structures with sections clad in different materials, near joins between beams/pillars and infill, inclusion of a galvanised or synthetic anti-alkali plaster-reinforcing mesh should be placed at mid-thickness in the GeoCalce® to rule out any chance of cracking.

Cleaning
GeoCalce® is a natural product and tools can be cleaned with water before the product hardens.

SPECIAL NOTES

When plastering walls from different historical periods, always apply GeoCalce® in advance as a render to even out uneven sections and substrate absorbencies. Later, check to make sure it has adhered properly.
Externally, provide for a separation between the floors, walkways or horizontal surfaces in general, to avoid possible capillary draw phenomena.

ABSTRACT

Reinforcement of vaults or flat roofs, façade substrates intended for glued coverings, arrangement, pointing, or structural rendering are done with a geo-mortar with very high hygroscopicity and breathability for internal and external walls, with a base of pure natural NHL 3.5 and mineral geo-binder, inert siliceous sand, and Dolomitic limestone on granulometric curve 0 - 2.5 mm, GreenBuilding Rating® Bio 5 (such as GeoCalce® by Kerakoll Spa). The natural geo-mortar must also meet the requirements of standard EN 998-2 – G/ M15, EN 998-1 – GP/ CS IV and EN 1504-3 – R1 PCC, A1 fire classification class. The geo-mortar covering must not exceed 20 mm per coat, levelling layers, rustic finish coat done with flattener, squaring up of edges and corners, and excluding the cost of scaffolding hire. To be applied by hand or using a plastering machine. GeoCalce® coverage: ≈ 14.5 kg/m² per cm of thickness.

TECHNICAL DATA COMPLIANT WITH KERAKOLL QUALITY STANDARD

Appearance	Powder	
Aggregate mineral content	silica – carbonate	
Grading	0 – 2,5 mm	
Shelf life	≈ 12 months in the original packaging in dry environment	
Pack	25 kg bags	
Mixing water	≈ 5.1 ℓ / 1 x 25 kg bag	
Apparent density of wet mortar	≈ 1,76 kg/dm³	EN 1015-6
Apparent density of dry, hardened mortar	≈ 1,61 kg/dm³	EN 1015-10
Temperature range for application	from +5 °C to +35 °C	
Maximum thickness obtainable by coat	≈ 2 cm	
Coverage	≈ 14.5 kg/m² per cm of thickness	

Values taken at +23 ± 2 °C, 50 ± 5% R.H. and no ventilation. Data may vary depending on specific conditions at the building site

00731GeoCalce® Code: B851 2014/05 EN

KERAKOLL
The GreenBuilding Company

PERFORMANCE

VOC INDOOR AIR QUALITY (IAQ) - VOLATILE ORGANIC COMPOUND EMISSIONS			
Conformity	EC 1-R plus GEV-Emicode		GEV certified 4092/11.01.02
ACTIVE INDOOR AIR QUALITY (IAQ) - DILUTION OF INDOOR POLLUTANTS *			
	Flow	Dilution	
Toluene	219 µg m³/h	+129%	JRC method
Pinene	170 µg m³/h	+5%	JRC method
Formaldehyde	1040 µg m³/h	test failed	JRC method
Carbon dioxide (CO_2)	33 mg m³/h	+53%	JRC method
Humidity (Humid Air)	15 mg m³/h	+7%	JRC method
BIOACTIVE INDOOR AIR QUALITY (IAQ) - BACTERIOSTATIC ACTION **			
Enterococcus faecalis	Class B+ no proliferation		CSTB method
BIOACTIVE INDOOR AIR QUALITY (IAQ) - FUNGISTATIC ACTION **			
Penicillum brevicompactum	Class F+ no proliferation		CSTB method
Cladosporium sphaerospermum	Class F+ no proliferation		CSTB method
Aspergillus niger	Class F+ no proliferation		CSTB method
HIGH-TECH EN 998-1			
Coeff. for resistance to vapour circulation (µ)	≥ 16		EN 1015-19
Water absorption through capillary action	W1 category		EN 998-1
Reaction to fire	class A1		EN 13501-1
Compressive strength after 28 days	*CS IV* category		EN 998-1
Adhesion to support (hollow clay block)	≥ 1 N/mm² - **FP**: B		EN 1015-12
Thermal conductivity (λ_{10}, dry)	0,67 W/mK (table value)		EN 1745
Durability (freeze/thaw)	NPD		EN 998-1
HIGH-TECH EN 998-2			
Compressive strength after 28 days	M15 category		EN 998-2
Permeability to water vapour (µ)	from 15 to 35 (table value)		EN 1745
Water capillary absorption	≈ 0,3 kg/(m² · min^{0,5})		EN 1015-18
Shear strength	> 1 N/mm²		EN 1052-3
Adhesion to the substrate after 28 days	> 1 N/mm² - FP: B		EN 1015-12
Thermal conductivity (λ_{10}, dry)	0,67 W/mK (table value)		EN 1745
Static modulus of elasticity	9,23 GPa		EN 998-2
Conformity	M15 resistance class		EN 998-2
HIGH-TECH EN 1504-3			

Performance characteristic	Test Method	Requirements foreseen by EN 1504-3 class R1	GeoCalce® Performance in PCC conditions
Compressive strength	EN 12190	≥ 10 MPa (28 days)	> 15 MPa (28 days)
Flexural tensile strength	EN 196/1	None	> 5 MPa (28 days)
Adhesive bond	EN 1542	≥ 0,8 MPa (28 days)	> 0,8 MPa (28 days)
Adhesion on clay brick	EN 1015-1	None	> 1 MPa (28 days)
Modulus of elasticity under compression	EN 13412	None	9,23 GPa (28 days)
Thermal compatibility with freeze/thaw cycles with de-icing salts	EN 13687-1	visual inspection	exceeded
Chloride ion content (Determined on the product in powder form)	EN 1015-17	≤ 0,05%	< 0,05%
Reaction to fire	EN 13501-1	Euroclass	A1

Values taken at +23 ± 2 °C, 50 ± 5% R.H. and no ventilation. Data may vary depending on specific conditions at the building site.
** Tests carried out according to JRC method - Joint Research Centre - European Commission, Ispra (Varese, Italy) - to measure the reduction of polluting substances in indoor environments (Indoortron Project). Flow and speed in proportion to a standard construction mortar (1,5 cm).*
*** Tests carried out according to CSTB method, bacterial and fungal contamination*

00731GeoCalce® Code: BB51 2014/05 EN

KERAKOLL
The GreenBuilding Company

Mortar M3:

MAPEI

IN COMPLIANCE WITH EUROPEAN STANDARD EN 998-1 R-CS II MAPEI RENDERING AND PLASTERING MORTAR

Mape-Antique MC

GEV-EMICODE EC1 PLUS very low emission

CE EN 998-1

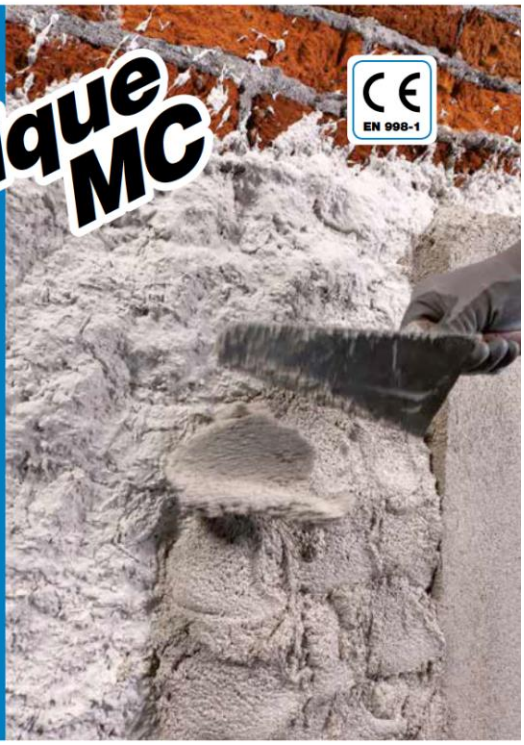

Macroporous, salt-resistant de-humidifying render, based on lime and Eco-Pozzolan, for restoring old masonry, including on buildings of historical interest

WHERE TO USE

Repairs to old masonry deteriorated by the presence of capillary rising damp, including on buildings of historical and artistic interest.
Repairs to masonry deteriorated by the disintegrating action of concentrated salts.
Rebuilding lime-based render deteriorated by the action of atmospheric agents and environmental conditions or by ageing.

Some application examples

- Internal and/or external macro-porous, de-humidifying render on old walls with capillary rising damp.
- Internal and/or external macro-porous, de-humidifying render on old stone, brick, tuff or mixed masonry with saline efflorescence.
- De-humidifying render on masonry in lagoon areas or close to the sea.
- New de-humidifying render or reconstructing old lime-based render on stone, brick, tuff and mixed masonry, including on buildings of historical and artistic interest with a conservation order or under the protection of the National Trust.
- Touching-up and plumbing facing walls with gaps and uneven surfaces.
- Pointing between layers of stone, brick and tuff on masonry with a "natural finish".

TECHNICAL CHARACTERISTICS

Mape-Antique MC is a pre-blended, cement-free mortar in powder form for de-humidifying render made from lime, Eco-Pozzolan, natural sand, special additives and micro-fibres with very low emission level of volatile organic compounds (EMICODE EC1 R Plus), according to a formulation developed in MAPEI's research laboratories. This product is classified as R according to EN 998-1 Standards: "*Renovation mortar. Mortar designed for internal/external render applied on damp masonry walls containing water-soluble salts*", Category CS II.
When mixed with water in a cement mixer, **Mape-Antique MC** forms a salt-resistant, macro-porous, de-humidifying rendering mortar with a plastic-thixotropic consistency which is easy to apply by trowel on both vertical surfaces and on ceilings.
The properties of mortar made using **Mape-Antique MC**, such as mechanical strength, modulus of elasticity and porosity, are very similar to mortar made using lime, lime-pozzolan or hydraulic lime originally used in the construction of old buildings.
Compared with these types of mortar, however, **Mape-Antique MC** also has properties which make the product resistant to various chemical-physical aggressive phenomena, such as the presence of soluble salts, freeze-thaw cycles, the leaching action of rainwater, alkali-aggregate reactions and the formation of cracks caused by plastic shrinkage.
When working on particularly damp internal walls or in cold weather, the setting and hardening times of **Mape-Antique MC** are considerably longer and much more time than usual must be allowed for the product to cure. The product may give off a different odour for a while when curing under such conditions and may turn green in some areas. The odour and green colour will gradually disappear as the product and wall dry out until it takes on its characteristic light colour.
Typical values are shown in the Technical Data table (see Application Data and Final Performance sections)

Mape-Antique MC

Applying Mape-Antique MC over Mape-Antique Rinzaffo

Levelling the surface of Mape-Antique MC with a straight edge

Levelling the surface of Mape-Antique MC

which refer to the main characteristics of **Mape-Antique MC** at both fresh and hardened states.

RECOMMENDATIONS

- In the presence of capillary rising damp and soluble salts, only apply **Mape-Antique MC** after applying a layer of **Mape-Antique Rinzaffo** approximately 5 mm thick.
- **Mape-Antique MC** must be applied in layers at least 20 mm thick.
- Do not use **Mape-Antique MC** for casting into formwork (**Mape-Antique LC** mixed with aggregates with a suitable grain size).
- Do not use **Mape-Antique MC** to make consolidating slurry for injection into structures (use **Mape-Antique I** or **Mape-Antique F21**).
- Do not use **Mape-Antique MC** for "reinforced" render (use **Mape-Antique Strutturale NHL**).
- Do not use **Mape-Antique MC** for skimming (use **Mape-Antique FC Ultrafine**, **Mape-Antique FC Civile** or **Mape-Antique FC Grosso**).
- Never add additives, cement or other binders (lime and gypsum) to **Mape-Antique MC**.
- Do not apply thin coats of paint or coloured coating which could have a significant impact on the transpiration properties and porosity of **Mape-Antique MC** and, therefore, obstruct the evaporation of the damp in the masonry. Use products from the **Silexcolor** or **Silancolor** ranges, lime-based paint and water-repelling products such as **Antipluviol S** or **Antipluviol W**.
- If the structures to be restored suffer from intense capillary rising damp and high concentrations of soluble salts, we recommend forming a horizontal chemical barrier (such as with **Mapestop**) before applying the de-humidifying render to reduce the ingress of damp into the masonry as much as possible.
- We recommend analysing the walls before applying the product to determine the concentration level of salts in the walls.
- Do not apply **Mape-Antique MC** if the temperature is lower than +5°C.

APPLICATION PROCEDURE

Preparation of the substrate

On masonry with capillary rising damp and soluble salts, completely remove the deteriorated render either manually or with mechanical means to a height of approximately 50 centimetres above the deteriorated area, and in all cases to a height of at least twice the thickness of the wall. Remove all traces of loose or crumbly material, dust, mould and any other element which could compromise the bond of the de-humidifying cycle of **Mape-Antique Rinzaffo** and **Mape-Antique MC** until the substrate is clean, sound and compact. Then clean the wall with low-pressure water jets to remove any efflorescence or soluble salts present on the surface. Repeat this operation several times if necessary.
Gaps and uneven areas in the masonry must be repaired by patching or tacking with **Mape-Antique MC**, **Mape-Antique Allettamento** or **Mape-Antique Strutturale NHL** in combination with pieces of stone, brick or tuff with characteristics as similar as possible to the original material.
Saturate the substrate with water to prevent it from absorbing water from the mortar and compromising its final performance characteristics. Excess water must be left to evaporate off, so that the masonry is saturated and the surface is dry. Compressed air may be used to speed up this process. If the substrate cannot be saturated with water, we recommend that it is at least dampened to allow the mortar to bond correctly.
If there is capillary rising damp, before spreading on the **Mape-Antique MC**, apply a layer of **Mape-Antique Rinzaffo** approximately 5 mm thick to completely cover the substrate to improve the bond, even out the absorption of the substrate and slow down the transfer of the salts.
On mixed walls or on walls out of plumb by more than 4-5 cm, which would lead to the layer of render having an irregular thickness, we recommend inserting Ø 2 mm zinc-plated metallic mesh with a mesh size of 5 x 5 cm before applying the **Mape-Antique Rinzaffo**. The mesh must be fixed in place to the wall with nails, chemical anchoring (such as **Mapefix PE SF**) and plugs with a small gap between the wall so that it becomes embedded in the middle of the layer of render.
Form levelling strips with **Mape-Antique MC** or place vertical guides in position to define the correct planarity and thickness of the render.

Preparation of the product

Prepare **Mape-Antique MC** with a vertical cement mixer. Small amounts of the product may be prepared using a low-speed electric drill with a mixing attachment. Mixing the product by hand is not recommended.
After pouring the minimum amount of clean water required into the mixer (3.5 litres per 25 kg bag of **Mape-Antique MC**), slowly add the powdered mortar in a continuous flow. Mix for approximately 3 minutes and check that the blend is well mixed, even and free of lumps and ensure that no material has stuck to the sides and bottom of the mixer. Add a further amount of water if required up to a total of 4 litres per bag, including the water added at the start of mixing. Then mix the **Mape-Antique MC** again for a further 2-3 minutes to obtain an even, "plastic" and thixotropic blend.

Application of the product

If a layer of **Mape-Antique Rinzaffo** has been applied, for example on masonry with capillary rising damp and soluble salts, wait until this layer has "set" and then apply a layer of **Mape-Antique MC** at least 20 mm thick with a trowel, starting from the bottom of the wall. If the thickness to be built up is thicker than 30 mm, **Mape-Antique MC** must be applied in several layers. Each layer must be applied without tamping the previous layer. After applying the mortar, wait a few minutes and level off using an aluminium H-type or blade-type straight edge by passing over the surface horizontally and vertically until it is flat. Remove the vertical

Mape-Antique MC

guides, if they have been used, and fill the gaps with **Mape-Antique MC**.
Finish off the surface of the render with a plastic, wooden or sponge float a few hours after application, according to the surrounding temperature and conditions. Never press down on the surface of the **Mape-Antique MC** otherwise the porosity of the render would reduce and, as a result, evaporation of the damp in the masonry would be obstructed.
Even though **Mape-Antique MC** contains products which constrict the formation of micro-cracks, it is good practice to apply the mortar when the wall is not exposed to direct sunlight and/or wind. In such cases, such as during hot and/or particularly windy weather, take special care when curing the render, especially during the first 36-48 hours. Spray water on the surface or employ other systems to prevent the mixing water evaporating off too quickly.

FINISHING COAT
If a finer-grained surface finish than the normal tamped finish of **Mape-Antique MC** is required, apply a layer of **Mape-Antique FC Ultrafine**, **Mape-Antique FC Civile** or **Mape-Antique FC Grosso** skimming compounds with different grain sizes. Even though **Mape-Antique FC Ultrafine** and **Mape-Antique FC Civile** may be applied on any type of lime-based render, including macro-porous de-humidifying render, the fine grain structure of these skimming compounds tends to slightly reduce the vapour permeability of the render. In such cases, it is better to use **Mape-Antique FC Grosso** which has a thick finishing or silicate-based **Silexcolor Tonachino** or siloxane-based **Silancolor Tonachino**, coloured coating products applied in thin coats after applying their corresponding primers (**Silexcolor Primer** and **Silancolor Primer**). Always wait until the render and skimming layer, if applied, are completely cured before painting the surface or applying any other type of finishing product. Paint the surface with **Silexcolor Paint** or **Silancolor Paint** after applying their corresponding primers. For constructions particularly exposed to rain, if the render does not require any coating, it may be protected with a transparent water-repellent product such as **Antipluviol S** siloxane resin impregnator in solvent or **Antipluviol W** siloxane resin impregnator in water dispersion.

Cleaning
Mortar may be removed from tools with water before it hardens. Once hardened, cleaning is difficult and must be carried out mechanically.

PACKAGING
25 kg bags.

COLOUR
White.

CONSUMPTION
15 kg/m^2 (per cm of thickness).

STORAGE
Store **Mape-Antique MC** up to 12 months in a dry, covered environment in its original, unopened packaging.

SAFETY INSTRUCTIONS FOR PREPARATION AND APPLICATION
Mape-Antique MC contains special hydraulic binders, that when in contact with sweat or other body fluids cause corrosion and damage to eyes. It is recommended to wear protective gloves and goggles and to take the usual precautions for handling of chemicals. If the product comes in contact with the eyes or the skin wash immediately with plenty of water and seek medical attention.
For further and complete information about the safe use of our product please refer to the latest version of our Material Safety Data Sheet.

PRODUCT FOR PROFESSIONAL USE.

WARNING
Although the technical details and recommendations contained in this product data sheet correspond to the best of our knowledge and experience, all the above information must, in every case, be taken as merely indicative and subject to confirmation after long-term practical application; for this reason, anyone who intends to use the product must ensure beforehand that it is suitable for the envisaged application. In every case, the user alone is fully responsible for any consequences deriving from the use of the product.

Please refer to the current version of the Technical Data Sheet, available from our website www.mapei.com

GEV EMICODE EC 1 PLUS very low emission

This symbol is used to identify Mapei products which give off a low level of volatile organic compounds (VOC) as certified by GEV (Gemeinschaft Emissionskontrollierte Verlegewerkstoffe, Klebstoffe und Bauprodukte e.V.), an international organisation for controlling the level of emissions from products used for floors.

GREEN INNOVATION

Our Commitment To The Environment
MAPEI products assist Project Designers and Contractors create innovative LEED (The Leadership in Energy and Environmental Design) certified projects, in compliance with the U.S. Green Building Council.

All relevant references for the product are available upon request and from www.mapei.com

604-5-2015 (GB)

MAPEI®
BUILDING THE FUTURE

TECHNICAL DATA (typical values)			
PRODUCT IDENTITY			
Type of mortar (EN 998-1):	R: "Renovation mortar. Mortar designed for internal/ external render applied on damp masonry walls containing water-soluble salts"		
Consistency:	powder		
Colour:	white		
Maximum size of aggregate (EN 1015-1) (mm):	2.5		
Bulk density (kg/m³):	1,500		
EMICODE:	EC1 R Plus - very low emission level		
APPLICATION DATA OF PRODUCT (at +20°C - 50% R.H.)			
Mixing ratio:	100 parts of **Mape-Antique MC** with 14-16 parts of water (3.5-4 litres of water per 25 kg bag of product)		
Consistency of blend:	plastic-thixotropic		
Consistency of fresh mortar (EN 1015-3) (mm):	170		
Bulk density of fresh mortar (EN 1015-6) (kg/m³):	1,700		
Porosity of the mortar while still fresh (EN 1015-7) (%):	> 20		
Application temperature range:	from +5°C to +35°C		
Workability time of fresh mortar (EN 1015-9):	approx. 60 minutes		
Minimum applicable thickness (mm):	20		
Maximum applicable thickness per layer (mm):	30		
FINAL PERFORMANCE (15% mixing water)			
Performance characteristic	**Test method**	**Requirements according to EN 998-1**	**Performance of product**
Compressive strength after 28 days (N/mm²):	EN 1015-11	CS I (from 0.4 to 2.5)	Category CS II
		CS II (from 1.5 to 5.0)	
		CS III (from 3.5 to 7.5)	
		CS IV (≥ 6)	
Bond strength to substrate (N/mm²):	EN 1015-12	declared value and failure mode (FP)	≥ 0.4 failure mode (FP) = B
Capillary action water absorption (kg/m²):	EN 1015-18	≥ 0.3 (after 24 h)	3.5
Coefficient of permeability to water vapour (μ)	EN 1015-19	≤ 15	≤ 10
Thermal conductivity ($\lambda_{10,dry}$) (W/m·K):	EN 1745	tabulated value	0.61
Reaction to fire:	EN 13501-1	value declared by manufacturer	Class A1
Resistance to sulphates:	Anstett test	not required	high
Saline efflorescence (after semi-immersion in water):	/	not required	absent

Finishing mortared joints pointed with Mape-Antique MC

Steel fiber:

BUILDING RANGE / Steel bars and sheets for structural strengthening of reinforced concrete and masonry structures

GeoSteel G600

GeoSteel G600 Hardwire™ is a unidirectional sheet made of ultra-high strength galvanized steel micro-cords, fixed to a fibreglass micromesh to facilitate installation, which can be installed using a GeoCalce® Fino or GeoLite® or GeoLite® Gel matrix according to project and building site requirements.

The structural strengthening GeoSteel sheet is thus extremely easy to handle and shape, and combines excellent mechanical and installation properties with high durability thanks to galvanization of the individual wires. Galvanized steel fiber sheets guarantee unique structural and mechanical properties, much higher than traditional carbon-glass-aramide fibre sheets, making them particularly effective in the various structural strengthening and seismic upgrade or compliance retrofit solutions, as well as the creation of suitable connection systems, when combined with GeoSteel Injector&Connector.

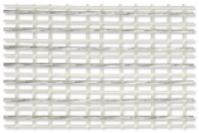

PRODUCT STRENGTHS

- High durability thanks to the special steel wire galvanization process, tested using strict durability tests in a chloride, freeze-thaw and high humidity environment
- Specifically intended for structural strengthening using:
  - GeoCalce® Fino, with pure natural hydraulic NHL 3.5 lime and mineral geo-binder base, ideal for retrofitting structural elements made of brick, natural stone, and tuff masonry and substrates that require advanced breathability along with high mechanical adhesion
  - GeoLite®, with mineral geo-binder base, ideal for retrofitting structural elements in reinforced concrete, prestressed reinforced concrete or good consistency masonry
  - GeoLite® Gel, epoxy-based mineral adhesive, ideal for structural retrofitting sections made of reinforced concrete, prestressed reinforced concrete, wood and steel
- Can be tensioned to create structural reinforcements and active devices using particular mechanical anchoring systems, thanks to the unique characteristics of the textile which do not require advance impregnation of the sheet, and at the same time allow it to be anchored and fastened with metal plates without having to take particular precautions, as is necessary for all the other types of fibre and textile on the market
- Can be shaped using GeoSteel Bender which allows the sheet to be modelled easily without altering its mechanical properties to create surround brackets for beams and pillars and other bent elements required during structural consolidation works

AREAS OF USE

Use

- Static and seismic upgrade or compliance retrofit of structural elements in brick, natural stone, tuff, reinforced concrete, prestressed reinforced concrete, wood, and steel walls
- Consolidation of brick masonry, natural stone and tuff arches, vaults and domes
- Confinement and wrapping of masonry and reinforced concrete structural elements
- Flexural, shear, and confinement strengthening of brick, natural stone, tuff, and masonry panels and reinforced concrete sections
- Flexural, shear, and confinement strengthening for timber elements
- Flexural strengthening for steel girders
- Execution of top ring beams or in breach in reinforced masonry
- Execution of special single- or double-fibre thread connectors for anchoring sheets and grids and executing reinforced injections

INSTRUCTIONS FOR USE

Preparation

The ultra-high strength galvanized steel fibre sheet, GeoSteel G600 Hardwire™, is ready-to-use.
The sheet can be cut at right angles to the cords with manual or electric shears, or parallel with the cords using a normal box cutter. The sheet, cut into strips even just a few cm wide and a number of metres long, ensures perfect stability without in any way compromising the workability of the material and its application.

Preparation of substrates

The substrate must be properly prepared and cleaned, always in accordance with the instructions dictated by the construction supervisor.
When the substrates are not damaged, simply clean and remove any dust or oils that could compromise the adhesion of the system, using compressed air or pressure water.
When the substrate is clearly degraded, uneven, or damaged by significant events, proceed as follows, always in accordance with the construction supervisor:

1. For masonry, tuff, and natural stone substrates:
   - Completely remove residues from previous processes that could compromise adhesion, and any quantity of inconsistent rendering mortars from between the stones;

0075GeoSteel G600 Code: E865 2014/07

KERAKOLL
The GreenBuilding Company

INSTRUCTIONS FOR USE

- Saturation, spray, or brush application, if required, of certified natural stabilizing cortical consolidant with base of pure stabilised potassium silicate in aqueous solution such as Biocalce® Silicato Consolidante or water-based eco-friendly solvent-free stabilizing agent, such as Rasobuild® Eco Consolidante;
- Reconstruction, if necessary, of material continuity according to design instructions and the construction supervisor.
- Levelling previously consolidated surfaces with geo-mortar with a base of pure natural hydraulic lime NHL 3.5 and mineral geo-binder such as GeoCalce® or GeoCalce® Fino, depending on the thickness required;

2. For substrates in reinforced concrete or prestressed reinforced concrete:
   - Thorough removal of weakened concrete if necessary, through mechanical scarification or hydro-demolition, making sure to roughen the substrate to a depth of at least 5 mm;
   - Removal of rust, if any, from reinforcing bars, which must be cleaned by brushing (manual or mechanical) or sandblasting;
   - Monolithic reconstruction or smoothing of the section, if needed, using geo-mortar based on a mineral geo-binder such as GeoLite®.
   - When applying the reinforcing system with an inorganic matrix, make sure that the substrate is appropriately dampened (follow the directions on the GeoLite® or GeoCalce® data sheets).
   - When applying the reinforcing system with an organic matrix, the substrate must be dry and free of humidity (follow the instructions on the GeoLite® Gel data sheet).

Application

Execution of steel fibre structural reinforcement in Steel Reinforced Mortar (combination of steel fibre and GeoCalce® Fino or GeoLite®), or Steel Reinforced Polymer (combination of steel fibre and GeoLite® Gel epoxy mineral adhesive) will be followed by application of a first layer of geo-mortar, making sure there is sufficient material for the substrate (average thickness ≈ 3 - 5 mm) to even it out and to lay and incorporate the reinforcing sheet. When using an epoxy mineral adhesive matrix, the substrate can be levelled using GeoLite® or GeoCalce®, taking care to allow the geo-mortar to cure for long enough to ensure that the humidity of the substrate is appropriate for application of GeoLite® Gel. The first layer of adhesive must be an average thickness of ≈ 2 - 3 mm. Afterward, working over the matrix while it is still wet, apply the ultra-high strength galvanized steel fibre sheet GeoSteel G600 Hardwire™, making sure that the sheet is perfectly incorporated into the matrix by pressing with a spreader or steel roller, and also checking that it comes out between the cords to ensure optimum adhesion between the first and second layers of matrix. At longitudinal overlapping points, overlay two layers of steel fibre sheet by least 15 cm for epoxy matrix and 30 cm for inorganic matrices. For organic and inorganic matrix, working wet on wet, perform the final protective smoothing (≈ 1 - 2 mm thick for organic matrix, ≈ 2 - 3 mm thick for inorganic), in order to fully incorporate the reinforcement and fill in any underlying voids. If there are additional layers after the first, proceed with laying of the second layer of steel fibre over the matrix while it is still wet, repeating the steps described above. In the event that the system installed with epoxy matrix must be plastered or concealed by smoothing, we recommend that, while the resin is still wet, you apply a spray of mineral quartz to provide better adhesion for subsequent layers.
If the reinforcing system is installed in especially aggressive environments, or you otherwise wish to ensure additional protection beyond that already provided by the matrix, we recommend applying:
- GeoLite® Microsilicato on reinforcement systems with GeoLite® or GeoCalce® Fino matrix;
- Kerakover Eco Acrilex Flex on reinforcement systems with GeoLite® Gel matrix.

If the works are in permanent or occasional contact with water, the cycles described above must be replaced with a polyurethane epoxy cycle or an osmotic cement depending on the needs of the worksite and the design specifications.
For technical specifications, application, and preparation of the matrix, as well as protective systems adequate for the matrix type, consult the relevant data sheets.

Creating a GeoSteel Connector

A steel-fibre thread connector system is created by including a band of fabric of appropriate width from the GeoSteel Hardwire™ line to provide the minimum number of cords in the connector according to the design, in order to achieve the required tensile strength; make sure to unravel the end of the fabric band by cutting the supportive mesh, making the cut parallel to the cords themselves to the length of the edge you want to create on the masonry. In the event of a connector with threads on both sides, this operation must be performed on both ends of the duly arranged fibre strip. Once the sheet is cut, roll the band onto itself, taking care to create a cylinder of an appropriate diameter compared to the hole.
Install the connector that has been created into the hole, and then insert the Geosteel glass fibre-reinforced polypropylene GeoSteel Injector&Connector, so that the end of the fibre bends 90°. Finally, using the special hole located on the head of the piece, inject the pourable mortar, such as GeoCalce® Fluido, to grout the fibre-thread connector system. When this phase is complete, the GeoSteel Injector&Connector must be duly sealed with the cap provided.
Depending on the type of substrate (concrete or masonry) for grouting the connector, as an alternative to the use of pourable natural hydraulic lime, the designer may choose to use pourable cement-based mortar Kerabuild® Eco Binder, thixotropic epoxy resin GeoLite® Gel or superfluid Kerabuild® Epofill.

Provided below is a table listing the tensile strength of a connector as a function of the type of GeoSteel Hardwire™ sheet and the corresponding widths of the band adopted:

Sheet	Width of the band (cm)	Number of Cords*	Tensile breaking load
GeoSteel G600	10	16	> 24 kN
GeoSteel G600	15	23	> 35 kN

*n° cords/cm = 1,57;
tensile breaking load of a cord > 1500 N.

In the event that a connector with another strength or a different number of cords from those listed is required, simply calculate the appropriate width of the band by dividing the required strength by the strength of one cord and then by the number of cords present per unit of width in the type of sheet selected.
Test reports are available upon request to determine the calculation parameters.

00175GeoSteel G600 Code: E865 2014/07

KERAKOLL
The GreenBuilding Company

ABSTRACT

SRM-GeoCalce® GeoSteel G600

Execution of structural reinforcement or repair, seismic upgrade of masonry, tuff, or natural stone elements and structures using a composite system based on ultra-high strength galvanized steel fibre sheet GeoSteel G600 Hardwire™ from Kerakoll Spa, with net fibre weight of ≈ 600 g/m², with the following mechanical characteristics: sheet tensile strength > 2800 MPa; sheet elastic modulus > 190 GPa; sheet break deformation > 1.50%; nominal area of a cord 3x2 (5 wires) = 0.538 mm²; no. cords per cm = 1.57; sheet equivalent thickness = 0.084 mm, impregnated with certified inorganic matrix of natural, structural, breathable, eco-friendly geo-mortar based on pure natural hydraulic lime NHL 3.5 and mineral geo-binder, such as GeoCalce® Fino by Kerakoll Spa, to be applied directly on the structure requiring reinforcement.

The procedure is conducted as follows:

1. *Any restoration of degraded, weakened, non-cohesive, or non-planar surfaces with GeoCalce® by Kerakoll Spa, in the case of masonry substrates, or GeoLite® by Kerakoll Spa, in the case of reinforced concrete substrates, and in all cases as dictated and approved by the construction supervisor;*
2. *Lay a first layer, an average of ≈ 3 - 5 mm thick of geo-mortar with pure natural NHL 3.5 and mineral geo-binder base, such as GeoCalce® Fino by Kerakoll Spa;*
3. *While the mortar is still wet, lay the ultra-high strength galvanized steel fibre sheet GeoSteel G600 Hardwire™ by Kerakoll Spa, and by pressing firmly with a smooth spreader or metal roller, make sure that the sheet is completely impregnated and avoid allowing any gaps or air bubbles to form, because these can compromise the adhesion of the sheet to the matrix or to the substrate;*
4. *Working wet on wet, apply the second layer of geo-mortar based on pure natural lime NHL 3.5 and mineral geo-binder, such as GeoCalce® Fino by Kerakoll Spa, ≈ 2 – 3 mm thick to fully incorporate the reinforcing sheet and fill in any remaining underlying gaps;*
5. *Repeat steps (3 and (4 if necessary for all subsequent reinforcing layers called for by the design.*

Delivery and installation of all the materials described above as well as everything else required to finish the job is included. The following are excluded: restoration of degraded areas and repair of the substrate; anchoring devices using connectors or metal plates; material acceptance tests; pre- and post-procedure testing, all aids required to perform the work.

The price is by unit of reinforcing surfaces actually laid, including overlaps and anchoring sections.

SRM-GeoLite® GeoSteel G600

Execution of structural reinforcement or repair, or seismic upgrade or compliance retrofit of reinforced cement, masonry, tuff, or natural stone elements and structures using a composite system based on ultra-high strength galvanized steel fibre sheet GeoSteel G600 Hardwire™ from Kerakoll Spa, with net fibre weight of ≈ 600 g/m², with the following mechanical characteristics: sheet tensile strength > 2800 MPa; sheet elastic modulus > 190 GPa; sheet break deformation > 1.50%; nominal area of a cord 3x2 (5 wires) = 0.538 mm²; no. cords per cm = 1.57; sheet equivalent thickness = 0.084 mm, impregnated with inorganic matrix of eco-friendly, thixotropic, normal-setting certified mineral geo-mortar, based on crystalline reaction geo-binder and zirconium, with very low petrochemical polymer content and free of organic fibres, specifically for passivation, restoration, smoothing, and guaranteed, long-lasting monolithic protection of structures in concrete, such as GeoLite® by Kerakoll Spa, to be applied directly on the structure requiring reinforcement.

The procedure is conducted as follows:

1. *Any restoration of degraded, weakened, non-cohesive, or non-planar surfaces shall be performed with GeoCalce® by Kerakoll Spa, in the case of masonry substrates, or GeoLite® by Kerakoll Spa, in the case of reinforced concrete substrates, and in all cases as dictated and approved by the construction supervisor;*
2. *Spread a first layer of approximate average thickness of ≈ 3 - 5 mm of geo-mortar with mineral geo-binder base, such as GeoLite® by Kerakoll Spa;*
3. *While the mortar is still wet, lay the ultra-high strength galvanized steel fibre sheet GeoSteel G600 Hardwire™ by Kerakoll Spa, and by pressing firmly with a smooth spreader or metal roller, make sure that the sheet is completely impregnated and avoid allowing any gaps or air bubbles to form, because these can compromise the adhesion of the sheet to the matrix or to the substrate;*
4. *Working wet on wet, apply the second layer of geo-mortar, such as GeoLite® by Kerakoll Spa, approximately ≈ 2 -3 mm thick, until the reinforcing sheet is fully incorporated and any underlying voids are filled;*
5. *Repeat steps (3 and (4 if necessary for all subsequent reinforcing layers called for by the design.*

Delivery and installation of all the materials described above as well as everything else required to finish the job is included. The following are excluded: restoration of degraded areas and repair of the substrate; anchoring devices using connectors or metal plates; material acceptance tests; pre- and post-procedure testing, all aids required to perform the work.

The price is by unit of reinforcing surfaces actually laid, including overlaps and anchoring sections.

SRP GeoSteel G600

Execution of structural reinforcement or repair, or seismic upgrade or compliance retrofit of reinforced cement, masonry, wood and steel using a composite system based on ultra-high strength galvanized steel fibre sheet GeoSteel G600 Hardwire™ from Kerakoll Spa, with net fibre weight of ≈ 600 g/m², with the following mechanical characteristics: sheet tensile strength > 2800 MPa; sheet elastic modulus > 190 GPa; sheet break deformation >1.50%; nominal area of a cord 3x2 (5 wires) = 0.538 mm²; no. cords per cm = 1.57; sheet equivalent thickness = 0.084 mm, impregnated with epoxy mineral matrix such as GeoLite® Gel by Kerakoll Spa to be applied directly on the structure requiring reinforcement without any need for primer.

The procedure is conducted as follows:

1. *Any restoration of degraded, weakened, non-cohesive, or non-planar surfaces shall be performed with GeoCalce® by Kerakoll Spa, in the case of masonry substrates, or GeoLite® by Kerakoll Spa, in the case of reinforced concrete substrates, and in all cases as dictated and approved by the construction supervisor;*
2. *Application of a first layer approximately average thickness of ≈ 2 - 3 mm of epoxy mineral adhesive such as GeoLite® Gel by Kerakoll Spa;*
3. *While the epoxy mineral adhesive is still wet, lay the ultra-high strength galvanized steel fibre sheet GeoSteel G600 Hardwire™ by Kerakoll Spa, and by pressing firmly with a smooth spreader or metal roller, make sure that the sheet is completely impregnated and avoid allowing any gaps or air bubbles to form, because these can compromise the adhesion of the reinforcing system to the substrate;*
4. *Working wet on wet, lay the second layer of matrix, such as GeoLite® Gel by Kerakoll Spa, at an average thickness of ≈ 1 – 2 mm, until the reinforcing sheet is completely covered;*
5. *Repeat steps (3 and (4 if necessary for all subsequent reinforcing layers called for by the design.*

Delivery and installation of all the materials described above as well as everything else required to finish the job is included. The following are excluded: restoration of degraded areas and repair of the substrate; anchoring devices using connectors or metal plates; material acceptance tests; pre- and post-procedure testing, all aids required to perform the work.

The price is by unit of reinforcing surfaces actually laid, including overlaps and anchoring sections.

TECHNICAL DATA COMPLIANT WITH KERAKOLL QUALITY STANDARD

Wire			
	- characteristic tensile stress	σ_{wire}	> 2900 MPa
	- elastic modulus	E_{wire}	> 205 GPa
	- area	A_{wire}	0,1076 mm²
Dry sheet/Cord			
Cord 3x2 obtained by joining 5 filaments, of which 3 straight and 2 wrapped with a high torque angle			
	- actual area of a cord 3x2 (5 wires)	A_{cord}	0,538 mm²
	- n° cords/cm		1,57 cords/cm
	- mass (inclusive of thermal welding)		≈ 670 g/m²
	- equivalent thickness of sheet	t_{sheet}	≈ 0,084 mm
	- tensile breaking load of a cord		> 1500 N
	- tensile strength of the sheet	σ_{sheet}	> 2800 MPa
	- tensile strength by unit of width	σ_{sheet}	> 2,35 kN/cm
	- normal elastic modulus of sheet	E_{sheet}	> 190 GPa
	- break warp of the sheet	ε_{sheet}	> 1,50%
Pack	50 m rolls (h 30 cm)		
Weight of 1 roll	≈ 24 kg including packaging		

WARNING

- **Product for professional use**
- abide by any standards and national regulations
- when handling the sheet wear protective clothing and goggles, and follow the instructions regarding methods for applying the material
- contact with the skin: no special measures required
- storage on the work site: store under cover in a dry place, well away from substances that might damage it or its ability to adhere to the chosen matrix
- if necessary, ask for the safety data sheet
- for any other issues, contact the Kerakoll Worldwide Global Service +39 0536 811 516 - globalservice@kerakoll.com

00175GeoSteel G600 Code: E885 2014/07

KERAKOLL S.p.a.
Via dell'Artigianato, 9 - 41049 Sassuolo (MO) Italy
Tel +39 0536 816 511 - Fax +39 0536 816 581
info@kerakoll.com - www.kerakoll.com

Glass fabric:

MAPEI

Mapegrid G 220

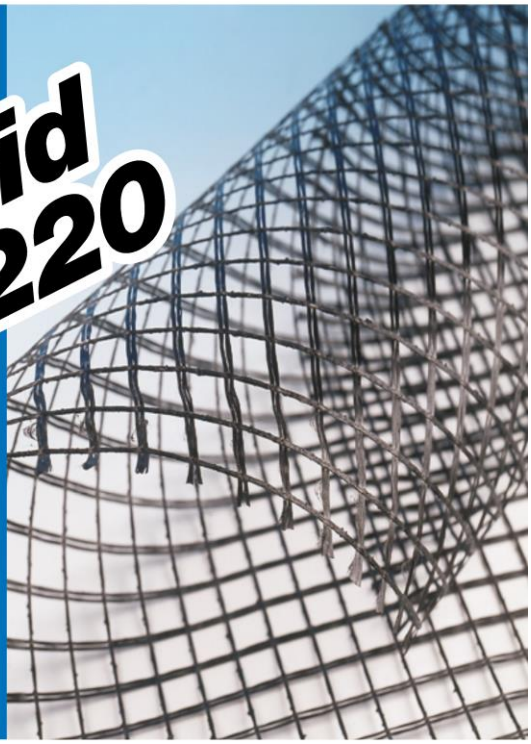

Primed alkali-resistant A.R. glass fibre mesh for structural "reinforced" strengthening of stone, brick, tuff and mixed masonry structures

WHERE TO USE

Primed alkali-resistant A.R. glass fibre mesh used in combination with **Planitop HDM Maxi** (two-component ready-mixed high ductility pozzolan-reaction fibre-reinforced cementitious mortar for structural "reinforced" strengthening of masonry structures) or **Planitop HDM Restauro** (two-component ready-mixed high-ductility fibre reinforced natural hydraulic lime (NHL) and Eco-pozzolan based mortar for structural "reinforced" strengthening of masonry structures) to strengthen stone, brick, tuff and mixed masonry structures in order to improve the resistance and the overall ductility.

Mapegrid G 220 mesh is part of the **Mapei FRG System**, a complete range of composite materials that use an inorganic matrix to guarantee excellent chemical-physical and elastic-mechanical compatibility with masonry substrates. This type of system offers several important advantages when used on buildings of historical or artistic interest. Rather than replace existing structures, the system works in parallel with them without altering the way the masses and rigidity within the structures are distributed.

The latter is a very important aspect, particularly in the field of seismic design, where stresses are proportional to the masses involved.

The system follows the approach defined by the guidelines for the approval of FRCM (Fibre Reinforced Cementitious Matrix) systems which stress the importance of obtaining approval for the entire strengthening package.

Some application examples

- Shear/tensile strengthening of bay walls through application to the internal and/or external face.
- Structural strengthening of masonry arches and vaulted roofs through application to both the external and internal faces.
- Strengthening reinforcement for more even distribution of stresses induced by seismic activity.

TECHNICAL CHARACTERISTICS

Mapegrid G 220 is a special square mesh made from primed, alkali-resistant A.R. glass fibres with a zirconium dioxide content of 17% which, thanks to its special weave, when applied on masonry structures makes up for their lack of tensile strength and increases their overall ductility so that stresses are distributed more evenly. As a result, in the event of movements in the structure, the strengthening package has the ability to distribute stresses and strains over the entire surface of the members and elements strengthened with the mesh so that its failure mode is transformed from fragile type to ductile type. The system adheres perfectly to the substrate and its mechanical properties are such that localised stresses always provoke a failure in the substrate rather than at the substrate/strengthening system interface. In the case of strengthening applied to arched or vaulted elements, the masonry acquires the ability to resist tensile loads and inhibit the formation of plastic hinge points on the side opposite to where the strengthening package is applied.

Mapegrid G 220

Application of the first layer of Planitop HDM Maxi

Positioning of Mapegrid G 220

TECHNICAL DATA (typical values)	
PRODUCT IDENTITY	
Type of fibre:	A.R. glass fibre
Zirconia content (ZrO_2) (%):	17
Weight (g/m²):	225
Mesh size (mm):	25 x 25
APPLICATION DATA	
Tensile strength (kN/m):	45
Modulus of elasticity (GPa):	72
Load-resistant area per unit of width (mm²/m):	35.27
Equivalent thickness of dry fabric (mm):	0.035
Elongation at failure (%):	1.8

ADVANTAGES

- Excellent tensile strength.
- Stable and resistant to chemical aggression by cement.
- Resistant to atmospheric agents.
- High dimensional stability.
- High durability and stability within the inorganic matrix.
- Limited intrusiveness concerning the aesthetical appearance of the existing structure.
- Does not rust.
- Light and easy to handle.
- Easy to cut and fold to suit the shape of the substrate.

APPLICATION PROCEDURE

Preparation of the substrate

Surfaces on which **Mapegrid G 220** is to be applied must be prepared according to specification. When used to strengthen bay walls or the internal face of arched or vaulted members and elements, the render must be completely removed either manually or with suitable power tools, along with any deteriorated or detached areas until the substrate is sound, compact and strong so that the strengthening package itself does not detach. This operation must be carried out until the underlying masonry is exposed. While the render is being removed, if new stones, bricks and/or tuff are required to fill large gaps in the wall, use material with characteristics as similar as possible to the material originally used to build the structure. When used to strengthen the external face of masonry vaulted members and elements, remove all the flooring and spandrels and any deteriorated or detached areas until the substrate is sound, compact and strong so that the strengthening package itself does not detach.

We recommend hydro-cleaning surfaces with low pressure water jets. Leave surface water to evaporate off so that the masonry is saturated and the surface is dry (s.s.d. condition). Compressed air may be used to speed up this process.

Application technique

Application of the first layer of mortar

Prepare **Planitop HDM Maxi** or **Planitop HDM Restauro** (see the relative Technical Data Sheet).
Apply an even layer of **Planitop HDM Maxi** or **Planitop HDM Restauro** around 5-6 mm thick with a flat metal trowel or by spray. Level off the surface of the wall to form a sufficiently flat layer.

Application of Mapegrid G 220
After applying the first layer of mortar and while it is still fresh, place **Mapegrid G 220** mesh all over the surface and press down lightly with a flat trowel so that it adheres perfectly to the mortar. Overlap adjacent pieces of **Mapegrid G 220** by at least 15 cm both lengthways and widthways.

Application of the second layer of mortar
Apply a second even layer of **Planitop HDM Maxi** or **Planitop HDM Restauro** around 5-6 mm thick so that it completely covers the mesh.

We recommend folding the strengthening package over the imposts by at least 40 cm, especially when working on the internal or external face of arched and vaulted elements and members.

Protecting the strengthening system
In order to improve the anchoring mechanism of the strengthening system, strategically placed connectors made from **MapeWrap FIOCCO** may also be applied (see relative Technical data Sheet) on the facing wall or on the imposts, keystones and around the springers of arched or vaulted members. The connectors eliminate any "debonding" phenomenon and increases the static efficiency of the strengthening package applied. The number and pitch of the connectors is defined during the design phase.

PACKAGING
Mapegrid G 220 is supplied in 0.90 m wide by 45.70 m long rolls packed in cardboard boxes.

STORAGE
Store in a covered dry area.

SAFETY INSTRUCTIONS FOR PREPARATION AND APPLICATION
Mapegrid G 220 is an article and referring to the current European regulations (Reg. 1906/2007/CE - REACH) does not require the preparation of the Safety Data Sheet. During use it is recommended to wear gloves and goggles and follow the safety requirements of the workplace.

PRODUCT FOR PROFESSIONAL USE.

WARNING
Although the technical details and recommendations contained in this product data sheet correspond to the best of our knowledge and experience, all the above information must, in every case, be taken as merely indicative and subject to confirmation after long-term practical application; for this reason, anyone who intends to use the product must ensure beforehand that it is suitable for the envisaged application. In every case, the user alone is fully responsible for any consequences deriving from the use of the product.

Please refer to the current version of the Technical Data Sheet, available from our website www.mapei.com

LEGAL NOTICE
The contents of this Technical Data Sheet ("TDS") may be copied into another project-related document, but the resulting document shall not supplement or replace requirements per the TDS in force at the time of the MAPEI product installation.
The most up-to-date TDS can be downloaded from our website www.mapei.com.
ANY ALTERATION TO THE WORDING OR REQUIREMENTS CONTAINED OR DERIVED FROM THIS TDS EXCLUDES THE RESPONSIBILITY OF MAPEI.

All relevant references for the product are available upon request and from www.mapei.com

Appendix II: Analytical modeling of pull-pull test configuration

The pull-out load versus fiber the end displacement relationship of pull-pull specimens can be summarized in the following equations. These equations are rewritten based on Naaman et al. [65,85].

The critical force and fiber slip in the elastic stage are:

$$P_{crit} = \frac{\tau_{max}\psi}{\lambda} \times \frac{QA_mE_m \sinh(\lambda L)}{\left[\cosh(\lambda L)(QA_mE_m - 1) + 1\right]} \quad \text{Eq.AII 1}$$

$$S = \frac{P(\cosh(\lambda L) - 1)}{\lambda \sinh(\lambda L)}\left(Q - \frac{2}{A_mE_m}\right) \quad \text{Eq.AII 2}$$

In addition, in the nonlinear stage, the pull-out load, the fiber slip, and the pull-out end slip at full debonding are equals to:

$$P = \frac{t_{(max)}}{\lambda} \frac{QA_mE_m \sinh(\lambda(L-u))}{\left[\cosh(\lambda(L-u))(QA_mE_m - 1) + 1\right]} + t_f u \quad \text{Eq.AII 3}$$

$$S = \frac{-PL}{A_mE_m} + \frac{Qu}{2}(2P - t_f u) + \frac{P - t_f u}{\lambda A_mE_m} \times \left[\frac{\cosh(\lambda(L-u)) - 1}{\sinh(\lambda(L-u))}(QA_mE_m - 2) + \lambda(L-u)\right] \quad \text{Eq.AII 4}$$

$$S_0 = t_f L^2\left(\frac{Q}{2} - \frac{1}{A_mE_m}\right) \quad \text{Eq.AII 5}$$

The pull-out load of the dynamic stage and its slip are equal to:

$$P_{dyn} = \left(1 - \exp\left\{\frac{-2\upsilon_f \mu x}{E_f r_f\left[\frac{(1+\upsilon_m)}{E_m} + \frac{(1+\upsilon_f)}{E_f}\right]}\right\}\right)\frac{\delta E_f \pi r_f}{\upsilon_f} \quad \text{Eq.AII 6}$$

$$S_{dyn} = \frac{-P(L-v)}{A_mE_m} + \frac{Qt_f}{2}(L-v)^2 + v \quad \text{Eq.AII 7}$$

where δ is the coefficient of fiber-matrix misfit and x is the embedded length of the fiber. Also, ν_f and ν_m are the Poisson's ratios for the fiber and the mortar, respectively. r_f is fiber radius, and μ is the friction coefficient assumed as 0.06. The formula for obtaining δ can be found in [44].

In order to calculate tmax and tf, the following three equations should solve:

$$t_f - t_{(max)}QA_mE_m\left[\frac{QA_mE_m \sinh(\lambda(L-u_p))}{\left(\cosh(\lambda(L-u_p))(QA_mE_m - 1) + 1\right)^2}\right] = 0 \quad \text{Eq.AII 8}$$

$$t_f u_p - \frac{t_{(max)}}{\lambda} Q A_m E_m \left[\frac{Q A_m E_m \sinh\left(\lambda\left(L - u_p\right)\right)}{\left(\cosh\left(\lambda\left(L - u_p\right)\right)\left(Q A_m E_m - 1\right) + 1\right)} \right] - P_p = 0 \qquad \text{Eq.AII 9}$$

$$\frac{-PL}{A_m E_m} + \frac{Q u_p}{2}\left(2P_p - t_f u_p\right) + \frac{-P_p - t_f u_p}{\lambda A_m E_m}\left[\frac{\cosh\left(\lambda\left(L - u_p\right)\right) - 1}{\sinh\left(\lambda\left(L - u_p\right)\right)}\left(Q A_m E_m - 2\right) + \lambda\left(L - u_p\right) \right] - S_p = 0 \qquad \text{Eq.AII 10}$$

λ can be calculated from the following equation:

$$\left(\frac{P}{S}\right) = \frac{\lambda \sinh\left(\lambda L\right)}{\left(Q - \frac{2}{A_m E_m}\right)\left(\cosh\left(\lambda L\right) - 1\right)} \qquad \text{Eq.AII 11}$$

Q and κ in above equations are expressed as:

$$Q = \frac{1}{A_f E_f} + \frac{1}{A_m E_m} \qquad \text{Eq.AII 12}$$

$$\kappa = \frac{\lambda^2}{\psi Q} \qquad \text{Eq.AII 13}$$

Appendix III: Analytical prediction of shear strength of reinforced panels

Masonry properties:

- Height of the wall [mm]: H_w= 540 mm
- Length of the wall [mm]: L'= 540 mm
- Net cross-sectional area [mm²]: A_n= 54000
- Compressive strength of masonry [MPa]: $f'_m = 11.1$
- Tensile strength of masonry [MPa]: $f'_t = 0.67\sqrt{f'_m} = 2.23$
- The inclined angle between the horizontal and main diagonal of the wall: θ= 45°

TRM properties:

- Area of fabric per unit width in both directions [mm²/mm]: A_f= 2×0.03527= 0.07054
- Ultimate tensile strain of TRM [mm/mm]: ε_{fu}= 0.0119
- Tensile modulus of elasticity of cracked TRM [MPa]: E_f= 62700
- Number of fabric layers: n= 1

Masonry contribution (V_m):

$$V_m = \frac{\tan\theta + \sqrt{21.16 + \tan^2\theta}}{10.58} f'_t A_n \left(\frac{L'}{H_w}\right) =$$

$$\frac{\tan 45 + \sqrt{21.16 + \tan^2 45}}{10.58} 2.23 \times 54000 \left(\frac{540}{540}\right) = 65025\,N \qquad \text{Eq.AIII 1}$$

TRM contribution (V_f)

$$\varepsilon_{fv} = \varepsilon_{fu} = 0.0119 \not\leq 0.004 \Rightarrow \varepsilon_{fv} = 0.004$$

$$f_{fv} = E_f \varepsilon_{fv} = 62700 \times 0.004 = 250.8\,MPa \qquad \text{Eq.AIII 2}$$

$$V_f = 2nA_f L' f_{fv} = 2 \times 1 \times 0.07054 \times 540 \times 250.8 = 19106\,N \qquad \text{Eq.AIII 3}$$

Nominal shear capacity (V_n)

$$V_n = V_m + V_f = 65025 + 19106 = 84131\,N = 84\,kN \qquad \text{Eq.AIII 4}$$

Appendix IV: Analytical prediction of flexural strength of reinforced panels

Masonry properties:

- The thickness of the masonry wallet [mm]: $t = 100$ mm
- Width of the masonry wallet considered in the flexural analysis [mm]: $b_m = 420$ and 330 for masonry PS and NS, respectively
- Compressive strength of masonry [MPa]: $f'_m = 11.1$

TRM properties:

- Area of fabric per unit width [mm²/mm]: $A_f = 0.03527$
- Effective tensile strain level in the TRM [mm/mm]: $\varepsilon_{fe} = 0.7\varepsilon_{fu} = 0.7 \times 0.0119 = 0.0083 \leq 0.012 \Rightarrow \varepsilon_{fe} = 0.0083$
- Tensile modulus of elasticity of cracked TRM [MPa]: $E_f = 62700$
- Thickness of TRM composite [mm]: $t_c = 10$

Flexural strength:

- Effective tensile stress level in the TRM composite [MPa]: $f_{fe} = E_f \varepsilon_{fe} = 62700 \times 0.0083 = 520.41\,\text{MPa}$
- Stress block coefficient related to c: $\beta_1 = 0.7$
- Stress block coefficient related to f'_m: $\gamma = 0.7$
- Depth of effective compressive block [mm]: $c = \frac{A_f f_{fe}}{\gamma f'_m \beta_1} = \frac{0.03527 \times 520.41}{0.7 \times 11.1 \times 0.7} = 3.375\,\text{mm}$
- Nominal flexural strength [N.mm]: $M_n = A_f b_m f_{fe}\left(t + \frac{t_c}{2} - \frac{\beta_1 c}{2}\right)$
- For PS (failure parallel to bed joint):

$$M_n = 0.03527 \times 420 \times 520.41\left(100 + \frac{10}{2} - \frac{0.7 \times 3.375}{2}\right) = 800343\,\text{N.mm}$$

For NS (failure normal to bed joint):

$$M_n = 0.03527 \times 330 \times 520.41\left(100 + \frac{10}{2} - \frac{0.7 \times 3.375}{2}\right) = 628840\,\text{N.mm}$$